Customized Instrumentation for Small-Volume Electrochemistry and Microfluidics used in Bioanalytical Applications

by

Mark David Holtan

A dissertation submitted to the Graduate Faculty of
Auburn University
in partial fulfillment of the
requirements for the Degree of
Doctor of Philosophy

Auburn, Alabama
December 15, 2018

Keywords: Microfluidics, 3D-Printing, Electrochemistry, Potentiostat, Circuits

Approved by

Christopher J. Easley, Chair, Knowles Professor of Chemistry and Biochemistry
Curtis Shannon, Andrew T. Hunt Professor and Chairman of Chemistry and Biochemistry
Vince Cammarata, Emeritus Associate Professor of Chemistry and Biochemistry
Wei Zhan, Associate Professor of Chemistry and Biochemistry

Abstract

Disease biomarker detection allows diagnosis of both chronic and acute conditions. Although current detection methods are adequate for several targets (e.g. enzymatic biosensors), the stability and limited number of targets leave room for new biosensor development. In this dissertation, new tools are developed in both microfluidic flow control and electrochemical instrumentation to further advance biosensor applicability.

Surface-confined electrochemical biosensors require uniform electrode surfaces free from fouling onto which self-assembled monolayers are formed. Researchers are required to laboriously hand polish multiple electrodes to carry out experiments. In Chapter 2, an electrode polishing robot (EPBot) is created and investigated. The EPBot is a 3D-printed articulating arm robot, drawing a figure "8" continuously over 10 min to mimic hand polishing. The EPBot is shown to be similar to hand polishing by both electrochemical experiments and atomic force microscopy.

Bioanalytical detection methods are also influenced by temperature. Chapter 3 describes the construction of two thermal controllers, applied to either optical or electrochemical detection method development. The first controller was based on the LabVIEW virtual instrument environment capable of generating precise temperature steps with a Peltier device. The controller was used to interrogate thermal response of branched DNA detection systems. These studies reiterate the importance of thermal conditions in DNA detection systems and present data showing shifts in detection sensitivity as temperature varies. The second thermal controller, driven by the Arduino programming environment was designed to incorporate portability and a second Peltier element capable of a 70 °C gradient generation. Finally, a single micro-Peltier version was successfully applied to quantitative microfluidic thermofluorimetric DNA melt detection of both insulin and thrombin.

The surface-confined nucleic acid based electrochemical detection methods used in the aforementioned chapter exhibit a trade-off between signal intensity and charging current when using pulse voltammetry techniques. We show that differential measurements between two identical working electrodes, where one electrode is exposed to Faradaic current, allow significant reduction of charging current. For this reason, a real-time analog differential potentiostat was designed, constructed, and characterized in Chapter 4. The differential potentiostat (DiffStat) was validated by comparison to a conventional potentiostat with common electrochemical experiments: chronoamperometry, cyclic voltammetry, and square wave voltammetry. A drastic removal of charging current was shown. The DiffStat was then applied to surface-confined DNA systems at duplicate gold electrodes with increasing surface area. A reduction in both noise and baseline current were shown with the DiffStat when compared to the conventional potentiostat. Various assay modes of operation were then demonstrated using the DiffStat, and matrix effects were shown to be negligible.

Chapter 5 details the construction of customized support equipment utilized in other chapters within this dissertation. Equipment included in this chapter are: CO_2 laser drill, UV LED photolithography exposure unit, microfluidic solenoid valve controller, electronic pressure meters, diode laser controller, PID laboratory oven controller, microscope LED light source, and a reflow soldering oven.

The lab-on-a-chip concept incorporates laboratory operations into a microfluidic device such as sample clean-up, separation, and detection, but these often require many actively-controlled valves on-chip. Moving fluidic valve control into the chip by creating microfluidic logic circuits can increase the number of operations on a chip and reduce external drive component requirements. Fluidic logic circuits can leverage fluidic analogs of electronic components, e.g. resistors, diodes, and transistors. Like electronic devices, such fluidic components would ideally be tunable, but few examples exist. Novel, tunable fluidic resistors, diodes, and transistors were designed and investigated in Chapter 6.

Finally, in Chapter 7 this dissertation is summarized, and future work is presented.

Acknowledgments

Attaining a doctoral degree has many challenges, I would like to thank the following people for their help in overcoming those challenges and supporting me during the process.

Firstly, I would like to extend my deepest appreciation to Dr. Chris Easley. He has guided me in these past 5 years with his mentorship, patience, and sense of humor. These qualities set a high standard for the person and scientist I would like to become.

Next, I would like to give sincere thanks to my committee: Dr. Wei Zhan, Dr. Leonardo De La Fuente, Dr. Vince Cammarata and Dr. Curtis Shannon who were meticulous and kind with their advice. I would like to highlight Dr. Bart Prorok and Mari Anne Sullivan, for training and allowing the use of the sputtering facilities. I extend my gratitude to Dr. Rik Blumenthal for allowing the use of tools from his lab.

I would like to thank Dr. Jessica Crumbley Brooks, a great friend and colleague lending expertise and an open mind. I would like to thank Dr. Subramaniam Somasundaram for his constructive input, quick wit and sense of humor. The lab would not have been as fun without you. Dr. Walter Casper III also brought enlightening discussion and I want to recognize him for that. I would like to thank Dr. Xiangpeng Li and Dr. Jean Negou for their microfluidic fabrication insights. I'd also like to thank Dr. Juan Hu for stretching my horizons, culturally and scientifically. Additionally, I would like to thank the rest of our group members for their contributions and the great times.

I extend a whole hearted thanks to my parents for providing constant support throughout my life. Finally, to my wife Raquel your patience, love, and encouragement throughout this whole process has made me a better scientist and I will be forever grateful.

Dedicated to my Wife.

Table of Contents

List of Figures

List of Tables

List of Abbreviations

μTFA	Microfluidic TFA
ABS	Acrylonitrile Butadiene Styrene
ADC	Analog to Digital Converter
AFM	Atomic Force Microscopy
CAD	Computer Aided Design
CV	Cyclic Voltammetry
DiffStat	Differential Potentiostat
DMD	Digital Micromirror Device
ELISA	Enzyme Linked Immunosorbet Assay
EPBot	Electrode Polishing Robot
FDM	Fused Deposition Manufacturing
GO_x	Glucose Oxidase
GoG	Gold on Glass electrodes
IC	Integrated Circuit
IMD	Integrated Microfluidic Devices
L_{ox}	Lactate oxidase
LDH	lactate dehydrogenase
NCV	Normally Closed Valve
PC	Polycarbonate
PCB	Printed Circuit Board
PCR	Polyermase Chain Reaction
PID	Proportional Integral Derivative
PJ	Polyjet Printing

PLA Polylactic Acid Filament

PLA Polylactic Acid

POC Point of Care

PS Polystyrene

Pstat Conventional Potentiostat

qPCR Real-Time Quantitative Polymerase Chain Reaction

SA Surface Area

SAM Self Assembled Monolayer

SLA Stereolithography Printing

SLS Selective Laser Sintering Printing

SWV Square-Wave Voltammetry

TFA Thermofluorimetric Analysis

TIA Transimpedance Amplifier

tsEC Thermal Scanning Electrochemical Detection

Chapter 1

Introduction

1.1 Biosensor Development

Biosensor development is a burgeoning field, which identifies new methods for detection of disease related in biological samples. Biosensor applications include use in clinical, military, consumer, food, agriculture, and veterinary services[1]. A biosensor is a chemical type sensor, detecting analytes by utilizing a biochemical recognition unit that undergoes a conformational change or reaction. For example, an electrochemical biosensor with recognition units immobilized on an electrode is exposed to an analyte, and recognition unit transfers electrons to the transducer which registers a current flow and generates a signal which is recorded by a signal processor (Figure 1.1)[2, 3].

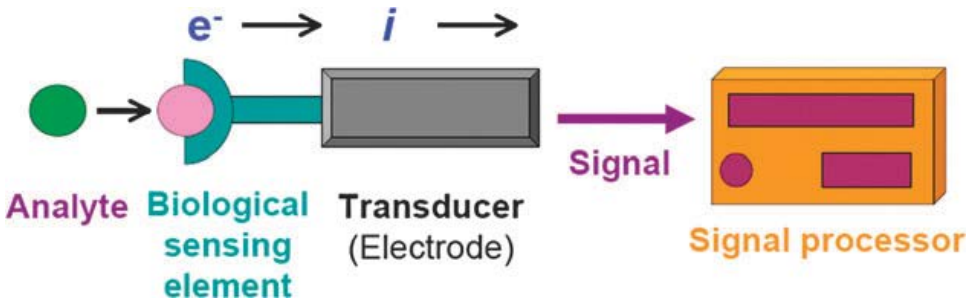

Figure 1.1: **Biosensor analyte detection scheme** Sensor converts the interaction of an analyte to an electrochemical signal, which is transduced to the signal processor. Reproduced in part from [3] with permission of , ©2010, The Royal Society of Chemistry.

The creation of new biosensor techniques for disease biomarkers is challenged by many factors including: versatility, economics, simplicity (ease of use), storage stability, rapid analysis, sensitivity, specificity, selectivity, robustness and portability[4]. A biosensor developed for the medical industry should be versatile, should function in multiple sample matrices, and

should be multiplexable for simultaneous detection of several analytes, reducing the requirement for larger sample gathering. A biosensors cost and ease of use drive its application and acceptance in the medical community, by affording minimally trained personnel to complete diagnoses. For example, a rapid detection method within timescales of a physician's office visit (20 min) would compete directly with the current bacterial screening methods, which still require culturing of bacteria and identification by trained personnel. Additionally, for remote, military, or developing world applications, storage considerations are paramount[1]. Finally, the dynamic range plays a role in method development, where dynamic range is the detection region of an assay.[5, 6]. When designing a biosensor system, the typical circulating concentration of analyte in a patient is not the target for limit of detection; the limit should extend below the circulating levels to allow monitoring of treatments, since it is not desirable to report an undetectable value of a disease biomarker[7].

Diseases biomarkers normally consist of nucleic acids or proteins in biological matrices at low concentrations, requiring signal amplification to achieve adequate sensitivity. Two types of amplification are used in biosensors: target-based amplification or signal-based amplification. In target-based amplification, the target interacts with the sensor, starting a chain reaction of amplification of the target or a surrogate. Methods based on amplification with polymerase chain reaction (PCR) are an example of this type. The signal-based amplification occurs from a single analyte binding event that is catalytically amplified. An example of a signal based amplification is enzyme linked immunosorbent assay (ELISA), a selected antibody binds to the target molecule and a second antibody associated with a reporter or reporter generating molecule then amplifies and creates a detectable signal[6].

Target-based amplification has exponential signal amplification and is considered higher sensitivity than signal-based methods. As a bioassays sensitivity increases, so does the potential of detecting lower concentrations of analyte in other bodily fluids rather than strictly blood or serum. However, as in the PCR example, instability and variability due to

enzymatic processes can limit use in medical settings, and optimization is usually required for a specific target especially if typical clinical multiplexing is required.

Selectivity is the ability to detect a specific biomolecule within a complex mixture of possibly similar biomolecules. Generally, biosensors exploit nature's machinery for high target specificity, such as enzymes' or antibodies' high binding and/or reaction specificities. Of course, such detection methods can sometimes suffer from nonspecific binding of proteins in the sample, increasing the baseline of the detection and reducing selectivity. Aptamers have emerged as a replacement to antibodies with higher stability, and their ease of modification/editing can be used to help in tailoring selectivity.

A robust biosensor can be used in multiple environments and does not require specialized storage conditions or tedious data set interpretation. Portability refers to the physical size, weight and ease of use of a medical device, if a developed device is too large, complex or temperature sensitive it may not be transfered to a commercial product. Currently, medical diagnostic labs are located remotely from the collection site such as a doctor's office or emergency outbreak outpost in the developing world, requiring expensive large equipment and trained personnel to operate. Bioassays sometimes do not incorporate robustness, portability and low cost into their final form, which would have otherwise driven them to application development. If large amounts of data are generated and the interpretation of the data set is complicated or requiring significant skill, the data is not translated into useful information for a patient in a timely manner[8, 9]. More recently, remote diagnosis has become popular, moving slowly from a centralized diagnostic laboratory which houses large instrumentation, into doctors' offices or patients' homes, underscoring the development of robust, and portable biosensor platforms.

Biosensor Recognition Elements The most prevalent biosensor available commercially is the pregnancy test, followed by the glucose sensor, and closely by sensors for lactate and glutamate.[1] These commercial biosensors rely on conversion of target recognition into a measurable signal. The analyte is detected by a recognition element, which interacts with

the transducer creating a signal, which is amplified and displayed. Successful biosensors require high sensitivity and specificity when interacting with the target molecule, and the output signal should be proportional to the concentration of the target analyte. These typically exploit biological recognition elements such nucleic acids or proteins (enzymes, antibodies). There are two main types of biosensors, biocatalytic devices or affinity sensors. Biocatalytic detection methods rely on recognition and downstream biochemical reactions, as in enzyme biosensors. Affinity sensors rely simply on the binding of the target to the recognition element, producing a signal such as an electrochemical current.

Enzymatic biosensors are amongst the most common and well-studied biosensors[1] and have very high selectivity in complex matrices. However, many biochemical analytes are not conducive to enzymatic biosensors, either they are not commonly found in living systems or there is no specific enzyme that will function with a sensor. Affinity biosensors combine a recognition element such as an antibody or aptamer, which strongly and specifically binds to the target analyte by structural matching. Immunosensors are antibody-based sensors with low detection limits and high selectivity. The antibodies are created by introducing an antigen to a living animal and separating the antibody produced to recognize the antigen. After many years of commercial development, these days a wide variety of analytes can be detected, including bacteria, viruses, hormones, drugs, pesticides, etc[9]. Nucleic acids are also used for detection, where short oligonucleotides selected specifically for a target are used to detect species of interest with very high selectivity and sensitivity[3].

One specific form of nucleic acid biosensor is based on aptamers. In the early 1990s, nucleic acid aptamers were introduced as in vitro selected binding agents with high specificity. Aptamers are oligonucleotide segments which are selected against the target molecule of interest, forming complex structures of secondary or tertiary components. Aptamers act as a sort of chemically synthesized antibody, demonstrating several benefits such as selectivity against a library of chemicals or even cells. PCR can be performed on selected aptamers, allowing large amounts of a single aptamer to be synthesized, removing animal or cell line

amplification from the process. The aptamer structure allows modification due to its simplicity and the advancement of nucleic acid synthesis and editing technologies. Finally, aptamers are more thermally stable than antibodies and can be reversibly denatured[10].

Commercial Biosensor Successes Small molecule detection has already been successfully transitioning to the commercial market. For example, glucose, lactate, and glutamate can be detected with enzyme-based biosensors, as discussed herein.

Diabetes is a growing epidemic amongst the US and other countries, and these patients rely heavily on glucose monitoring devices. The enzymatic glucose sensor is the most widely used electrochemical biosensor. Human blood normally contains between 4.0 and 5.9 mM glucose, and a concentration above 6.9 mM after an 8 hour fast is considered a diabetic diagnosis. The main component of the glucose sensor is glucose oxidase (GO_x), and proportionally generated H_2O_2 in the presence of glucose. The oxidization of H_2O_2 (facilitated by molecular O_2) at an electrode is a two-electron process, and results in a current flow proportional to the concentration of glucose in solution. The basic principle of glucose sensing was commercially viable, however sensors still required molecular oxygen and were sensitive to blood interferences. The second generation GO_x sensor relied on a mediator (non-physiological electron transfer mediator) operating at lower potentials to reduce electroactive interferences from being redox cycled in blood. Third generation GO_x sensors strive to directly detect precursor cofactors and directly transfer electrons rather than rely on H_2O_2 detection. Commercially viable examples of both generation two and three exist and are used extensively. Both generations still rely on glucose oxidase, an enzyme, requiring storage at $<44\,^{\circ}C$ and pH 2-8, which significantly limits storage conditions and therefore require expensive methods to attain long term storage[3, 9, 11].

Lactate results from oxygen deficiency in humans, which can be caused by respiratory failure, hemorrhage, ischemia from lactate acidosis, trauma and diabetes. Anaerobic glucose breakdown in tissue results in lactic acid, which in normal humans is between 0.5 – 1.0 mM; any level above 4.0 mM is considered out of range and a result of serious illness.

Liver metabolism reconverts lactic acid back to pyruvate quickly, maintaining serum pH between 7.2 and 7.4 under normal conditions. Two enzymes are used to detect Lactate, lactate oxidase (L_{ox}) or lactate dehydrogenase (LDH) which generate electroactive species resulting from conversion of lactate. Electrochemical methods of lactate sensing require immobilization of the enzyme close to the electrode surface, and typically use membrane entrapment, physical adsorption, or covalent coupling by cross-linking agents. As with GO_x, the lactate enzyme requires close coupling to the electrode surface requiring an electron transfer medium.Lactate biosensors play a large role in diagnosis of the disease and are used extensively in commercial applications. [3, 9, 11, 12].

Glutamate is considered a primary neurotransmitter, playing a major role in neural activation. When detected in brain fluids, glutamate can be the result of brain trauma, stroke, or possibly disease (multiple sclerosis, Alzheimer's, Parkinson's). Typical extracellular concentrations are $\sim$0.05 mM. Biosensors are based on glutamate oxidase or glutamate dehydrogenase, which evolves H_2O_2 or directly transfer an e^- as with the previous enzyme based biosensors.[9, 13].

These three examples of biosensors highlight the medical necessity for accurate and sensitive detection methods. Several other notable enzymatic biosensor assays are for dopamine, acetylcholine, norepinephrine, nitric oxide, lactose, uric acid, urea, cholesterol, creatine, creatinine, ketone bodies, and xanthine[3, 14, 15]. Most enzymatic biosensors,are sensitive, inexpensive, and have fast response time solidifying there place in the commercial biosensor market. However, enzymatic electrochemical biosensors are plagued by biofouling, sample interferences, and instability of the transduction system.[9, 11, 12]. Furthermore, many other molecules do not have compatible selective enzymes which participate in redox reactions electrochemical biosensing.

Electrochemical Detection Techniques Electrochemical detection is easy to perform, low cost, and portable. Signals can be generated by potentiometry, amperometry, electrochemical impedance spectroscopy, and conductometry[3, 11]. Electrochemistry is largely volume

independent, allowing small volume measurements, and possible detection limits are in the attomole to zeptomole range[3, 16]. An electrochemical cell is required to carry out an electrochemical analysis. The most common electrochemical cell consists of three electrodes: working, counter, and reference. Electrochemical processes occur at the working electrode by precisely driving its potential/current and measuring the resulting signal output. The reference electrode maintains a stable and known potential without interfering with electrochemical reactions at the working electrode surface, an example is the silver/silver chloride reference. The counter electrode allows current to flow to the working without disturbing the reference electrode's stable potential, ensuring repeatability of measurements[11, 15, 17]. The working and counter electrodes are usually made of an inert metal such as the platinum group metals (platinum, gold, silver) where the electrode has minimal influence on the electrochemical reaction occurring at its surface. A reference electrode consists of a redox system generating a known potential to drive the working electrode's potential precisely. Other types of electrodes exist for specific applications, such as metal coated glass, screen printed electrodes, and microelectrodes[11, 15, 17].

Voltammetry is performed by varying the potential at the working electrode and recording the current response from the electrochemical cell, resulting in a peak or plateau which is proportional to the concentration of analyte. Alternatively, in amperometry a potential step is applied to the working electrode and held, and the current decay is recorded versus time[3, 11]. Multiple experiments can be formulated from the combination of parameters (current, potential, time, charge) present in both voltammetry and amperometry. One technique commonly employed in electrochemical biosensors is square wave voltammetry (SWV), a pulsed voltammetry technique[18]. SWV is a complex combination of step and scanning techniques, creating an alternating step profile. The excitation potentials are a mixture of a square wave and a staircase potential (Figure 1.2). The square wave component alternatively oxidizes and reduces the species of interest, while the step component varies the potential, scanning a range of potentials. The output has a large non-Faradaic current, which can decay before

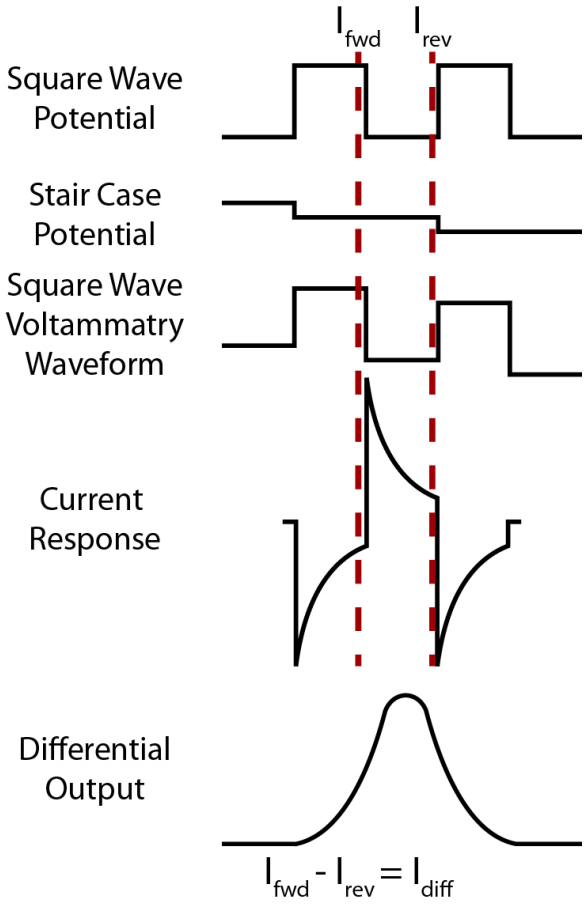

Figure 1.2: **Principles of square wave voltammetry** Square wave voltammetry, a square wave is superimposed on a stair step signal. The current response is idealized, and the measurement points are at the red dotted lines, the difference of those measurements is then plotted in the final waveform. Reprinted in part with permission from [18]. © 1969 American Chemical Society.

a measurement is recorded (Figure 1.2 red dashed line) and is termed the forward current (I_{fwd}). The square wave then reverses creating a second large non-Faradaic component in the reverse direction (I_{rev}) and another current is recorded after the non-Faradaic current decays. The difference of the resulting forward and reverse currents is the current difference (I_{diff}), which is plotted resembling a traditional Gaussian peak[19].

Potentiostat Function and Circuitry Electrochemical instrumentation centers around the potentiostat which applies signals to the electrochemical cell, measures the response from the cell, and records the resulting output. A potentiostat consists of an input stage driving the counter electrode, the output transducer connected to the working electrode, and

a feedback stage to monitor and set the cell's potential accurately against a known standard reference potential. A typical three-electrode potentiostat circuit is depicted in Figure 1.3. User Input is fed into an operational amplifier from a computer (PC) to set the desired potential of the cell, and a buffer (B) allows high current to flow into the electrochemical cell via the counter electrode. A unity gain buffer amplifier connects to the reference and through a resistor drives the input to maintain a set potential in the cell with respect to the reference electrode. Current flow between the working and counter electrode is measured at the working electrode by a transimpedance amplifier (TIA) or current follower circuit. The TIA's output is equal to the current flow through the amplifier and resistor combination. By changing resistor 2 (R_2), different sensitivities can be selected for the TIA allowing versatility in the circuit[17].

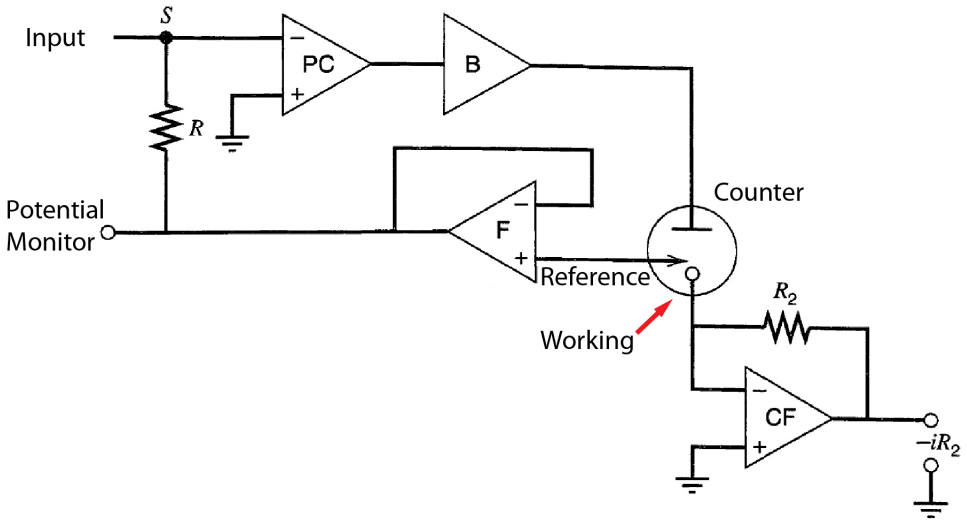

Figure 1.3: **Potentiostat Circuit.** Common potentiostat circuit configuration. Reproduced in part from reference [17] with permission from,©2001, John Wiley and Sons.

Electrochemical detection in Microfluidic Platforms Small volume analysis has many benefits including: reduction of reagent costs and waste generation, speed of analysis, and facility overhead costs. Electrochemical detection methods are compatible with microfluidics. The combination of both microfluidics and electrochemical detection paves the way for point of care (POC) applications. A POC device is a fully contained handheld portable

laboratory, where a sample is placed in the instrument and the system performs the analysis automatically, outputting a number to aid in diagnosis of a medical condition. POC devices for measurement of clinically relevant molecules ideally should be accurate, fast, inexpensive, highly sensitive, selective, non-invasive, portable, and simple for medical staff to operate[12].

Future Outlook on Biosensors Optimization of assays is critical in increasing sensitivity, and much work has been performed to create robust, sensitive bioassays[20], yet the development of customized instrumentation related to these assays is still relatively unexplored. Instrumentation development falls under signal amplification rather than target amplification. Instead of creating new biosensor detection methods, analog amplification of an already established biosensor system can increase sensitivity without modification. This approach is promising for already robust, validated biosensors with possibly shorter approval times than a new detection method. Additionally, analog amplification could be applied to many other biosensors.

One challenge for new biosensor methods is industry reluctance to incorporate new methods without long-term studies for effectiveness and validation against current methods. Enzymatic sensing is the standard commercialized method of clinically relevant small molecule detection as they are reliable, sensitive, and cost effective. However, enzymatic sensing systems require well-regulated storage conditions and suffer from interferences. Enzymatic sensing is not practical for larger molecules or DNA, which requires other detection methods[9]. Few biosensors have been commercialized and accepted, and those are primarily enzymatic sensors, leading to opportunities to develop new biosensors[4, 21–25]. New biosensors ideally would have homogeneous work flow, where no separation between detection steps is required, and multiplexing capabilities allowing multiple analytes to be measured simultaneously to reduce the biological sample volume required[3, 26].

Within this dissertation work, we take strides to develop new instrumentation in the form of a differential potentiostat to increase sensitivity in previously established DNA based biosensors systems (Chapter 4). This dissertation also investigates the thermal effects on

DNA biosensing platforms when using either electrochemical or optical detection methods. Thermal effects are interrogated by incorporating either a computer based or portable Peltier driven thermal regulation system into the biosensor platform (Chapter 3).

1.2 Microfluidics Introduction

Microfluidics is the science and engineering of systems in which fluid behavior differs from conventional flow due to small length scales. Major benefits of microfluidics include small reagent and waste volumes, automation and integration of components (lab on a chip), and portability. The name derives from the fluid analogy to microelectronics, and much of the technologies parallel each other—in some cases having the same origins, silicon devices[27]. It is important to distinguish microfluidics from an absolute scale (channel dimensions of tens to hundreds of micrometers), but rather to focus on the fluid behaviors at small scales which differ from conventional fluid flow (e.g. laminar flow). The fundamental physics changes more rapidly as the scale decreases in microfluidics comparable to microelectronics, which have utilized classical physical phenomena up until very recently with the introduction of quantum computing. Typical volumes in microfluidics are between microliters and picoliters, as an example a 1 inch square microfluidic chip has channels that are 10 mm long, by 100 μm wide, by 10 μm deep, yielding a volume of 10 nL (10 mm^3 = 0.01 μL = 10 nL)[28–32]. Other variants of small volume fluidics include inertial[33], paper[34], digital[35], and nanofluidics[36]. It is important to first explore several governing equations of microfluidics before discussing the applications.

Microfluidic Governing Equations The Reynolds number (R_e) is a dimensionless value, which relates the inertial forces of a fluid to the viscous forces. The Reynolds number is equal to the inertial forces over the viscous forces. where the inertial forces are equal to density (ρ), times velocity (ν), times characteristic length (L) of the system, over the viscous forces (μ). (Equation 1.1).

$$R_e = \frac{inertial forces}{viscous forces} = \frac{\rho \nu L}{\mu} \tag{1.1}$$

For R_e values $\gg$ 2000, the flow is dominated by inertial forces causing turbulence, and when the R_e is $\ll$ 2000 the flow is dominated by viscous forces, in the case of microfluidics causing laminar flow or layers of uniform thickness to form. The layer boundaries remain fixed as the liquid moves between them, maintaining parallel and distinct streams[11]. The only mixing occurs by diffusion across the liquid-liquid interface which is typically a slow process. Note this is at dynamic steady state, where continuous flow of liquid is necessary to maintain this interface, and any change in flow rate modifies the ratios of the layers.

The Péclet (P_e)number which relates the diffusive time scale to the advective transport time scale. It allows the calculation of mixing over the fluid passage characteristic length (L) considering the diffusion coefficient (D) of the solute in the solvent and fluid velocity (ν). (Equation 1.2). With typical dimensions of a microfluidic channel where the P_e is <1000, it can take hundreds of channel widths to mix laminar flows completely[11].

$$P_e = \frac{\nu L}{D} \tag{1.2}$$

Generally, R_e and P_e are low in microfluidics systems. Meaning that viscous forces dominate inertial forces (resulting in laminar flow), and diffusion dominates advection. Microfluidics mass transport is generally dominated by viscous dissipation, and inertial effects are generally negligible. Since inertia provides the nonlinearity responsible for numerous instabilities and turbulence, the low mass involved in microfluidics leads to laminar, non-mixing flows in microfluidics[37, 38].

Microfluidic Devices and Applications Microfluidic concepts have been adapted to traditional detection methods and coupled with fluidic flow control creating a class of devices called lab on a chip (LOC) or micro total analysis systems[39]. The LOC concept stems from the reduction in overall footprint of a common laboratory performed analysis including reduction of reagent use, cost of facility, personnel, and potential analysis time. An

LOC includes several sections of the analysis from sample clean up, separation, and detection with the expectation of sample-in/result-out. Some examples of traditional detection methods applied to microfluidic LOCs include: optical[40–42], mass spectroscopy[43], nuclear magnetic resonance[44], electrochemical[45, 46], surface plasmon resonance and surface enhanced Raman spectroscopy[47], and various others beyond these[48, 49]. These detection methods are applied to cell sampling[42, 50], drug screening, disease diagnosis, protein analysis, environmental monitoring, etc. The versatility of microfluidics makes it an attractive development platform for new methods. For microfluidic technology, even after 2 decades of development, much work still needs to be performed to truly utilize this technology. It took 70 years for microelectronics to mature from physical phenomena to quantum computing, and microfluidics is similarly still growing. This is exemplified by a literature search and number of citations as of this year, showing a constant growth over almost all years to date, highlighting the continued growth of the microfluidics field (Figure 1.4).

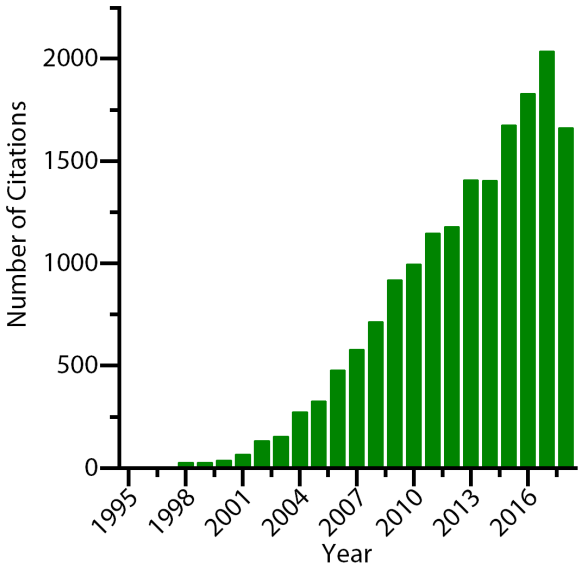

Figure 1.4: **Microfluidic citations per year.** Scientific journal citations per year for search term "microfluidics", compiled from Web of Science as of Sep18.

The first microfluidic device was a silicon gas chromatograph developed in the late 1970s[27]. During the 1980s and 1990s, microelectromechanical systems (MEMS) were developed borrowing heavily from the well-established microelectronics community and funded

by government interest[51]. In the late 1990s, chemical analysis took over with other materials such as glass[52] , and finally in the 2000s polymers began to be used readily, still leaning on the microfabrication from the silicon industry in a process called soft lithography[53, 54]. Use of soft lithography is widespread, however other fabrication methods and materials are used (PMMA, Glass, Paper, 3D printing, etc.) with benefits and drawbacks to each. Here we focus on soft lithography due to its outstanding benefits over other methods.

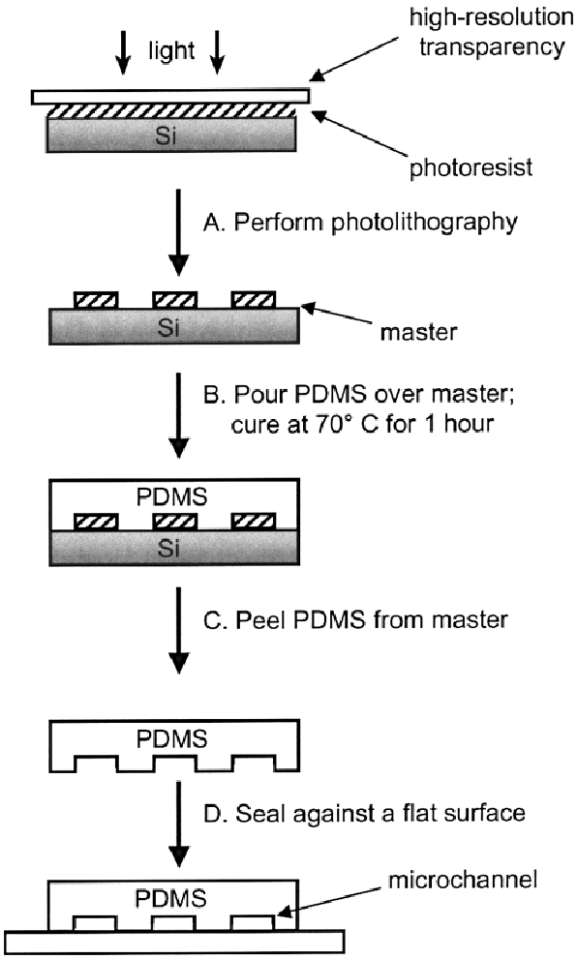

Figure 1.5: **Soft lithography fabrication method.** Soft lithography fabrication method.(A) Traditional photolithography is performed (B)PDMS is cured over the photolithography features (C&D)PDMS pealed from master and bonded to glass. Reprinted in part from reference [55] with permission from, ©2002 American Chemical Society.

Soft Lithography Soft lithography refers to monolithic fabrication of microfluidic features in a polymer by using electronic lithography fabrication techniques involving photoresist and

silicon wafers. The process begins by designing a high-resolution photo mask with the desired features for each layer. Then a polished silicon wafer is spin coated with a photoresist. The now thin layer of photoresist is exposed to UV light through the mask, creating fine details. The wafer is then developed creating a master wafer with micrometer sized features on its surface (Figure 1.5A). A layer of poly(dimethylsiloxane) (PDMS) is poured over the master and cured forming a semi-rigid polymer (Figure 1.5B). The PDMS is peeled from the master, and using oxygen plasma it is bonded permanently to a glass substrate (Figure 1.5C&D). This process was usually carried out in clean room conditions, however with the development of high power UV light emitting diodes[56] and a properly assembled projector system (see Chapter 5)[57], clean room conditions are not required any longer, making soft lithography even more suitable for microfluidics.

PDMS Characteristics Silicones were first synthesized by Berzelius in 1824, popularized by Kipping in the early 1900s, and commercialized by Dow Chemical Company in the 1940s[58] . PDMS is supplied in a kit of oligomers 60 siloxane groups in length (Figure 1.6-1) and platinum curing agent mixed with shorter linker oligomers (Figure 1.6-2). When both components are mixed, silicon hydride bonds form between the terminal vinyl groups of the oligomers and the hydrogens of the curing agent linkers. This reaction yields no by products and proceeds at room temperature[59]. Varying the ratio of base to curing agent affects the cross-linking and therefore the final structure of the PDMS, modifying the physical properties of the cured product[60]. PDMS can also be spin coated to form flexible polymer sheets useful for deflectable membrane formation. Bonding PDMS both reversibly and irreversibly is straightforward, by using the natural adhesion of PDMS or oxygen plasma for irreversible bonds[61]. Chemical properties of PDMS are also favorable, most importantly it is biocompatible with wide acceptance already established. PDMS also is semi-permeable to gas[62]. Its optically transparent between 300 and 2200 nm making PDMS very amiable to optical detection methods. Additionally, it is relatively chemically compatible with exceptions to

organic solvents and some bases[61]. Finally, PDMS is inexpensive when compared to the cost of both glass and silicon masters.

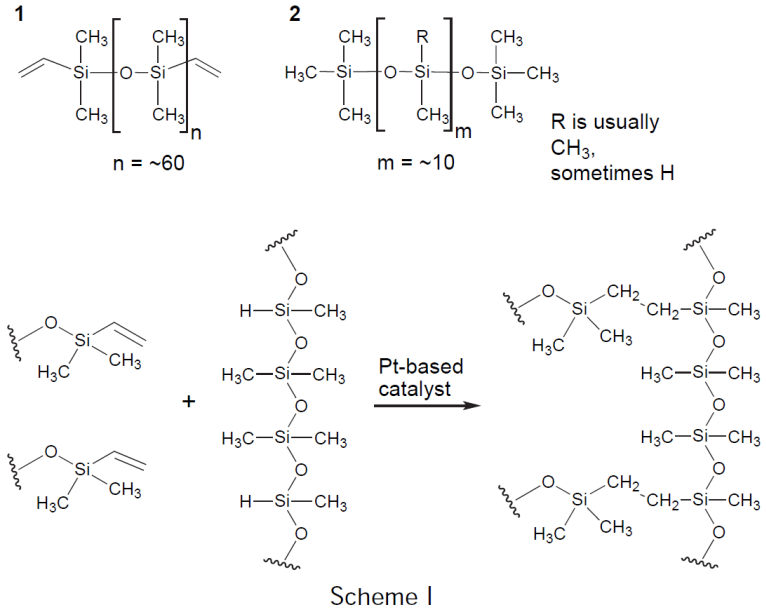

Figure 1.6: **PDMS polymerization reaction.** Long prepolymer oligomers are combined with shorter linking oligomers mixed with platinum based catalyst to polymerize at room temperature. Reprinted in part from reference [59] with permission from, ©1999 American Chemical Society.

Microfluidics relies on PDMS due to several features, related to its silicon birthplace. A single master wafer allows creation of multiple PDMS devices, without further photolithographic fabrications. PDMS can be irreversibly bonded in multi-layer devices creating complex microfluidic networks to perform analysis[63]. As a polymer it allows friction fit external connections to interface between the micro and macro fluidic worlds[64]. PDMS has proven to be very useful and versatile in development of microfluidic devices.

Microfluidic Electronic Circuit Analogy Flexible membranes and easily fabricated devices paved the way for higher complexity microfluidic devices. Two common methods used to divert fluid flow in microfluidic devices are active and passive methods. Active microfluidics refers to the driving of individual elements in a microfluidic chip by an external source such as acoustic, electrical, thermal, pressure, valves, or pumps[65, 66]. The benefits are simplicity in design, fabrication, and precise control over chip function. One limiting factor

is the number of connections possible on a certain device, since only a specific number of tubes per area is possible without considering potential microfluidic line conflicts. Active microfluidic devices commonly are driven by pneumatic solenoid valves, which interface to the tubes on the microfluidic chip to drive the functions of the device from digital inputs delivered from a computer. The large number of support devices and power requirements prohibit the true portability of a microfluidic device, maintaining its place firmly in the research laboratory.

Passive fluid control is another method of fluid steering in microfluidic devices. Passive control typically requires fewer external connections and can operate without direct input in some cases. Examples of passively controlled devices are mixing technologies, centrifugal microfluidics, and paper/capillary microfluidics[32, 67]. Ideally, a microfluidic chip could be programmed to function in a specific way, with few inputs similarly to an integrated electronic circuit (IC). The IC consists of a complex layout of basic components fabricated to interact with each other from a few inputs in one physical package[68]. This could be extended to microfluidic phenomena, creating integrated microfluidic circuits similarly with common components packaged together receiving a few inputs to drive fluid flow[69–72].

A convenient method for creating microfluidic circuits is to compare them directly to electronic circuit analogy. Molecules can be compared to electrons, fluid flow to flow of electricity, volumetric flow rate Q (m^3/s) to electrical current (I), pressure drop (ΔP) to voltage drop (ΔV), and hydraulic resistance (R_h) can be compared to electrical resistance (R_E). With these considerations, Ohms law $V = I*R_E$ is easily related to the Hagen-Poiseuille Law $\Delta P = Q*R_h$; pictorially this is illustrated for both hydraulic and electrical resistors in Figure 1.7A. This example also extends to hydraulic capacitors and inductors[71, 74, 75].

Fluidic Logic Electronic circuits are not made of only passive components (resistors, capacitors, inductors) but active components (transistor, FETs, gates, amplifiers etc.), which require input signals and controlled voltages. Unfortunately for microfluidics, the signals sent to active components are not in the same form as the output, in electronics voltage/current

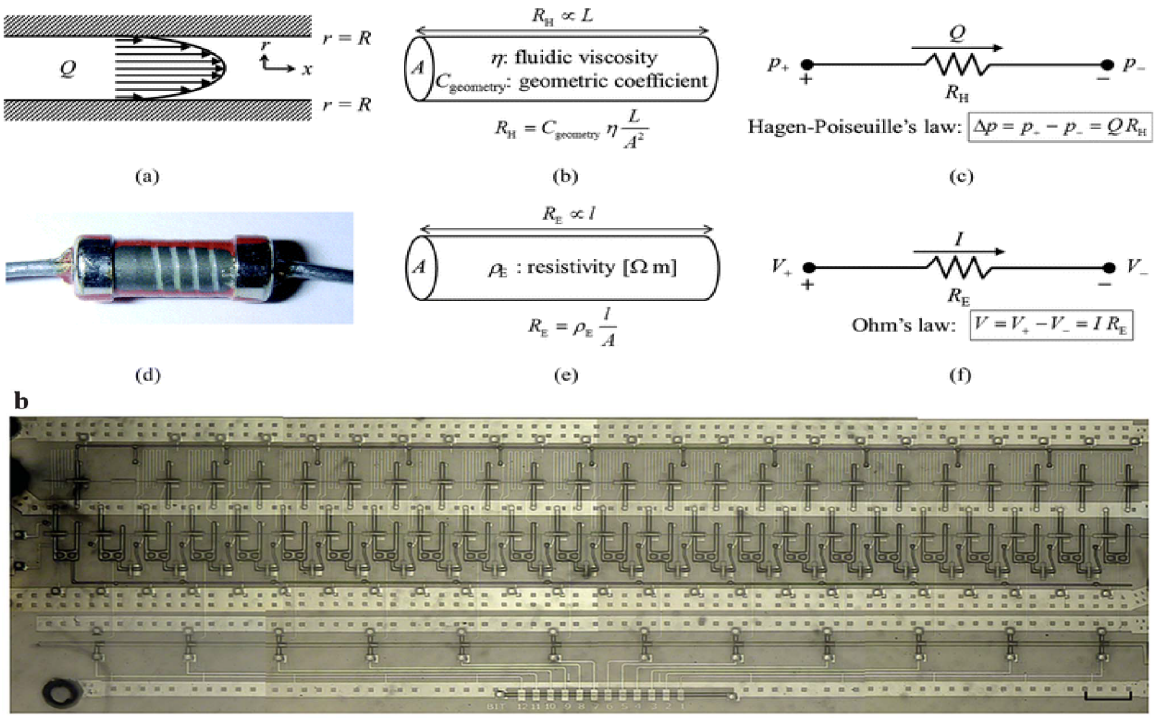

Figure 1.7: **Fluidic circuit analogy and fluidic resistor.** Microfluidic devices share similarities with electrical components where current and voltage compare to flow and pressure. Extended to microfluidic circuits, complex systems can be fabricated such as a microfluidic shift register. Scale bar 1 mm. Reproduced in part from ref [71] with permission of, ©2012, The Royal Society of Chemistry. Reproduced in part from ref [73] with permission of, ©2010, The Royal Society of Chemistry.

flow to control and direct current flow, microfluidics fluid control comes from electrical signals transduced to pressure[64, 76–79]. This concept then builds until the microfluidic devices complexity can no longer be controlled by individual signals, but rather a condense control system is required, fluidic logic. Fluidic logic is a physical device that performs a logical operation on one or more inputs to give a logical output. For example an AND gate compares two input signals, if both are logically HIGH then the logical output is HIGH[69]. Ideally as was previously discussed, the logical functions of a device should be embedded instructions, reagents are fed directly to a device which has inbuilt processes that automatically function ignoring external factors. When designing for widespread testing or environmental testing this is the preferred method, where a repeatable device is required. Fluidic logic should be based on device properties not on fluid properties[73]. This should not be confused with

the emerging technologies of digital microfluidics, which describe the movement of droplets by electric fields in a 2D array, allowing operations to be performed at specific locations on the array[80]. An example of fluidic logic is shown in Figure 1.7B, a 12-bit shift register, using normally closed valves. The device incorporates semiconductor like components, which function similar to FET transistors but are not perfect analogs of semiconductors[73].

Layer to Layer Connections As the complexity of microfluidic devices increase, the number of connections increases, so does the potential number of channels and the likelihood the channels will intersect in a single layer[81–84]. The limited density is similar to Moore's law, ultimately the number of functions in a single microfluidic layer will reach a maximum based on physical design limitations. To overcome this limitation a second layer containing interconnecting channels is fabricated, however the previous layer does not connect to the layer above unless a hole or via is created to connect both layers.

Microfluidic vias are created in several ways: punching, tearing, molding, and drilling. Punching and tearing are accomplished by using either a 250 μm biopsy punch or fine tipped forceps to create holes in the membranes above a microfluidic channel[85]. This method requires hand held tools, experienced technicians, and vias dimensions are limited by the tools used. Microfluidic molds are fabricated with post structures, which protrude above the spin coated surface, when the microfluidic device is assembled, hole is present at each protrusion's location connecting the lower and upper layers[82, 84, 86]. Molding creates vias successfully, however careful tuning of the spin coating system is required for formation of both the mold and the polymer coating. The mold's post must not be excessively long, as the polymer is prone to tearing, rather than releasing cleanly. A thick polymer coating would prevent hole formation, additionally the polymer coating tends to form filets at the edges of the mold again causing potential bonding issues with layers above. Another method of via formation is laser machining or laser drilling. A high-power laser (CO_2, NdYAG) are focused and pulsed at the intersection of the two layers channels creating vias between layers. Dimensions of a CO_2 laser drilled hole are 170 μm (Chapter 5) and others have

shown dimensions of 100 μm in diameter[67, 70, 87]. Laser drilling can be used to perforate multiple layers, though optimization is required to perforate single layers.

Microfluidic Active Components Fluidic logic cannot exist without microfluidic active components, including microfluidic diodes and transistors. Diodes and transistors are challenging to construct using monolithic fabrication methods, due in part to materials and assembly difficulty at micron size features.

The microfluidic diode or check valve allowing flow in only one direction, ideally has low forward resistance, and no reverse flow. Three major designs exist, the membrane, flap, and ball shown in (Figure 1.8). One version of the microfluidic diode consists of a 3-layer device, which has a central post extending from the top channel contacting a central membrane with a whole. Fluid flowing from left to right, deflects the membrane into an empty chamber below the post, while in the reverse direction, the fluid pressurizes the membrane against the post blocking flow[88] (Figure 1.8A). The next design relies again on a flap, however the flap closes against an orifice and is mounted from the top of the microfluidic chamber, deflecting out of the fluid path in one direction and closing the orifice in the reverse direction (Figure 1.8B)[89]. In the early 2000s the Whitesides group at Harvard demonstrated the membrane diodes fashioned in PDMS[81]. The membrane design consists of 3 layers PDMS the central layer is a membrane of PDMS several microns thick. It is shaped in a square with a hole in the center, fluid flows from the bottom left up through the hole, while fluid flowing from the top right pressurizes the membrane against the central opening closing the valve tightly (Figure 1.8C). The last design shown here by Sochol et al.[90], demonstrates a ball check valve. The ball seats against a tiny opening at the end of the channel in the reverse direction, otherwise allowing fluid flow in the forward direction and being trapped by pillars (Figure 1.8D).

Each of these designs are unique, and prime examples of microfluidic design and engineering. However, each design also has a drawback in either fabrication or function. The ball valve is both difficult to fabricate and is very large (mm dimensions) making high density

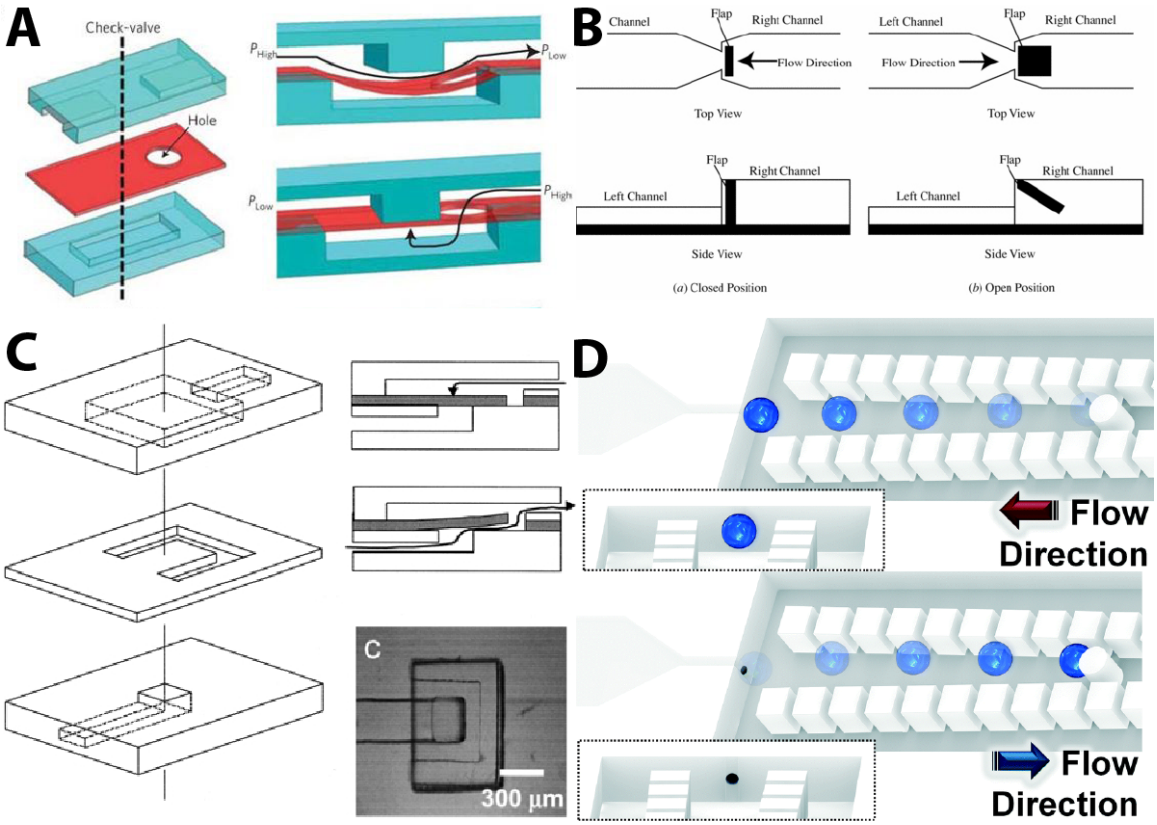

Figure 1.8: **Microfluidic diode types** (A) Post and membrane type valve. (B & C) Flap type valves. (D)Bead based diode structure. (A) Reprinted in part with permission from ref [88] ©2015, Nature Publishing Group. (B) reprinted in part with permission from IOP Ltd. ref [89] ©2005 , (C) reprinted in part with permission from ref [81] ©2002, Nature Publishing Group (D) Reproduced in part from [90] ©2014 with permission of The Royal Society of Chemistry.

fabrication challenging. To successfully create this design, an orifice must tightly seal around the ball and a ball must be precisely placed when bonding layers together. The hanging flap design (Figure 1.8B), is also difficult to fabricate, as the flap being a thin PDMS membrane tends to roll up and therefore failing in function. Both Jeon et al.[81] and Mosadegh et al.[88], rely on plasma oxidization to permanently bond the 3-layer devices together. The bonding technique is irreversible and provides higher pressure function, however if the valving sections are not treated property, to inactive the bonding at the membrane/flap locations, bonding prevents function of the devices. This deficient creates yet another step (plasma blocking) in the fabrication process and another opportunity for device failure.

Other designs which can create active components are non-Newtonian fluid rectifiers[91, 92], Tesla type valves[93], and pinch check valves[94, 95]. A second type of active component is the transistor, a voltage controlled variable resistor. A field effect transistor behaves similarly, where a gate voltage controls the current flow from source to drain. Mosadegh et al.[88] also applied their design to microfluidic transistors by interfacing a channel to the lower layer chamber and modulating the membrane on command. This allowed the creation of oscillators and finite state machines[65, 96–99]. A similar principle was created by Grover et al.[100] and Nguyen et al.[101], both using a lower chamber to deflect a membrane allowing creation of fluidic logic circuits and semi-autonomous pumping systems. Logic gates were demonstrated by Rhee and Burns where multiple gates were strung together forming higher complexity devices[102].

The devices presented are very promising and serve specific needs that the authors addressed in design, function and characterization. Several major design challenges have yet to be addressed, these include fabrication difficulties, stage to stage gain, and intra-device tunability. Fabrication challenges exist when creating valves, having posts or pillars interacting with membranes. The assembly process requires blocking or masking of the pillar/membrane location to prevent irreversible sealing. To make a truly autonomous device, signals must be transmitted from microfluidic sections within a device, which requires gain. Gain is the increase in output amplitude from an input signal in a device. Microfluidic gain devices have proven difficult to create and implement. Finally, following the electronic microcontroller or field-programmable gate array (FPGA) examples, the ability to tune the function of a microfluidic chip, rather than a complete redesign and re-fabrication has not been addressed and would be significantly beneficial in creating commercially viable devices. We address this deficiency in Chapter 6 by developing tunable components.

Finally, following the electronic microcontroller or field-programmable gate array (FPGA) examples, the ability to tune the function of a microfluidic chip, rather than a complete re-design and re-fabrication has not been addressed and would be significantly beneficial in

creating commercially viable devices. We address this deficiency in Chapter 6 by developing tunable microfluidic components.

1.3 3D Printing Applications in Bioanalysis

Additive manufacturing, rapid prototyping, or 3D printing is the process of creating physical objects from computer aided design (CAD) files, by successive material deposition on a build surface. Material is deposited in areas where structures are to be formed, and if required support structures are constructed under overhanging features. The first example of 3D printing, stereolithography (SLA), was introduced by Charles Hull in the early 1980s, and he was awarded a patent in 1986 for his SLA printer. He went on to introduce the primary computer file format used today for 3D printing, .STL, or stereo lithography file[103–105].

The 3D printing work-flow begins with a file created in a CAD program, which is then sent to a slicer program to create Gcode, the numerical control programming language read by a 3D printer to position the nozzle in 3D space and set the feeds and speeds of the printer to reproduce the device accurately. Gcode is then sent to the printer, which using any number of processes creates a 3D replicate of the computer model[103].

Traditional manufacturing techniques include injection molding, hot embossing, milling, casting, and turning. The machining process for these techniques can be complicated and time consuming and require skilled personnel for reliable device fabrication. As an example, injection molding requires milling master molds with inverse features, forming a sealed vessel, where molten plastic is forced into the vessel filling the features of the mold. The resulting plastic part usually requires further processing to clear flashing, or support materials to form the final product. In some cases, multiple parts are then fitted together to form a finished device[106]. The machining process is a subtractive manufacturing process, material is removed, and large amounts waste are created[107].

In contrast, 3D printing is an additive process, has fast iterative design cycles, can be easily scaled, has multiple materials, and can have higher complexity designs. The additive

process precisely places material to create a final device, rather than removing material in successive matching processes to form the completed device. Once a CAD file is created for a device or part, the iteration time for correcting deficiencies in the model is very fast, essentially the amount of time required to print plus adjustments to the CAD file in comparison to the complex matching processes and setup required for traditional manufacturing processes[108]. After the design is optimized and shown functional, the design files can be sent anywhere in the world to be replicated with the same materials rather than sending completed tooling and molds to the manufacturing facilities. Additionally, the replication time for multiple parts can be reduced by splitting the part's fabrication amongst a larger number of general manufactures rather than a single specialized facility. This can be extended to the consumer market; a print file could be purchased rather than a finished product, and simply printed at home assuming the raw materials were on hand. Finally, a 3D-printed device based on its layer by layer construction can be fabricated with internal structures not possible to make with traditional machining, opening new design possibilities.

The last 40 years has seen significant growth in the use and types of 3D printers, the four main commercially available printers are: fused deposition manufacturing (FDM), stereolithography (SLA), inkjet or Polyjet (PJ), and selective laser sintering (SLS). FDM printers function by extruding thermoplastic in a semi molten state through a heated nozzle, which is positioned in the XY plane. This creates a layer of material on the build surface, the build surface then moves in the Z direction and another layer is deposited on top of the first (Figure 1.9A). FDM positioning resolution is 50 μm, but layer and nozzle resolution is hundreds of micrometers due to effects of the extruded polymer. An FDM print can be paused and restarted, allowing embedding of objects or changing filament material during printing, additionally multiple heads and materials can be used during a print cycle[109]. Defects are common resulting from either the slicing software or the materials heterogeneities (filament diameter/composition). Typical materials are plastics, poly lactic acid (PLA), acrylonitrile

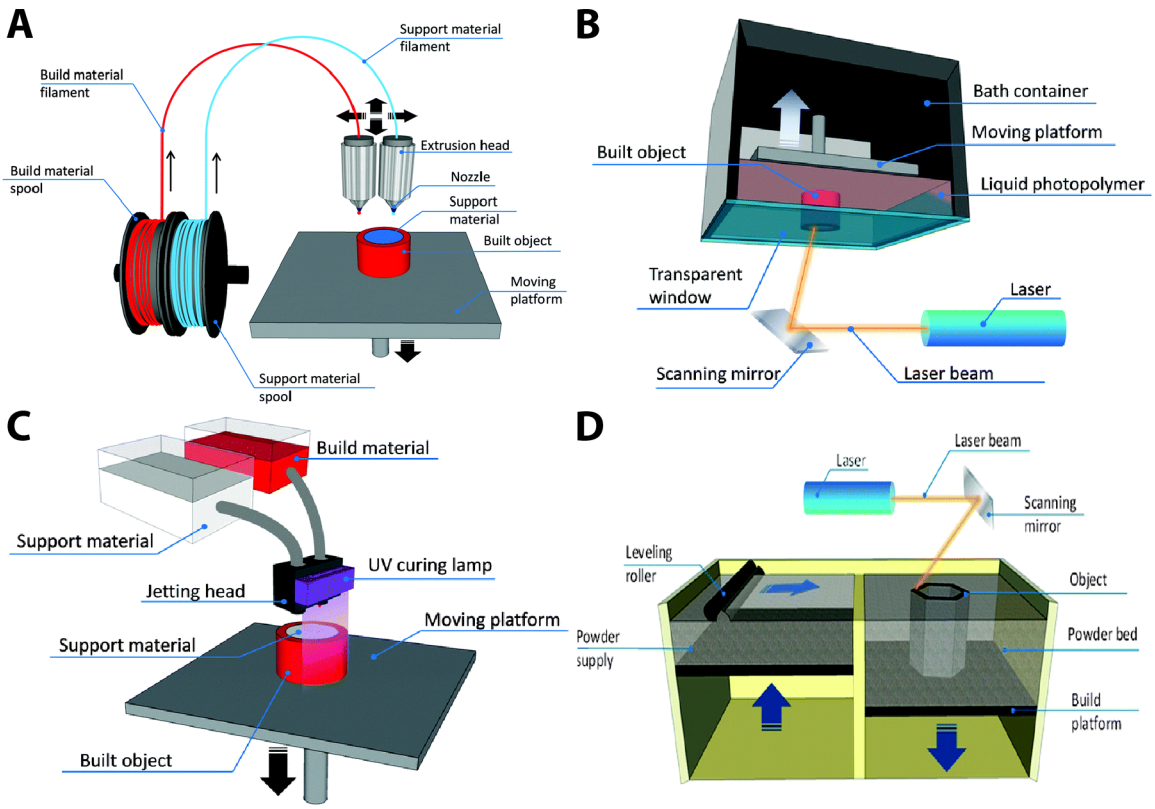

Figure 1.9: **3D printing methods.** (A) Fused deposition printing, thermoplastic is extruded in XYZ axis. (B) Stereolithography printing,optical curing of light onto build platform. (C)Jet printing, UV curable polymer deposited on build surface and UV cured. (D) Selective laser sintering, a metal powder on a build plate is melted by intense laser radiation. Reproduced in part from [107] with permission of, ©2016, The Royal Society of Chemistry.

butadiene styrene (ABS), polycarbonate (PC), polystyrene (PS), ceramic, metal, biodegradable, or water-soluble filaments. High melting point materials (ceramic/metal) in powdered form can also be bound into a filament for printing, then a post processing step burns away the polymer to form the final devices. Post processing is typical but not strictly required, as some parts can be used directly from the printer if designed and oriented properly during print.

SLA Printing SLA printing is accomplished by forming an image in UV light by either a projector or drawn by laser, onto a vat of UV curable polymer, which contains a build plate. After the polymer layer is cured, the build plate is incremented in the Z-axis and another image is projected creating another layer (Figure 1.9B). Resolution is high, tens

of micrometers, but long build times result from higher resolution. Interior channels are filled by uncured resin, which can be low viscosity and somewhat easier to remove than FDM or PJ alternatives. For projecting images, three main categories exist, liquid crystal displays, digital micromirror devices (DMD), and liquid crystal on silicon[110]. Manufactures of commercial systems typically state pixel sizes 30 μm and this limits practical printing to 500 μm channel dimensions. Through significant optimization in both the projection system and the resin formulation 20 μm square channels can be printed, however this is still a research tool[111]. Higher resolution printers capable of features 1 μm in size are available, however these two photon printers take even longer to print (>10 h/mm^3), due to individual pixel addressing, making them suitable only for a few specific purposes[112]. Cost of two photon laser printers is prohibitively high, again driving the suitability of the extremely high resolution printers to defined applications. A major drawback of SLA printers is a required post resin cure fully solidify the device, and rinse off excess resin to maintain high surface detail[103]. Layer thickness, depends on factors such as scan speed, intensity of laser/UV LED or source duration of exposure. Layer cure time by DMD is much faster than UV laser scanning, due to full exposure of full build area at once. Ultimately, the limiting factor for SLA printers is the resin, its properties (cure time, resolution, absorbance, toxicity etc.) determine much of the final device's characteristics, additionally only a single resin can be used for a print due to the full immersion of the part in resin.

Polyjet or Inkjet Printing Polyjet or inkjet 3D printing functions by depositing droplets of resin on a surface and UV curing, the build surface is incremented in the Z direction and the next layer is deposited (Figure 1.9C). Resolution is slightly higher when compared with SLA at 25 μm resolution unlike SLA printing, multiple jets can be used to print simultaneously allowing varied resin properties to be incorporated into a single device[109]. Polyjet is very versatile, used for multiple materials, including biological materials.

SLS Printing Selective laser sintering is performed by spreading a thin layer of metal powder evenly over a flat build plate. A laser (CO_2 or Nd:YAG) is focused onto the layer

in a specific pattern, sintering or melting the metal powder together. The metal plate is then lowered, a fresh layer of powder is scraped over the surface, and another pattern drawn/sintered into the surface, causing the solidification of a pattern and the formation of a plastic/metal/ceramic or other durable part to emerge after the powder is blown away and recycled (Figure 1.9D). If polymers are used, then the polymer can be heated to just under its melting point, allowing lower energy to be deposited by the laser and therefore more control over the printing process. One benefit is that the un-sintered material is effectively support material and provides structure for the print. However, the extreme heat used for the sintering process causes warping and shrinkage, which does limit the prints, though features 50 μm are reliably possible[103].

3D Printing Applications in Chemistry Additive manufacturing processes are being developed for many types of biological applications. One application is biomedical engineering or printing of biological tissues[104, 113–115]. Laser sintering of ceramics can be used to create artificial bones, having the added benefit of porosity, allowing tissues to fuse with and fill in the bone structures. Furthermore, tissue/veins[116] are possible while incorporating modifications (bionic ears, microvascular formations, and plausibly organs) using hydrogel printing, which incorporates a biodegradable gel matrix. Unique pharmaceutical manufacture is possible by 3D printing drug delivery solutions and surgeons could create 3D models of scanned tissue, to better train for operations[117, 118].

The educational impacts of 3D printing are widespread, for example the self-assembly of a viruses[119] or 3D printed molecules for teaching symmetry and point groups[120, 121] and visualization of complex bond angles and interactions. Amongst many other applications known or unknown. Finally, custom lab-ware and instrumentation are possible with 3D printing. Lab-ware in the form of custom reaction vessels[122–124], purpose specialized instrumentation[125–129] , and common lab supplies (racks, holders, pipettes etc.) could be 3D printed rather than purchased as in consumer goods mentioned above.

3D Printed Microfluidics As discussed earlier in this chapter, microfluidics plays a pivotal role in the development of point of care analysis and micro total analysis systems. The recent innovations in 3D printing make it possible to now print microfluidic devices. Previously, microfluidic devices were constructed using photolithographic methods, creating master molds to then template polymers creating microfluidic features[130–132]. With the prevalence of FDM printers, milli-fluidic devices are common and routine, and frequently misclassified as microfluidic[109]. To combat the resolution limitations of the FDM printers, Li et al.[133] investigated orientation optimization of FDM printers, ultimately choosing to transfer to SLA printing techniques with the Eden and Miicraft printers (Figure 1.10A) , which clearly exemplifies the surface structures of the microfluidic devices fabricated in the higher resolution printers. Comparing 3D printing platforms for microfluidics, the best surface structure was SLA based on <1 μm surface structure, the smallest internal channel of the three printing methods (FDM, Polyjet, SLA) at 150 μm, and the fastest print time per device[134]. Creating truly microfluidic devices with channel dimensions <100 μm wide requires significantly more effort to achieve. The Nordin/Wooley labs demonstrate these capabilities by creating microfluidic valves, 300 μm in diameter and channels 100 μm wide with a custom 3D printer and systematic optimization of resin formulations (Figure 1.10B)[135, 136]. The resins were optimized by printing structures which overhung, through holes in solid material, and they were also tested with commercial 3D printing services, to evaluate possible reproduction of microfluidic devices. The commercial services were not able to reliably create microfluidic devices, which drove Nordin/Wooley to develop a high resolution 3D-printer, in which they used the optimized resins to create 18 x 20 μm channels[111]. The high resolution printing process was then applied to microfluidic interfacing devices allowing chip to chip connection at high density and microfluidic circuits[137, 138].

3D printing can be used to interface with microfluidic channels, rather than directly create the channels. In papers published recently, the Easley group was able to create cell culture wells for endocrine tissue by 3D printing rather than using an older, more laborious

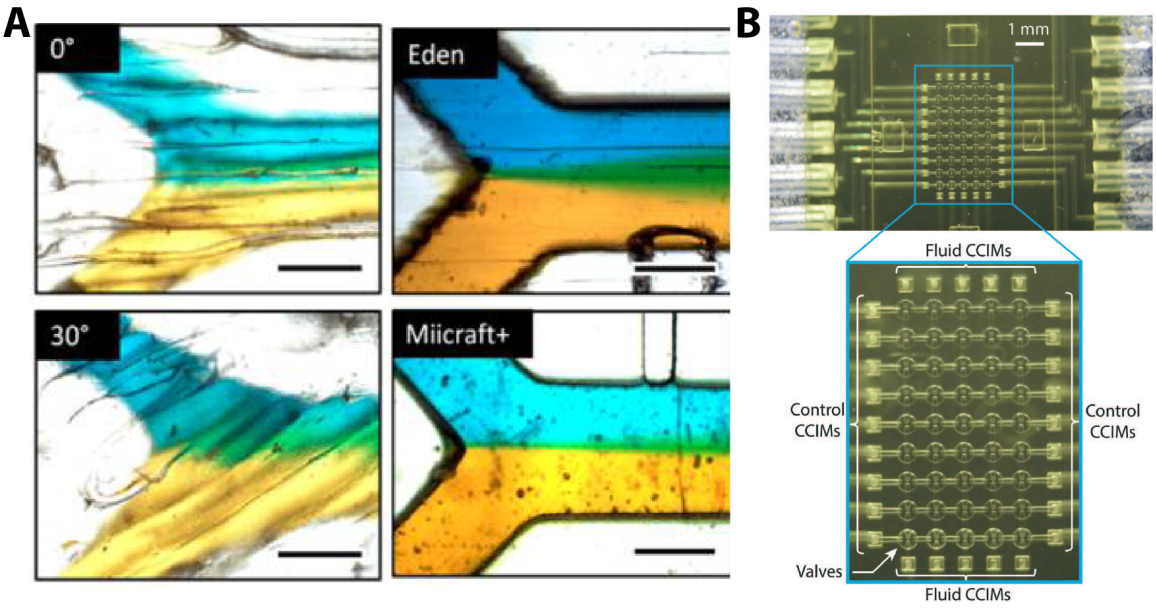

Figure 1.10: **3D printed microfluidic devices.** (A) FDM and SLA 3D printed microfluidic features. (B)High density microfluidic valves, SLA printed. (A)Reprinted in part from reference [133] with permission from, ©2017 American Chemical Society. (B) Reproduced in part from [137] with permission from, ©2018, The Royal Society of Chemistry

technique[125, 128]. This philosophy can be extended further to Luer lock type connections, directly molded to SLA created channels[139]. As with soft lithography, 3D printed templates which molds are created from are very promising, due to the precise pattern transfer. Molding is attractive due to the fast turnaround, and wider variety of materials which are possible[140, 141].

The challenges involved in creating 3D printed microfluidic devices are: resolution, surface roughness, internal feature creation, and biocompatibility. Many of these have been addressed (resolution, surface roughness) however, the widespread use of 3D printing to fabricate microfluidic devices is still a future endeavor leaving many innovation opportunities.

1.4 Conclusions

This chapter covered three distinct topics. Firstly, biosensor development for applications in bioanalytical chemistry was outlined, along with the associated electrochemical detection methods and instrumentation used to carry out those methods. The challenges

involved in creation of new biosensor methods was underscored. Secondly, the discussion focused on the development of microfluidics for analytical purposes, and the fluidic to circuit analogy utilized to create programmable microfluidic devices, which can benefit the POC industry and small volume analysis. Thirdly, the revolution in 3D printing was introduced and its application in both analytical chemistry and microfluidics were highlighted.

Electrochemical measurements made with commercially available disk electrodes require a standardized surface which is accomplished by mechanically polishing the surface with abrasives. This process is usually performed by hand, but in Chapter 2, a 3D printed robot is presented, which performs this process automatically without the intervention of the scientist. Chapter 3 outlines the development of a thermal control system interfaced to microfluidic devices and electrochemical devices. This system is capable of actively stabilizing temperature and is programmable to vary the temperature during an experiment. A differential potentiostat (DiffStat) was created and reported in Chapter 4. The DiffStat is utilized to correct for background current in multiple electrochemical experiments and is then applied to a nucleic acid system demonstrating application to nucleic acid detection in serum. Chapter 5 addresses the requirement for auxiliary equipment when creating new microfluidic devices. This chapter contains the details for construction of a via drilling CO_2 laser system, construction of a UV LED based photolithographic projector, design of a microfluidic solenoid valve controller, electronic pressure gauges for both Arduino and LabVIEW environments, a UV laser controller for photopolymer curing, assembly of a high intensity LED illuminator, assembly of a PCB fabricating reflow oven, and a PID oven controller to stabilize PDMS curing temperatures. Chapter 6 discussed tunable architectures for microfluidic circuit analogies. Microfluidic technologies have a long and tedious design and fabrication process, creating masters and then molds. If a standardized "component" was developed and its functionality was programmable, then a general microfluidic device component could be created in large numbers then programmed. This is similar to the semiconductor analogy, where components can be programmed in circuit to modify their functions such as in

a field programmable array. This final chapter outlines the creation of tunable microfluidic resistors, diodes, and transistors demonstrating their functionality, which is an important step toward field programmable microfluidics.

References

[1] E. B. Bahadir, M. K. Sezgintürk, *Analytical Biochemistry* **2015**, *478*, 107–120.

[2] D. A. Giljohann, C. A. Mirkin, *Nature* **2009**, *462*, 461–464.

[3] N. J. Ronkainen, H. B. Halsall, W. R. Heineman, *Chem. Soc. Rev.* **2010**, *39*, 1747–1763.

[4] C. Zhu, G. Yang, H. Li, D. Du, Y. Lin, *Analytical Chemistry* **2015**, *87*, 230–249.

[5] J. R. Porter, *Bacteriological reviews* **1976**, *40*, 260–9.

[6] D. A. Skoog, F. J. Holler, S. R. Crouch, *Principles of Instrumental Analysis*, 2nd, Thomson Brooks/Cole, Belmont, CA, **2007**, p. 529.

[7] S. O. Kelley, *ACS Sensors* **2017**, *2*, 193–197.

[8] G. Gauglitz, *Annual Review of Analytical Chemistry* **2014**, *7*, 297–315.

[9] M. Labib, E. H. Sargent, S. O. Kelley, *Chemical Reviews* **2016**, *116*, 9001–9090.

[10] A. B. Iliuk, L. Hu, W. A. Tao, *Analytical Chemistry* **2011**, *83*, 4440–4452.

[11] R. Pethig, S. Smith, *Introductory Bioelectronics*, John Wiley & Sons, Ltd, West Sussex, UK, **2013**, p. 441.

[12] F. Alam, S. RoyChoudhury, A. H. Jalal, Y. Umasankar, S. Forouzanfar, N. Akter, S. Bhansali, N. Pala, *Biosensors and Bioelectronics* **2018**, *117*, 818–829.

[13] G. Hughes, R. M. Pemberton, P. R. Fielden, J. P. Hart, *TrAC - Trends in Analytical Chemistry* **2016**, *79*, 106–113.

[14] G. S. Wilson, M. A. Johnson, *Chemical Reviews* **2008**, *108*, 2462–2481.

[15] C. G. Zoski, *Handbook of Electrochemistry*, 1st ed., Elsevier, Oxford,UK, **2007**, p. 935.

[16] A. T. Sage, J. D. Besant, B. Lam, E. H. Sargent, S. O. Kelley, *Accounts of Chemical Research* **2014**, *47*, 2417–2425.

[17] A. J. Bard, L. R. Faulkner, *Electrochemical Methods : Fundamentals and Applications*, 2nd, John Wiley & Sons, Inc, New York, **2001**, p. 833.

[18] L. Ramaley, M. S. Krause, *Analytical Chemistry* **1969**, *41*, 1362–1365.

[19] J. G. Osteryoung, R. A. Osteryoung, *Analytical Chemistry* **1985**, *57*, 101–110.

[20] P. D'Orazio, *Clinica Chimica Acta* **2011**, *412*, 1749–1761.

[21] D. Grieshaber, R. MacKenzie, J. Voeroes, E. Reimhult, *Sensors* **2008**, *8*, 1400–1458.

[22] T. G. Drummond, M. G. Hill, J. K. Barton, *Nature Biotechnology* **2003**, *21*, 1192–1199.

[23] V. Gubala, L. F. Harris, A. J. Ricco, M. X. Tan, D. E. Williams, *Analytical Chemistry* **2012**, *84*, 487–515.

[24] J. J. Gooding, *Electroanalysis* **2002**, *14*, 1149–1156.

[25] J. Kirsch, C. Siltanen, Q. Zhou, A. Revzin, A. Simonian, *Chemical Society Reviews* **2013**, *42*, 8733–8768.

[26] C. Dincer, R. Bruch, A. Kling, P. S. Dittrich, G. A. Urban, *Trends in Biotechnology* **2017**, *35*, 728–742.

[27] S. C. Terry, *IEEE* **1979**.

[28] N.-T. Nguyen, Steven T. Wereley, *Fundamentals and Applications of Microfluidics*, second edi, Artech House Inc., Norwood,MA, **2006**, p. 497.

[29] D. G. Rackus, M. H. Shamsi, A. R. Wheeler, *Chemical Society Reviews* **2015**, *44*, 5320–5340.

[30] K. F. Lei in *Microfluidics in Detection Science*, (Eds.: F. H. Labeed, H. O. Fatoyinbo), 5, **2014**, pp. 1–28.

[31] D. J. Beebe, G. A. Mensing, G. M. Walker, *Annual Review of Biomedical Engineering* **2002**, *4*, 261–286.

[32] P. N. Nge, C. I. Rogers, A. T. Woolley, *Chemical Reviews* **2013**, *113*, 2550–2583.

[33] J. Zhang, S. Yan, D. Yuan, G. Alici, N. T. Nguyen, M. Ebrahimi Warkiani, W. Li, *Lab on a Chip* **2016**.

[34] D. M. Cate, J. A. Adkins, J. Mettakoonpitak, C. S. Henry, *Analytical Chemistry* **2015**, *87*, 19–41.

[35] A. E. Kirby, A. R. Wheeler, *Analytical Chemistry* **2013**, *85*, 6178–6184.

[36] J. C. Eijkel, A. van den Berg, *Microfluidics and Nanofluidics* **2005**, *1*, 249–267.

[37] H. Bruus in *Microscale Acousto?uidics*, **2015**, pp. 1–28.

[38] P. Zhu, L. Wang, *Lab on a Chip* **2017**, *17*, 34–75.

[39] A. Manz, H. M. Widmers, N. Graber, *Sensors and Actuators B: Chemical* **1990**, *1*, 244–248.

[40] X. Li, C. J. Easley, *Analytical and Bioanalytical Chemistry* **2018**, *410*, 791–800.

[41] J. T. Negou, L. A. Avila, X. Li, T. M. Hagos, C. J. Easley, *Analytical Chemistry* **2017**, *89*, 6153–6159.

[42] L. A. Godwin, J. C. Brooks, L. D. Hoepfner, D. Wanders, R. L. Judd, C. J. Easley, *Analyst* **2015**, *140*, 1019–1025.

[43] S. Koster, E. Verpoorte, *Lab on a Chip* **2007**, *7*, 1394–1412.

[44] H. Ryan, A. Smith, M. Utz, *Lab on a Chip* **2014**, *14*, 1678–1685.

[45] M. D. M. Dryden, D. D. G. Rackus, M. H. Shamsi, A. R. Wheeler, *Analytical Chemistry* **2013**, *85*, 8809–8816.

[46] A. Gencoglu, A. R. Minerick, *Microfluidics and Nanofluidics* **2014**, *17*, 781–807.

[47] D. E. Patabadige, S. Jia, J. Sibbitts, J. Sadeghi, K. Sellens, C. T. Culbertson, Micro Total Analysis Systems: Fundamental Advances and Applications, **2016**.

[48] P. J. Viskari, J. P. Landers, *Electrophoresis* **2006**, 1797–1810.

[49] J. P. Lafleur, A. Jönsson, S. Senkbeil, J. P. Kutter, *Biosensors and Bioelectronics* **2016**, *76*, 213–233.

[50] R. Dhumpa, M. G. Roper, *Analytica Chimica Acta* **2012**, 9–18.

[51] K. Brendley, R. Steeb, *Military applications of MEMS*, Defense Technical Information Center, Santa Monica, CA, **1993**, p. 74.

[52] D. J. Harrison, A. Manz, H. Lüdi, H. M. Widmer, Z. Fan, *Analytical Chemistry* **1992**, *64*, 1926–1932.

[53] G. M. Whitesides, *Nature* **2006**, *442*, 368–373.

[54] M. A. Unger, M. A. Unger, H.-P. Chou, T. Thorsen, A. Scherer, S. R. Quake, *Science* **2013**, *113*, 113–117.

[55] J. C. McDonald, G. M. Whitesides, *Accounts of Chemical Research* **2002**, *35*, 491–499.

[56] S. Nakamura, T. Mukai, M. Senoh, *Applied Physics Letters* **1994**, *64*, 1687–1689.

[57] M. Erickstad, E. Gutierrez, A. Groisman, *Lab on a Chip* **2015**, *15*, 57–61.

[58] B. Ratner, A. Hoffman, F. Schoen, J. Lemons, *Biomaterials Science: An Introduction to Materials in Medicine*, 2nd, Academic Press, Cambridge, MA, **2004**, p. 864.

[59] D. J. Campbell, K. J. Beckman, C. E. Calderon, P. W. Doolan, R. M. Ottosen, A. B. Ellis, G. C. Lisensky, *Journal of Chemical Education* **1999**, *76*, 537.

[60] I. D. Johnston, D. K. McCluskey, C. K. Tan, M. C. Tracey, *Journal of Micromechanics and Microengineering* **2014**, *24*, 1–7.

[61] A. Mata, A. J. Fleischman, S. Roy, *Biomedical microdevices* **2005**, *7*, 281–293.

[62] T. C. Merkel, V. I. Bondar, K. Nagai, B. D. Freeman, I. Pinnau, *J Polym Sci B: Polym Phys* **2000**, *38*, 415–434.

[63] M. A. Unger, H. P. Chou, T. Thorsen, A. Scherer, S. R. Quake, *Science* **2000**, *288*, 113–116.

[64] J. Liu, C. Hansen, S. R. Quake, *Analytical Chemistry* **2003**, *75*, 4718–4723.

[65] P. N. Duncan, T. V. Nguyen, E. E. Hui, *Proceedings of the National Academy of Sciences* **2013**, *110*, 18104–18109.

[66] E. C. Jensen, W. H. Grover, R. A. Mathies, *Journal of Microelectromechanical Systems* **2007**, *16*, 1378–1385.

[67] K. Xu, M. R. Begley, J. P. Landers, *Lab on a Chip* **2015**, *15*, 867–876.

[68] P. Horowitz, W. Hill, *The Art of Electronics*, 2nd, Cambridge University Press, Cambridge, UK, **1990**, p. 1131.

[69] B. Mosadegh, T. Bersano-Begey, J. Y. Park, M. A. Burns, S. Takayama, *Lab on a Chip* **2011**, *11*, 2813–2818.

[70] P. N. Duncan, S. Ahrar, E. E. Hui, *Lab on a Chip* **2015**, *15*, 1360–1365.

[71] K. W. Oh, K. Lee, B. Ahn, E. P. Furlani, *Lab on a Chip* **2012**, *12*, 515–545.

[72] J. P. Urbanski, W. Thies, C. Rhodes, S. Amarasinghe, T. Thorsen, *Lab on a Chip* **2006**, *6*, 96–104.

[73] N. S. G. K. Devaraju, M. A. Unger, *Lab on a Chip* **2012**, *12*, 4809–4815.

[74] D. Kim, N. C. Chesler, D. J. Beebe, *Lab on a Chip* **2006**, *6*, 639–644.

[75] Q. Zhang, M. Zhang, L. Djeghlaf, J. Bataille, J. Gamby, A. M. Haghiri-Gosnet, A. Pallandre, *Electrophoresis* **2017**, 953–976.

[76] S. Attiya, A. B. Jemere, T. Tang, G. Fitzpatrick, K. Seiler, N. Chiem, D. Jed Harrison, *Electrophoresis* **2001**, *22*, 318–327.

[77] M. W. Toepke, V. V. Abhyankar, D. J. Beebe, *Lab on a Chip* **2007**, *7*, 1449–1453.

[78] I. E. Araci, P. Brisk, *Current Opinion in Biotechnology* **2014**, *25*, 60–68.

[79] I. E. Araci, S. R. Quake, *Lab on a Chip* **2012**, *12*, 2803–2806.

[80] M. J. Jebrail, M. S. Bartsch, K. D. Patel, Digital microfluidics: A versatile tool for applications in chemistry, biology and medicine, **2012**.

[81] N. L. Jeon, D. T. Chiu, C. J. Wargo, H. Wu, I. S. Choi, J. R. Anderson, G. M. Whitesides, *Biomedical Microdevices* **2002**, *4*, 117–121.

[82] T. Silva Santisteban, R. Zengerle, M. Meier, *RSC Advances* **2014**, *4*, 48012–48016.

[83] E. P. Kartalov, C. Walker, C. R. Taylor, W. F. Anderson, *Proc. Natl. Acad. Sci. U. S. A.* **2015**, *103*, 12280–12284.

[84] E. P. Kartalov, C. Walker, C. R. Taylor, W. F. Anderson, A. Scherer, *Proceedings of the National Academy of Sciences* **2006**, *103*, 12280–12284.

[85] B. Mosadegh, M. Agarwal, Y. S. Torisawa, S. Takayama, *Lab on a Chip* **2010**, *10*, 1983–1986.

[86] K. Zhou, X. G. Zhu, Y. Li, J. Liu, *RSC Advances* **2014**, *4*, 31988–31993.

[87] J. Huft, D. J. Da Costa, D. Walker, C. L. Hansen, *Lab on a Chip* **2010**, *10*, 2358–2365.

[88] B. Mosadegh, C. H. Kuo, Y. C. Tung, Y. S. Torisawa, T. Bersano-Begey, H. Tavana, S. Takayama, *Nature Physics* **2010**, *6*, 433–437.

[89] M. L. Adams, M. L. Johnston, A. Scherer, S. R. Quake, *Journal of Micromechanics and Microengineering* **2005**, *15*, 1517–1521.

[90] R. D. Sochol, A. Lu, J. Lei, K. Iwai, L. P. Lee, L. Lin, *Lab on a Chip* **2014**, *14*, 1585–1594.

[91] A. Groisman, S. R. Quake, *Physical Review Letters* **2004**, *92*, 1–4.

[92] P. C. Sousa, F. T. Pinho, M. S. N. Oliveira, M. A. Alves, *Journal of Non-Newtonian Fluid Mechanics* **2010**, *165*, 652–671.

[93] A. R. Gamboa, C. J. Morris, F. K. Forster, *Journal of Fluids Engineering* **2005**, *127*, 339.

[94] Q. Yu, J. M. Bauer, J. S. Moore, D. J. Beebe, *Applied Physics Letters* **2001**, *78*, 2589–2591.

[95] I. Doh, Y.-H. Cho, V. Namasivayam, R. G. Larson, D. T. Burke, M. A. Burns, P. K. Dasgupta, S. Liu, D. J. Laser, J. G. Santiago, C. Yamahata, C. Vandevyver, F. Lacharme, P. Izewska, H. Vogel, R. Freitag, M. A. M. Gijs, Y. Tanaka, K. Morishima, T. Shimizu, A. Kikuchi, M. Yamato, T. Okano, T. Kitamori, N. J. Graf, M. T. Bowser, B. T. Good, C. N. Bowman, R. H. Davis, Y. H. Choi, S. U. Son, S. S. Lee, C.-C. Hong, J.-W. Choi, C. H. Ahn, S. Matsumoto, Y.-C. Tai, B. Yang, Q. Lin, B. Yang, Q. Lin, E. P. Kartalov, C. Walker, C. R. Tayler, W. F. Anderson, A. Scherer, D. Maier-Schneider, J. Maiback, E. Obermeier, H. Huang, C. Fu, *Lab on a Chip* **2009**, *9*, 2070.

[96] V. B. Dang, S. J. Kim, *Lab on a Chip* **2017**, *17*, 286–292.

[97] J. A. Weaver, J. Melin, D. Stark, S. R. Quake, M. A. Horowitz, *Nature Physics* **2010**, *6*, 218–223.

[98] M. Wehner, R. L. Truby, D. J. Fitzgerald, B. Mosadegh, G. M. Whitesides, J. A. Lewis, R. J. Wood, *Nature* **2016**, *536*, 451–455.

[99] J. Shin, H. Park, V. B. Dang, C. W. Kim, S. J. Kim, *RSC Advances* **2015**, *5*, 23239–23245.

[100] W. H. Grover, R. H. Ivester, E. C. Jensen, R. A. Mathies, *Lab on a Chip* **2006**, *6*, 623–631.

[101] T. V. Nguyen, P. N. Duncan, S. Ahrar, E. E. Hui, *Lab on a chip* **2012**, *12*, 3991–3994.

[102] M. Rhee, M. A. Burns, *Lab on a Chip* **2009**, *9*, 3131–3143.

[103] B. C. Gross, J. L. Erkal, S. Y. Lockwood, C. Chen, D. M. Spence, *Analytical Chemistry* **2014**, *86*, 3240–3253.

[104] B. Gross, S. Y. Lockwood, D. M. Spence, *Analytical Chemistry* **2017**, *89*, 57–70.

[105] C. W. Hull, Apparatus for Production of Three-Dimensional Objects by Stereolithography, **1986**.

[106] M. P. Groover, *Fundamentals of Modern Manufacturing: Materials, Processes, and Systems*, 4th, John Wiley & Sons, Inc, Hoboken, NJ, **2010**, p. 1025.

[107] A. Ambrosi, M. Pumera, *Chemical Society Reviews* **2016**, *45*, 2740–2755.

[108] A. Waldbaur, H. Rapp, K. Länge, B. E. Rapp, *Analytical Methods* **2011**, *3*, 2681–2716.

[109] M. J. Beauchamp, G. P. Nordin, A. T. Woolley, *Analytical and Bioanalytical Chemistry* **2017**, *409*, 4311–4319.

[110] A. I. Shallan, P. Smejkal, M. Corban, R. M. Guijt, M. C. Breadmore, *Analytical Chemistry* **2014**, *86*, 3124–3130.

[111] H. Gong, B. P. Bickham, A. T. Woolley, G. P. Nordin, *Lab on a Chip* **2017**, *17*, 2899–2909.

[112] B. B. Xu, Y. L. Zhang, H. Xia, W. F. Dong, H. Ding, H. B. Sun, *Lab on a Chip* **2013**, *13*, 1677–1690.

[113] S. Bose, S. Vahabzadeh, A. Bandyopadhyay, *Materials Today* **2013**, *16*, 496–504.

[114] H. W. Kang, S. J. Lee, I. K. Ko, C. Kengla, J. J. Yoo, A. Atala, *Nature Biotechnology* **2016**, *34*, 312–319.

[115] G. Huang, F. Li, X. Zhao, Y. Ma, Y. Li, M. Lin, G. Jin, T. J. Lu, G. M. Genin, F. Xu, *Chemical Reviews* **2017**, *117*, 12764–12850.

[116] Y. Chen, H. N. Chan, S. A. Michael, Y. Shen, Y. Chen, Q. Tian, L. Huang, H. Wu, *Lab on a Chip* **2017**, *17*, 653–662.

[117] A. Håkansson, M. Rantatalo, T. Hansen, A. Wanhainen, *Vasa* **2012**, *40*, 453–459.

[118] D. G. Yu, C. Branford-White, Z. H. Ma, L. M. Zhu, X. Y. Li, X. L. Yang, *International Journal of Pharmaceutics* **2009**, *370*, 160–166.

[119] G. E. Höst, C. Larsson, A. Olson, L. A. Tibell, *CBE Life Sciences Education* **2013**, *12*, 471–482.

[120] V. F. Scalfani, T. P. Vaid, *Journal of Chemical Education* **2014**, *91*, 1174–1180.

[121] P. P. Rodenbough, W. B. Vanti, S.-W. Chan, *Journal of Chemical Education* **2015**, *92*, 1960–1962.

[122] V. Dragone, V. Sans, M. H. Rosnes, P. J. Kitson, L. Cronin, *Beilstein Journal of Organic Chemistry* **2013**, *9*, 951–959.

[123] P. J. Kitson, M. D. Symes, V. Dragone, L. Cronin, *Chemical Science* **2013**, *4*, 3099–3103.

[124] C. Parra-Cabrera, C. Achille, S. Kuhn, R. Ameloot, *Chemical Society Reviews* **2018**, *47*, 209–230.

[125] J. C. Brooks, K. I. Ford, D. H. Holder, M. D. Holtan, C. J. Easley, *Analyst* **2016**, *141*, 5714–5721.

[126] S. Somasundaram, M. D. Holtan, C. J. Easley, *Analytical Chemistry* **2018**, *90*, 3584–3591.

[127] J. Prikryl, F. Foret, *Analytical Chemistry* **2014**, *86*, 11951–11956.

[128] X. Li, J. C. Brooks, J. Hu, K. I. Ford, C. J. Easley, *Lab on a Chip* **2017**, *17*, 341–349.

[129] F. Cecil, M. Zhang, R. M. Guijt, A. Henderson, P. N. Nesterenko, B. Paull, M. C. Breadmore, M. Macka, *Analytica Chimica Acta* **2017**, *965*, 131–136.

[130] A. K. Au, W. Huynh, L. F. Horowitz, A. Folch, *Angewandte Chemie - International Edition* **2016**, *55*, 3862–3881.

[131] S. Waheed, J. M. Cabot, N. P. Macdonald, T. Lewis, R. M. Guijt, B. Paull, M. C. Breadmore, *Lab on a Chip* **2016**, *16*, 1993–2013.

[132] C. K. Dixit, K. Kadimisetty, J. Rusling, *TrAC - Trends in Analytical Chemistry* **2018**, *106*, 37–52.

[133] F. Li, N. P. Macdonald, R. M. Guijt, M. C. Breadmore, *Analytical Chemistry* **2017**, *89*, 12805–12811.

[134] N. P. Macdonald, J. M. Cabot, P. Smejkal, R. M. Guijt, B. Paull, M. C. Breadmore, *Analytical Chemistry* **2017**, *89*, 3858–3866.

[135] P. Juskova, A. Ollitrault, M. Serra, J. L. Viovy, L. Malaquin, *Analytica Chimica Acta* **2018**, *1000*, 239–247.

[136] H. Gong, M. Beauchamp, S. Perry, A. T. Woolley, G. P. Nordin, *RSC Advances* **2015**, *5*, 106621–106632.

[137] H. Gong, A. T. Woolley, G. P. Nordin, *Lab on a Chip* **2018**, *18*, 639–647.

[138] H. Gong, A. T. Woolley, G. P. Nordin, *Lab on a Chip* **2016**, *16*, 2450–2458.

[139] R. D. Sochol, E. Sweet, C. C. Glick, S. Y. Wu, C. Yang, M. Restaino, L. Lin, *Microelectronic Engineering* **2018**, *189*, 52–68.

[140] G. Comina, A. Suska, D. Filippini, *Lab on a Chip* **2014**, *14*, 424–430.

[141] G. Comina, A. Suska, D. Filippini, *Micromachines* **2015**, *6*, 437–451.

Chapter 2

Customized Electrode Polishing Robot for Bioanalytical Electrochemistry

2.1 Introduction

Various nucleic acid based electrochemical biosensors require formation of a self-assembled monolayer (SAM) on a gold electrode surface. To reproducibly prepare such a SAM, the surface should be uniform and free from fouling. For proper SAM formation, high electron transfer rates, and minimal background current, the metallic electrode requires activation [1]. Surface activation consists of standardizing the electrode surface's physical, chemical and electronic properties [2]. This can be accomplished through thermal, chemical, mechanical, or electrochemical means [3]. Thiol-based SAMs typically use a combination of mechanical, chemical, and electrochemical pre-treatment techniques for surface activation [4–13]. In most cases, surface activation protocols includes mechanical polishing to prepare the surface for SAM formation.

Mechanical polishing by hand is performed by grasping the macro-electrode, holding the electrode perpendicular to a very flat surface (eg. glass) bathed in a solution of finely divided abrasive (alumina, diamond powder) and pressing down. The electrode is then manipulated in circles or "figure 8" patterns to evenly polish the surface of the electrode, for beftween 3 and 30 minutes. The process is repeated with progressively smaller abrasive particle sizes until the electrode surface is a mirror finish. This process can take 9 minutes per electrode if three abrasive particles sizes were used (1.0, 0.3 and 0.05 μm). A basic experiment would use 3 electrodes, requiring approximately 30 min preparation, not accounting for polishing media exchange. This example expanded to a more realistic number of replicates would consume large amounts of time and energy [3, 5, 14–17].

Mechanical polishing can be performed by machine rather than by hand to conserve the scientists' time. The authors were unable to identify a device that was purpose built for mechanically polishing electrochemical macro-electrodes. A device does exist to polish micro-electrodes which costs greater than $7000. An alternative for research labs is to purchase a lapping/polishing machine. These devices consist of a variable speed rotating metal plate onto which a polishing cloth is affixed. Polishing media is pumped onto the rotating disk, while the electrode is manipulated by hand in a jig. Lapping/polishing machines can cost between $1000-$16000, are large (13x15x10 in^3) and heavy (35 lbs), all of which are impractical for academic research labs.

To meet the needs of academic research lab electrochemical experiments, the electrode polishing robot (EPBot) was constructed. The EPBot has two articulating arms, where the electrode is affixed at the apex and gently pressed against a polishing surface. The arms then move the electrode in a "figure 8" pattern typical of mechanical hand polishing, usually for 10 minutes.

In this chapter, hand and EPBot polishing methods are compared using gold substrates. To compare the polishing methods, the following techniques were used to interrogate the substrates' cleanliness: stripping chemisorbed oxygen monolayer, ferrocyanide/ferricyanide ($[Fe(CN)_6]^{-3/-4}$) redox couple probe, and atomic force microscopy (AFM) . Since it performs as well as hand polishing while saving time and effort through workflow automation, the EPBot should be a promising research tool for any electrochemist.

2.2 Materials and Methods

Reagents and Materials All solutions were prepared with deionized water. 100 mM phosphate buffer was prepared from solutions of 100 mM sodium phosphate dibasic heptahydrate (BDH, Poole, England) and 100 mM sodium phosphate monobasic monohydrate (BDH, Poole, England). Phosphate buffer solutions were combined to obtain a pH of approximately 7. The ferri/ferrocyanide couple ($[Fe(CN)_6]^{-3/-4}$) was prepared by combining

potassium ferricyanide (Fisher Scientific, Waltham, MA), potassium ferrocyanide trihydrate (Sigma Aldrich, St. Louis, MO), and potassium chloride (BDH, Poole, UK) to yield final concentrations of 10 mM, 10 mM, and 200 mM respectively. The solutions were sonicated briefly to aid dissolution.

Electrode Preparation 2 mm diameter gold electrodes (CH Instruments, Austin, TX) were contaminated by placing the electrodes gold side up on a laboratory shelf for between 2-3 weeks. The electrodes were immersed in piranha solution (3:1, conc. sulfuric acid (J.T. Baker):35% H_2O_2 (Alpha Aesar, Haverhill, MA) for 15 minutes and rinsed with deionized water. For manual polishing, the electrodes were mechanically polished on microfloc polishing pad (Buehler, Lake Bluff, IL) affixed to a glass substrate, saturated with water and 0.05 μm alumina suspension (Allied High Tech Products Inc., Rancho Dominguez, CA) for 10 minutes. The electrodes were then immersed in 1:1 deionized water (BDH, Poole, UK): 99.9% ethanol (Pharmco-Aaper, Toronto, ON) and sonicated 10 minutes, rinsed (DI H_2O) and dried under a stream of nitrogen.

Polishing Robot The robot design files began from freely available files on Thingiverse.com, which were originally designed as a plotter for drawing. These files were modified using Sketchup©software (Trimble Navigation Limited, SunnyVale, CA), where all superfluous parts were removed leaving only the structural members, articulating arms, and plate. Since the basic structure when printed warped and was flexible when assembled, all structural components were increased to 3 mm wall thickness and printed at 50% infill, with a 0.2 mm layer thickness for a total mass 91.4 g. The electrode holder was modified to securely hold a standard 6.35 mm diameter Kel-F, 55-mm long working electrode (CH Instruments). The polishing plate was increased in size to accommodate an 8 x 8 x 0.7 cm^3 glass plate, and a lip around the edge reduced water overflow. Finally, all holes were resized for either standard 4-40 hardware or the hardware included with the mechanical servos.

Software The EPBot uses the open-source Arduino (Arduino LLC, Turin, IT) programming environment. After the initial program upload, the polishing robot draws a "figure

eight“ pattern repeatedly on a surface for 10 min without connection to a computer. The software was modified to utilize the numeral eight, and all other drawing functions were removed. The initial and final arm positions were set to hold the electrode above the polishing surface, to allow access to exchange electrodes. A light emitting diode and piezoelectric buzzer were incorporated to indicate that the system was active and when a cleaning cycle was complete. Finally, four buttons were included in the program. Two buttons start or stop the system prematurely if needed. The remaining two buttons were used to raise and lower the arms to adjust the amount of force on the electrode during the polishing cycle.

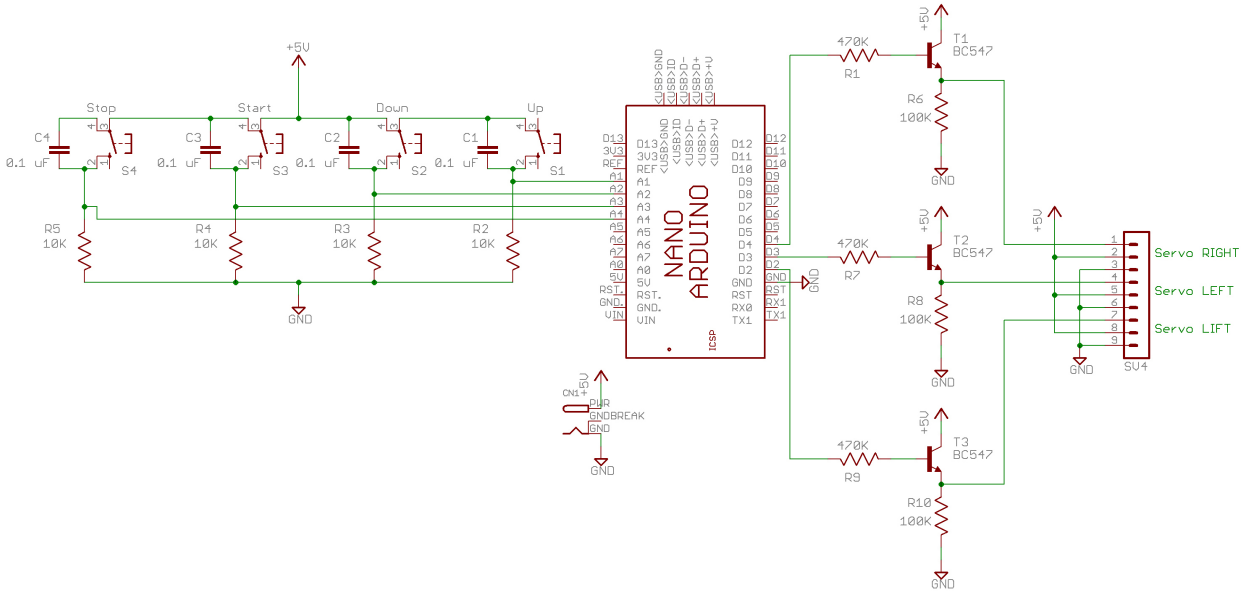

Figure 2.1: **EPBot Schematic.** EPBot schematic consisting of four hardware debounced switches, Arduino Nano microcontroller, and three transistors to interface standard servos.

Electronic Hardware To drive the components in the system, an Arduino Nano V3.0 (Arduino LLC) utilizing an Atmega328 processor was used. The microcontroller was soldered to a prototyping board (Datak 12-617), and all other components were affixed to the board as well. The three high-torque metal gear servos (PowerHD HD-1711MG) typically draw approximately 190 mA each, a total greater than the Arduino Nano 500 mA, 5 V regulator can supply. An external powersupply provides 5 V at 1500 mA (Triad Magnetics) to the Arduino and associated circuitry. The servos signal lines were isolated from the Arduino

Nano by NPN transistors, which alleviated electronic noise generated by the servos and provided supplemental power to the signal line. A large capacitor was placed across the power line circuit to reduce power spikes introduced by the servos. The four buttons were also debounced (the act of stabilizing a switch's output signal in a digital circuit) using a resistor-capacitor network (Figure 2.1).

Roughness Factor Determination A Gamry Reference 600 potentiostat was used to carry out standard oxide adsorption electrochemistry [3] The electrode was interrogated by CV, scanned at 50 mV s^{-1} between -0.3 V to 1.3 V vs Ag/AgCl reference, in 100 mM phosphate buffer pH 7.4. The counter, reference, and working electrodes were platinum mesh, Ag/AgCl (CH Instruments), and 2 mm diameter gold disk, respectively. Each experiment was performed in 5 mL of fresh phosphate buffer.

Atomic Force Microscopy The AFM (Multimode 8 – Bruker Corporation, Billerica, MA) images of gold foil were created by scanning a 10 μm by 10 μm area at 1 Hz scan rate, 512 samples per line, and 1.0 aspect ratio. Data was collected with ScanAsyst imaging mode, which applies an algorithm to peakforce tapping mode to reduce operator adjustment during imaging. Gold foil squares (0.1 mm thickness, 5 mm by 5 mm area, 99.99% purity, Sigma Aldrich) were epoxied onto six separate glass microscope slide substrates. The substrates and gold were washed with deionized water ($\sim$20 s/sample) and dried with a stream of nitrogen. Individual substrates were analyzed by scanning three randomly chosen spots. The six substrates were then immersed in piranha solution solution (3:1 conc. sulfuric acid (Mallinckrodt, Staines-upon-Thames, UK):30% H_2O_2 (Macron, Radnor, PA)) for ten minutes, and three randomly chosen spots were scanned with the same parameters previously mentioned. To evaluate polishing, the six substrates were split into two groups of three. Each group was polished with 0.05 μm alumina polishing suspension solution for ten minutes, either by hand polishing or EPBot polishing. Each substrate was washed with deionized water for 20 s, sonicated in ethanol:water (1:1 v/v) 10 min, dried under a stream of N_2 gas. Finally, each substrate was scanned by AFM at three randomly chosen spots.

2.3 Results and Discussion

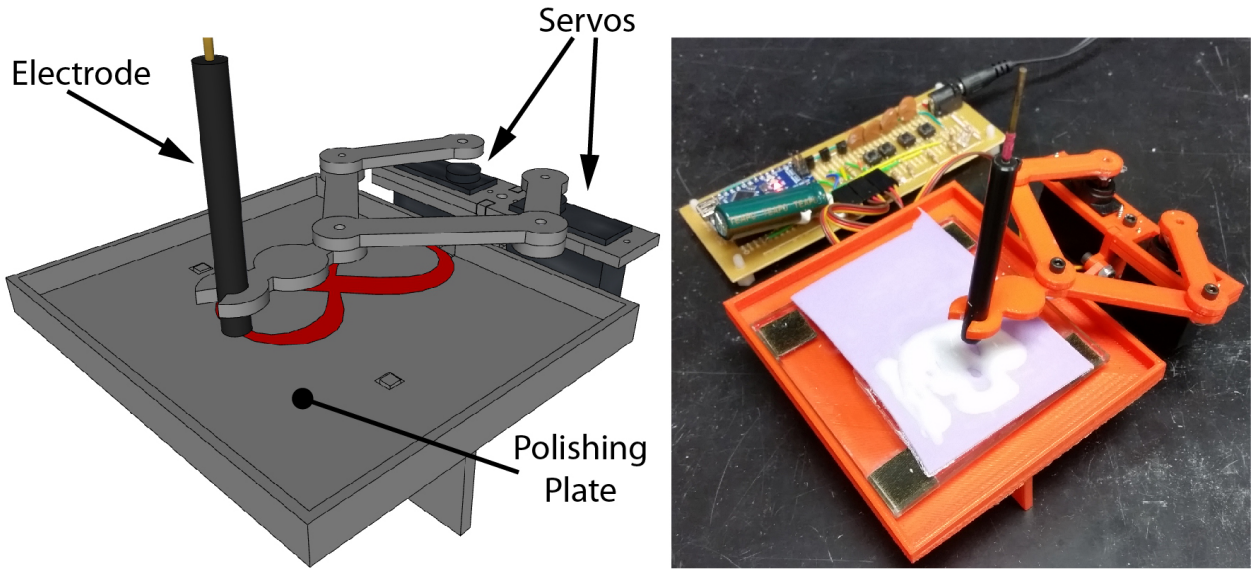

Figure 2.2: **EPBot Rendering and Assembled Device.** 3D rendered file, defining a "figure eight" motion on its surface, and the corresponding 3D printed functional device including circuitry and a gold disk electrode mounted in the holder.

An electrode polishing robot (EPBot) was developed to meet the needs for research quality macro-electrode polishing for electrochemistry applications (Figure 2.2). The EPBot resulted from a significant custom modifications in both design and firmware of the Plotclock. The robot uses two single joint arms to draw a "figure eight" pattern repeatedly over the course of 10 minutes. The EPBot requires 5 hours to 3D print and about 3-4 hours to assemble. The device's footprint is 19 cm x 13 cm x 7 cm, weighing 165 g and costing ~$60. The EPBot's effectiveness was compared to hand polishing using electrochemistry and microscopy techniques. Three techniques were used to evaluate differences between polishing methods (hand vs robot): cyclic voltammetry (CV) of a chemisorbed oxygen monolayer, ferrocyanide/ferricyanide $[Fe(CN)_6]^{-3/-4}$ redox couple probe, and atomic force microscopy.

The potential difference (ΔE_p) between peak anodic and cathodic currents in a CV trace is an indicator of surface cleanliness [18]. By definition, a single electron transfer such as the $[Fe(CN)_6]^{-3/-4}$ redox couple should yield an $\Delta E_p = 58$ mV on perfectly clean polycrystalline gold surface [18, 19]. The average pre-activation (mechanical polish, piranha solution) value

for our gold electrodes was $\Delta E_p = 213.4 \pm 41.4$ mV; the electrodes in this study were worn, therefore the 58 mV response was not expected. The ΔE_p data for the $[Fe(CN)_6]^{-3/-4}$ redox couple is presented in Table 2.1. The student's t-test was performed on post-hand polishing versus post-EPBot polishing, returning $p = 0.828$ (two-tailed, unequal variance). This value supports the hypothesis that hand polishing and robot polishing can produce equivalent electrochemical surfaces.

Polishing Method	**Average** mV
ΔE_p Pre-Hand Polishing	212.8 ± 29.01
ΔE_p Post-Hand Polishing	189.1 ± 33.03
ΔE_p Pre-EPBot Polishing	214.0 ± 29.56
ΔE_p Post-EPBot Polishing	190.8 ± 20.62

Table 2.1: Hand vs EPBot Polishing $[Fe(CN)_6]^{-3/-4}$ Redox Couple Data

Surface roughness is another common measure of how well a gold surface is prepared for use as a biosensor [3, 15, 20]. Surface roughness can be evaluated by measuring the oxygen stripping current from a gold surface. The roughness factor is calculated from the stripping current, a conversion factor present in the literature [3] (482 μC cm^{-2}), and the geometrical surface area. Acceptable values for the roughness factor, which is the ratio of microscopic surface area (A_m) to the geometric surface area (A_g), are between 2 to 3. Equation 2.1 is used to determine the roughness factor, ρ, where the geometric surface area is $A_g = 0.0314$ cm^2 for 2 mm diameter electrodes [19].

$$\rho = \frac{A_m}{A_g} \tag{2.1}$$

Surface roughness was determined before and after polishing, for two sets of electrodes hand polished (7 electrodes, 22 replicates) and EPBot polished (4 electrodes, 14 replicates). The average surface roughness apparently increased by ∼0.46 after polishing, for both polishing methods. It should be noted, however, that the error in the data suggests that roughnesses before and after polishing were equivalent. When comparing the average peak height,

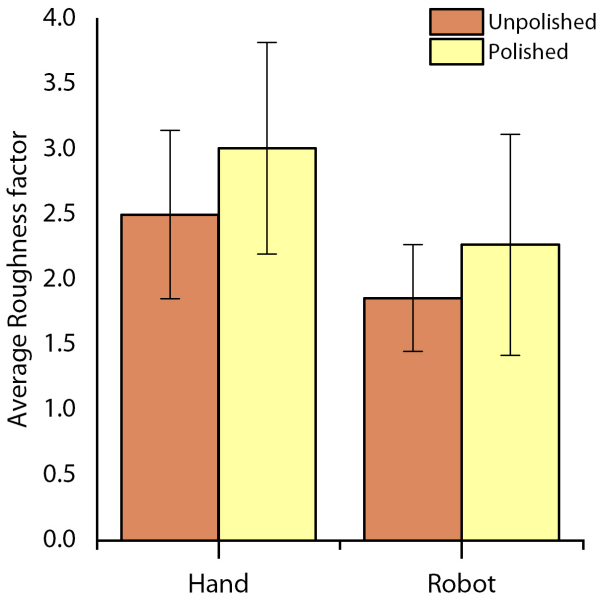

Figure 2.3: **Average Roughness Factor - Hand vs. Robot Polished.** Standard oxide adsorption electrochemisty was performed to determine the electrochemical roughness factor for electrodes polished by either hand or EPBot. Data show an increase of approximately the same for both electrodes, however the large standard deviation of each data set suggests the electrodes are similar pre and post polishing.

the surface roughness appeared to increase slightly, which is not ideal, but the increase was generally the same for both sets of electrodes, as shown in (Figure 2.3).

The surface morphology was then studied by atomic force microscopy (AFM) imaging of polished gold foil, bonded to glass (Figure. 2.4). The hand and robot polished samples were compared by choosing three random spots on each sample's AFM image, before piranha treatment, after piranha, and after polishing. The average root mean square roughness (R_q) is plotted in (Figure 2.5). While the absence of a decrease in surface roughness was unexpected, again the hand polishing method and robot polishing method were essentially equivalent, while the EPBot provided the additional advantage of an automated workflow. When comparing the roughness ratio of the gold foil substrate and gold foil after polishing, the average ratio of roughness after polishing versus substrate was 1.22 ± 0.56 for the hand polished group and 1.28 ± 0.63 for robot polished group. It appears that the robot polishing method results in electrodes with statistically equal ($p=0.8$, t-test) surface roughness ratio

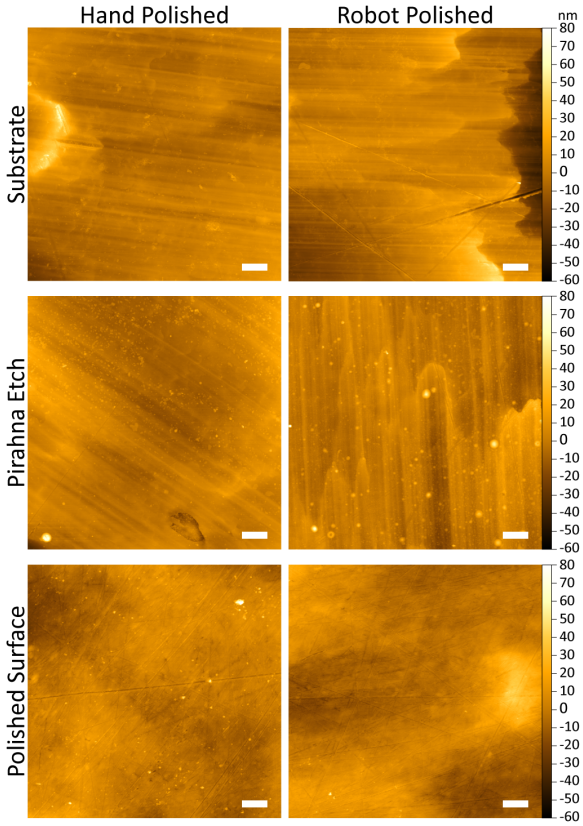

Figure 2.4: **AFM Output Images.** Hand polished versus EPBot polished gold foil, substrate alone, Piranha etched, and Polished surfaces. Scale bar 1 μm.

compared to the hand polishing method. However, the deviations in roughness for robot polishing were smaller after polishing, which suggests that the robot polishing method gave slightly more consistent surface roughness. This can be exemplified by data in (Figure 2.5), as the post-polish variance was much smaller with the robot polishing approach.

Finally, a long term (100 day) study of the roughness factor was conducted by oxygen stripping analysis of 2 mm diameter gold disk electrodes, polished by the EPBot (Figure 2.6). Although, a drift in roughness factor did occur over the course of 100 days, the change was not drastic and can be attributed to normal wear of the electrodes. Considering that the roughness fell within the acceptable range for at least 100 days while using entirely automated polishing (EPBot), the robot has certainly earned a place in our lab for electrode polishing.

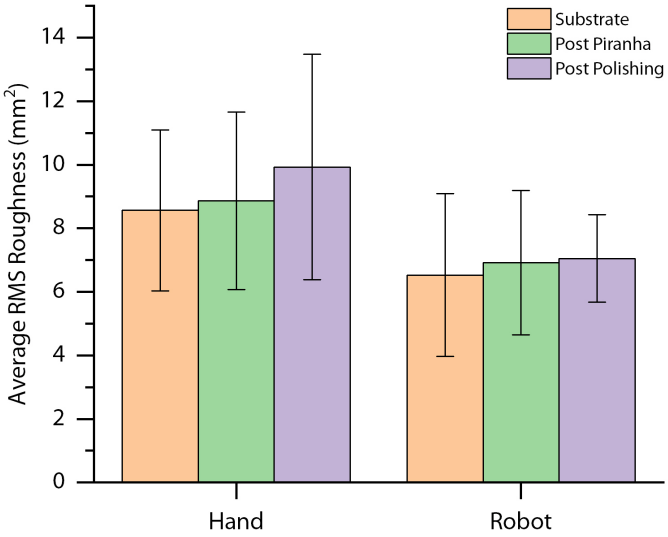

Figure 2.5: **Average RMS roughness from AFM** Triplicate AFM roughness factor measurements were plotted for hand and EPBot polishing methods.

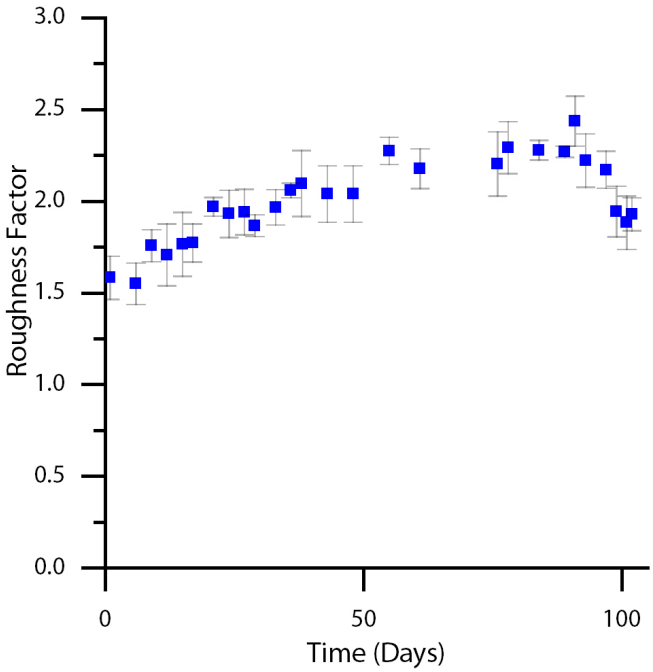

Figure 2.6: **Roughness Factor versus Time (100 days)** The roughness factor was calculated from electrodes polished by the EPBot over the course of 100 days showing the long term effectiveness of the EPBot.

2.4 Conclusions

Commercially available electrodes require conditioning before formation of nucleic acid SAMs commonly used in biosensing applications. In this chapter, we have demonstrated that our custom EPBot can provide an automated, inexpensive alternative to hand polishing of electrodes. While surface roughness of electrodes appeared to be unchanged with either EPBot or manual polishing, it was shown that the EPBot could provide statistically equal results when compared to manually polishing by hand. Finally, the EPBot was validated with a 100-day study, where electrodes of acceptable surface roughness were cleaned, polished in an automated fashion, and used by others in the lab for successful biosensing of proteins and nucleic acids [21], similar to sensing done by others in the field [7, 10, 12, 13]. At the least, this method provides researchers with a portable, inexpensive, automated alternative to assist in the standard protocols for electrode preparation.

References

[1] J. Tkac, J. J. Davis, *Journal of Electroanalytical Chemistry* **2008**, *621*, 117–120.

[2] C. G. Zoski, *Handbook of Electrochemistry*, 1st ed., Elsevier, Oxford,UK, **2007**, p. 935.

[3] J. C. Hoogvliet, M. Dijksma, B. Kamp, W. P. Van Bennekom, *Analytical Chemistry* **2000**, *72*, 2016–2021.

[4] R. J. White, H. M. Kallewaard, W. Hsieh, A. S. Patterson, J. B. Kasehagen, K. J. Cash, T. Uzawa, H. T. Soh, K. W. Plaxco, *Analytical Chemistry* **2012**, *84*, 1098–1103.

[5] J. Liu, S. Wagan, M. Dávila Morris, J. Taylor, R. J. White, *Analytical Chemistry* **2014**, *86*, 11417–11424.

[6] A. A. Lubin, B. V. S. Hunt, R. J. White, K. W. Plaxco, *Analytical Chemistry* **2009**, *81*, 2150–2158.

[7] P. Jolly, P. Zhurauski, J. L. Hammond, A. Miodek, S. Liébana, T. Bertok, J. Tkáč, P. Estrela, *Sensors and Actuators B: Chemical* **2017**, *251*, 637–643.

[8] P. Dauphin-Ducharme, K. W. Plaxco, *Analytical Chemistry* **2016**, *88*, 11654–11662.

[9] R. J. White, N. Phares, A. A. Lubin, Y. Xiao, K. W. Plaxco, *Langmuir* **2008**, *24*, 10513–10518.

[10] M. Staderini, E. González-Fernández, A. F. Murray, A. R. Mount, M. Bradley, *Sensors and Actuators B: Chemical* **2018**, *274*, 662–667.

[11] L. R. Schoukroun-Barnes, S. Wagan, R. J. White, *Analytical Chemistry* **2014**, *86*, 1131–1137.

[12] Y. Wu, R. Y. Lai, *Analytical Chemistry* **2017**, *89*, 9984–9989.

[13] N. Hong, L. Cheng, B. G. Wei, C. D. Chen, L. L. He, D. R. Kong, J. X. Ceng, H. F. Cui, H. Fan, *Biosensors and Bioelectronics* **2017**, *91*, 110–114.

[14] E. Boubour, R. B. Lennox, *Langmuir* **2000**, 4222–4228.

[15] Z. Li, L. Zhang, S. Zeng, M. Zhang, E. Du, B. Li, *Journal of Electroanalytical Chemistry* **2014**, *722-723*, 131–140.

[16] R. F. Carvalhal, R. S. Freire, L. T. Kubota, *Electroanalysis* **2005**, *17*, 1251–1259.

[17] J. Hu, T. Wang, J. Kim, C. Shannon, C. J. Easley, *Journal of the American Chemical Society* **2012**, *134*, 7066–7072.

[18] L. M. Fischer, M. Tenje, A. R. Heiskanen, N. Masuda, J. Castillo, A. Bentien, J. Émneus, M. H. Jakobsen, A. Boisen, *Microelectronic Engineering* **2009**, *86*, 1282–1285.

[19] A. J. Bard, L. R. Faulkner, *Electrochemical Methods : Fundamentals and Applications*, 2nd, John Wiley & Sons, Inc, New York, **2001**, p. 833.

[20] G. Feng, T. Niu, X. You, Z. Wan, Q. Kong, S. Bi, *Analyst* **2011**, *136*, 5058–5063.

[21] K. I. Ford, PhD thesis, **2016**, p. 111.

Chapter 3

Customized Thermal Control Systems for Bioanalytical Applications

3.1 Introduction

It is commonly known that DNA undergoes denaturation or melting based on several factors including temperature, pH, ionic strength, and guanine-cytosine pair content[1]. Our group focuses on developing biosensors based on DNA, and one factor which has proven useful in understanding and controlling these assays is temperature manipulation. In one example of our work, a bivalent fluorescent probe in the presence of its target is thermally scanned, yielding a melting curve exhibiting two distinct peaks. One peak, usually at lower temperature, is considered the background, because the target-independent annealing of bivalent probes is more unstable. The second peak, usually at higher temperature, corresponds to the assembly of the target-bivalent probe complex, which consists of the target molecule bound to DNA-probe conjugates and is inherently more stable, requiring greater thermal energy to denature. This thermofluorimetric analysis (TFA) of bivalent probes (see Figure 3.5 below) can be applied quantitatively to protein analysis[2, 3]. The second example is that of an electrochemical DNA-based biosensor. Recently, our lab developed a single stranded DNA detection method, where two DNA strands simultaneously hybridize to the target DNA. The structure forms a "Y" shape, where the target DNA sits in the crook of the "Y" shape, bridging the two oligos. One oligo is surface-bound, while the second DNA strand is redox labeled and free in solution. The second DNA strand can hybridize with the target, and once the target hybridizes with the surface bound DNA, the redox label is brought near the surface providing a signal when interrogated by square-wave voltammetry (SWV) (see Figure 3.10 below)[4]. Both of these methods required precise thermal control to carry out the experiments. In the TFA method, continuous thermal scanning was applied

while measuring fluorescence. In the branched DNA assay, isothermal SWV was carried out at many different temperatures.

Such thermal scanning requires time to transition and stabilize to a defined temperature, at which time a measurement can be made. Standard instrumentation is available for TFA methods, such as real-time quantitative polymerase chain reaction (qPCR) systems. However, thermal scanning systems compatible with microfluidic TFA or small volume electrochemistry measurements are not readily available. The work outlined in this chapter highlights the development of customized systems for these purposes. To meet the needs of these assays, a customized Peltier thermal regulator was outfitted with a PID-based feedback controller using LabVIEW software, which was capable of $\pm$ 0.2 °C stability over a 65 °C range. Additionally, the design and characterization of a thermal gradient device is presented, with the goal of overcoming the need for longer scanning times in future work. The thermal gradient is created by two temperature zones controlled by neighboring Peltier devices (dual Peltier; Arduino hardware), ideally suited for application to a microfluidic chip due to its low thermal dissipation in the z-axis. Several examples of this have been demonstrated[5–7] and applying this technique to our TFA approach would make a more rapid, mix-and-read measurement system possible.

3.2 Materials and Methods

LabVIEW Controlled Peltier Driver The Peltier controller is made up of a computer running a custom LabVIEW (National Instruments, Austin TX) application[8, 9], which controls a MAX1978 integrated Peltier driver board (Digi-Key, Thief River Falls, MN), through a NI-DAQ USB-6008 module (NI Austin, TX) (Figure 3.1). The MAX1978 board drives a Peltier module (Cui inc. CP30138) sandwiched between an aluminum block and a fan cooled heat sink (910-40-1-23-2-B-0 Wakefield-Vette) held in place by thermal tape (3M10315-ND 3M). Thermal feedback was provided by a 10k precision thermistor (US Sensor

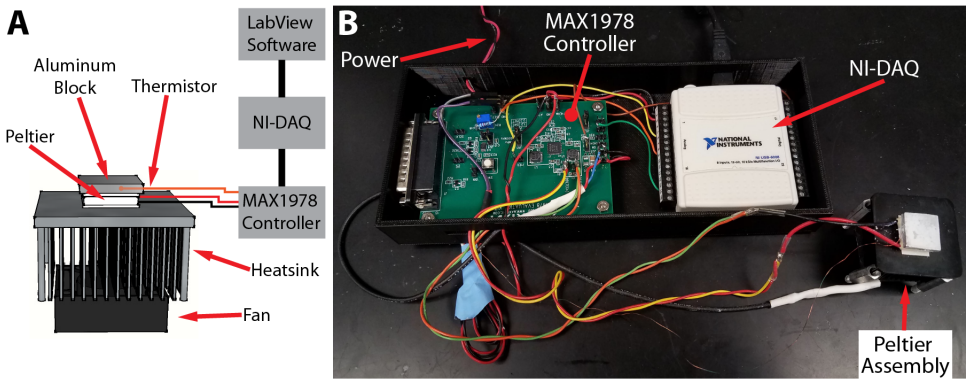

Figure 3.1: **LabVIEW based Peltier controller.** A. 3D rendering overview of the Peltier device. An aluminum block thermally coupled to the Peltier, sits on a heatsink cooled by a fan. B. Connections for both power, and the thermistor are made to the Peltier/Aluminum block. The connections lead to the MAX1978 Peltier driver, then the NI-DAQ and finally to LabVIEW software.

USP12837) embedded in the aluminum block. A 5 V, 10 A switching power supply (Digi-Key Thief River Falls, MN) provided power to the Peltier controller. A 3D-printed box was created in Sketchup (Trimble Inc. Sunnyvale, CA) 3D modeling software and printed on a MakerBot Replicator 2X (MakerBot Industries LLC. New York, NY) with polylactic acid filament (PLA), to contain both the DAQ USB-6008 and the MAX1978 controller board. The system is capable of ± 0.115 °C stability and a ± 1.04 °C set point error over 65 °C range.

The MAX1978 controller board required setup, firstly the Peltier maximum driving current and voltage are set before powering the board on. If a Peltier was connected and the controller was not limited, the Peltier could be destroyed. The board defaults to ± 2.2 amps and 4 V, similar to the CP30138 Peltier module's max input ratings (3 A, 3.8 V). See the Dual Peltier Driver section for details on modifying maximum current/voltage values for the MAX1978 board. The remaining connections for the board are shown in (Figure 3.2) [modified from MAX1978 Datasheet]. The shutdown pin, when held low (0 V) prevents power up of the Peltier driver, and it was used when initializing the LabVIEW program preventing Peltier thermal runaway and damage. A 0-3 V (DC) signal from the LabVIEW application was applied to "control signal in" pin; 1.5 V corresponded to zero

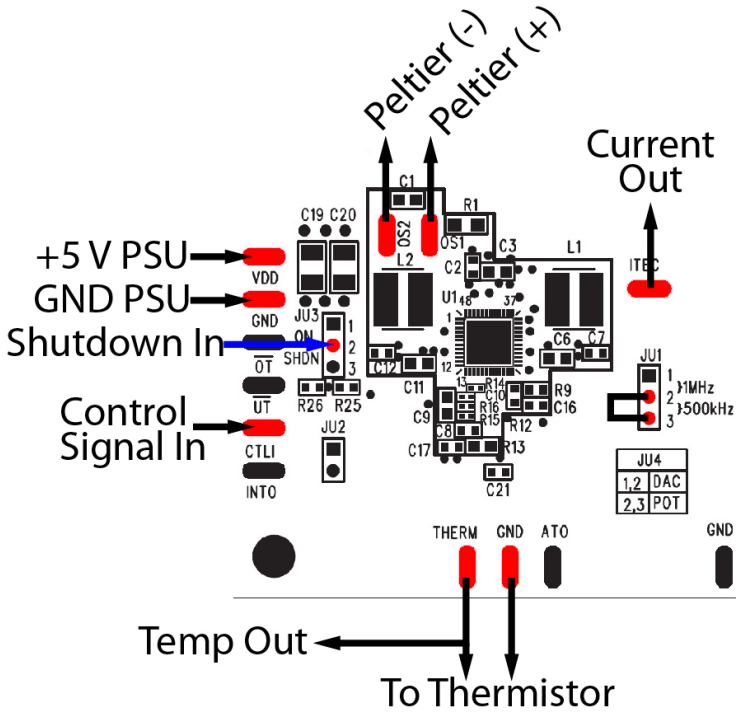

Figure 3.2: **Maxium MAX1978 controller board connections.** The MAX1978 evaluation board relevant connections are highlighted in red and labeled accordingly.

output, 3 V to full heating, and 0 V to full cooling. Two inputs were measured by LabVIEW via a NI-DAQ USB-6008, the thermistor output and Peltier current. The 10k thermistor was connected across "therm" and "GND" pins, where the therm pin was in series with a precision 10k resistor and was connected to 1.5 V, creating a voltage divider and an output voltage proportional to temperature. The thermistor in all Peltier circuits in this document was an NTC USP12837 micro 10k thermistor with ± 1% tolerance in the operating range between -55 to 125 °C; the company (US Sensor Corp. Orange, CA) provided Steinhart-Hart coefficients for this component. See Appendix B for equations and coefficients related to calculating the temperature from the resistance. The switching frequency of the controller was set to 500 kHz by jumper JU1 for higher efficiency. Current output could be monitored on pin "ITEC", where a voltage from 0-3 V was proportional to the current consumption by the Peltier, and zero current gave a 1.5 V signal. The final connections were made to the Peltier module's positive and negative wires. Custom modifications to the LabVIEW

virtual instrument application included the addition of the thermistor voltage measurement then conversion to temperature and the incorporation of a current read function. The full LabVIEW program is available in the Appendix A. The PID settings found in Appendix A can be manipulated if the Peltier is replaced or if an alternate response is required (faster heating, less overshoot).

Characterization The LabVIEW based Peltier driver was tested at room temperature, where the aluminum block was exposed to air. The test parameters were: Initial Temp = 0 °C ,Final Temp = 65 °C , Step size = 5 °C, Step Time = 2 min.

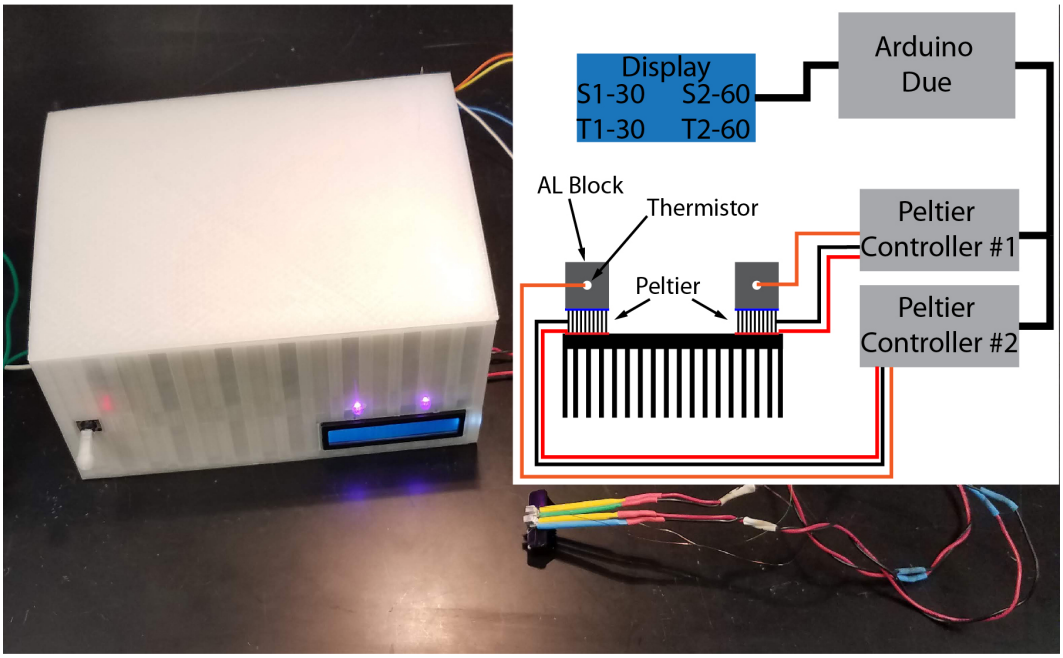

Figure 3.3: **Dual Peltier controller and system connections.** The dual Peltiers and MAX1978 controllers and LCD display are controlled by an Arduino DUE. Initially, the system boots into a safe mode, allowing both Peltiers set points to be adjusted then the system begins operation.

Portable Dual Peltier Driver A portable dual Peltier driver constructed in-house was controlled by custom programmed Arduino software, and the overall system is shown in (Figure 3.3). The driver has an Arduino Due microcontroller board, a 16 x 2 LCD display (Meeeno IIC LCD-1602 Blue Screen LCD), and a Bluetooth wireless module (JY-MCU Bluetooth Wireless Serial Port) for data logging; all of these components were obtained

from Deal Extreme (www.dx.com). In addition, duplicate MAX1978 driver boards, 5-way switches, 3.4 mm x 5 mm Peltiers (Laird OT08,08,F0,0303,GG, W2.25), 10k precision resistors (USP12837; US Sensor Corp. Orange, CA) were all purchased from Digi-key (Thief River Falls, MN). System power was provided by a 5 V, 10 A switch-mode mains power supply (Digi-key Thief River Falls, MN) and regulated to 3.0 V by a LM317t adjustable voltage regulator (Digi-key Thief River Falls, MN) providing power to the Arduino Due, which was 5 V intolerant. The Arduino Due board controlled the Peltier devices by a 12-bit internal ADC measuring the thermal signal's voltage through in-line low pass filters with cutoff at 1 kHz, then sending a PID corrected signal via serial peripheral interface (SPI) to each MAX1978 onboard 16-bit DAC (MAX5144), driving a Peltier to heat or cool accordingly. An Arduino PID library provided precise control over the duplicate Peltiers, where was determined to be $\pm$ 0.07 °C with <0.02 °C set point error over 75 °C range.

Characterization

Step Test Duplicate Peltiers were affixed close to each other on a 29 mm x 10 mm x 20 mm (L x W x H) heat sink. The heatsink was submerged in a water bath at room temperature, and the following settings were used. Peltiers were identically set at: Initial Temp = 0 °C, Final Temp = 75 °C, Step size = 5 °C, Step Time = 2 min. Data were analyzed by exclusion of the initial 40 s of the temperature step data, and statistics were derived from the remaining 80 s at each step.

Divergent Step Test Peltiers were tested at room temperature for this experiment. Peltier 1: Initial Temp = 35 °C, Final Temp = 75 °C, Step size = 5 °C, Step Time = 2 min. Peltier 2: Initial Temp = 35 °C, Final Temp = −5 °C, Step size = 5 °C, Step Time = 2 min. Data were analyzed as per the step test above.

Thermal Imaging Thermal images were taken of dual Peltiers mounted on communal heat sink, where one Peltier was set at 0 °C and the second at 80 °C. Thermal images were

taken with a FLIR50E camera, which has a built-in visible light camera, simultaneously capturing both IR and visible images.

3.3 Results and Discussion

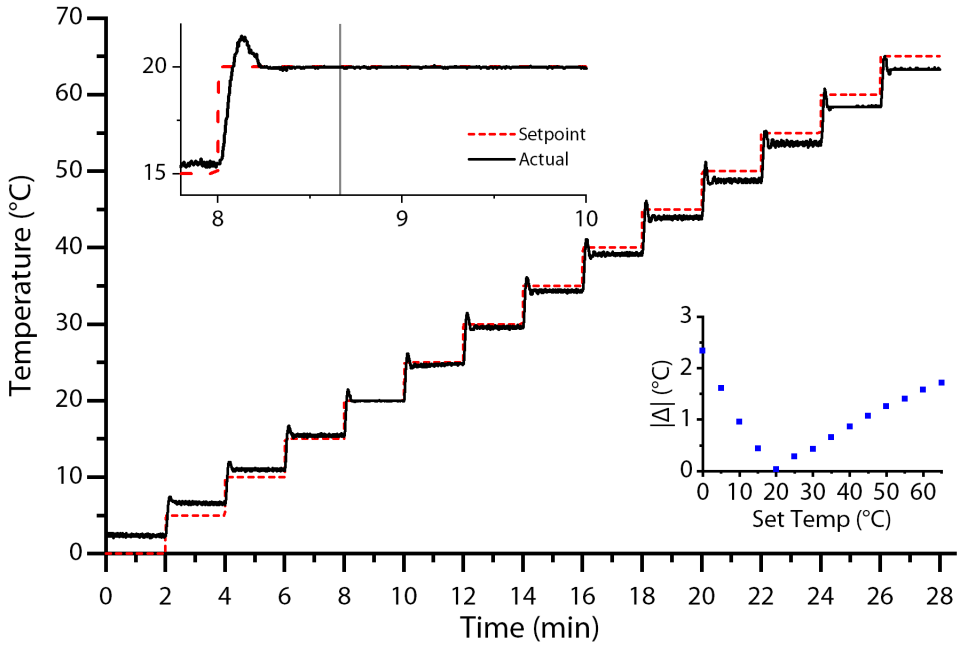

Figure 3.4: **LabVIEW Controlled Peltier Step Response.** A 5 °C setpoint was incremented every 2 min between 0 and A 75 °C and the response was plotted. The upper inset is a typical step showing the set point and the thermal response. The lower inset demonstrates accuracy of the system.

The Peltier controllers' function was evaluated by a step test, where the set point was incremented 5 °C every 2 min, and the resulting data is plotted in (Figure 3.4). The parameters were chosen to allow 40 s stabilization time (inset gray line) and 80 s for measurements before the next step was applied. Although the Peltier system was capable of a faster response, the current PID settings were optimized for stability over speed. Thermal masses of both the aluminum block and electrochemical cell ultimately limited the step response. The inset image emphasizes the accuracy after equilibration of the thermal system. The starting set point was 0 °C, and from (Figure 3.4) the temperature never reached 0 °C before the step program began running. This offset error is a consequence of the PID settings,

where the integral term which adjusts the steady state error was too low. The PID's initial settings were optimized for room temperature 25 °C, and therefore at that point minor offset error was observed. In general, the PID settings were considered acceptable based on the fast input response, limited overshoot, and rapid settling time. Since the temperature was recorded continuously, the need for temperature stability was more important than high set-point accuracy.

The Peltier exhibited a finite cooling capacity, which was only realized in thermally well insulated and isolated systems, where the heat generated from the Peltier is pumped from one surface to another. Additionally, Peltiers (as with most semiconductors) have stronger heating response[10] than cooling, limiting the lowest possible temperature attainable. Total fluctuation in temperature of this system was ± 0.115 °C, and offset error was 1.05 °C.

Peltier Thermal Controller Applications

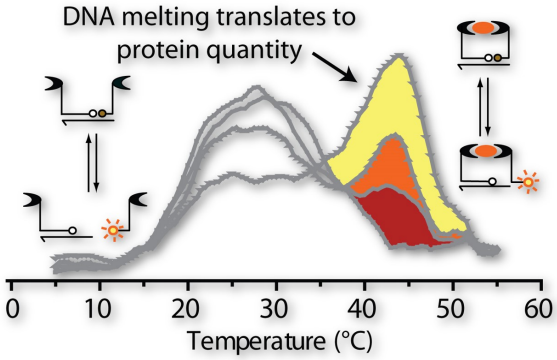

Figure 3.5: **Fundamental principles of TFA analysis.** FRET labeled oligos bound to antibodies are free in solution. In the unbound state a background signal is formed ∼30 °C. In the bound state, with a target present in solution a thermal scan of the system demonstrates a change in melting point of the structure, yielding peaks shift to ∼45 °C. When the concentration of the target is varied, the peak area varies proportionally allowing quantitative measurements. Reprinted in part from reference [2] with permission from, ©2015 American Chemical Society.

This LabVIEW controlled Peltier driver was then applied to both TFA and thermal scanning electrochemical detection (tsEC). Thermofluorimetric analysis was carried out with the LabVIEW controlled Peltier in contact with a microfluidic device to detect both insulin and

thrombin at nanoliter and picoliter volumes while the temperature was scanned. With the tsEC, either 2 mm diameter disk electrodes or GoG fabricated electrodes were immobilized with the detection system, then thermally scanned the and recorded voltammetry data.

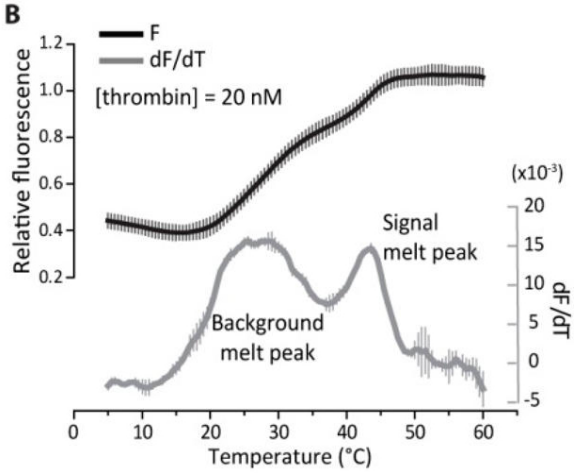

Figure 3.6: **Raw fluorescence data converted to quantifiable data.** The derivative of the raw temperature scanned fluorescence data yield background and signal melt peaks for Thrombin.Reprinted in part from reference [2] with permission from, ©2015 American Chemical Society.

Thermofluorimetric Analysis (TFA) TFA methods rely on melting of DNA at elevated temperatures, where the melting temperature is indicative of the bound or unbound state of the proximity complex or probe-target complex. Dr. Joonyul Kim and Dr. Juan Hu in our lab previously developed the TFA system shown in Figure 3.5. The system is made up of a FRET pair, where either unit is bonded to an oligo which is covalently bonded to an antibody (insulin detection) or is part of an aptamer sequence (thrombin detection). Additionally, a connector DNA sequence was used to stabilize the FRET pair. The first state of the system is without target, where at low temperatures the FRET pair is brought together by the connector in free solution, creating a background. The second state is when a target is present, where the antibody-oligos or aptamers bind to the target molecules, bringing the FRET pair near to each other (along with connectors) to promote quenching of the fluorescence. The target complex is inherently more stable when compared to the background complex, and since DNA hybridization is temperature dependent, this results in separate melting

points for background and signal. By calculating the derivative of the temperature scanned fluorescence data, distinct peaks of unbound and target-bound probes are uncovered; the raw/processed data is shown in Figure 3.6. The concentration dependences of TFA methods were validated by creation of standard curves for insulin and thrombin, with detection limits of 0.81 nM and 1.88 nM in serum[11, 12]. TFA demonstrated sub-nanomolar detection limits and high selectivity. The assay is homogeneous, requiring no physical separation of analytes from the original sample, e.g. Mix-and-Read, and were analyzed by commonly available qPCR.

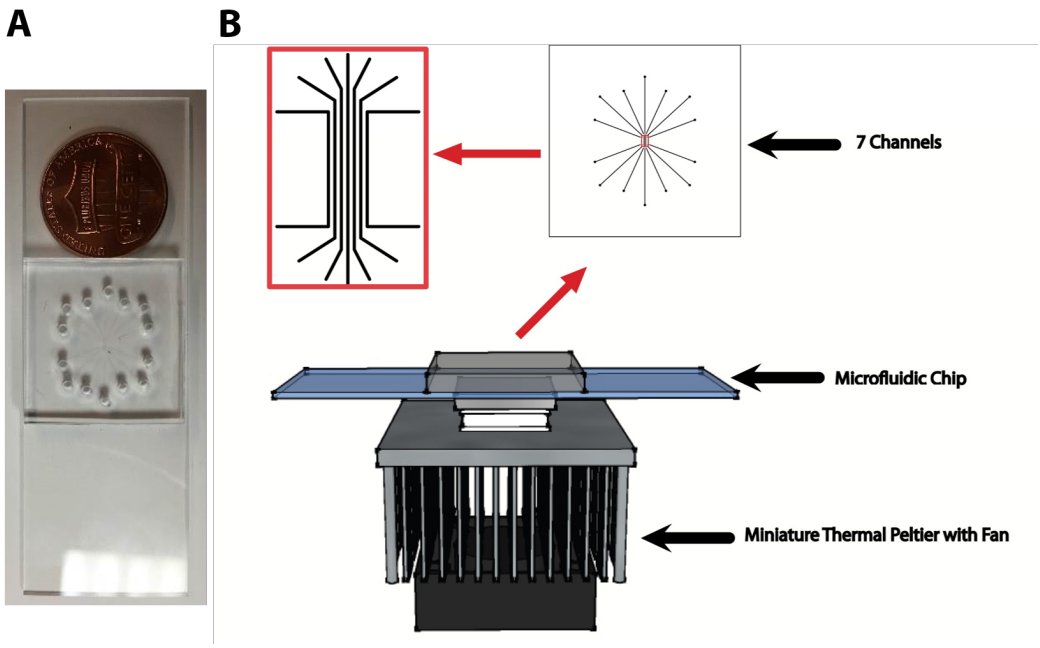

Figure 3.7: **7 Channel microfluidic chip setup.** (A)The assembled microfluidic chip. (B)7 parallel channels are arranged across the viewing area of the microfluidic chip, the device is then placed on top of the Peltier element and inverted on the microscope to capture fluorescence images. Reprinted in part from reference [2] with permission from, ©2015 American Chemical Society.

As TFA has been proven useful, miniaturization of the system for microfluidic applications at nanoliter or picoliter volumes was the next step, but this required customized thermal control instrumentation, as reported herein. A 7-channel microfluidic device was constructed, and a miniature Peltier element was embedded in the detection region of the

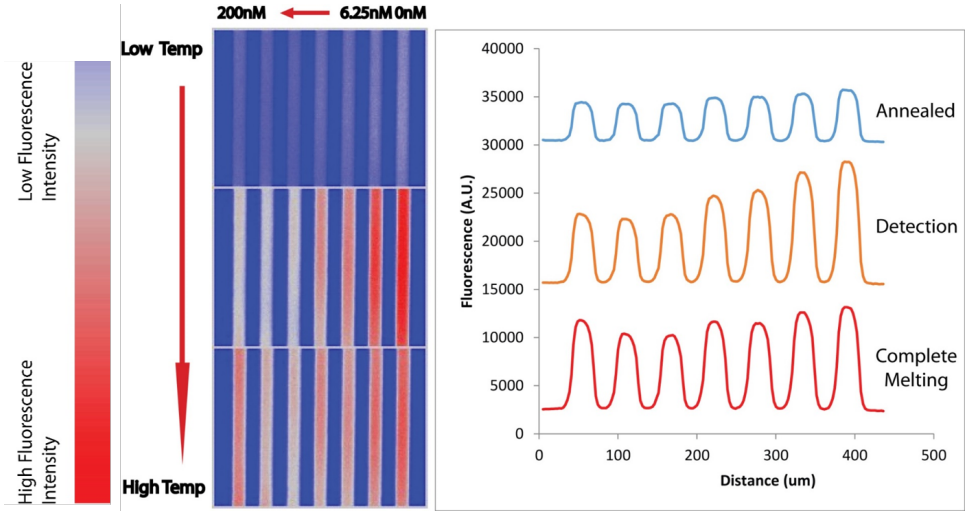

Figure 3.8: **Parallel 7 channel raw fluorescence output.** Concentration of thrombin was increased from right to left in the 7 channels. Three (low to high)temperature points were chosen to represent. The fluorescence intensity across the channels was extracted by ImageJ and represented in the plot as fully annealed, the detection region, and completely melted complex. Reprinted in part from reference [2] with permission from, ©2015 American Chemical Society.

device to scan various temperatures while collecting fluorescence data (Figure 3.7). This microfluidic TFA (μTFA) device was applied to thrombin detection directly in the microchannels. Fluorophore- and quencher-labeled thrombin aptamers were added with varying concentrations of thrombin, increasing from right to left (0 to 200 nM) in Figure 3.8. A stepped thermal scan was performed on the chip, and at each step a fluorescence image was acquired with the microscope and CCD camera. ImageJ processing yielded profiles of each channel, and it was observed that the labeled aptamers changed from fully annealed to fully melted. The fluorescence output was observed to be concentration dependent, notably at the mid-range temperatures as expected for the melting region (Figure 3.8). The resulting output was corrected, and the derivative taken (Figure 3.9). From these data, it was clear that the signal peak at $\sim$43 °C emerged and increased with target concentration. The resulting peak heights were then plotted versus concentration yielding a standard curve for thrombin with a LOD of 0.75 attomoles. Similarly, this system was applied to the insulin detection with Ab-oligos, yielding a LOD of 2.6 amol. These results were possible due to the stability

afforded by the Peltier based temperature control system that was developed as part of this dissertation work.

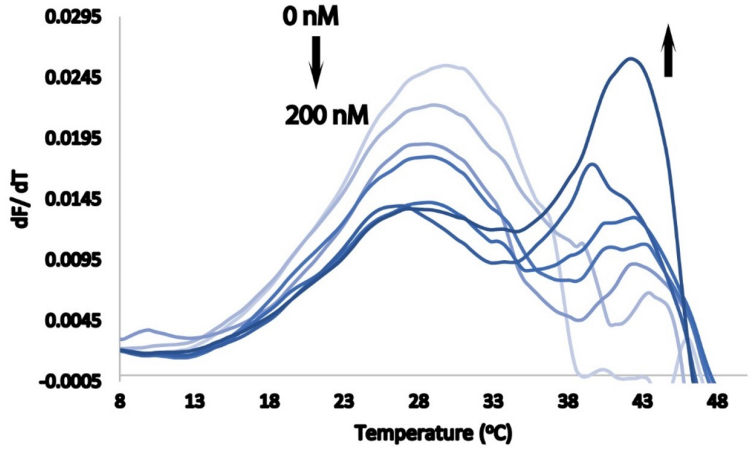

Figure 3.9: **Processed μTFA output data.** The derivative (dF/dt) thrombin thermal scanning data is presented. The higher stability thrombin complex melts at a higher temperature 43 °C in comparison to the background 30 °C. Reprinted in part from reference [2] with permission from, ©2015 American Chemical Society.

Thermal Scanning Electrochemical Detection (tsEC) The Peltier driver was then applied to optimization of a novel electrochemical assay employing a single branched DNA sensor architecture. This assay system was designed for eventual application to blood circulating DNA/RNA detection and was developed in our lab by Dr. Somasundaram[4]. This work explored SWV frequency, temperature, and oligonucleotide binding affinities of a two-oligo, proximity-dependent target capture design. Target binding was stabilized partially by interaction with the thiolated-DNA and with MB-DNA (Figure 3.10), and these interaction energies were varied experimentally. The hybridization regions (colored in green, blue, or red) were modified and compared against each other while the SWV frequency and temperature were varied.

To accomplish the collection of such a large data set, automation of the potentiostat and thermal systems was required. The physical electrochemical cell and Peltier system is depicted in (Figure 3.11A). The GoG working electrodes (patterned in duplicate pairs) were

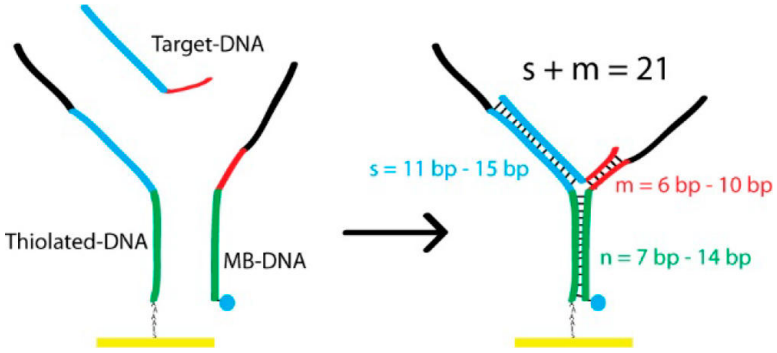

Figure 3.10: **Single-branched DNA detection system.** For the detection of DNA, a branched nucleic acid system made up of a thiolated DNA and methylene blue labeled oligo. The system was optimized for DNA hybridization at two locations, target DNA toe-hold and MB-DNA to thiolated-DNA. Regions in black did not participate in optimization. Reprinted in part from reference [4] with permission from, ©2018 American Chemical Society.

plasma oxidized to PDMS chambers, the chambers were filled with buffer during the measurement, and counter and reference electrodes were submerged into the buffer to complete the three-electrode cell. The LabVIEW controlled thermal system coordinated the sequencing of the electrochemical measurement and the thermal step. Once the thermal step and potentiostat parameters were entered, the system was ready. Then the LabVIEW thermal program was started, the Peltier's initial temperature was reached, and this temperature stabilized before the experiment began. Once the actual temperature was within 1 °C of the set point, thermal data collection began. LabVIEW was configured to then trigger the potentiostat (Gamry Reference 600) via an external data line, causing the potentiostat's program to run, collecting voltammograms. After electrochemical data was collected, the potentiostat delayed until another trigger input was received. The thermal program stepped the preset value and stabilized before again triggering the potentiostat to collect data. A labeled, 3D rendering of the full system is shown in Figure 3.11B.

Characterization and optimization of the single-branched DNA detection system was initially carried out by modifying the hybridization energy (number of base pairs) at each

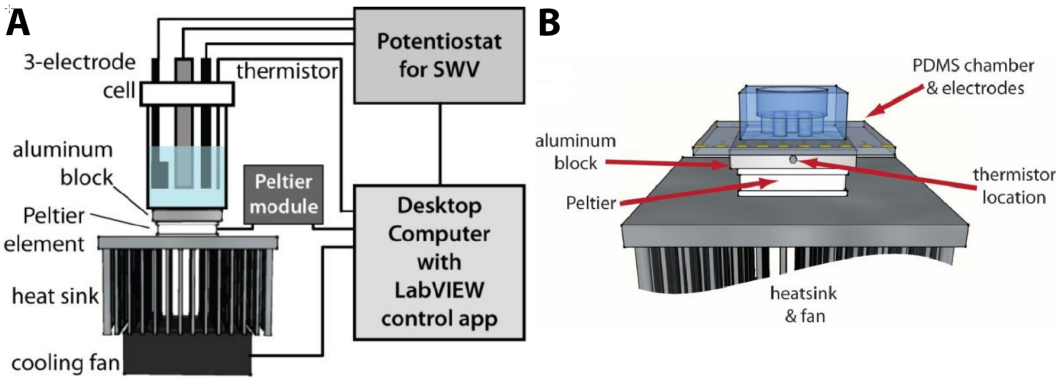

Figure 3.11: **Thermal scanning electrochemical detection system.** A) The thermal electrochemical experiments were performed on a programmable Peltier system. The system consists of an electrochemical cell, atop an aluminum block coupled to a Peltier element driven by LabVIEW software. B) Rendering of PDMS well, bonded to GoG electrode on Peltier device. Reprinted in part from reference [4] with permission from, ©2018 American Chemical Society.

detection region in the sensor, and separate experiments were conducted at each oligo combination while thermally scanning. Heat maps of all conditions are presented in Figure 3.12.

Generally, two "regions" were studied, namely the methylene blue reporter length (green) and the target binding region to the either surface immobilized DNA (blue) or the redox labeled DNA (red). The bottom row, where no target DNA was present, exemplified the need for thermal scanning studies on nucleic acid based biosensors. Even when lacking a target, significant signal was still generated at both lower temperatures and higher affinity labeled oligo strand, potentially causing false positives in assays where the binding affinities were poorly designed. Varying the other strand affinities allowed fine tuning of the hybridization energies for optimization at different temperatures. For instance, at n = 10 bp, m = 8 or 9, as the number m increases, the intensity and temperature increases for the detection region, which can be used to tailor the response of the system to a specific temperature.

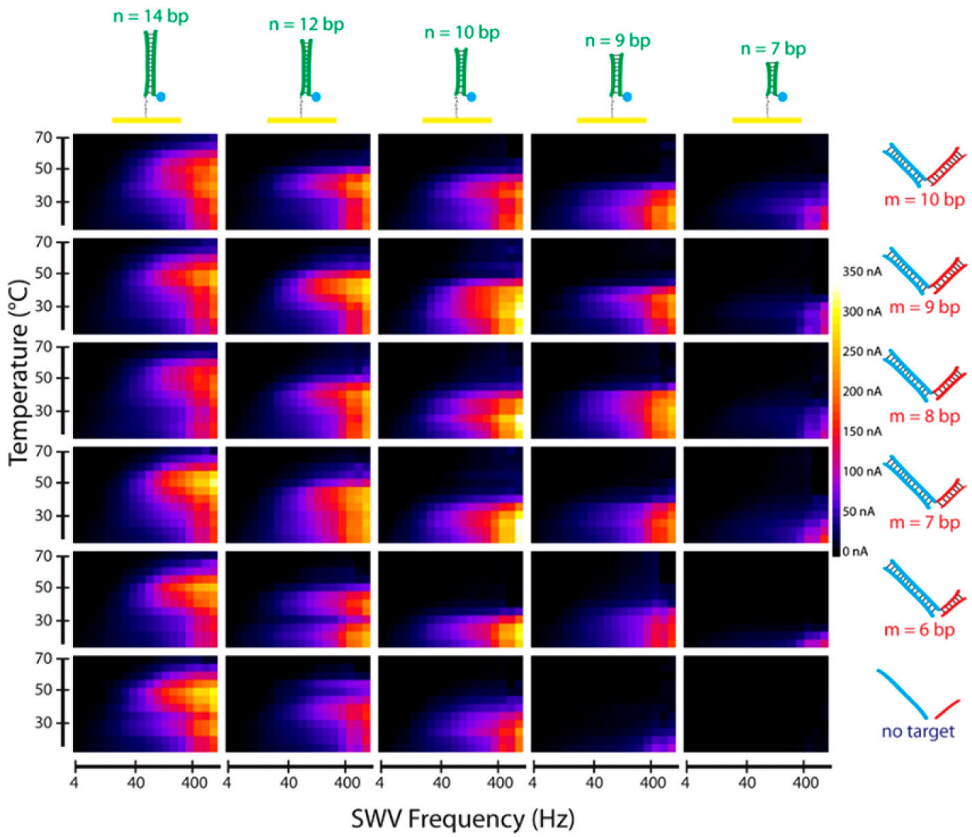

Figure 3.12: **Heat map of optimization of tsEC DNA system.** The lengths of MB binding region and target binding region, were varied and evaluated against each other. Each pixels intensity represents peak height at a temperature step (y-axis) versus frequency (x-axis) at the 25 DNA combinations. The data represents the complex nature of hybridization systems and highlights experimental optimization of these systems. Reprinted in part from reference [4] with permission from, ©2018 American Chemical Society.

Dual Peltier Driver

Although this method was used in the studies described thus far, stepwise thermal scanning of a detection cell and data collection at each point during the scan is an inherently slow approach. If instead the sample were spread over a detection area which contains a thermal gradient, we hypothesized that it would be possible to capture the full spectrum of data at once. Such a system would require at least two Peltier devices. Since data could feasibly be collected in a single "snapshot," the dual Peltier controller would be self-contained using a microcontroller and be more portable than the previous design, allowing measurements to be made away from a computer (LabVIEW). Although the proposed controller still relies

on power from the wall, battery conversion is possible considering the high energy density batteries available today.

In this work, we set out to design and validate instrumentation to provide such a thermal gradient detection system. The dual Peltier controllers' main components were: Arduino Due, LCD Screen, 5-way switch, 2X MAX1978 controllers, two 10k resistors, and two Peltiers. The Arduino Due is a stand-alone microcontroller board, which can be interfaced to a wide variety of projects. On board the Arduino Due is an Atmel SAM3X8E ARM Cortex-M3 CPU, running at 84 MHz clock speed, containing 54 digital I/O lines and 12 analog inputs, amongst many other features. It was chosen for its higher speed to aid in calculating the PID algorithm while also reading temperatures and currents, sending voltage signals out and driving an LCD.

The Arduino program flow chart is given in (Figure 3.13). The Arduino initializes and sets the output LOW to reduce the possibility of damaging Peltiers by thermal runaway. Measurements of the thermistors were taken and converted to temperature by the previously mentioned Steinhart-Hart equations. Calculated temperatures were compared with set values, and if the values are greater than 2 °C from the set point, aggressive PID tuning was used; once temperatures were below the 2 °C threshold, conservative PID tunings were used. With the tunings determined, the actual (measured) and set temperatures were passed to the PID algorithm, and the resulting output was scaled for 16 bits and passed via SPI communication to the MAX1978 onboard DAC. The DAC output was then sent to the "CTLI" connection on the MAX1978 controller, which directly drives the Peltier. Voltage was measured from the "ITEC" pin on the MAX1978

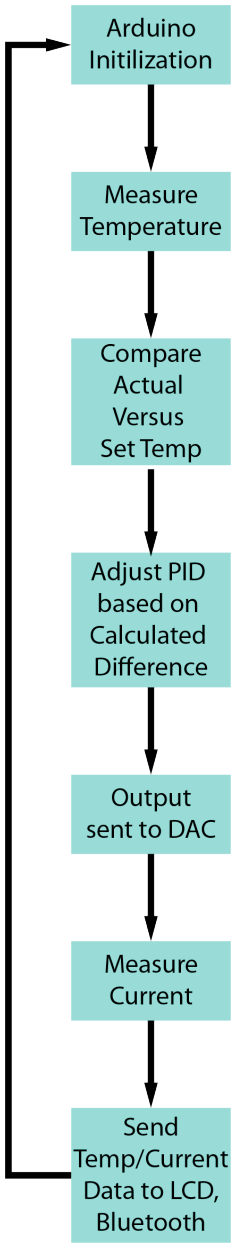

Figure 3.13: **Arduino Peltier program flow.**

and converted via the datasheets equations to Peltier current draw. Current draw, set temperatures, and actual temperatures were displayed on the LCD screen and also transmitted to a computer via Bluetooth.

The MAX1978 boards needed to be modified to function with the micro Peltiers rated at 1 V, 800 mA maximum current. Resistors R2-R3 set the maximum voltage applied to the Peltier, and R4-R7 set the max heating and cooling currents. The datasheet provided details on calculating all resistor values and corresponding voltages required. The components were all surface mount resistors, making exchanging them by hand difficult, therefore the resistors were removed and replaced by 100k potentiometers off board, connected between 1.5 V reference voltage from the MAX1978 and ground. The wipers of each potentiometer were routed to the specific pins on the MAX1978, which set the max voltage (pin 41) and currents (pin 39,40) for a new Peltier configuration. The required voltages for the micro Peltiers were as follows: 0.25 V to max voltage pin and 0.544 V for max current pins. The Peltier controller was powered on, and the potentiometers on the respective pins were adjusted to the correct voltage values.

Operation of the Peltier controller was straightforward. The 5-way joystick allowed setting the temperatures (set point 1 UP/DN, set point 2 Left/right), and depressing shut the system down in emergency mode. After powering up, the controller would initialize and wait for a key press before it operated. Alternatively, the firmware could be adjusted to perform a specific program (hold temp, step, etc.). When exchanging Peltiers, the PID settings should be tuned for best performance.

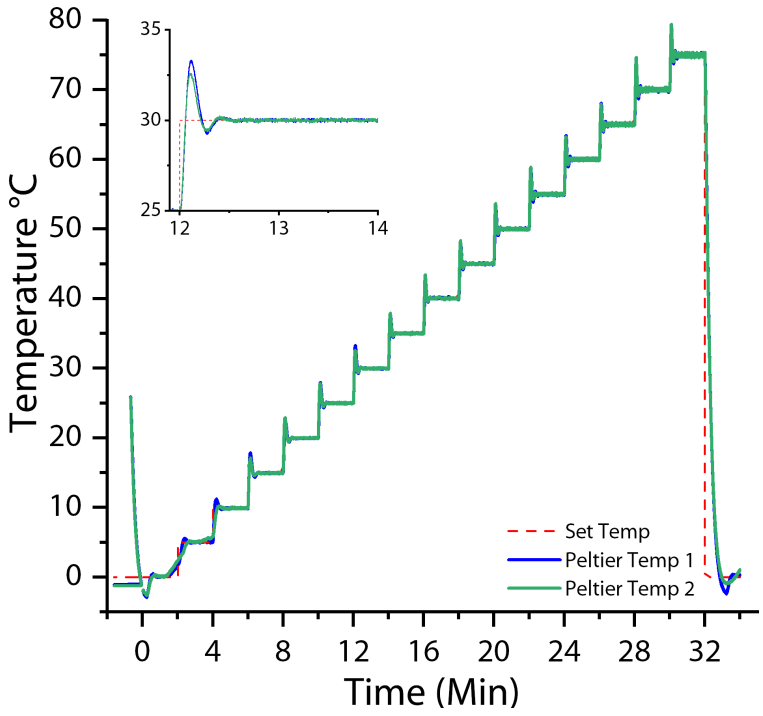

Figure 3.14: **Duplicate temperature dual Peltier step response.** Peltiers were initially driven to 0 °C, the setpoint was then incremented 5 °C per 2 min interval until final 75 °C final temperature. The temperature step at 30 °C is shown in the inset, to emphasize the low settling time and fast response.

Dual Peltier Characterization Initial characterization was carried out by a 5 °C, 2 min each, between 0 to 75 °C (Figure 3.14). The Peltiers were held on a single heat sink, which was submerged in water to provide optimal heat transfer. The duplicate Peltiers were designed to create a thermal gradient, where one surface is hot and the other cold. This also applies to the heatsink, where it forms a thermal loop, cooling the "heating Peltier" and heating the "cooling Peltier". If both Peltiers are stepped at the same time in the same thermal direction, the net effect of both Peltiers on the heatsink will eventually affect the final temperature reached. A Peltier element is a heat pump, only transferring thermal energy from one location to another, and each Peltier can maintain a specific temperature difference, with a specific amount of power introduced.

At time zero, the Peltiers were strongly cooling, where they overshot the lowest temperature due to aggressive PID settings which are present at each step causing an 2 °C

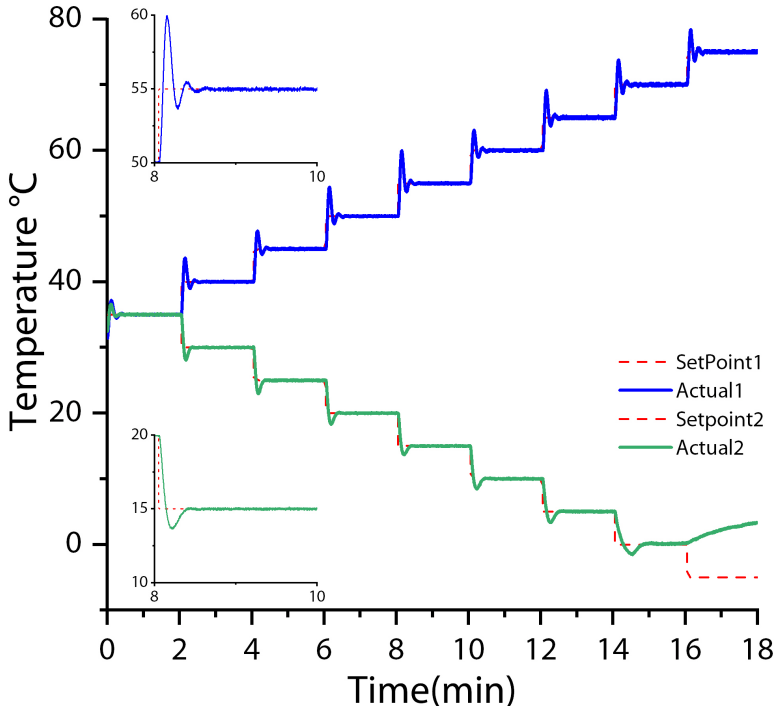

Figure 3.15: **Dual Peltier Divergent temperature step response.** Peltiers began at 35 °C and stepped 5 °C every 2 min, one heating the other cooling. The temperature step at 30 °C is shown in the inset, to emphasize the low settling time and fast response.

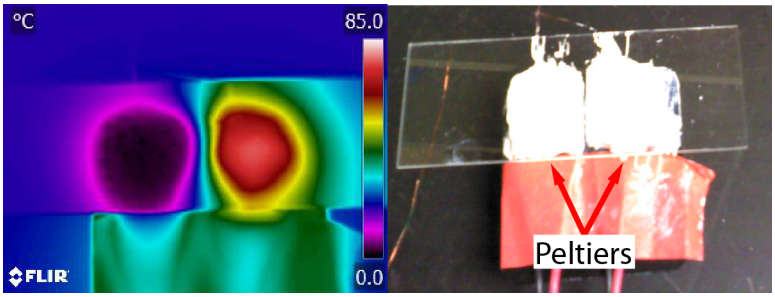

Figure 3.16: **FLIR thermal and optical images of dual Peltier.** The Peltiers are thermally connected by a heatsink on the bench, have thermal probes embedded in aluminum blocks on top of the Peltiers. A glass slide with thermal grease was placed on the Peltiers to mimic a microfluidic chip. The Peltiers were set at 0 °C (left) and 80 °C (right) clearly showing a thermal gradient at the junction of the devices over 6 mm distance.

observed overshoot (Figure 3.14). The PID settings were optimized for fast transition times rather than precision transitions. Settling time, or the time it takes to stabilize, was set to 40 s in all cases. At each step, stability and offset from the set value were calculated and then averaged, giving $\pm$ 0.07 °C stability and 0.02 °C deviation from the set point in general, suggesting a very stable system with low noise and accurate set points. The speed at which thermal switching could take place would facilitate the use of the system in thermal cycling studies. The final step shown in (Figure 3.14) was from 75 to 0 °C, which was accomplished in 51 s for a ramp rate of 1.5 °C/s.

Gradient generation capability was evaluated next by applying a program where both Peltiers diverged from each other, creating a gradient between them. The profiles stepped 5 °C, starting at 35 °C, in either direction (Figure 3.15). Peltier 2 was cooling, and it can be clearly seen that while Peltier 1 was at 75 °C, the lowest step (-5 °C) of Peltier 2 was not attainable, and in fact the temperature began to rise. This was due to two factors, the close proximity of a heating element (Peltier 1) and lower cooling efficiency compared to heating in Peltiers due to internal Joule heating [10]. When the stability and set-point accuracy were calculated as previous (excluding -5 °C), the stability was determined to be $\pm$ 0.07 °C, and setpoint accuracy was 0.02 °C. Furthermore, thermal images were taken of Peltiers in close proximity to illustrate the gradient generated. The Peltiers were held at 0 and 80 °C, where a FLIR thermal camera was used to take images of the system (Figure 3.16). The full temperature gradient was present over 6 mm, demonstrating the possibility of use in a microfluidic device. This demonstrated the system's capabilities to perform gradient generation, suggesting its potential use in new applications such as μTFA with rapid, snapshot style readout.

3.4 Conclusions

A customized, LabVIEW controlled Peltier system was constructed, capable of $\pm$ 0.115 °C precision and offset error of 1.05 °C in a 65 °C range in bench top tests. The system was

then applied to both microfluidic applications[11] and electrochemical studies[4], proving it a valuable and versatile instrument. Additionally, a customized dual Peltier controller was constructed using the Arduino programming environment. This system was shown to maintain high stability and accuracy over wide temperature ranges, and we believe that it has promise for future applications involving multi-temperature, rapid measurement assays or μTFA systems.

References

[1] H. Lodish, A. Berk, P. Matsudaira, C. A. Kaiser, M. Krieger, M. P. Scott, L. Zipursky, J. Darnell, *Molecular Cell Biology*, *Vol. 29*, **2003**, p. 973.

[2] J. Kim, J. Hu, A. B. Bezerra, M. D. Holtan, J. C. Brooks, C. J. Easley, *Analytical Chemistry* **2015**, *87*, 9576–9579.

[3] J. Hu, Y. Yu, J. C. Brooks, L. A. Godwin, S. Somasundaram, F. Torabinejad, J. Kim, C. Shannon, C. J. Easley, *Journal of the American Chemical Society* **2014**, *136*, 8467–8474.

[4] S. Somasundaram, M. D. Holtan, C. J. Easley, *Analytical Chemistry* **2018**, *90*, 3584–3591.

[5] X. Yang, J. Liu, Y. L. Xie, Y. Wang, H. Ying, Q. Wu, W. Huang, G. Jenkins, *Analyst* **2014**, *139*, 2683–2686.

[6] G. B. Crews N, Nittwer C, *Biomed Microdevices* **2008**, *10*, 187–195.

[7] H. Mao, T. Yang, P. S. Cremer, *Journal of American Chemical Soceity* **2002**, *124*, 4432–4435.

[8] C. J. Easley, J. M. Karlinsey, J. M. Bienvenue, L. A. Legendre, M. G. Roper, S. H. Feldman, M. A. Hughes, E. L. Hewlett, T. J. Merkel, J. P. Ferrance, J. P. Landers, *Proceedings of the National Academy of Sciences* **2006**, *103*, 19272–19277.

[9] C. J. Easley, J. M. Karlinsey, J. P. Landers, *Lab on a Chip* **2006**, *6*, 601–610.

[10] F. J. Disalvo, *Science* **2011**, *703*, 703–707.

[11] J. Kim, J. Hu, A. B. Bezerra, M. D. Holtan, J. C. Brooks, C. J. Easley, *Analytical Chemistry* **2015**, *87*, 9576–9579.

[12] J. Hu, J. Kim, C. J. Easley, *Analytical Methods* **2015**, *7*, 7358–7362.

Chapter 4

Non-Faradaic Current Suppression in DNA Based Electrochemical Assays by a Differential Potentiostat

4.1 Introduction

Direct electrochemical analysis of living systems requires highly selective recognition and the ability to removed background interferences in matrices such as cell lysates, whole blood, or serum. Electrochemical readout has even been accomplished in vivo, although this was previously limited to enzyme-based biosensors or direct detection of endogenous electrochemically active species[1]. More recently, systems relying on DNA monolayers on gold electrodes for sensing or positioning of binding reagents have offered new opportunities for selective electrochemistry in complex backgrounds[2–10]. For example, the electrochemical DNA based (E-DNA) or aptamer-based (E-AB) biosensors introduced by the Plaxco group[11] have emerged as alternatives to DNA sensors or immunoassays because of their sensitivity, affordability, selectivity, and minimal instrumentation requirements[12–16]. Other high-performance approaches have been devised such as nanostructured electrodes[17], membrane-protected aptamers[18], or antibody-oligonucleotide sensors (ECPA)[19–22], all similarly relying on DNA- or RNA-based monolayers at gold electrode surfaces using standard three-electrode electrochemical cells. While these methods afford the necessary high selectivity and sensitivity for analysis of living systems, there is significant room for improvement in reducing background interferences such as non-Faradaic currents and signal drifts.

Optimization of such systems have focused on instrumental parameters[23], redox reporter molecules[21, 24], DNA structures[25], self-assembled monolayer (SAM) coverage[26, 27] and chemistry[28], electrode surface area[17, 29], and melting studies[30, 31]. Although

these are comprehensive studies, few reports have focused on reducing non-Faradaic current at the electrode surface by hardware subtraction[32]. To our knowledge, there have been no reports exploiting hardware subtraction of non-Faradaic currents with the nucleic acid-based monolayer sensors discussed above. This non-Faradaic current, which originates from the formation of a double layer at the electrode and monolayer surface, is defined by a time-dependent capacitive current in the electrochemical measurement. These currents serve as interferences (or background) to the analytical Faradaic current, compromising the effectiveness of the sensors[33].

One approach to reducing non-Faradaic current is a working electrode surface area reduction, as the magnitude is directly proportional to surface area (SA)[33]. This, however, has the consequence of also reducing Faradaic current, requiring higher sensitivity instrumentation. Conversely, when the surface area is made large, corresponding to higher currents (Faradaic and non-Faradaic), the instruments amplifiers can saturate, limiting high surface area electrode use, which ultimately limits the detection sensitivity of the instrument. The non-Faradaic component of the electrochemical signal can also be removed during data analysis by differential measurement techniques. In fact, differential electrochemical measurements are common methods for noise and background reduction[33–36]. Techniques such as square-wave voltammetry or pulse voltammetry are usually applied with nucleic acid-based sensing, and recent reports have even used clever fitting of chronoamperometric data to remove background[37]. However, these subtractions or corrections are carried out digitally; for example, currents from specific points in the voltammogram are subtracted by means of computer processing[36]. This process affords a digital reduction in non-Faradaic current, yet these currents remain in the raw data and consequently can limit usable electrode SA, detection range, and sensitivity.

If non-Faradaic current is removed by hardware subtraction prior to measurement of the biosensor output, analysis can be fixated on the important Faradaic components of

the signal. Furthermore, larger SA electrodes should be accessible, allowing larger amplitude output signals with low background, thus higher sensitivities. This approach could also open new experimental possibilities such as continuous correction in complex matrices. While other groups have shown that sequential collection and subtraction of background and signal[38–41] can provide some of these benefits with in vivo neurotransmitter detection, the measurements are fundamentally made at different times, restricting the noise rejection capabilities. A few reports have applied hardware or analog subtraction of background, such as the glucose monitoring by Deman et al.[42] or high density CMOS devices[32, 43–45], yet these works are specialized or focused on integrated microelectrode devices. Realizing that hardware background subtraction could be very useful if applied to nucleic-acid monolayer based sensors (E-DNA, AB-DNA, ECPA, etc.), we set out to construct a differential potentiostat for this purpose, starting from an open source design, which could be used with standard electrochemical equipment.

In this paper, a differential potentiostat (DiffStat) is constructed to utilize two working electrodes, where one electrode provides a signal and the second provides a background, which is subtracted from the first. The background subtraction is performed synchronously, during data collection from both electrodes by a differential operational amplifier configuration. The differential potentiostat is then applied to a DNA monolayer based sensor and validated against a standard potentiostat with several techniques such as chronoamperometry, cyclic voltammetry (CV), and SWV. As envisioned, this instrument shows improvements in surface area accessibility, increased signal, decreased background, and decreased noise. Finally, we show unique applications such as converting a traditionally "signal-off" assay to a "signal-on" assay, as well as real-time background correction in human serum.

4.2 Materials and Methods

Reagents and Materials All solutions were prepared with deionized and ultrapure water (Thermo Scientific). The following reagents were used as received: 4-(2-hydroxyethyl)-1-piperazineethanesulfonic acid (HEPES), 0.5 M solution pH 7.5 (Alpha Aesar), tris (2-carboxyethyl) phosphine hydrochloride (TCEP), Mercapto Hexanol (MCH), Standard gold and chromium etchants (Sigma-Alrich, St.Louis, MO), HPLC-purified, methylene blue-conjugated DNA (MB-DNA) was obtained from Biosearch Technologies (Novato, CA). Thiolated (SH-DNA) and 40 nt control DNA (CTR-DNA) were purchased from Integrated DNA technologies (IDT; Coralville, Iowa), with purity and yield confirmed by mass spectrometry and HPLC. Sequences were optimized computationally using the nucleic acid package web server (NUPACK)[46]. All DNA sequences used in experiments are given in Table 4.1. Glass microscope slides (1" x 3") coated with chromium and gold, 5 nm and 100 nm respectively were obtained from Deposition Research Labs Inc. (St. Charles, MO). AZ-40XT positive photoresist and AZ-300 MIF developer was purchased from Integrated Micro Materials (Argyle, TX). Photomasks were designed in Adobe Illustrator and printed at 50k dpi by Fine Line Imaging (Colorado Springs, CO). Dimethoxy sulfoxide (DMSO) was obtained from Anachemia (Montreal, QC Canada). Polydimethylsiloxane (PDMS) polymer GE Sylgard 184 was purchased from Ellsworth Adhesives (Germantown, WI). Concentrated Sulfuric Acid and 30 % hydrogen peroxide (Avantor,Center Valley, PA). Normal human serum was pathogen screened and obtained from Bioreclamination LLC. (Westbury, NY)

Differential Potentiostat Fabrication Circuit development and simulation was performed in Tina-TI V9 (DesignSoft Inc. – Texas Instruments). Schematics and printed circuit boards (PCB), were created in KiCad EDA software. Electronic parts were obtained from Mouser Electronics (Mansfield, TX) and Digi-Key Electronics (Thief River Falls, MN) and PCBs were ordered from Pentalogix Inc. (Tualatin, OR). The DiffStat is a daughterboard fitted to the front end of an open source potentiostat [47]. To compare function of the DiffStat, a conventional potentiostat (Pstat) was constructed as described in reference [47]. DiffStat

DNA Designator	DNA Sequence
Thiolated DNA	5'-/5ThioMC6-D/GCA TGG TGA CAT TTT TCG TTC GTT AGG GTT CAA ATC CGC G-3
CTRL DNA	5'-CGC GGA TTT GAA CCC TAA CGA ACG AAA AAT GTC ACC ATG C-3'
MB DNA	5'-CGC GGA TTT GAA CCC TAA CGA ACG AAA AAT GTC ACC ATG C/C7-MB-3'
	DNA Sequences for Kinetic Studies
Thiolated DNA	5'-/5ThioMC6-D/AAA AGC ATG GTG ACA TTT TTC GTT CGT TAG GGT TCA AAT C-3'
MB-DNA	5'-CCA CCC TCC TCC TTT TCC TAT CTC TCC CTC GTC ACC ATG C/MB-C7/-3'
Competitor DNA	5'-TTG AAC CCT AAC GAA CGA AAA ATG TCA CCA TGC-3'

Table 4.1: DNA sequences for experiments

construction requires a partially populated Pstat board, unpopulated components are found in Table 4.2. To mount DiffStat on modified Pstat board, long header pins were soldered into Pstat board holes marked (red arrow) in Figure 4.1C, then into corresponding holes in DiffStat daughter-board. To maintain, matched impedance working electrode coaxial wires should be precisely the same length. See Appendix A for schematic.

Component Type	Component Identifier
Capacitor	C17,C28,C37,C38,C39,C40,C41
Resistor	R15,R16,R17,R18,R19,R20,R21
Integrated Circuits	U9,U10,U12

Table 4.2: Unpopulated components for DiffStat main circuit board

Electrochemical Cell Preparation

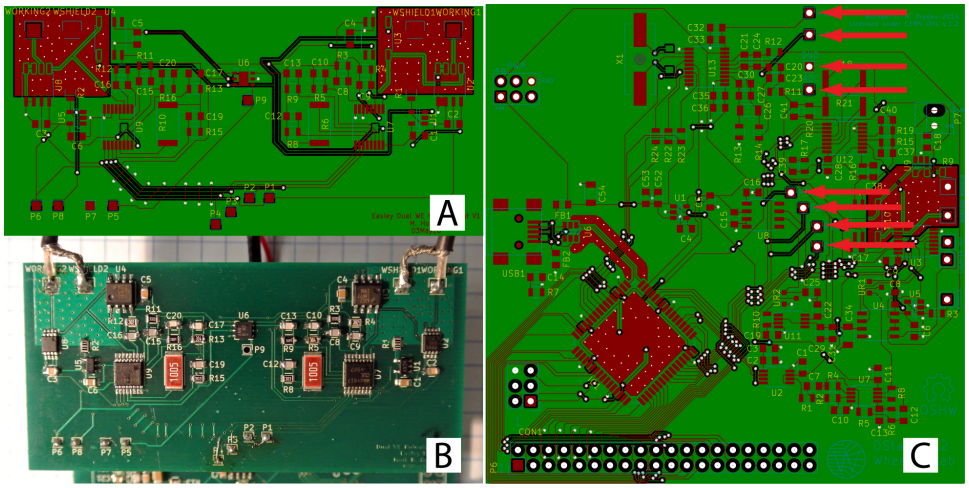

Figure 4.1: **DiffStat printed circuit board fabrication.** (A)DiffStat PCB artwork (B)Assembled, reflow soldered DiffStat board ready to use (C)Pstat board modified to accept DiffStat daughterboard, connections are made at red arrows.

Gold on Glass Electrode Fabrication DNA experiments were conducted on photolithographically patterned gold on glass electrodes (GoG). GoG electrodes and PDMS were fabricated similar to our previous work[31]. Briefly, GoG slides were heated to 200 °C >15 min, cooled to RT, 20 μm thick AZ40XT photoresist was spin coated, and baked onto the GoG. A photomask was illuminated (5 min) at 365 nm above the photoresist. The resulting pattern was baked (105 °C) and developed in MIF-300 developer (6 min), rinsed in deionized water and dried under nitrogen. To remove the excess gold and chromium, patterned GoGs were then immersed in gold etchant and chromium etchant (30 s), the cured photoresist was dissolved by DMSO (100 °C,30 min), rinsed with deionized water, dried under a stream of nitrogen then the electrodes were separated by scribing with a carbide tipped pen and fractured by hand. The electrodes were cleaned with piranha solution (3:1 conc. H_2SO_4:30% H_2O_2) immediately before use.

PDMS Chamber Fabrication 3D printed templates were modeled in Sketchup (Trimble Inc. Sunnyvale, CA) to align with GoG electrodes then models were sliced in Makerbot Desktop software (New York, NY), and printed on a Makerbot 2 3D printer at high resolution (100 μm layer) and 75% infill. PDMS was mixed 10:1 prepolymer to initiator, degassed, poured over a silanized 100 mm polished silicon wafer, the 3D printed mold was placed in

the PDMS, the mold and PDMS were degassed and cured at 60 °C for 24 hours[48]. After demolding the PDMS was sliced to shape, sonicated in pure methanol for 30 min dried and placed in 100 °C oven overnight. The molds were then plasma bonded (45 s) Harrick Plasma (Ithaca, NY) to the GoG electrodes.

DNA Immobilization Previously we explained the process of thiolated DNA immobilization on gold electrodes[31]. Briefly, 200 μM thiolated DNA in buffer(10 mM HEPES solution, 0.5 M $NaClO_4$) was combined with 10 mM TCEP (H_2O) at 1:3 ratio, incubated 1 hour at RT in darkness. The resulting reduced thiolated DNA, was diluted to 1.25 μM in buffer (10 mM HEPES, 0.5 M $NaClO_4$) and applied to working electrodes contained in PDMS chambers, incubated 1 hour at RT in darkness. Thiolated DNA solution was removed from wells, and electrodes rinsed 3X with 10 mM HEPES, 0.5 M $NaClO_4$, and 3 mM mercaptohexanol in HEPES was applied to the electrodes then incubated 1 hour at RT in darkness. The electrodes were rinsed three times in buffer (10 mM HEPES, 0.5 M $NaClO_4$) and incubated 30 min MB-DNA and CTR-DNA were diluted to working concentrations (10 or 100 nM) in buffer (10 mM HEPES, 0.5 M $NaClO_4$) and applied to the working electrode well, incubated over night at 4 °C unless otherwise noted. All DNA sequences can be found in Table 4.1.

Classical Electrochemical Experiments Immobilized (40 nt) 2 mm diameter GoG electrodes were equilibrated to RT before measurements. Two working electrodes, one containing MB-DNA and the other CTR-DNA. Depicted in Figure 4.2 is the system used to interrogate the DiffStats function. The high affinity 40 nt MB-DNA, hybridizes with thiolated DNA immobilized on the surface causing electron transfer and signal. The DiffStat, one electrode is exposed to MB-DNA and the other electrode is exposed to unlabeled 40 nt DNA, providing a capacitive match for the labeled DNA, and preventing any contamination of the second electrodes SAM. A custom split platinum counter electrode and split reference electrode were used in these experiments. Split reference electrode is made of 2 mm ID glass tubing, in the shape of "U" Figure 4.3A&B. One end of a 60 mm silver wire (15 mm) was chlorinated by

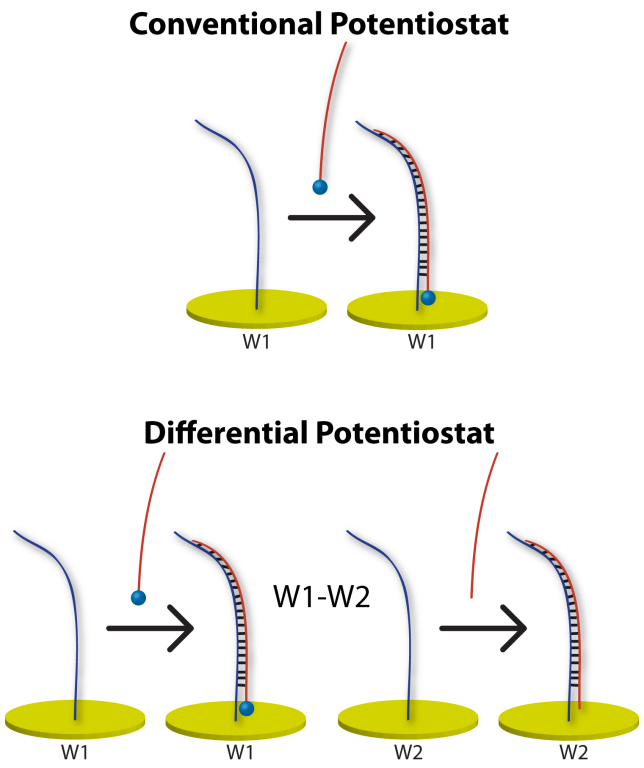

Figure 4.2: **Nucleic acid system for DiffStat characterization.** 40 nt immobilized DNA hybridizes strongly with 40 nt complementary methylene blue labeled DNA in the conventional potentiostat. Differential potentiostat has second electrode immobilized with identical 40 nt DNA, but hybridizes with unlabeled complementary 40 nt DNA to create background conditions.

immersion in 3 M KCl (Ref wire) and connected to positive terminal of battery, a second silver wire to act as a counter electrode was dipped in the same solution, 9 volts was applied until the reference wire looked grey/white in appearance 10-15 s. A 1 mm diameter rubber plug was created from a rubber stopper, the un-chlorinated end of the reference wire was threaded through it, until reaching 15 mm before the chlorinated tip. The chlorinated silver wire was threaded into the split reference electrode 20 mm but not into the U-shaped glass, the rubber plug was seated 5 mm below the end of the glass tube, epoxy (Loctite, Düsseldorf, Germany) was applied to the end, where the rubber stopper prevents epoxy from entering the split counter electrode. After curing (5 min), a long 22-gauge blunt needle was inserted into the split reference, and 3 M KCl was injected, removing bubbles. After filling, CoralPor frits (Basi Inc., West Lafayette, IN) were affixed to the ends of each leg of the reference, held in

place by heat shrink tubing. The reference should be equilibrated 24 hours, before use. The split counter electrode is a 100 mm length of silver wire and 50 mm U shaped platinum wire crimped to the end of the silver wire Figure 4.3C. Electrochemical experiments were carried out as follows. Counter and reference electrodes were placed in PDMS wells, measurements taken by Pstat and DiffStat separately with Faraday cage over wells. CA parameters: step 1 -350 mV 3 s, step 2 -150 mV 2 s. CV parameters: potential scanned between -450 and 0 mV, slope 100 mV/s. SWV parameters: sample rate 3.75 kHz, cleaning potential -450 mV 5s, start -450 mV, stop 0 mV, step size 1 mV, pulse height 25 mV, frequency 100 Hz.

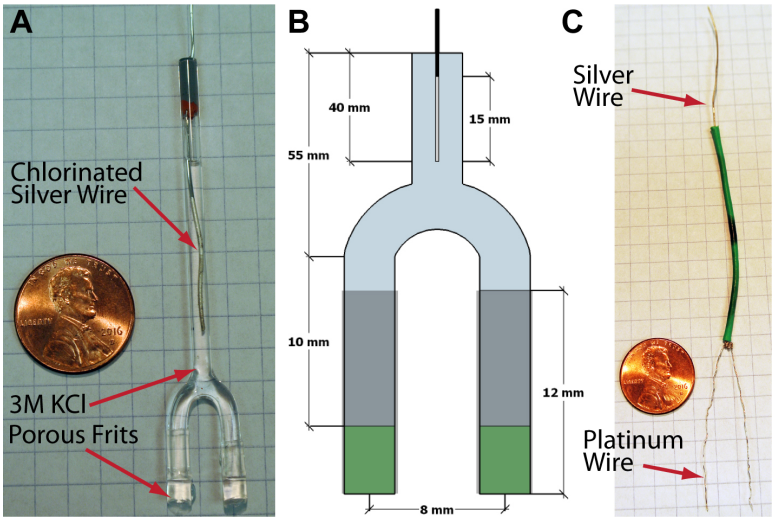

Figure 4.3: **Custom split reference and counter electrodes.** (A)Assembled Ag/AgCl split reference, filled with 3M KCl and closed by porous frits. (B)Split reference dimensions, depiction not to scale. (C)Split counter electrode, silver wire crimped onto "U" shaped platinum wire.

Effect of Surface Area GoG electrode pairs were fabricated, their diameters were 0.1, 0.25, 0.5, 1, 2, 4, 6 mm (Figure 4.4A). Individual PDMS wells were patterned from a 3D printed template, and plasma bonded onto GoG electrodes (Figure 4.4B&C). 40 nt thiolated DNA was immobilized on the surface and 10 nM CTRL-DNA or MB-DNA was applied to either a control or signal well, incubated overnight. The split reference and split counter electrode were used, and SWV was performed at the electrodes with the same parameters as classical electrochemical experiments.

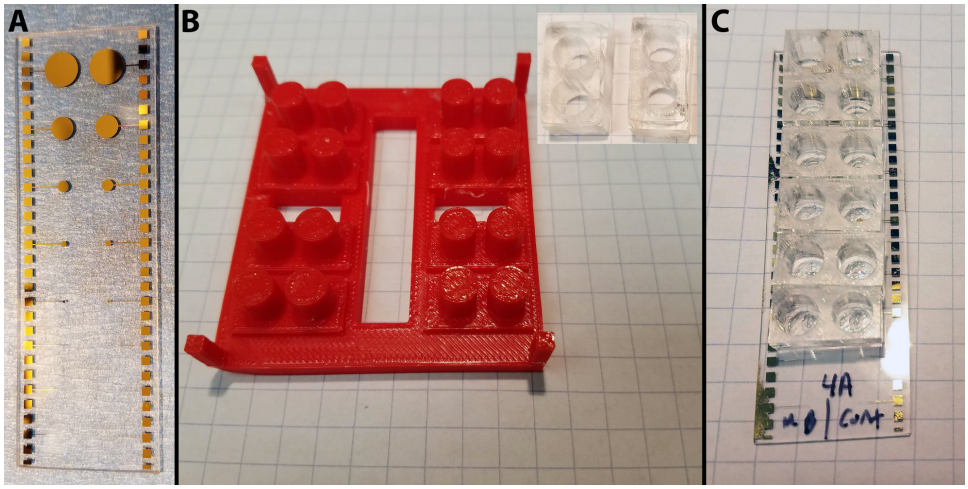

Figure 4.4: **Electrochemical cell construction.** (A)GoG electrodes with diameters 0.1 - 6 mm (B) 3D printed PDMS mold, pins extending into PDMS create wells. (C) Completed assembly, with PDMS wells bonded to GoG electrodes.

Kinetic Measurements Kinetic measurement DNA sequences can be found in Table 4.1. SAM formation was described in DNA immobilization section. Signal-on to signal-off experiments were carried out with 2 mm diameter GoG electrodes, 40 nt MB-DNA was added to working electrode 1, and then to working electrode 2 at 30-minute time point. The competitor experiment was carried out as follows: a SWV trace was recorded at time = 0 min and immediately C33L-DNA 100 nM competitor DNA was introduced into working electrode 2. A SWV scan was collected at 3 min intervals for 21 min total (6 mm electrode) and 0.33 min intervals for 16.67 min (4 mm electrode).

Human Serum Experiments 40 nt thiolated DNA was immobilized on 2 mm diameter gold electrodes. The electrodes were then exposed in intervals of 20 minutes to HEPES buffer, then HEPES buffer + 10 nM MB-DNA. The buffer solution was removed, and the electrodes were exposed in intervals of 20 min to 50% Serum in HEPES Buffer, then 50% Serum in HEPES buffer + 10 nM MB-DNA. Data was collected at 5 min intervals, by SWV, following the same parameters as in classical experiments above.

Data Analysis

Classical Electrochemical Experiments Chronoamperometry, cyclic voltammetry and square wave voltammetry, are presented as raw data.

Surface Area Experiments Peak height current data was baseline corrected by applying a 3rd order polynomial to the data, then averaging the 5 max points of the peak. Average baseline current was calculated between -100 and -110 mV. Baseline noise was camputed from the standard deviation of baseline current between -15 mV and -30 mV.

Kinetic Measurements The peak current was extracted from a third order polynomial fit baseline correction and the 5 max points were averaged and plotted.

Human Serum Measurements CV data was 100 point box car averaged, capacitance current was the average of 57 points starting at -449 mV, the Faradaic current is the difference of the forward and reverse currents at 210 mV.

4.3 Results and Discussion

The differential potentiostat was designed to remove non-Faradaic current by on-board analog subtraction of two working electrodes where one is exposed to target (Faradaic current) and the other is background (non-Faradaic current). The DiffStats versatility was evaluated with classical electrochemical experiments (CA, CV, SWV) while being compared to a conventional potentiostat. With the significant reduction of non-Faradaic current, larger surface area electrodes producing larger Faradaic current can potentially be leveraged in surface confined electrochemical nucleic acid bioassays. To investigate the influence of surface area, 7 electrode diameters ranging between 0.1 mm - 6 mm were created and interrogated with SWV yielding a higher sensitivity. The DiffStat was then applied to subtraction of Faradaic current rather than non-Faradaic current to modify biosensor output schemes. Matrix affects commonly reduce biosensors sensitivity. To demonstrate the potential benefits of the DiffStat when used with biosensors a human serum study was undertaken.

Concept of Differential Potentiostat E-DNA sensors output signals consist of a Faradaic current (signal) and a non-Faradaic current (background), which after correction can be concentration dependent. When non-Faradaic currents are high due too, for example high surface area, the instruments sensitivity is limited. Our solution to non-Faradaic current

reduction is the DiffStat, where an on-board instrumentation amplifier analog subtracts the non-Faradaic current before measurement, effectively correcting the signal and reducing noise.

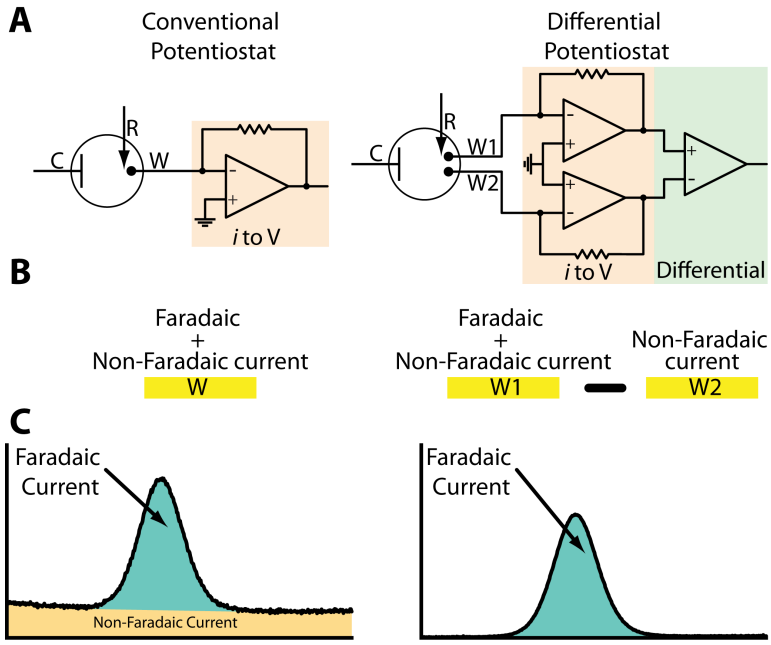

Figure 4.5: **Comparison of conventional potentiostat and differential potentiostat function.** (A) Potentiostat circuit has Counter, Reference and Working electrodes. Current from a redox active molecules is measured and converted to voltage, by a transimpedance amplifier circuit (TIA) made of an operation amplifier and resistor. The DiffStat has a second identical working electrode for background correction. Both signal and baseline currents are subtracted by a differential amplifier, yielding a corrected output. (B) Pstat working electrode measures both Faradaic and non-Faradaic signals, DiffStat subtracts non-Faradaic from working electrode 1 returning only Faradaic signal contributions. (C) Stylized SWV data, the Pstat (left) signal contains both Faradaic and non-Faradaic currents, DiffStat significantly reduces non-Faradaic current (right).

A conventional potentiostat consist of a single working electrode (W1) connected to a current to voltage converter or a transimpedance amplifier (TIA) circuit, which feeds a measurement circuit (Figure 4.5A). The Pstats output consists of both Faradaic and non-Faradaic currents which can be corrected post experiment by mathematical processing. Conversely, the DiffStat has two working electrodes (W1 & W2) and matching TIA circuits, which feed an on-board differential instrumentation amplifier. The signal from W1 & W2 are collected simultaneously, analog subtracted by the instrumentation amplifier, and quantified. If W1 &

W2 are treated identically, except W1 contains a redox moiety, the resulting DiffStat output would be the Faradaic current present at W1 (Figure 4.5B). To illustrate the subtracted output from the DiffStat, representative raw voltammetry data for both Pstat and DiffStat is presented in Figure 4.5C. The differences are striking where the Faradaic current (blue shading) remains approximately equal between the potentiostats but non-Faradaic current (tan shading) is removed in the DiffStat voltammogram.

Potentiostat Circuit Design

Component Selection Traditional potentiostats use an operational amplifier and resistor ladder to transduce electrochemical current flow into a proportional voltage termed: current to voltage converter (I-V)[33]. The DiffStat incorporates duplicate I-V converters (and resistor ladders), which send output signals to the analog to digital converter and finally to the microcontroller. The Pstat[47] used a LMP7721 precision operational amplifier for I-V conversion which was adopted by the DiffStat after evaluating possible replacements (LMP7715, MAX4238, MAX4475, OPA350) for availability, input bias current, gain, noise, and slew rate.

After I-V conversion, the voltage is quantized by a 24 bit analog to digital converter (ADC) Analog Devices ADS1255. The 24 bit analog to digital converter receives the signal from the LMP7721 TIA through a pseudo - 2nd order low pass filter. This is passed through to the internal multiplexer, which in the ADS1255 is only two channels, sampling both the I-V and reference electrode voltage. This data is buffered and, sent to a programmable gain amplifier (64X) which is followed by the 4th order delta-sigma ADC section, followed by a programmable digital filter, the signal is then sent via SPI bus to the microprocessor. The ADC can receive a differential signal, however this method would be slower, after switching and reading the multiplexer, and having a single buffer to bottleneck the data between the inputs, which would likely degrade the signals fidelity with respect to baseline measurements.

This approach does not afford a truly analog solution to differential measurements, but rather relies on hardware switching.

Although 3 operational amplifiers can be assembled to create an instrumentation amplifier (Figure 4.6), the noise of each of the components adds, significantly increasing output noise when compared to a single component instrumentation amplifier[49, 50]. The differential instrumentation amplifier chosen is a single device, designed so that its internal amplifiers and resistors are precisely matched. The chosen component was Maxium Integrated MAX4462U, amongst 8 other instrumentation amplifiers, by comparing the rail-rail operation, input referred noise, offset voltage and slew rate[51]. A MAX4462Us gain is preset at 10X, this required all resistors/capacitor ladders to be adjusted to maintain amplification factors equivalent to the Pstat, allowing direct interface with the DiffStat. This change shifts all values of resistors down by 10X in the I-V converters, which for all but the lowest resistor value was acceptable. The lowest value 10 ohms would allow 150 mAs to be sourced/sunk from the LMP7721 I-V amplifier, which is 7.5X the max rating of the component, the first position of the TIA ladders is replaced with a 300 ohm resistor to prevent any noise from entering the input. This unfortunately limits the upper current range to 500 μA instead of 15 mAs This although unfortunate will provide ample range for the measurements we are interested in. The MAX4462U was only available in a 6-TDFN-EP package, which stands for thin dual flat pack no leads-exposed pads, is a

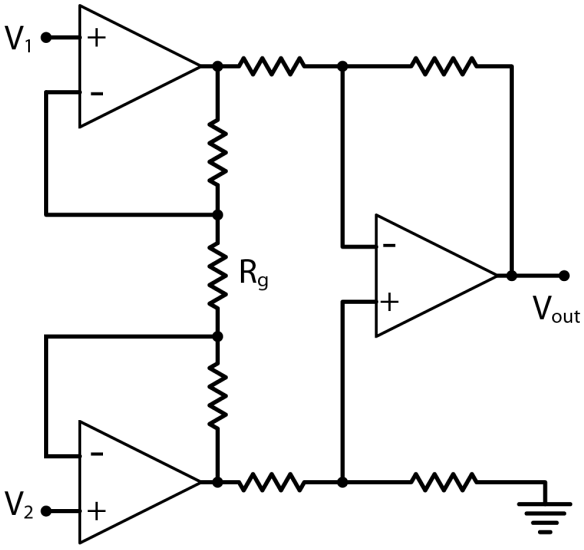

Figure 4.6: **Instrumentation amplifier circuit.** Instrumentation amplifiers consist of 3 operational amplifiers, two input buffering amplifiers are coupled to a third which acts as a differential amplifier. The gain for all devices is set by one resistor[49, 50].

3 mm square semiconductor, applicable to high density designs, for our purposes it required special care in alignment and solder paste application to connect properly.

PCB Layout As the Pstat is an open source potentiostat, the DiffStat was to be incorporated directly onto the Pstat board, however our intention was also to use the Pstat to test against the DiffStat. With the addition of the extra I-V channel, support components had to be added. Firstly, the potentiostat inputs are isolated from the cell (to prevent damage to cell or potentiostat) using an electronic SPST switch (MAX4737), which had no extra inputs for the additional I-V channel/working electrode. Additionally, using the same component to make measurements could result in crosstalk between channels, and physically locating the two channels of one device on the same board increases layout difficulty (physically locating analog and digital signal lines in close proximity, increases the likelihood of interfering noise). A MAX4641, which is equivalent to the MAX4737, with two switches was substituted for each of the I-V inputs, to isolate them electrically and physically from each other, and driven with the same digital input. The extra switches are grounded to eliminate noise they may generate. Finally, a second LMP7715 unity gain amplifier was added to act as a 1.5 volt shield/guard voltage around the second LMP7721 (Figure 4.7).

The layout of the extra components on the original board became unwieldly. More importantly the original Pstat board needed to be functional regardless of the modifications. The daughter-board architecture was chosen for two reasons. Firstly, the daughter-board would be faster to layout and interface with the original 'working' Pstat, when several components were not populated. Secondly, the dual electrode system has not been tested and therefore designing/redesigning a full board with an untested design is a potential waste of resources. PCB fab houses have minimum area requirements and purchasing several potentially faulty boards was a concern.

To function, the DiffStat daughter-board requires 8 connections to the original board, these connection points were added to the original board using header pins and placed to minimize interference with the original circuitry (Figure 4.1C). The pin placement was

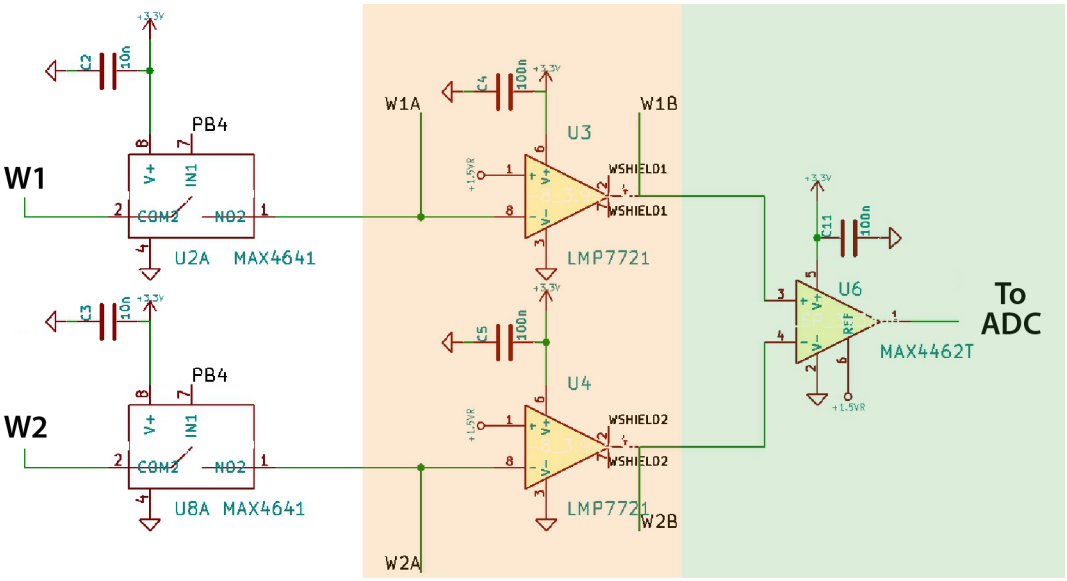

Figure 4.7: **DiffStat daughterboard schematic.** Two working electrodes signal routes through solid state relays (MAX4641), to duplicate transimpedance operational amplifiers (LMP7721), then to the instrumentation amplifier (MAX4426t).

transferred onto a board with the same width and a PCB was created for the daughter-board (Figure 4.1A) and actual PCB image (Figure 4.1B) The daughter-board isolates working electrode inputs to either corner of the board (large red outlines), which allows the instrument amplifier to be centrally located to subtract the working electrode signals. This is then sent to the ADC connection on the main Pstat board. The daughter board features stitched guard zones held at 1.5 vDC, for protection against noise. It was decided not to further shield these a soldered mountable Faraday shield, because the original Pstat required no further shielding, however it may be needed in future designs. Noise from the digital section could possibly affect the right I-V converter because of its proximity to the underlying DAC section, this is however unlikely due to the ground planes effect. The resistor ladder digital lines run under the board and to the left side, have been stitched with ground straps to mitigate noise generated by long runs. The I-V's layouts were mirrored where possible, to provide true differential input to the instrument amplifier.

Resistor Verification A potentiostats function can be quickly verified by a simple resistor between the counter & reference and working electrode (e.g. dummy cell). Ohms law predicts

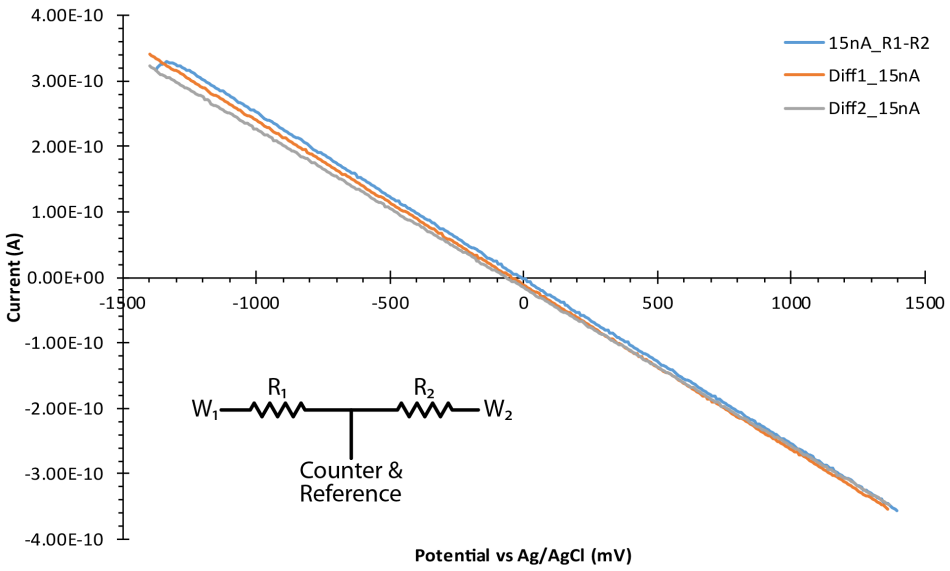

Figure 4.8: **DiffStat resistor verification.** Two 100 M Ω resistors in series, center point connected to counter and reference electrodes, and either end connected to working electrodes 1 & 2. A linear sweep between ± 1.4 V is performed, the resulting output is the difference between resistors. The conventional potentiostat measured resistor 1 and resistor 2 separately, then manually subtracted and plotted as 15nA_R1-R2. Two differential potentiostats were constructed and both verified with the same resistors. This results in traces Diff1_15nA and Diff2_15nA. The output is a representation of the errors in the resistors and in the potentiostats. Both DiffStats agree with the manually subtracted resistors.

a current will be developed when applied resistance and potential are known. In the DiffStats case, two resistors in series are required to verify the systems function owing to the dual working electrodes. One working electrode is connected to resistor 1 and the second is connected to resistor 2. The resulting differential output represents the errors between the resistors and errors in the potentiostats, not an output proportional to the value of the resistor.

Two DiffStats were constructed and tested versus a conventional potentiostat. For example, to test the 15 nA range 100 M Ω resistors were used (R1, R2) and the potential is sweep through the full potentiostat voltage range (± 1.4 V). The conventional potentiostat is used to measure first R1 then R2 and manually subtracted (15nA_R1-R2 Figure 4.8).

Both DiffStats were then verified and the raw outputs overlayed with the conventional potentiostats subtracted signal (Diff1_15nA and Diff2_15nA Figure 4.8). Nearly identical responses from all potentiostats verify the newly constructed devices are functioning similarly.

Ferri\Ferrocyanide redox couple The $[Fe(CN)_6]^{-3/-4}$ is another system used to verify the functionality of a potentiostat. Two 2 mm diameter gold electrodes were rinsed with water, and immersed in $[Fe(CN)_6]^{-3/-4}$ solution. The CV was performed between -200 mV and 700 mV at 100 mV scan rate. The data was then collected with a conventional potentiostat, which can be seen in the Figure 4.9A. The raw DiffStat output is seen in Figure 4.9B (gray trace) where the CV output is corrected to near baseline, allowing quantification of the peak, as the capacitive current was suppressed effectively. Additionally, the manually subtracted conventional potentiostats output is plotted in Figure 4.9B (red trace) reaffirming the output from the DiffStat coincides with the conventional potentiostat.

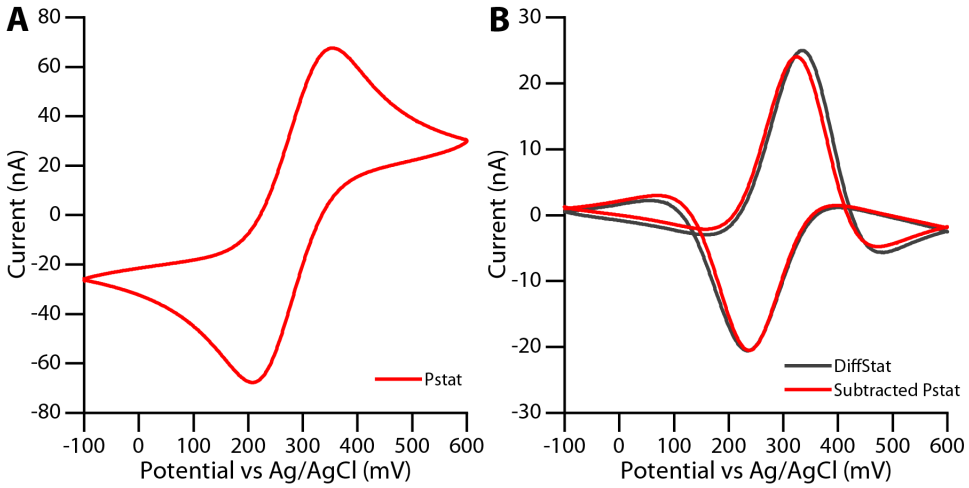

Figure 4.9: **DiffStat verification by $[Fe(CN)_6]^{-3/-4}$ redox couple.** (A) The $[Fe(CN)_6]^{-3/-4}$ redox couple, was initially measured by the Pstat. (B)The Pstat target and background signals were subtracted manually (red trace), and the DiffStats raw output was overlayed (grey trace). A significant reduction in non-Faradaic current is displayed, while both outputs are very similar.

Versatility of Differential Potentiostat After initial Diffstat verification by dummy cell and $[Fe(CN)_6]^{-3/-4}$ redox couple, the DiffStat and Pstat were evaluated against three common electrochemical experiments which demonstrate the DiffStats flexibility.

Chronoamperometry and Cyclic voltammetry. Chronoamperometry and Cyclic voltammetry are both continuous electrochemical experiments, which do not require sophisticated instrumentation or significant resources to perform. Both CA and CV are significantly affected by non-Faradaic current, which was the reason for the development of pulsed voltammetry techniques. Pulse voltammetry experiments are non-continuous, requiring complex instrumentation for both experiment and data analysis but provide a non-Faradaic correction.The signal output from pulse voltammetry uses complex mathematical operations to derive a concentration dependent signal, which is not a direct measurement technique such as the afore-mentioned methods. This drives the need for simplified instrumentation to automatically correct the CA and CV analysis, for non-Faradaic current thus creating a concentration dependent output. The DiffStat is a solution to reduce non-Faradaic current and baseline noise in the final output. Duplicate electrodes which are generally similar or equivalent, when treated equally, create similar capacitive currents. The DiffStat can use this to essentially cancel out the capacitive current from W1 and W2.

Two GoG electrodes plasma oxidized to 3D templated PDMS wells, were treated with thiolated-DNA then interrogated by CA and CV with both the Pstat (measured only W1) and the DiffStat while the electrodes were only exposed to buffer (0 nM) (Figure 4.10A&B) gray trace. The non-Faradaic current is reduced by 5-fold and 160-fold for CA and CV respectively. This demonstrates a significant reduction in non-Faradaic current by the DiffStat. Then a 10 nM complementary methylene blue redox labeled DNA (MB-DNA) was introduced to W1, and an identical complementary unlabeled DNA, CTR-DNA was introduced to W2, counteracting capacitive effects and excluding signal from W2 to match both electrodes (Figure 4.10A&B red trace). Although, the DiffStats signal mirrors the conventional potentiostats signal, a slight offset is present in 4.10B, which is attributed to mismatches in the amplifiers and can be corrected in circuitry in later versions of the DiffStat. In both CA and CV, the reduction in non-Faradaic current by the DiffStat would allow

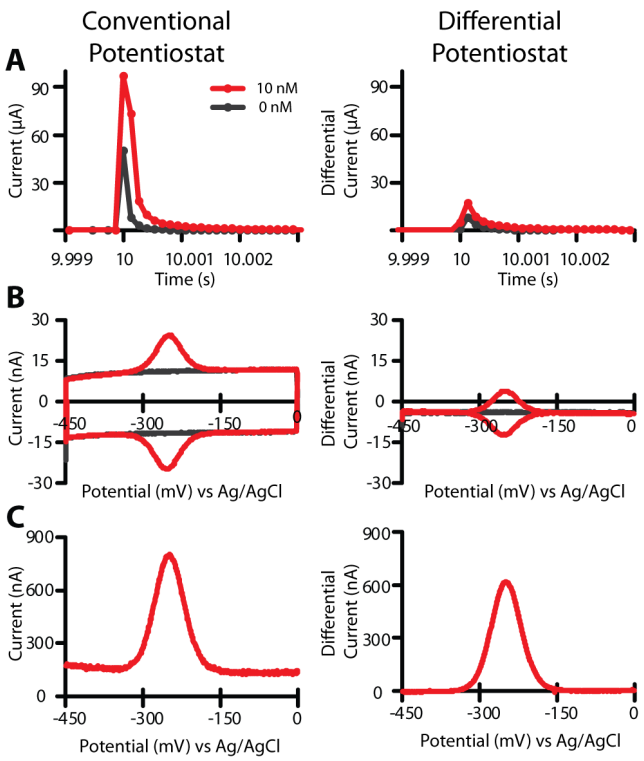

Figure 4.10: **CA, CV, SWV experiments performed by Pstat and DiffStat.** Electrochemical nucleic acid experiments CA, CV, SWV performed by Pstat and DiffStat. (A) Chronoamperometry of 0 nM and 10 nM, 40 nt MB-DNA system for both Pstat and DiffStat. (B) Cyclic voltammetry of the same DNA system. (C) Square wave voltammetry of 10 nM 40 nt MB-DNA by both Pstat and DiffStat.

both assays to use lower ranges (CA 500 μA$\rightarrow$50 μA and CV 50 nA$\rightarrow$15 nA), improving both, the signal to noise ratio and sensitivity.

Square Wave Voltammetry Square wave voltammetry is a potentiometric technique, which superimposes a minor stair step waveform, onto a square wave, where the measurement is taken at each inflection point of the square wave, creating a reduction and oxidation current, which are then software subtracted yielding a differential current[36, 52]. The delayed measurement allows the decay of the non-Faradaic current. The measurement nevertheless includes some non-Faradaic current. The DiffStats synchronous analog subtraction of the non-Faradaic current could further reduce the background and amplify primarily the Faradaic current in SWV.

We then performed SWV on the same electrochemical system as in CA/CV Figure 4.10C. Most strikingly, the baseline is essentially removed in the DiffStat trace, where the Pstat displays the characteristic non-Faradaic baseline contribution (275 nA) and the maximum peak current was reduced from 800 nA to 600 nA. Additionally, the Faradaic current is nearly the same when comparing the Pstat and DiffStat. The DiffStat, clearly reduces the non-Faradaic current, corrects for background interferences and amplifies Faradaic signal.

Effect of Surface Area on Nucleic Acid Measurements Non-Faradaic current is derived from the double layer capacitance which is formed by the metal working electrode-solution interface. Double layer capacitance is directly proportional to the metal electrodes surface area[33]. This leads to the exploration of larger surface area electrodes, producing both greater non-Faradaic current and in the case of surface confined nucleic acid bioassays larger Faradaic current. If the non-Faradaic current was removed at high surface area electrodes, by the DiffStat, this leads to a larger Faradaic signal, and higher sensitivity. Additionally, larger Faradaic signals allow more primitive detection systems which are amiable to POC devices.

To investigate the DiffStats function at various surface area electrodes an array of 7 duplicate GoG electrodes was fabricated with diameters between 0.1 mm and 6 mm, and plasma bonded to individually molded wells (Figure 4.4). Thiolated-DNA was immobilized on the electrode surfaces, then either 100 nM MB-DNA (W1-signal), or cDNA(W2-background) were added to the wells and incubated overnight. SWV voltammograms were collected for each pair of electrodes, with both Pstat (measured each electrode separately) and DiffStat (simultaneous measurement of both electrodes), one immediately after the other, to minimize drift. An example raw signal output for both Pstat and DiffStat at 4 mm electrode diameter is Figure 4.11A inset.

Electrode similarities were compared first, where peak current at each diameter was baseline corrected and plotted versus surface area (Figure 4.11A). The 6 mm diameter data was omitted, because the peak height was lower than that of 4 mm diameter electrode, in

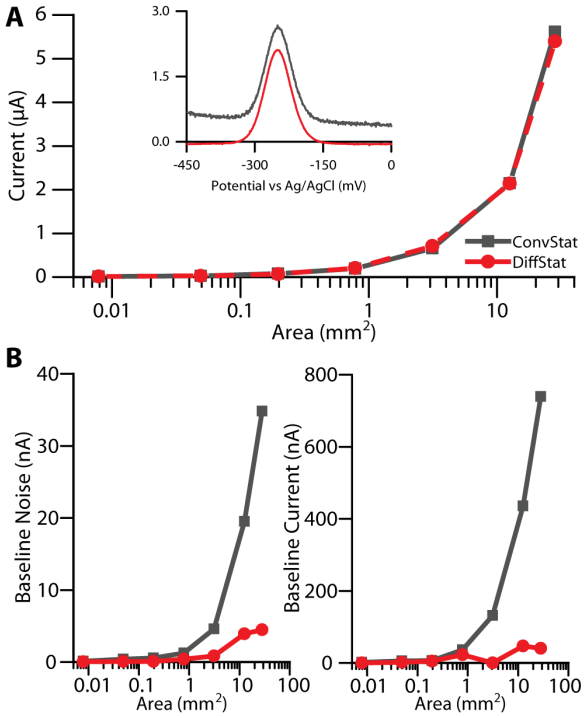

Figure 4.11: **DNA surface area study, DiffStat vs. Pstat.** Multiple surface area electrodes with nucleic acid SAMs were measured by both Pstat and DiffStat. The baseline corrected peak current of the nucleic acid assay at 0.25, 0.5, 1, 2, 4 mm diameter electrodes are plotted, both potentiostats outputs overlay, giving confidence that the response of the DiffStat is very similar to a traditional potentiostat. The inset depicts, 4 mm diameter raw data from both Pstat and DiffStat illustrating the Pstats 700 nA non-Faradaic current which is significantly reduced by the DiffStat. (A). Baseline noise was calculated by standard deviation of the baseline current between -15 and -30 mV, and plotted versus electrode area. Baseline current was calculated by averaging the current between -100 and -110 mV at each surface area (B).

both Pstat and Diffstat, which can be attributed to open source potentiostats function, which the DiffStat is based on. Overlaying both the potentiostats signal, yields nearly identical Faradaic response, When not corrected as in the Pstats signal, 700 nA non-Faradaic current and 1800 nA Faradaic current are observed (Figure 4.11A inset). The DiffStat can produce data comparable to Pstat when interrogating DNA at various surface areas by SWV.

We next looked at the baseline noise which directly impacts the SNR and therefore the sensitivity of the instrument. Noise was calculated from the standard deviation of the baseline current at -10 mV. The 6 and 0.25 mm diameter electrodes exhibit a 8 and 4 fold decrease in baseline noise respectively, when comparing Pstat versus DiffStat Figure 4.11B(left). The

increase in noise at the Pstat is a result of thermal noise created by the gain resistor in the potentiostat which grows as the sensitivity is reduced. The differential instrumentation amplifier in the DiffStat combats environmental noise (including thermal), by subtracting the common mode noise (noise present on both input terminals to the amplifier) during the analysis, which decreases the overall noise floor for the instrument.

To exemplify the DiffStats baseline current reduction capabilities we then calculated the baseline current, as the average current between -100 and -110 mV and plotted it versus surface area. An 18 and 3-fold decrease in baseline current occurs at 6 and 0.25 mm diameter electrodes respectively Figure 4.11B(right). This highlights the significant effect the DiffStat can produce on baseline current.

The surface area study allows investigation of the DiffStats operating range when compared to the Pstat. The potentiostats have 6 ranges between $\pm$ 500 μA and $\pm$ 15 nA, at each range 7 electrode diameters between 0.1 and 6 mm were interrogated with 10 nM MB-DNA as per previous. The range versus surface area data was plotted in Figure 4.12. A point was plotted if the data was valid, where the SWV forward and reverse currents were within the range. The points at the edge of each potentiostats range are highlighted. Stylized shading was used to emphasize the out of range region for both potentiostats (tan) and the DiffStats extended range region (light blue). The larger surface area and larger capacitance forces the conventional potentiostat to use lower sensitivity, where the DiffStat allows larger surface area by lowering the non-Faradaic contribution effectively increasing sensitivity. Generally, speaking the DiffStat demonstrates a full range or 10X increase in gain, which can be used to detect yet lower analyte concentrations with higher resolution.

DiffStat Applications

Kinetic Measurements The DiffStats fundamental property is to subtract one electrode from the other, while simple it allows innovative nucleic acid constructs to be developed. Thiolated-DNA was immobilized on duplicate 2 mm electrodes, MB-DNA was then added

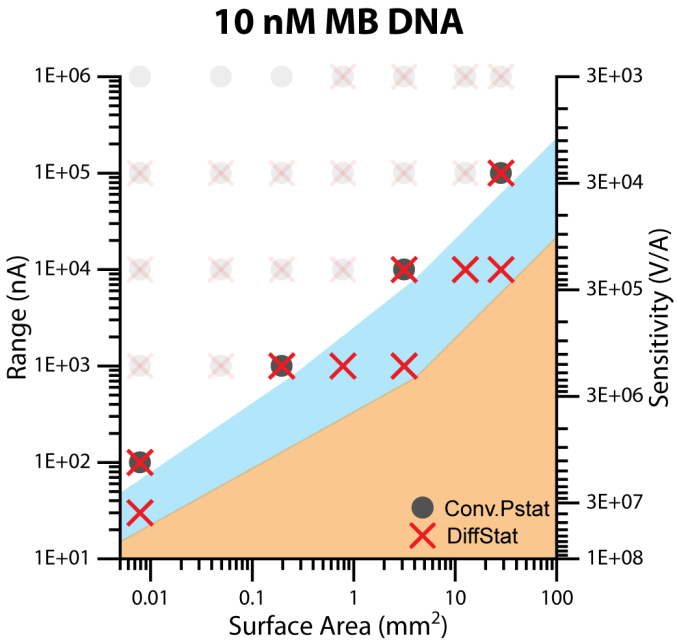

Figure 4.12: **DiffStat range is extended in comparison with Pstat.** When surface area is varied at 10 nM of MB-DNA. Square wave voltammetry experiments were performed on 7 electrodes, with diameters between 0.1 and 6 mm. Each electrode was exposed to 10 nM MB-DNA, the range of the potentiostat was varied between 15 nA and 500 μA. If a peak was considered valid at both a range and diameter, a mark was placed on the graph indicating it could be used for measurement at that concentration. A peak was considered valid when both forward and reverse currents did not exceed the current range. The graph shading is a stylized representation of the instruments operating limit. The tan shading represents a "forbidden" region, where neither Pstat or DiffStat operate. The blue region outlines the extended operating region where the DiffStat can be used, and where the Pstat is not able to operate.

to working electrode 1, which was monitored over time and plotted Figure 4.13A (blue trace). At the apex of the kinetic curve, MB-DNA was added to working electrode 2, yielding the red trace in Figure 4.13A. The initial hybridization of MB-DNA over time is characteristic of E-DNA assays, where through diffusion, the redox labeled DNA approaches the surface increasing signal then plateauing, this is termed a "signal-on" assay. Conversely, when working electrode two is exposed to MB-DNA, the signal declines in a diffusion limited manner indicative of a "signal-off" assay. These elementary experiments suggest that any assay can be setup in either a signal-on or signal-off mechanism by choosing which electrode carries the redox probe. Effecively, changing the function of the bioassay by choosing how

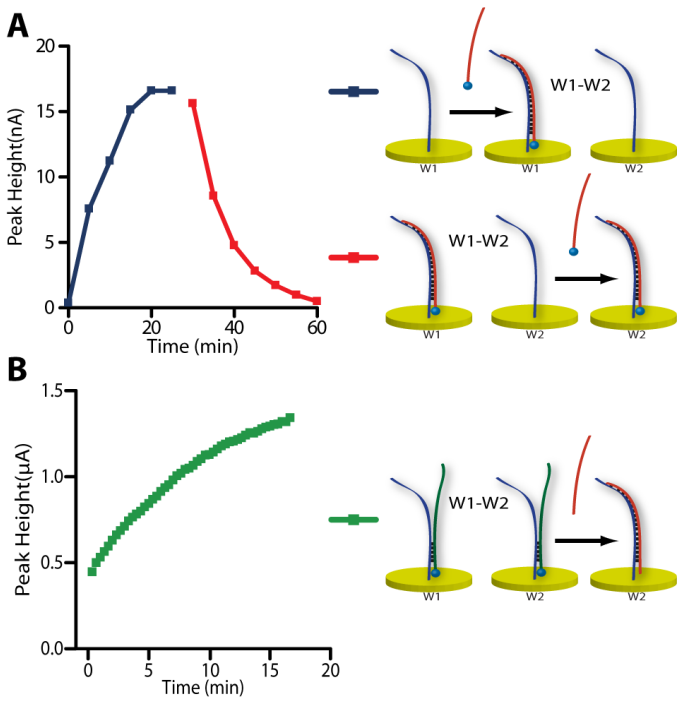

Figure 4.13: **Kinetic characterization and Signal-off to Signal-on by DiffStat.** DiffStat operates in several modes depending on chosen nucleic acid system. Signal-on nucleic acid system, immobilized DNA hybridizes to complimentary MB-DNA on W1 blue trace and signal-off immobilized DNA hybridized to complimentary MB-DNA on W2 red trace (A). MB-DNA loosely (10 nt) hybridized to immobilized DNA, a tightly hybridizing (33 nt) complimentary unlabeled strand is introduced to working electrode 2 to displace the loosely hybridized MB-DNA causing a drop in W2s signal and an increase in overall signal (B).

the Faradic current is subtracted. To demonstrate this, thiolated DNA was immobilized on two working electrodes, both electrodes were exposed to a 7 bp MB-DNA which loosely hybridizes to the thiolated DNA. A 33 bp unlabeled complementary DNA was then added to working electrode 2, which displaces the 7 bp MB-DNA from the thiolated DNA, reducing the current at working electrode two. The net current output increases as can be seen in Figure 4.13B, turning this sensor into a pseudo-signal-on assay. With this innovation, other unique E-DNA systems can be realized.

Human Serum Measurements The final experiment consisted of challenging the DiffStat to both a difficult matrix and long-term measurement stability. Human serum when added to an electrochemical cell increases the baseline capacitance. Duplicate gold on glass electrodes were immobilized with thiolated-DNA, one being designated the control and the other signal.

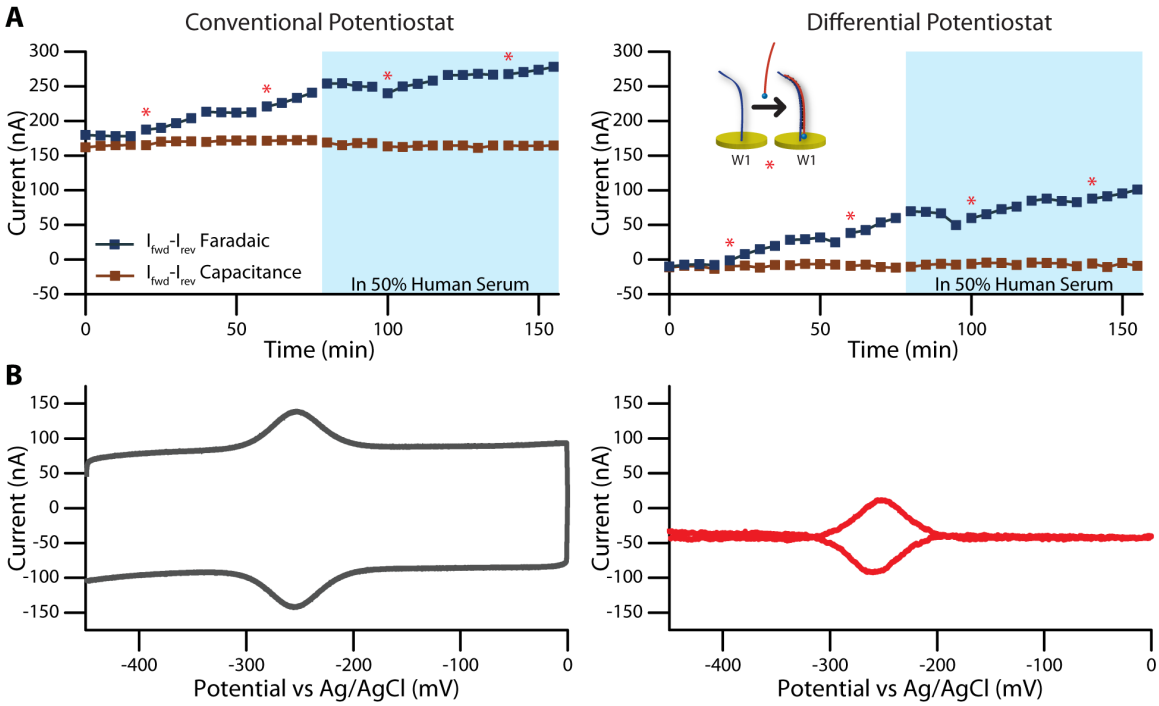

Figure 4.14: **Background correction of nucleic acid detection in serum.** (A) Experiments were performed firstly, in buffer, then MB-DNA spiked buffer, then Human serum then MB-DNA spiked human serum. Peak current at 250 mV, reverse current was subtracted from forward, yields the change in Faradaic current over the course of the experiment. Reverse current at the baseline (-450 mV) subtracted from forward current gives baseline current (160 nA). Initially only HEPES buffer was applied to working 1 electrode, after 20 minutes 10 nM MB-DNA in buffer was incubated on the electrode and then replaced with buffer after 4 time points. At each MB-DNA exposure a red asterix denotes these points. After 80 minutes, the buffer was switched to 50% human serum in buffer, and at each asterix a 10 nM MB-DNA human serum/buffer was incubated on working electrode 1. (B)Raw CV data from the experiments in Figure 4.14A, demonstrate the effective reduction of capacitance in human serum by the DiffStat at 155 min.

Each change to the system was carried out at 20 min intervals, and measurements were captured at 5 min intervals for a total of 155 min. The first condition interval was baseline data, with HEPES buffer. At each transition time point an asterisk is used to denote addition of MB-DNA spiked buffer or serum. Once the 20-minute segment elapsed, the spiked solution was removed and replaced with either buffer or 50% serum solution for 20 minutes, creating an oscillating pattern in the data. A representative raw output CV (155 min) for the collected data is shown in Figure 4.14B, and exemplifies the major reduction in the non-Faradaic current by the DiffStat. Cyclic voltammetry data was processed by

differential calculation at either the redox potential (-250 mV) or the base-line potential (450 mV) to yield either a Faradaic (blue trace) or non-Faradaic (brown trace) current. The blue shading denotes human serum measurements (Figure 4.14A). The Pstat shows a baseline of 170 nA where the DiffStat is -10 nA, showing a significant decrease in the capacitive current. We expected a response, where the signal increased over time, and at each buffer/DNA time point either in-creased signal or decreased signal. This trend although subtle is present, where signal drop occurs, and resumes after reintroduction of the target moiety. Slight variations in the data arise from timing delays due to both systems measuring on the same GoG device. We expected, the serum to cause a capacitance shift, caused the Pstats to exceed its operating range, however we did not see this shift, due to the stability of our nucleic acid system. It should be noted, that along with the conventional potentiostat, the DiffStats performance was unaffected by the serum, even though both wells contained serum. The stability of the DiffStat proves that it can be an effective device for use in other methods and in other electrochemical instrumentation.

4.4 Conclusions

A differential potentiostat was constructed to remove non-Faradaic current by analog subtraction of duplicate working electrodes signals. The Diffstat was applied to chronoamperometry, cyclic voltammetry and square wave voltammetry, yielding similar results as a conventional potentiostat. The DiffStat was used to investigate various surface area electrodes, demonstrating non-Faradaic current subtraction, noise reduction and range extension. Kinetic measurements were made to emphasize alternative sensing methods, converting a signal-off assay to a signal-on assay. Finally, the DiffStat can function in long term analysis with challenging matrices (human serum), proving its utility for biosensors.

References

[1] G. S. Wilson, M. A. Johnson, *Chemical Reviews* **2008**, *108*, 2462–2481.

[2] J. Somerson, K. W. Plaxco, *Molecules* **2018**, *23*, 912.

[3] N. Arroyo-Currás, J. Somerson, P. A. Vieira, K. L. Ploense, T. E. Kippin, K. W. Plaxco, *Proceedings of the National Academy of Sciences* **2017**, *114*, 645–650.

[4] H. Li, P. Dauphin-Ducharme, G. Ortega, K. W. Plaxco, *Journal of the American Chemical Society* **2017**, *139*, 11207–11213.

[5] H. Li, N. Arroyo-Currás, D. Kang, F. Ricci, K. W. Plaxco, *Journal of the American Chemical Society* **2016**, *138*, 15809–15812.

[6] A. J. Bonham, N. G. Paden, F. Ricci, K. W. Plaxco, *Analyst* **2013**, *138*, 5580–5583.

[7] B. S. Ferguson, D. A. Hoggarth, D. Maliniak, K. Ploense, R. J. White, N. Woodward, K. Hsieh, A. J. Bonham, M. Eisenstein, T. E. Kippin, K. W. Plaxco, H. T. Soh, *Science Translational Medicine* **2013**, *5*, 213ra165.

[8] A. Vallée-Bélisle, F. Ricci, T. Uzawa, F. Xia, K. W. Plaxco, *Journal of the American Chemical Society* **2012**, *134*, 15197–15200.

[9] S. S. Mahshid, F. Ricci, S. O. Kelley, A. Vallée-Bélisle, *ACS Sensors* **2017**, *2*, 718–723.

[10] Y. Liu, Y. Liu, Z. Matharu, A. Rahimian, A. Revzin, *Biosensors and Bioelectronics* **2015**, *64*, 43–50.

[11] C. Fan, K. W. Plaxco, A. J. Heeger, *Proceedings of the National Academy of Sciences* **2003**, *100*, 9134–9137.

[12] Y. Xiao, B. D. Piorek, K. W. Plaxco, A. J. Heeger, *Journal of the American Chemical Society* **2005**, *127*, 17990–17991.

[13] S. S. Mahshid, S. Camiré, F. Ricci, A. Vallée-Bélisle, *Journal of the American Chemical Society* **2015**, *137*, 15596–15599.

[14] Y. Liu, N. Tuleouva, E. Ramanculov, A. Revzin, *Analytical Chemistry* **2010**, *82*, 8131–8136.

[15] F. Ricci, K. W. Plaxco, *Microchimica Acta* **2008**, *163*, 149–155.

[16] A. A. Lubin, K. W. Plaxco, *Accounts of Chemical Research* **2010**, *43*, 496–505.

[17] L. Soleymani, Z. Fang, E. H. Sargent, S. O. Kelley, *Nature Nanotechnology* **2009**, *4*, 844–848.

[18] M. Santos-Cancel, R. J. White, *Analytical Chemistry* **2017**, *89*, 5598–5604.

[19] J. Hu, T. Wang, J. Kim, C. Shannon, C. J. Easley, *Journal of the American Chemical Society* **2012**, *134*, 7066–7072.

[20] J. Hu, Y. Yu, J. C. Brooks, L. A. Godwin, S. Somasundaram, F. Torabinejad, J. Kim, C. Shannon, C. J. Easley, *Journal of the American Chemical Society* **2014**, *136*, 8467–8474.

[21] K. Ren, J. Wu, F. Yan, H. Ju, *Scientific Reports* **2014**, *4*, 1–6.

[22] J. Zhu, H. Gan, J. Wu, H. Ju, *Analytical Chemistry* **2018**, *90*, 5503–5508.

[23] P. Dauphin-Ducharme, K. W. Plaxco, *Analytical Chemistry* **2016**, *88*, 11654–11662.

[24] D. Kang, F. Ricci, R. J. White, K. W. Plaxco, *Analytical Chemistry* **2016**, *88*, 10452–10458.

[25] K. C. Huang, R. J. White, *Journal of the American Chemical Society* **2013**, *135*, 12808–12817.

[26] R. J. White, N. Phares, A. A. Lubin, Y. Xiao, K. W. Plaxco, *Langmuir* **2008**, *24*, 10513–10518.

[27] F. Ricci, R. Y. Lai, A. J. Heeger, K. W. Plaxco, J. J. Sumner, *Langmuir* **2007**, *23*, 6827–6834.

[28] H. Li, P. Dauphin-Ducharme, N. Arroyo-Currás, C. H. Tran, P. A. Vieira, S. Li, C. Shin, J. Somerson, T. E. Kippin, K. W. Plaxco, *Angewandte Chemie - International Edition* **2017**, *56*, 7492–7495.

[29] A. Hauke, L. S. Kumar, M. Y. Kim, J. Pegan, M. Khine, H. Li, K. W. Plaxco, J. Heikenfeld, *Biosensors and Bioelectronics* **2017**, *94*, 438–442.

[30] A. H. Yang, K. Hsieh, A. S. Patterson, B. S. Ferguson, M. Eisenstein, K. W. Plaxco, H. T. Soh, *Angewandte Chemie - International Edition* **2014**, *53*, 3163–3167.

[31] S. Somasundaram, M. D. Holtan, C. J. Easley, *Analytical Chemistry* **2018**, *90*, 3584–3591.

[32] A. Hassibi, T. H. Lee, *IEEE Sensors Journal* **2006**, *6*, 1380–1388.

[33] A. J. Bard, L. R. Faulkner, *Electrochemical Methods : Fundamentals and Applications*, 2nd, John Wiley & Sons, Inc, New York, **2001**, p. 833.

[34] M. J. McGrath, E. I. Iwuoha, D. Diamond, M. R. Smyth, *Biosensors and Bioelectronics* **1995**, *10*, 937–943.

[35] P. Jacobs, J. Suls, W. Sansen, *Sensors and Actuators: B. Chemical* **1994**, *20*, 193–198.

[36] J. G. Osteryoung, R. A. Osteryoung, *Analytical Chemistry* **1985**, *57*, 101–110.

[37] N. Arroyo-Currás, P. Dauphin-Ducharme, G. Ortega, K. L. Ploense, T. E. Kippin, K. W. Plaxco, *ACS Sensors* **2018**, *3*, 360–366.

[38] J. Wang, H. D. Dewald, *Talanta* **1984**, *31*, 387–390.

[39] J. O. Howell, W. G. Kuhr, R. E. Ensman, R. Mark Wightman, *Journal of Electroanalytical Chemistry* **1986**, *209*, 77–90.

[40] C. I. Dorta-Quinones, X. Y. Wang, R. K. Dokania, A. Gailey, M. Lindau, A. B. Apsel, *IEEE Transactions on Biomedical Circuits and Systems* **2016**, *10*, 289–299.

[41] A. Hermans, R. B. Keithley, J. M. Kita, L. A. Sombers, R. M. Wightman, *Anal. Chem.* **2008**, *80*, 4040–4048.

[42] P. Deman, J. Suls, W. Sansen, *Sensors and Actuators B: Chemical* **1997**, *44*, 304–308.

[43] S. M. Martin, F. H. Gebara, T. D. Strong, R. B. Brown, *IEEE Sensors Journal* **2009**, *9*, 135–142.

[44] M. H. Nazari, R. Genov, *Proceedings - IEEE International Symposium on Circuits and Systems* **2009**, *9*, 2177–2180.

[45] W. S. Wang, W. T. Kuo, H. Y. Huang, C. H. Luo, *Sensors* **2010**, *10*, 1782–1797.

[46] J. N. Zadeh, C. D. Steenberg, J. S. Bois, B. R. Wolfe, M. B. Pierce, A. R. Khan, R. M. Dirks, N. A. Pierce, *Journal of Computational Chemistry* **2011**, *32*, 170–173.

[47] M. D. Dryden, A. R. Wheeler, *PLoS ONE* **2015**, 1–17.

[48] J. C. Brooks, K. I. Ford, D. H. Holder, M. D. Holtan, C. J. Easley, *Analyst* **2016**, *141*, 5714–5721.

[49] R. Pethig, S. Smith, *Introductory Bioelectronics*, John Wiley & Sons, Ltd, West Sussex, UK, **2013**, p. 441.

[50] D. A. Skoog, F. J. Holler, S. R. Crouch, *Principles of Instrumental Analysis*, 2nd, Thomson Brooks/Cole, Belmont, CA, **2007**, p. 529.

[51] W. Jung, *Op Amp Applications Handbook*, Newnes, Burlington,MA, **2005**, p. 878.

[52] L. Ramaley, M. S. Krause, *Analytical Chemistry* **1969**, *41*, 1362–1365.

Chapter 5

Modified Instrumentation for Photolithography and Channel Interconnections in Microfluidic Device Fabrication

5.1 Introduction

Fabrication of microfluidic devices is complex and requires multiple tools to complete successfully. Traditional, monolithic, multilayer devices are fabricated using established soft lithography techniques which were discussed in Chapter 1[1]. Instrumentation was designed and constructed to meet device fabrication needs in our lab. The instrumentation begins with a laser drill to create vias in PDMS devices. A UV exposure system was then constructed to speed device fabrication processes. For active microfluidic control, valving is required and an electronic buffer system capable of driving fluid controlling solenoids was then built. The pressure at which that valving was performing needed to be measured, which was accomplished by construction of electronic pressure gauges. For tunable normally closed valves, a photopolymer is cured in a channel, at a specific location, performed by a focused UV laser which was constructed for the purpose. Next, the PDMS used in device fabrication is cured at specific temperatures, which require stability and consistency over time, to achieve this a oven controller was constructed to retrofit existing ovens. To aid in visualization of created PDMS chips, a high intensity illuminator was created to fit a fluorescence microscope. Then to properly assemble circuits, a reflow soldering oven was assembled.

5.2 CO_2 Laser Drill

Introduction

As was discussed in the introduction, vias (interlayer connections) play a large part in creating higher density microfluidic chips using monolithic fabrication techniques. In this section a CO_2 laser is used to create the vias allowing fabrication of microfluidic diodes and test structures for microfluidic transistors.

Materials and Methods

Reagents and Materials The following reagents were used as received: Sylgard 184 PDMS prepolymer and catalyst (Dow Corning, Midland, MI), MeOH (VWR, Radnor, PA)

CO_2 Laser Construction

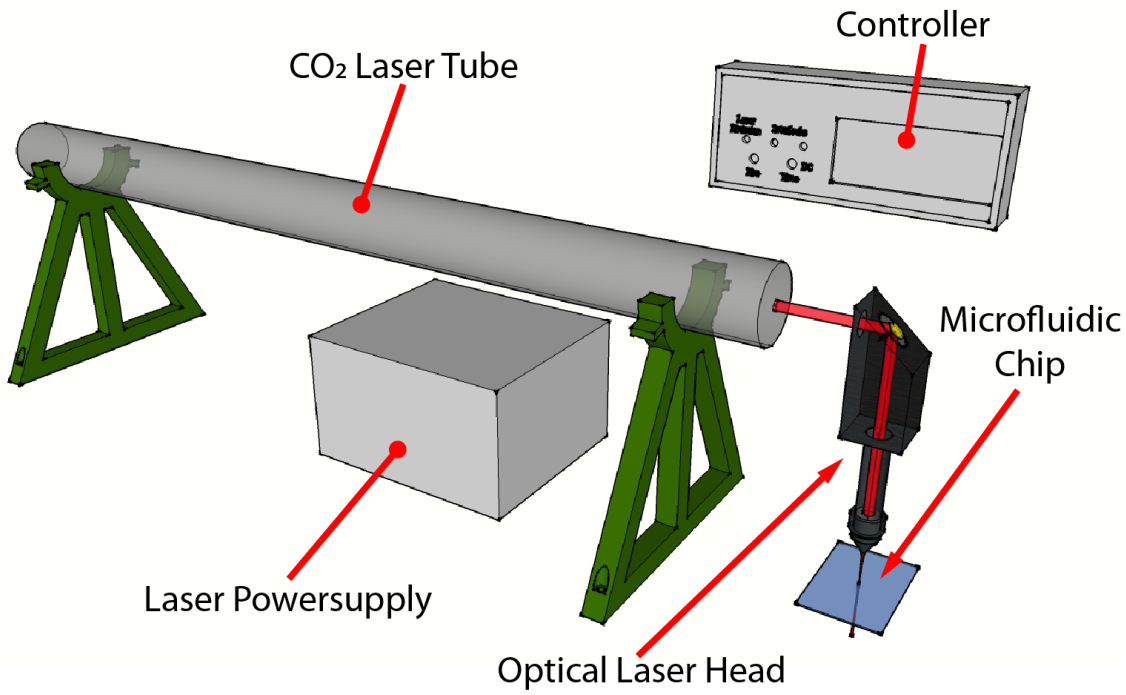

Figure 5.1: **CO_2 Laser 3D rendering of the system.** The CO_2 laser tube, powersupply controller and optical laser head are shown. The optical path is highlighted in red.

Optical and Electronic Components A 40-Watt sealed CO_2 laser tube, power supply, and laser focusing head with 38 mm focal length lens were obtained from Cole Technologies Co. (Hefei city, CN). Electronic/Mechanical parts were sourced as follows: Arduino Nano microcontroller board (Arduino LLC, Turin IT), SPDT key-switch (Lorlin SRL5CD2), Solid State Relay (SSR-25DA HOYMK), were all obtained from MPJA Inc. in West Palm Beach, FL. The following were sourced from Digikey Thief River Falls, MN : "fire" pushbutton (EG2015-ND E-Switch) and 10K thermistor (USP16673 US Sensor Orange, CA). Remaining parts were from various sources: 20x4 LCD display (PN1219 – Pololu Inc. Las Vegas, NV), 12v pneumatic solenoid (ESW-AIRTAC1V025-08 LightObject Sacremento, CA), 5-way switch (ALPS SKQUCAA010- Newark Electronics, Chicago,IL), safety interlock button, 12V switch mode powersupply(WA24C12V APD Taipei, TW) and submersible water pump (4RK99 Little Giant – Grainger Lake City, IL).

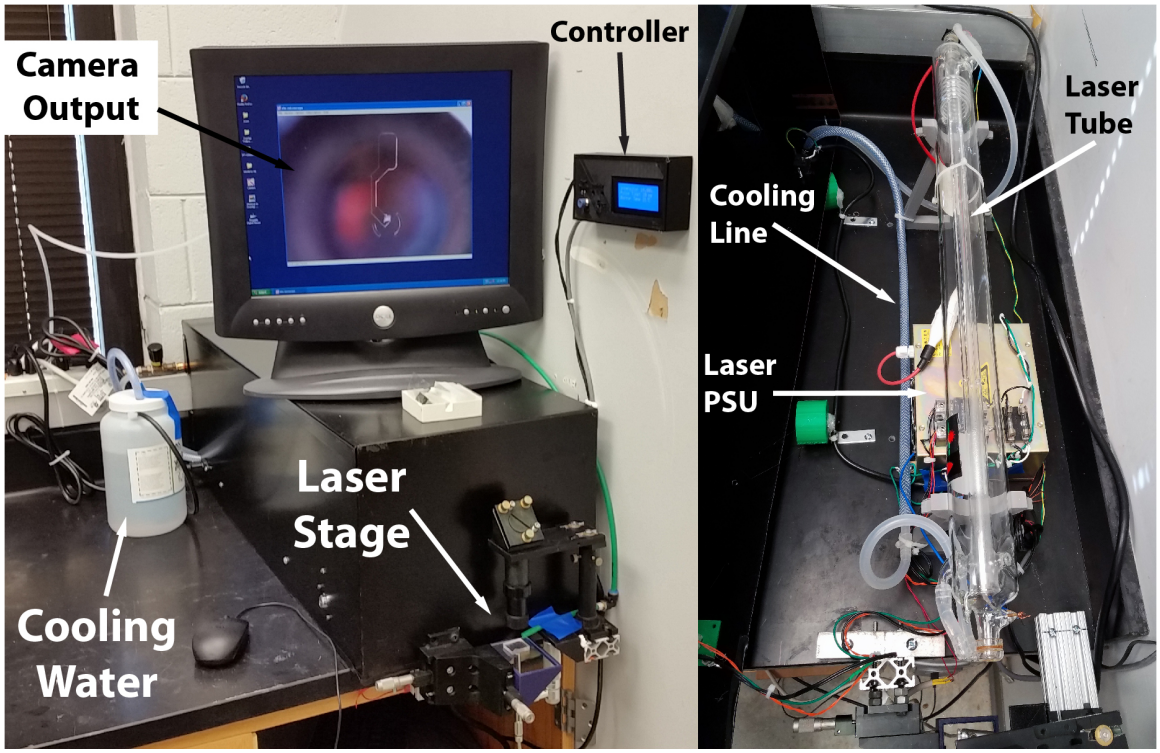

Figure 5.2: **The assembled CO_2 laser system.** The complete system is shown here, including:computer, water cooling, optical head, controller and camera output.

CO_2 Laser Assembly Laser tube was supported by 3D printed cradles designed in Sketchup (Trimble Inc. Sunnyvale, CA) sliced, printed by a MakerBot 2X (MakerBot LLC, New York NY) in PLA material (Hatchbox – Amazon Seattle, WA) at 0.2 mm layer resolution and 75% infill rendering of components can be seen in Figure 5.1. Cradles, and laser power supply were bolted to laboratory bench. Two sections of T-slot aluminum extrusion (2RCR1, Grainger Lake City, IL) were cut and bolted to the lab bench. One T-slot section was used to mount the laser focusing head aligned to the output of the laser, the second was used to mount a one-inch travel XY optical mount (460A – Newport Corp. Irvine, CA) fitted with precision micrometers to move the microfluidic chip. XY mounts were fitted with a 3D printed stage which accepted a 75x50 mm glass slide (Figure 5.1). A USB Digital Endoscope/Microscope was (EhEV2-USB-S Oasis Scientific Inc. Taylors, SC) installed on T-slot extrusion with 3D printed mount, facing upwards viewing the focusing lens from beneath the glass slide. Silicon tubing was routed from and too the laser head, and to the submersible pump, in a large plastic container with 2 liters of distilled water. Air assist is provided by routing house air through $\frac{1}{4}$" OD nylon tubing (2VDU9, Grainger, Lake City, IL), to the pneumatic solenoid, then to the XY stage. The completed assembly is depicted in Figure 5.2.

An Arduino Nano microcontroller drives the high voltage power supply by a 20 kHz PWM signal, controls the 4x20 LCD display by 8 digital I/O pins, and actuates the pneumatic solenoid. The microcontrollers 10 bit analog to digital converter is used to measure the 10k thermistor voltage divider and convert to temperature. A digital pin is used to monitor the safety interlock before a fire sequences can proceed (Figure 5.3). A box was 3D printed to house the electronic controller, and buttons.

Laser Ablation Studies Sylgard 184 PDMS was mixed at a 1:10 ratio, spin coated at 1350 rpm onto 75 x 50 mm glass slides (VWR Int. Radnor, PA) and cured overnight at 60 °C. Coated glass slides were placed in the focused beam while the laser was pulsed, after each pulse the stage was moved, performed in triplicate. Duration (1-10 ms) and intensity

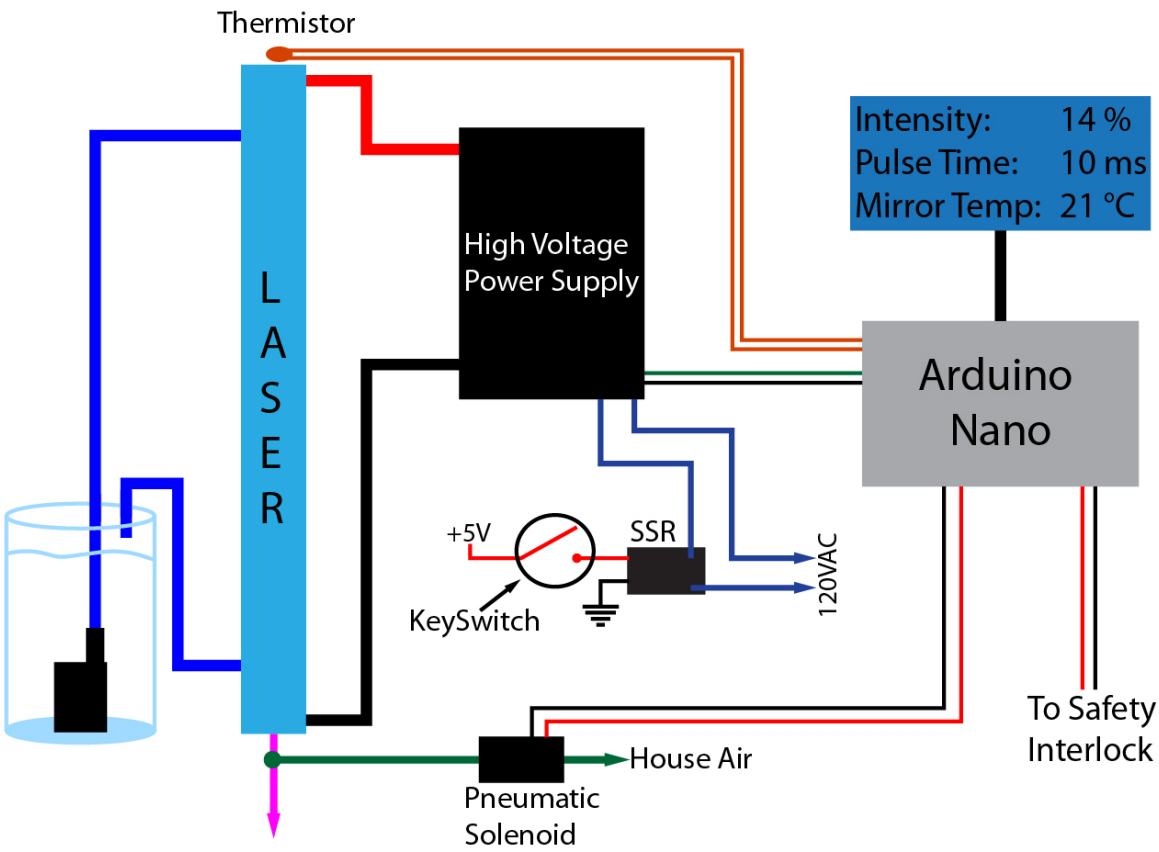

Figure 5.3: **CO_2 laser system connections.** The CO_2 tube is connected to a water cooling pump, high voltage powersupply and thermistor for temperature monitoring of the water cooled optics. The controller consists of an LCD display and Arduino Nano microcontroller. The microcontroller sets the pulse width and duration for the high voltage powers supply and controls the pneumatic solenoid.

(20-100%) were varied, the resulting laser spots were rinsed with MeOH, air dried and Scotch tape cleaned (3M, Maplewood, MN). PDMS slabs 4 mm thick, were formed in 100 mm petri dishes (VWR Int., Radnor, PA) cured overnight at 60 °C. Slabs were plasma oxidized to ablated PDMS on glass slides, resulting bonded PDMS was pealed from slides, sliced and imaged (Nikon Ti-E).

Results and Discussion

Component Selection Other systems have been proposed to drill PDMS vias precisely[2], however the extreme final cost >$30,000 was prohibitive for research laboratories. The CO_2 laser system built here, was designed with functionality and cost in mind. The total cost of

this system is <$1,000, the laser tube and power supply are the most expensive components. The laser is cooled by closed loop system, a reservoir holds water circulating it through the tube to cool it. During drilling, the laser is only on for short periods of time causing little heat to be built up in the tube.

System Operation The laser startup is as follows: system is powered on, which applies power to the key switch and Arduino controller. System initialization begins with temperature measurement of the laser optic, and pneumatic solenoid test. The microfluidic device is aligned on the stage via the microscope. When the key switch is activated, mains power is applied to the laser power supply. The system is in a ready state, assuming optic temperatures are less than 60 °C. To set the laser intensity, the "up-down" buttons are depressed, and to set the laser time the "left-right" buttons are pressed. Once the desired power is chosen and the laser is aligned to your work piece, the "fire" button can be pressed to start the laser cycle. The Arduino checks the state of the handheld safety interlock button to ensuring awareness of the system. The pneumatic solenoid shield gas is activated, and the laser is pulsed. See Appendix C for laser alignment instructions.

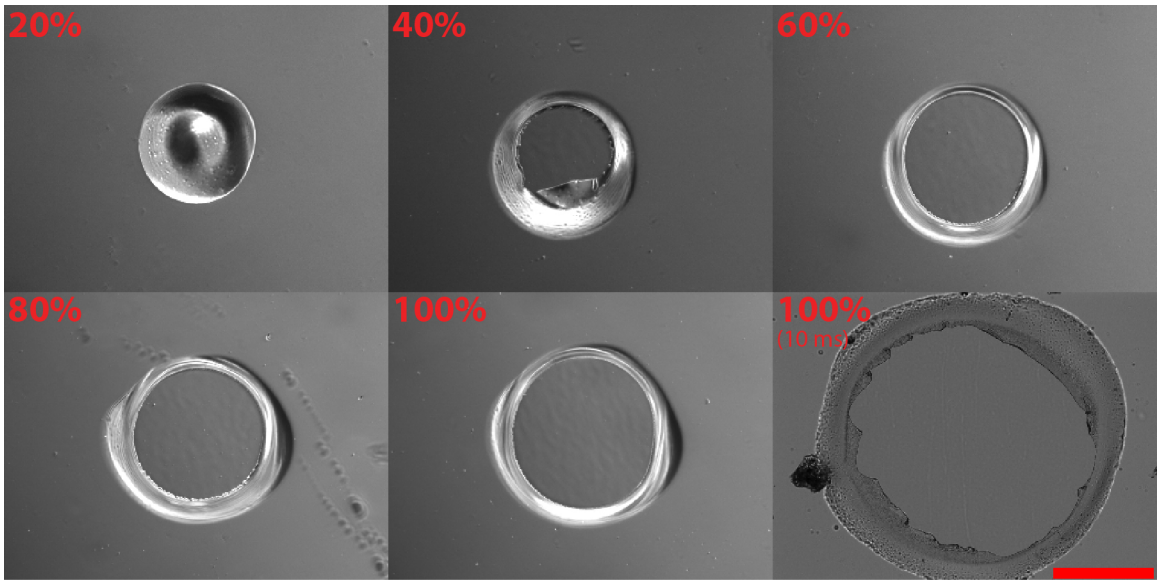

Figure 5.4: **CO_2 laser intensity study.** The laser was focused on PDMS and holes were drilled at various intensities (10-100 %) All images at 1ms duration. Scale bar is 150 μm.

Laser System Characterization The goal of this work was to create a system with positional accuracy and a high intensity beam to drill through PDMS membranes <100's μm thick. Initial studies were carried out by systematically ablating a 40 μm PDMS membrane on a glass surface. Data is plotted from studies of 20-100 % intensity, and 1-10 ms duration pulse parameters. Intensity was compared while pulse time was held constant (Figure 5.4). The lowest power at 20 %, did not fully penetrate the 40-μm thick PDMS layer, hence the "donut" shaped image. As expected, the intensity increases, and the diameter of the hole increases due to thermal spreading e.g. as more energy is dumped into the spot more material is ablated from the surface. The lower right spot as a comparison is at 10 ms duration, showing a significantly larger spot size and the geometry is significantly different in comparison to the concentric circles of the 100 % at 1 ms. If the intensity is calculated via the power, time, and spot size, for example 100 % power at 1 ms is 40 mJ of energy assuming the CO_2 laser output is correct from the manufacturer. Then a 10 ms pulse time would generate an intensity of 400 mJ, 10-fold increase in power delivered. The resulting drilled holes are expected, showing far more charred PDMS and ragged holes due to reflection. Energy density accounts for focused spot size, where in this case a 100 μm spot would yield factor of 10 greater energy (509 $\frac{J}{cm^2}$ vs 5090 $\frac{J}{cm^2}$) (Equation 5.1)

$$E_{\text{density}} = 40W \cdot 100\% \cdot 1ms \cdot 7.85 \times 10^{-5} cm^2 \tag{5.1}$$

Each PDMS spot was then plasma bonded to bulk PDMS and sliced to evaluate the profile of the laser spots (Figure 5.5). The laser beam penetrated from the top of the image causing a focal cone of ablation. The trend follows as the intensity and time increase the spot size increases. As previously mentioned, at 20 % intensity the laser beam didn't penetrate the PDMS, but caused a donut shaped feature to be produced, which may be useful for further study. Inset of lower left 80 % power further emphasizes the conical nature of the laser beam penetrating the PDMS film.

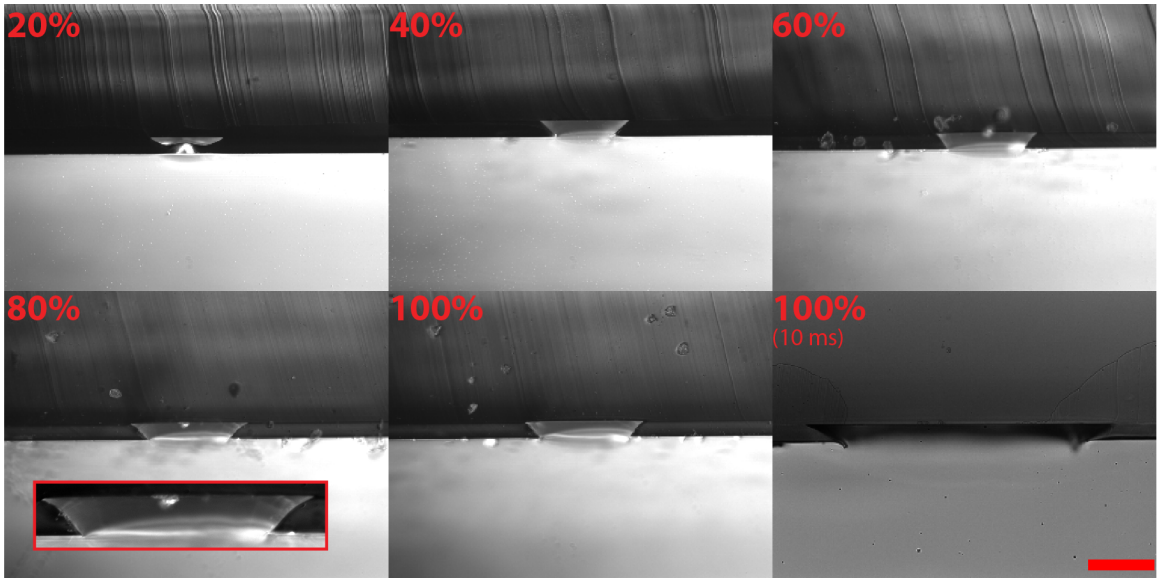

Figure 5.5: **CO_2 laser profile study.** After measurement of the drilled holes were recorded (Figure 5.4), bulk PDMS was plasma bonded to the spots and slices were created to evaluate the drilling profile. At 80 % power the drilling profile was enlarged to show a cone shaped sides. A 10 ms duration at 100 % power is also shown in the lower right. Scale bar is 150 μm.

The intensity, duration and spot diameter were then plotted simultaneously (Figure 5.6). The data was aggregated from triplicate measurements and averaged to create the plot. The average lowest spot size at 40 % intensity and 1 ms duration was 121 $\pm$ 15.3 μm diameter. The theoretical minimal beam diameter for the lasers 38 mm diameter focal length lens is 70 μm, and although almost twice the expected diameter, that assumes no material is ablated from the spot when a laser pulse is applied. Interestingly, the 20 % at 1 ms pulse showed large variation in diameters 92.9 $\pm$ 58 um diameters. The suspected cause of this, lies with the laser and its' electronics. The lasers power supply pulse response time is rated at $\leq$ 1 ms, it is suspected at lower power and duration the CO_2 laser tube is not fully energizing causing erratic behavior in the output response. Future work could include a full study of the drilling behavior at between 1-40 % intensity and fractions of millisecond durations. Partial laser ablation of the surface can be used to create membranes[3].

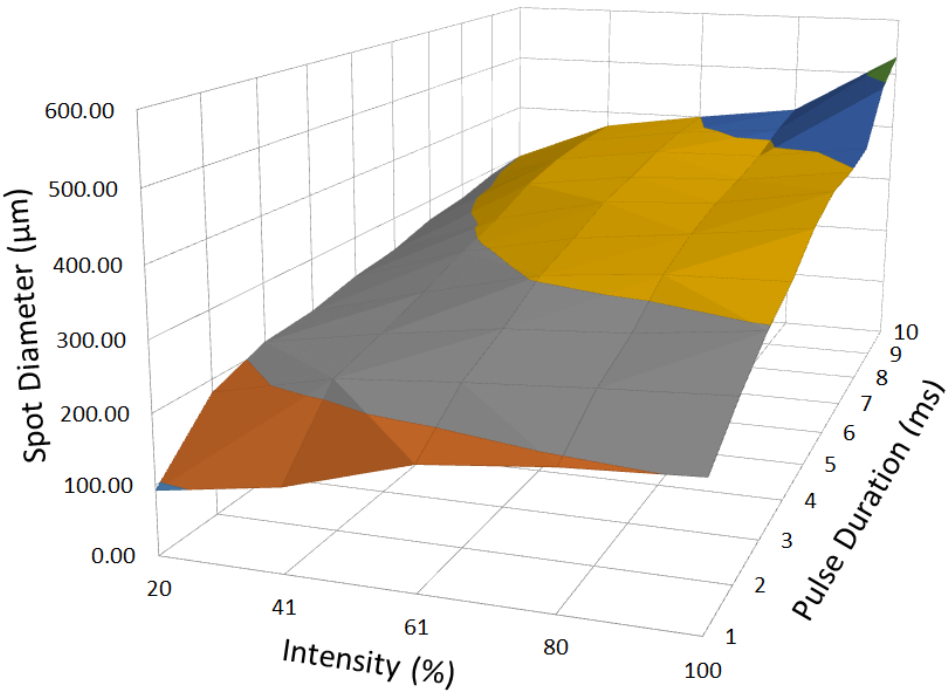

Figure 5.6: **Aggregated drilling study data.** Spot diameter, intensity and pulse duration plotted to easily determine drilling requirements for PDMS holes.

Summary

A CO_2 system was designed and constructed for drilling vias in PDMS to allow construction of higher complexity devices. The CO_2 laser drill provides accurate and controllable drilling of holes in PDMS substrates. Holes ~120 μm were reliably drilled in PDMS and the pulse parameters were investigated for future work.

5.3 UV LED Based Photolithography Exposure Unit

Introduction

To create microfluidic devices, traditional photolithography techniques used in the semiconductor industry are employed. They include, the use of photosensitive polymers, photoresists, spin coated onto silicon wafers, which are then exposed to high intensity UV light, causing a chemical reaction within the polymers and creating a pattern on the wafer based on a mask the excludes UV light from the wafer. Traditionally, the UV exposure systems are

large, initially expensive, have high maintenance costs, and producing large amounts of heat and waste light. They are usually based on arc lamps, either xenon or mercury vapor having specialty optics to both reduce the infrared light emitted and to collimate the light, into a uniform exposure for the wafer as the lamps are typically point sources. Several challenges in our lab existed, we were allowed access to a semiconductor facility on campus, however it was only open 8am-5pm on weekdays and was across campus. Both limited the fabrication of microfluidic masters significantly, slowing down the fabrication process.

A paper published by the Groismans group[4] in 2015, describing the construction of a UV illuminating system used for microfluidic masters fabrication was a solution to the mask aligner issue. At the heart of the UV illumination system is a 3 x 3 matrix of high intensity 365 nm UV LEDs, each mounted within reflectors and then collimated by Fresnel lenses to produce a uniform high intensity light source for the exposure of microfluidic masters. The system was upgraded by replacement of inefficient current limiting potentiometers to microcontroller driven PWM MOSFETs and a timing circuit was added.

Materials and Methods

The UV laser exposure system, is constructed of a 12 x 12 x 3/16 in^3 thick aluminum plate (3DTC5 – Grainger, Lake City, IL), which the UV LED's (LZ1-10U600-Engin, San Jose, CA), accompanying lens/reflector assemblies (FCN12592-LE1-D-COP, Ledil,Sycamore, IL), 4 - 60 x 30mm fans – (OA60AP-11-1WB Orion, Dallas TX), and 1 – 119 x 32 mm fan (EBM-Papst, Mulfingen, Germany) are mounted. The LED driver is constructed on a prototyping board (PN590 – Adafruit, New York, NY) and affixed to the aluminum plate. A sheet of black acrylic (1UPA1-Grainger, Lake City, IL) 8x12" was cut to accept 5.4 x 8.4 cm, 16 cm focal length, Fresnel lenses (401B-3Dlens Corp. Taiepa, TW) spaced per Erickstad et al. paper. T-slot extruded aluminum channels (2RCR1-Grainger, Lake City, IL) was bolted to the aluminum plate via gusset corners (5JRV8- Grainger, Lake City, IL), and the black acrylic was fastened, and aligned by aluminum inside corners (2RCW2-Grainger, Lake City,

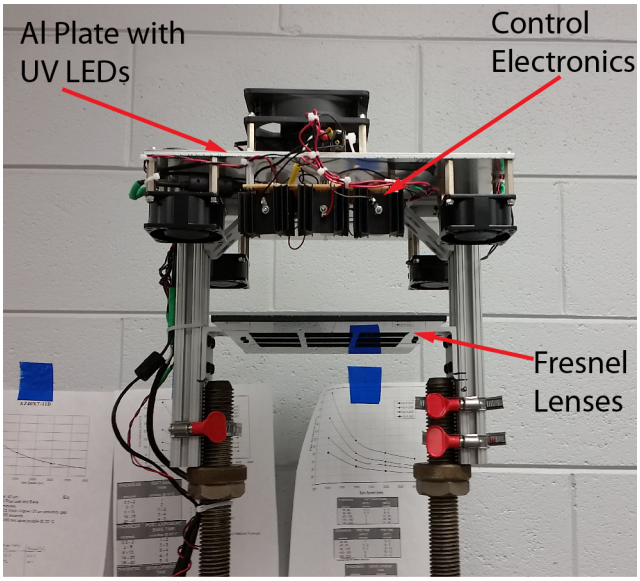

Figure 5.7: **UV LED exposure unit detail.** The UV LED exposure system contains 9 - 365 nm UV LEDs mounted in a 3 x 3 matrix on an aluminum plate. It is cooled by 4 fans. The LEDs output is collimated by Fresnel lenses mounted below the LEDs. Associated control electronics and power supply are mounted on the aluminum plate.

IL) per Erickstad et al. The exposure unit (LED's, Fans, controller, Fresnel lenses) was affixed to a heavy frame consisting of two 1" diameter threaded rods fastened to a cast metal base again maintaining the same distances from Erickstad et al. paper (Figure 5.7). A Lexan block, on top of the metal base is the exposure area, where a 2 mm thick glass sheet holds the items to be exposed in place. Surrounding the Lexan block are red LEDs, providing alignment assistance. Finally, the whole system is wrapped in PVC welding curtain (36 X 28-Grainger, Lake City ,IL) to minimize stray UV radiation into the room.

The UV controller circuit modified from the basic potentiometers used in the reference paper. The UV LED's draw 0.7 A at 4.1 V nominal, and were arranged in two strings of 4 LED's each, and a single UV LED for the center position. Erickstad et al. state that the corner LED's should have a different illumination power compared to the central LED's, which make up 4 LEDs each. All LEDs are driven in a constant current mode, where a MOSFET/transistor feedback loop allows adjustment of current, a power resistor limits overall current in the LED string. The Arduino Nano (Arduino LLC, Turin IT)

is set to PWM drive the MOSFET circuit, which allows adjustment of current in each string. A timer module (H3DK-S1 AC/DC24-240-Omron, Kyoto, JP), sets the exposure time between 1 second and 12 hours. The timer module through a relay controls only the power applied to the LEDs. Additionally, the timer module requires 12 VDC which is supplied by a common LM7812T (Texas Instruments, Dallas, TX) voltage regulator from the 24VDC supply. Verification of the UV exposure unit was carried out by fabrication of master wafers. PDMS was molded on these wafers, features were then measured and compared to the design files. A multichannel emulsion generator (Jul2012) mask was chosen due to the various channel widths present. Wafer cleaned 30 min, 1 M sulfuric acid, rinsed DiH2O, cleaned 30 min in DIH2O, dried with N2, rinsed with IPA, placed in 60 °C oven. Spin coated SU-8 2015 1250 rpm 30 s, soft bake 5 min at 95 °C, UV exposed 4 min, PEB 5 min at 95 °C, developed 5 min, rinsed with IPA blew dry with N2. PDMS SYLGARD 184 1:10 covered wafer and created bulk PDMS to plasma bond too. Sliced at 8 points, corresponding to 160, 80, 40 μm channel widths per the master. Imaged on Ti-E microscope, measurement data were compiled in ImageJ.

Results and Discussion

The high intensity LEDs used in this project were received containing mounting boards, which act as both connection locations and heatsinks. The LEDs are therefore directly mounted to the aluminum plate. This was accomplished by creating a 3D printed drill template (SketchUp Inc. Trimble, Sunnyvale CA), printed in PLA on a MakerBot 2 (MakerBot, New York, NY) to guide the drill bit both in location and perpendicularity to the aluminum surface to allow taping of the holes rather than using bolts and screws. It is very important to place the screws such that they don't apply any undue stress to the semiconductor, which could potentially cause premature failure.

To verify the UV setups suitability for use in microfluidics, a master mask containing 40,80,160 μm width channels, was fabricated, PDMS molded, and imaged. A total of 18

points were collected, 7 at 160 μm, 2 at 80 μm, 8 at 40 μm, data are summarized in Table 5.1. With a 40 um channel, the average percent difference was 20%, which although significant, can be the result of several factors. The first, is the imaging and measurement process, the second is physical changes in the PDMS during curing causing changes in the structure of the PDMS not truly in the mold master. Finally, these are not direct measurements of the mold, due to the difficulty in performing those measurements. In general, the expected with is similar to that from the mask, allowing corrections to be made if high density features are required.

Expected Width (μm)	**Average Percent Difference** %	**Standard Deviation** %
160	7.97	1.81
80	14.46	2.43
40	31.16	5.46

Table 5.1: SU-8 UV exposure study data.

Summary

UV exposure system used for microfluidic photolithography was constructed, by modification to Erickstads et al. paper. The system was evaluated against a master mask yielding $\sim$20% deviation from the mask at lowest feature size tested.

5.4 Microfluidic Solenoid Valve Controller

Introduction

Microfluidics drive mechanisms can be either active or passive. Historically, our laboratory has used passive microfluidics, where vacuum is pulled manually by a syringe and

the flow is controlled solely by the fluidic device. Recently, we have switched to active control of microfluidic devices, which requires the use of solenoid valves to direct pressurized gas or liquid to a specific channel in a microfluidic device. The typical control mechanism is LabVIEW virtual instrument environment (National Instruments, Austin, TX), where a NI-DAQ element is used to drive external devices. The NI-DAQs in our lab (PCI-6259, USB-6008,USB-6002) that are available typically deliver 5 or 20 mA at 5 volts, and the fluid handling solenoids LHDA0533115H (The Lee Co., Westbrook, CT) require 130 mA to actuate at 5 volts, well in excess of both controllers current delivery capabilities. Additionally, the PCI-6259 NI-DAQ has 48 digital I\O pins, requiring significantly larger numbers of available buffering channels. To allow control of fluid control valves by LabVIEW VI's, a high voltage/current buffer was constructed from a Darlington pair transistor array.

Materials and Methods

Darlington pair transistor arrays were used to construct a 24-channel solenoid driver. The driver is built around a ULN2803 (Texas Instruments, Dallas, TX) 8 channel transistor array IC, maximum 50 volts, and 500 mA per channel. The custom driver integrates 3 – 10 segment bar graph LEDs (XGCBDX10D-SUNled, Walnut, CA), which can be switched off for light sensitive applications (6 unused LEDs), dual 25-pin male D-sub connectors for easy input/output connections, and a power supply active LED. Power for the driver is provided by a wall mount adapter 5 V at 4 A (WSU050-4000 – TriadMagnetics, Perris, CA). A full schematic can be found in the Appendix A.

Circuit schematics and PCB's were designed in Eagle electrical design software (Autodesk, San Rafael, CA). PCB CAD files were fabricated by Pentalogix (Tualatin, OR). PCBs were populated with surface mount components and reflow soldered in-house. The remaining through hole devices were hand soldered and the devices were tested, in total 4 boards were created. Boards were then housed in 3D printed boxes with lids, designed

in Sketchup (Trimble Inc. Sunnyvale, CA) and printed on a MakerBot 2x (MakerBot New York, NY).

Results and Discussion

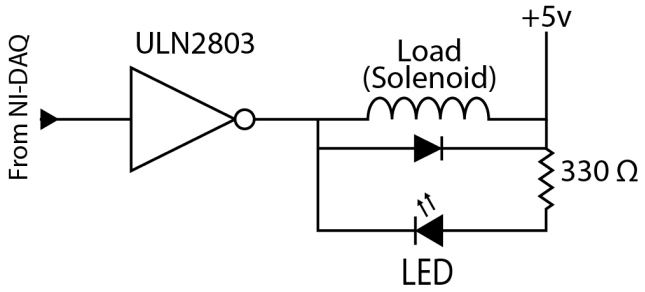

Figure 5.8: **Individual channel valve driver schematic.** Voltage is applied to the solenoid valve and LED, current only flows when the transistor arrays input is high. The diode in the image is essential for system function and is conveniently included in the ULN2803 IC package.

The ULN2803 was chosen due to its high current/voltage capabilities and its small form factor. The 24-channels per device are the same and are depicted in Figure 5.8. A digital signal from the LabVIEW NI-DAQ activates the ULN2803 channel, which has a built in flyback diode to suppress inductive kick. If the LED switch is closed, an LED will be powered through a 330-ohm resistor indicating the channel is active. The driver could be powered by up to 50 volts, however damage will occur to the LED's if they are powered. The PCB artwork and completely assembled PCB are shown in Figure 5.9.

Summary

A device to buffer up to 24 channels of digital data was constructed. It can drive loads up to 50 V (DC) and 500 mA per channel, has fast switching time (130 ns),standard 25 pin parallel port connections, and LED indicators for troubleshooting all housed in a 3D printed box. The active microfluidics that are performed in our lab, require this buffer system between the LabVIEW interface and pneumatic solenoids. Invariably anyone performing active microfluidics in our lab uses this system[5].

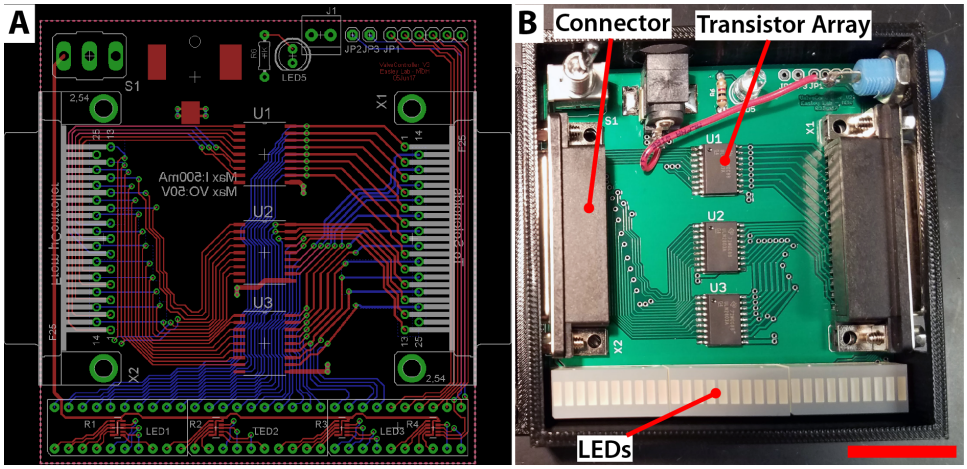

Figure 5.9: **Completed solenoid valve buffer device.** (A) PCB artwork of controller board. (B)Assembled device including PCB, connectors, LEDs and 3D printed box. Scale Bar 25 mm.

5.5 Electronic Pressure Meters

Introduction

Since our lab has switched to pressure driven microfluidics and research directed towards microfluidic circuit analogies (Chapter 6), a way to precisely measure and set the pressure in control lines was required. Both Arduino and LabVIEW based systems were constructed. The Arduino based system was used as a portable device, whereas the LabVIEW incorporated 3 sensors and more flexibility in data capture.

Materials and Methods

The pressure sensors (MPX5700DP-Freescale Semiconductor, Austin, TX) signal output between 0.2-4.7 V corresponding to 0-100 psi is measured by a 12-bit MCP3221 ADC (Microchip Technologies, Chandler, AZ), which sends the resulting digital data to an Arduino Nano (Arduino LLC, Turin, IT) by I2C communication. The received data is converted to pressure and displayed on an LCD screen. Upon power up the Arduino Nano, initializes and follows a calibration procedure then requests input for "set" pressure which is used to

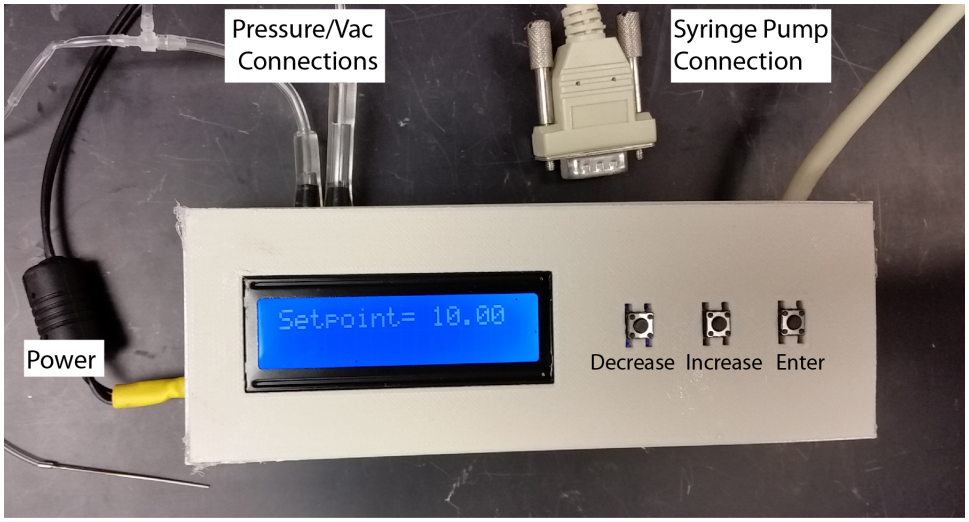

Figure 5.10: **Assembled Arduino based pressure meter.** The Arduino pressure meter features:pressure and vacuum connections, standard TTL pump drive connector, LCD display and increase\decrease, control buttons. The device initializes, calibrates and waits for setpoint input if desired, then displays current pressure.

control a syringe pump (New Era Pump Systems Inc., Farmingdale, NY) by TTL signal output. The pressure sensor is setup to start the syringe pump until 1 psi above the set point including hysteresis in the system. A real-time serial data stream at 9600 bps is broadcast by a Bluetooth module JY-MCU (104299-Deal Extreme, Kowloon, HK), containing timing, set and actual pressures, which can be captured by a cell phone or computer. All components were built on a prototyping board (Adafruit Inc., New York, NY) and assembled in a 3D printed box (Figure 5.10). See Appendix A for schematic.

Pressure verification was performed with a Fluke PV350 pressure transducer connected to a Fluke 89 IV multimeter. The pressure module had a new battery and was zeroed per the manual. Pressure was supplied to both PV350 and Arduino pressure sensors simultaneously from ultra-pure nitrogen compressed gas regulator (AirGas, Radnor, PA). Triplicate pressures were collected for 34 points, between 0 – 600 kPa, between 0-100 kPa increments were 5 kPa, between 100 – 200 kPa increments were 10 kPa, and between 200 – 600 increments were 100 kPa.

LabVIEW Based Pressure Meter

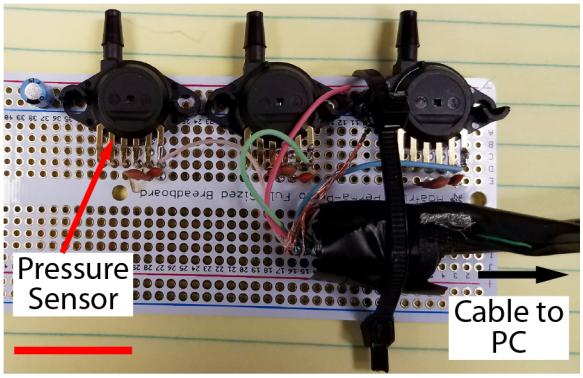

Figure 5.11: **LabVIEW triplicate pressure sensors.** Triplicate pressure sensors were mounted on a prototyping board, connected to power and LabVIEW data capture system. Scale bar 25 mm.

Three MPX5700AP pressure transducers were mounted to a board, and connected to a LabView NI-DAQ PCI-6259, using 5 volts from the NI-DAQ for power. The triple sensor board was then enclosed in a 3D printed box. The Arduino code was ported to the LabView VI, calibration of each sensor takes place before the system moves forward, data collection can be activated and deactivated while the VI runs, saving the data in spreadsheet format. Decoupling capacitors are added between the V+ (0.01 μF and 100 μF) and signal output (470 pF) to ground, Figure 5.11 shows prototyping board and components.

Results and Discussion

Initial evaluation of the Arduino based pressure sensor, yielded poor resolution due to the built in 10-bit ADC, with a step size of 4.88 mV\bit. A 12-bit ADC external IC was added to increase the resolution to 1.22 mV\bit, a four-fold increase in resolution. This change can be seen in representative data collected before and after the 12-bit ADC was added (Figure 5.12).

The MPX5700DP was chosen for the pressure transducer because of its accuracy ($\pm$ 2.5 % over 0-80 °C), range (0-700 kPa), linear output and simplified circuitry with temperature compensation. The Arduino pressure gauges output was verified by measurement against a

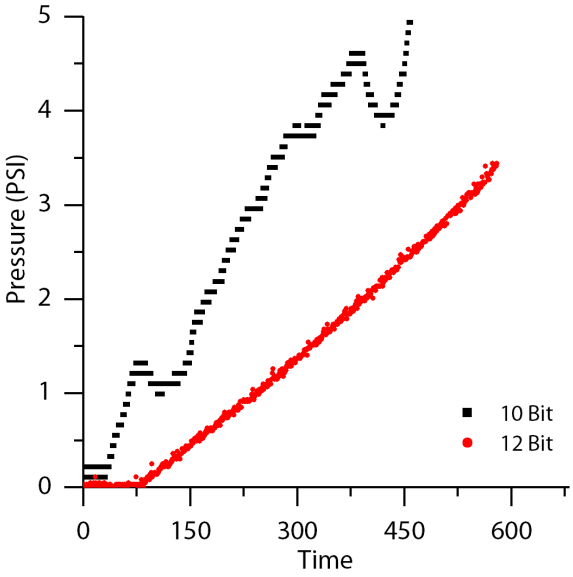

Figure 5.12: **ADC resolution comparison.** Pressure measurements taken with both the Arduinos built-in 10 bit ADC and the external 12-Bit ADC.

Fluke PV-350 pressure transducer with ± 0.25 % accuracy. The overlayed data is plotted in Figure 5.13. Measurements were made in three distinct step sizes, of 5 kPa, 10 kPa, 100 kPa, corresponding to the probability of use in that pressure region. Microfluidic devices rarely operate above 50 psi or 345 kPa, hence fewer data points above that value, and our systems operate below 30 psi or 202 kPa, which is why a greater number of measurements were made in those areas. The average standard deviation for the PV350 for the full range 600 kPa is ± 0.26 kPa, for the Arduino pressure meter in the same range it is ± 0.30 kPa a very marginal difference. In general both device are in close agreement with the applied pressure, leading to our systems validity in making measurements.

Summary

Pressure measurement devices were constructed for both portability (Arduino) and multiple sensor integration (LabVIEW). Both were applied to fabrication and characterization of microfluidic devices see Chapter 6.

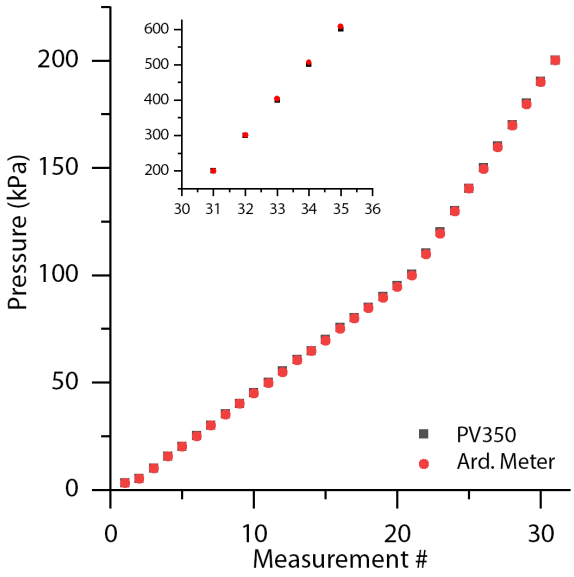

Figure 5.13: **Arduino pressure meter calibration measurements.** Using a Fluke PV-350 pressure transducer and the Arduino pressure meter, measurements were taken on the same pressure line simultaneously with both instruments and compared.

5.6 Laser Diode Controller

Introduction

Microfluidic circuit analogies introduced in Chapter 1, can aid in design of complex microfluidic chips. One challenge in construction is normally closed valves, a solution was proposed by Devarju and Unger in 2012[6] where a channel is compressed into another channel closing it off. To permanently close the channels off a low viscosity photocurable polymer is pressurized and cured in the channel, and this is done for a whole chip[6]. They demonstrate this by filling an entire chip and curing all photocurable polymer at once. This although easy to fabricate, limits the tunability of each microfluidic junction, and our solution is to selectively cure each point individually, using a single channel and varying its pressure. We use a focused 405 nm 40 mW laser diode to cure each point.

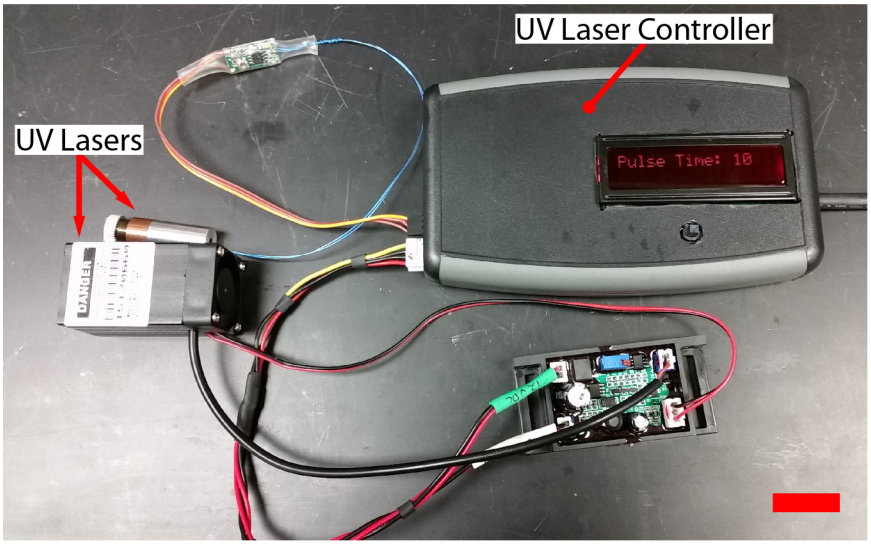

Figure 5.14: **Diode laser controller and lasers.** Pulse duration is programmed into controller, button pressed a TTL high signal is sent to the output pins to control either the 150 mW (12 volt) or 40 mW (5 volt) laser diode. Scale bar 25 mm

Materials and Methods

Two 405 nm lasers a 150 mW module (AIX-405-150T-Aixiz LLC, Houston, TX) and a 40 mW laser diode (PHR-803t-DTR Lasers, St. Louis, MO) laser diode. The 40 mW laser diode was press fit into a laser host (DTR Lasers, St. Louis, MO) which combines a focusing lens and heatsink in one package, the diode was connected to a laser driver module (AIX-RBD-2-Aixiz LLC, Houston, TX). Both modules have TTL logic inputs, capable of being driven by a microcontrollers output. The lasers required different voltages 150 mW – 12 V, and 40 mW 5 volts. Both could not be driven by the same power source, but by the same TTL source. To control the lasers, an Arduino Nano (Arduino LLC, Turin, Italy) was programmed to apply pulses of between 1 ms and 10 s with a 3 second countdown delay. The laser pulse time is displayed on a serial 2x20 LCD (Sparkfun Electronics, Boulder, CO), and controlled by a 5-way switch (Digikey, Thief River Falls, MN). Power supplied by a dual output 12V/5V switchmode powersupply (Rexon Technology Corp - Taiwan) image of completed system (Figure 5.14).

Laser intensity measurements were made by directing the continuous wave unfocused beam from each laser at the thermopile sensor of the LaserBee 2.5W (J. Bauer Electronics – St. Telesphore, Quebec, CA), the laser and sensor were spaced 6 inches apart.

Results and Discussion

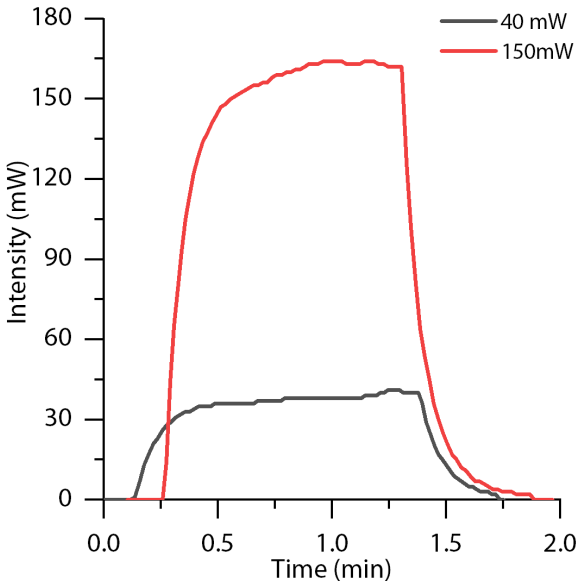

Figure 5.15: **Optical power measurement of laser diodes.** Using a LaserBee 2.5W thermopile sensor, the output of both a 40 mW and 150 mW 405 nM lasers was measured.

The laser intensity was measured for both lasers, to verify rated output, and plotted over time in Figure 5.15. The peak power rating for the 40 mW laser was 41 mW, and average was 37.5 mW. The peak measured power for the 150 mW laser was 164 mW, and the average 151.6. The lasers both performed at or very near there rated outputs. The verification is important to match the manufactures claims and to compare amongst systems, the true output of the lasers in a pulsed operation mode may be significantly different. This is exemplified by the intensity increase in both lasers over a minute of measurement. This may also be thermal drift in the sensor.

Summary

A laser controller was designed and constructed to drive two laser diodes (405 nm) in pulse mode. The laser outputs were measured to verify raw power of each device. The laser diodes were used to point cure photopolymer in microfluidic devices (Chapter 6). Other applications requiring high intensity point source radiation can benefit from the developed devices.

5.7 PID Controller for Laboratory Oven

Introduction

PDMS mechanical properties are affected by curing temperature fluctuations[7, 8], which can detrimentally affect microfluidic devices function and reproducibility. Typical laboratory curing ovens consist of a proportional controller, made up of a bimetallic strip, which expands and contracts with temperature fluctuations, causing heating elements to energize to full power when the temperature is below the set point. This causes large fluctuations in temperate in the oven. To reduce the thermal cycling an oven, a PID controller can be used. The cost of PID modules has dropped significantly with the availably of microcontrollers making it possible to retrofit ovens with these types of controllers. This comes at a significantly lower cost than replacing the oven.

Materials, Methods and Discussion

A PID controller (SYL-2362) was connected to a miniature resistance temperature detector (Pt100MN) and solid state relay (SRDA25) all parts were purchased from Auber Ins. , Alpharetta,GA. A heatsink (80 x 50 x 50 mm-www.amazon.com) was affixed to the solid state relay and a 3D printed box enclosed the wiring. A male mains plug was used to supply power to both the PID controller and the solid-state relay, and a female receptacle delivers

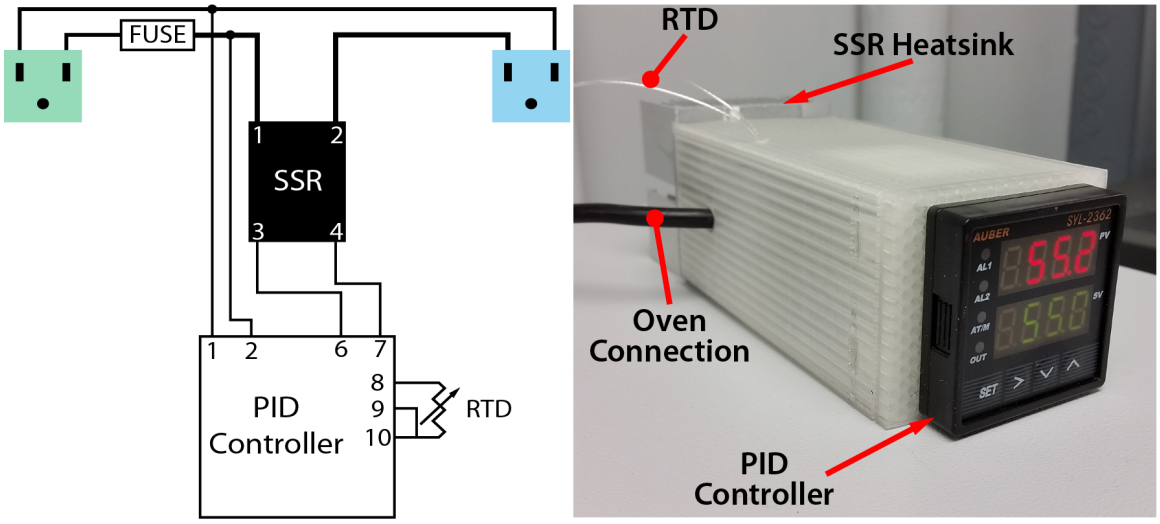

Figure 5.16: **PID Oven controller connections.** The controller has an input power and output receptacle for 120 V (AC). The voltage is controlled by a solid state relay (SSR) driven from the PID controller. A temperature sensor (RTD) is inside the oven and connected to the PID controller for feedback.

the solid state relay controlled output to an oven a connection diagram and the assembled controller are depicted in Figure 5.16.

The wiring diagram shows all required connections for the PID controller (Figure 5.16). The PID controller is then installed on an oven and the autotune function is run, where a step temperature is applied and new PID parameters are loaded based on the oven's response, see manual for operation of the PID controller. The oven controller is versatile, accurate and proven reliable having been installed for $\sim$ 2 years in our lab. It contributes to the consistence of PDMS based microfluidic devices created in our lab.

5.8 Microscope LED Light Source

Introduction

The original American Optical Corporation Series 20 fluorescent microscope contained a 100 watt high intensity incandescent lamp. Since, the light source had been removed from the instrument,an LED based source was retrofitted to the microscope.

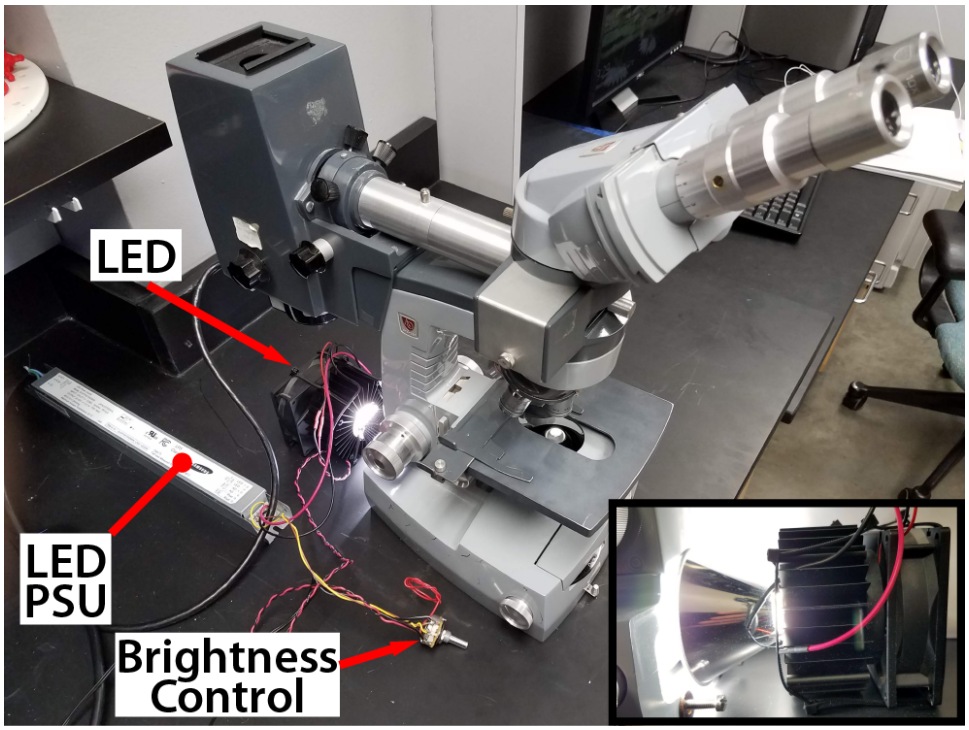

Figure 5.17: **Microscope LED Light Source.** The LED light source fitted to the microscope and powered on. Inset, close up of the light source at full power.

A cob type LED array was chosen based on its high color rendering index (90), high output power (5038 lm) and small size (BXRC-40G4000-C-73 – Bridgelux, Freemont, CA) and a matching heatsink (NX301116 – Bridgelux, Freemont, CA) was affixed to the LED. The LED requires a suitable reflector to direct the LEDs output, the reflector (F13702-BARBARA-WW-PF – Ledil, Salo, FI) was glued to the LED permanently. The LED is driven by a constant current power supply with built in dimming capability (SI-EPF007040WW – Samsung, Seoul, KR). The LED dimming circuit requires a 0-10 VDC analog input to set the brightness. A 10k Ω potentiometer connected to create a voltage divider with a 12 VDC power supply (AEC-4112C) supplied the dimming pins for the LED. The 12 V (DC) power supply also powers a standard computer 80 x 80 mm fan (Antec, Freemont, CA). The power supplies current limit was set to 1.17 A, by connecting a 2k Ω resistor across the Rset terminals on the power supply. The 2k Ω resistor value was measured and corrected using a 47

Ω resistor, to allow the maximum brightness possible. The inputs of the power supply are connected to mains voltage, and the LED connections are soldered to the LED's positive and negative terminals. The microscope, power supply for the LED, and LED operating are all depicted in Figure 5.17. The fluorescence microscope was coupled with a Nikon F1 camera and breakthrough pressure measurements were collected on it (Chapter 6).

5.9 Reflow Soldering Oven

Introduction

When fabricating printed circuit boards, which contain surface mount devices (SMD), a reflow soldering operation is required. A solder paste, containing balls of solder and flux is applied to the component solder pads, then the components are set on the solder paste on the PCB. The reflow process heats the board predictably in 4 phases: preheat (0-150 °C), soak (150-185 °C), reflow (185-230 °C), cool (230 °C-RT). For a total of 10 min run time. The preheating and soak prepare the parts thermally for soldering, some semiconductors can be damaged by high temperatures and fast thermal changes. The reflow phase is meant to be only long enough to cause the solder to liquidity, and flow by surface tension under each of the solder pads[9]. The reflow oven was used extensively for the electronics built in this document.

Materials, Methods and Discussion

A 1400 watt conventional toaster oven (30005 - Proctor-Silex, Glen Allen, VA) was converted for reflow soldering by adding an Arduino Uno (Arduino LLC, Turin, IT) , and reflow oven controller shield (Rocketscream Electronics, Malayasia). The controller, interfaces to the board by a type K thermocouple (1286-1099-ND - Digikey, Theif River Falls, MN) for temperature measurement. A mains connected solid state relay (31932 RL - MPJA Inc. in West Palm Beach, FL) controls the heating elements based on the PID output from the reflow controller. The switches, LED, and LCD display of the reflow controller are remotely

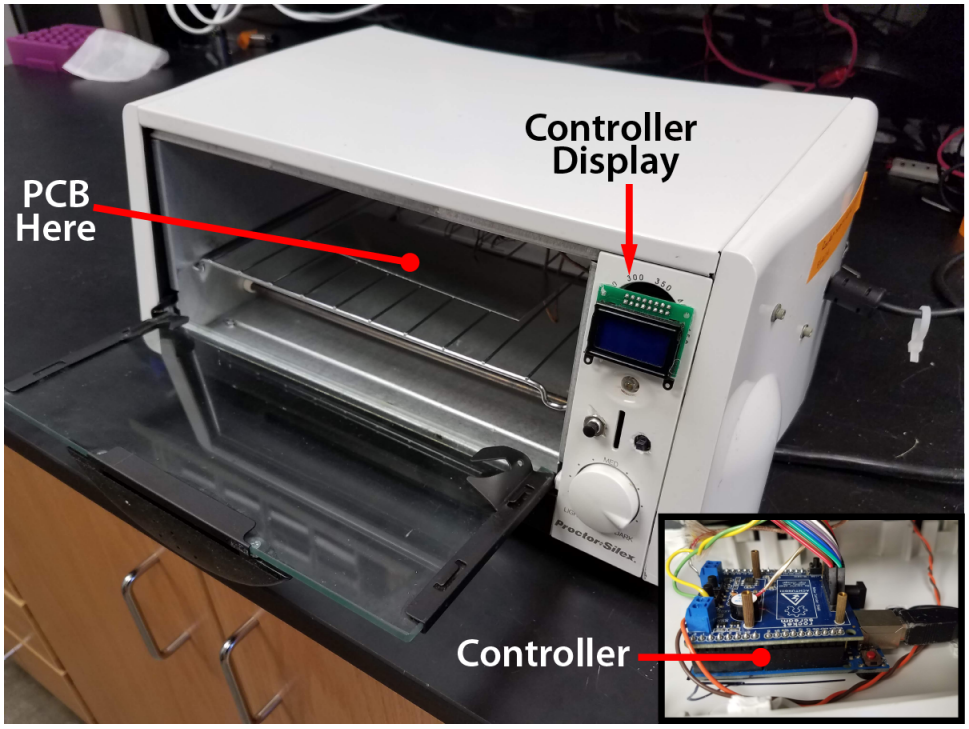

Figure 5.18: **Reflow soldering oven.** Assembled reflow soldering oven created from standard toaster oven and fitted with a PID controller and K type thermocouple.

mounted on the front panel of the toaster oven for ease of use. The finished oven is shown in Figure 5.18, the inset is the Arduino and reflow board.

The Arduino is programmed with firmware provided by Rocketscream, and the temperature profile is adjusted based on the solder paste used. The PID settings can be adjusted for the specific oven if performance isn't adequate with the default settings. Finally, a PCB in the oven should be in contact with the thermocouple tip to ensure accurate temperature measurements. The reflow soldering oven was used in the fabrication of microfluidic valve controller, and all of the differential potentiostat assembly(Chapter 4) proving its utility in our lab.

5.10 Conclusions

This chapter covered instrumentation purpose built for microfluidic device construction and characterization. Microfluidic devices created in Chapter 6 utilized the instrumentation

built in the current chapter. PDMS devices require thermally stable curing conditions for long term device consistency, which was provided by the PID oven controller. The CO_2 laser drilled precisely aligned $\sim$120 μm holes on microfluidic devices creating vias between layers allowing higher complexity devices. The laser diodes were used to individually program tunable microfluidic junctions. Both LabVIEW and Arduino pressure meters facilitated collection of temporally resolved breakthrough pressure data in the characterization of microfluidic diodes and transistors. The electronic valve controller was created to allow active microfluidic devices in our lab and is commonly used by everyone. Finally, the UV LED exposure system was used to create master wafers for projects in this manuscript. The exposure system, plays a larger role in our lab however, any microfluidic master wafer or photolithography (gold on glass electrodes) use this system, emphasizing its value in our lab.

References

[1] M. A. Unger, H. P. Chou, T. Thorsen, A. Scherer, S. R. Quake, *Science* **2000**, *288*, 113–116.

[2] J. Huft, D. J. Da Costa, D. Walker, C. L. Hansen, *Lab on a Chip* **2010**, *10*, 2358–2365.

[3] K. Xu, M. R. Begley, J. P. Landers, *Lab on a Chip* **2015**, *15*, 867–876.

[4] M. Erickstad, E. Gutierrez, A. Groisman, *Lab on a Chip* **2015**, *15*, 57–61.

[5] X. Li, J. C. Brooks, J. Hu, K. I. Ford, C. J. Easley, *Lab on a Chip* **2017**, *17*, 341–349.

[6] N. S. G. K. Devaraju, M. A. Unger, *Lab on a Chip* **2012**, *12*, 4809–4815.

[7] I. D. Johnston, D. K. McCluskey, C. K. Tan, M. C. Tracey, *Journal of Micromechanics and Microengineering* **2014**, *24*, 1–7.

[8] R. Seghir, S. Arscott, *Sensors and Actuators A: Physical* **2015**, *230*, 33–39.

[9] P. Horowitz, W. Hill, *The Art of Electronics*, 2nd, Cambridge University Press, Cambridge, UK, **1990**, p. 1131.

Chapter 6

Tunable Architectures for Microfluidic Resistors, Diodes, and Transistors

6.1 Introduction

Active microfluidic components require interfacing to the macro-world, to transmit pressure signals to the chip, causing redirection of fluids within a device. The macro-micro interfacing is a limiting factor in the number/density of operations a microfluidic device can perform. The number of connections is limited by the overall size of the device and connection size, limiting the total number of possible operations in a given space. One solution to this interfacing issue is to incorporate automatic fluid direction in a microfluidic device or microfluidic logic.

Microfluidic logic design requires a system to efficiently layout components. To easily visualize and conceptualize a complex microfluidic system, an electrical analogy can be used. Early accounts of electricity equated it to the flow of a fluid in pipes. Ohms law can be rewritten for flow, pressure and fluidic resistance as an example, as discussed in Chapter 1. With the basic tools (resistance, capacitance) of circuit based microfluidics already well established[1, 2] , non-linear active components are the next to be investigated[3–8].

Non-linear electrical components (diodes, transistors, FETs, amplifiers etc.) are active components, which direct or amplify electrical signals. Several microfluidic analogies have been demonstrated of non-linear devices. Microfluidic diodes have been created using a flap over an orifice, membrane deflection, flexible pinchers, moveable piston, or Tesla style valves[10–13]. Additionally, transistor/FET devices have also been shown, in general a membrane is deflected against a weir closing off the flow channel. Devaraju and Unger, created a microfluidic amplifier by applying additional pressure at the weir location, creating a normally closed valve which was preloaded (Figure 6.1)[9] . The preloaded valve was created

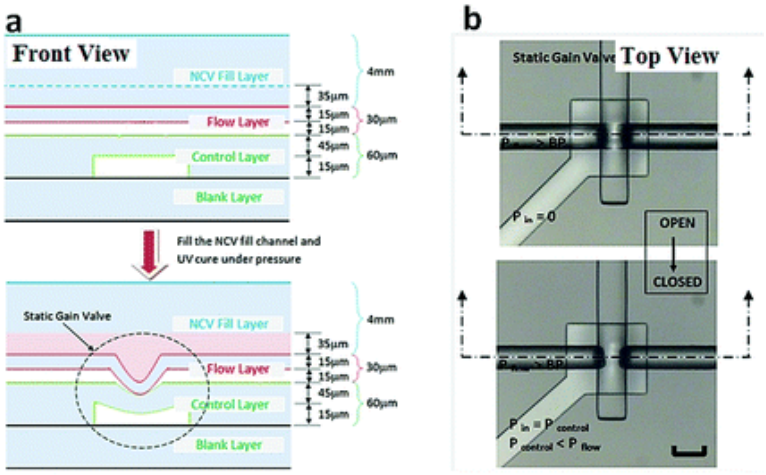

Figure 6.1: **Normal closed valve architecture.** (A) A 3 layer microfluidic device, incorporating normally closed valves. (B) Fabricated and photopolymer cured PDMS normally closed valves. Reproduced in part from ref [9] with permission of, ©2012, The Royal Society of Chemistry.

by an additional channel above the flow layer, which was filled with a photocurable polymer, then cured while under pressure. Another version created by Mosadegh et al. relied on a weir above the channel to deflect against, one of their innovations was to place a hole in the membrane on one side of the weir, where pressure from the side containing the hole would compress the membrane tightly against the weir cutting flow off (Figure 6.2) [14].

Additionally, in the creation of these valves the location of the weir can not permanently bond to the membrane preventing movement. Fabrication of multi-layer microfluidics requires plasma bonding layers together, thus Mosaegh et al. proposed a stamping method, where the plasma oxidized PDMS was stamped with native PDMS[15]. At the surface of non-plasma oxidized PDMS, free monomers in low concentration are still present, if the PDMS is patterned to interact with the device being constructed, and only transfer uncured monomers to the specific locations on the surface of the plasma oxidized PDMS, then irreversible bonding does not occur at the stamped site.

In this chapter, principles from both Devaraju et al.[9] and Mosadegh et al.[14] principles will be combined to create microfluidic circuit analogies with tunable properties. The tunable properties will extend to microfluidic resistors, diodes, and transistors.

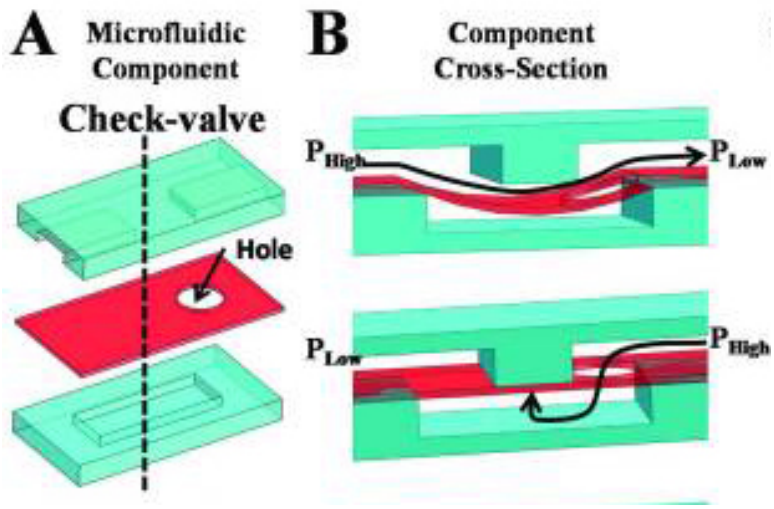

Figure 6.2: **Post and membrane type diode.** (A) Post and membrane type three layer diode structure. (B) Rendering of diode function, where one direction flow easily moves forward and the reverse closes off valve.Reprinted in part with permission from ref [14] ©2010, Nature Publishing Group.

6.2 Materials and Methods

Reagents and Materials PDMS silicon elastomer kit (SYLGARD 184, Dow Corning, Midland, MD), consisting of base and curing agent, were mixed 10:1 unless otherwise noted. Bovine serum albumin (BSA) (Millipore Sigma, Burlington, MA). Fluorescein (Alfa Aesar, Haverhill,MA) was weighed and diluted in DMSO to 100 μM, then diluted to 100 nM in phosphate buffered saline (PBS). AZ40XT-11D photoresist and AZ 300 MIF Developer (Microchemicals, Ulm, Germany), SU-8 2050 photoresist and SU-8 Developer (Microchem, Westborough, MA), Esacure KT-046 (Lamberti S.p.A, Albizzate, Italy), hexamethyldisilazane (HMDS) and di(trimethylolpropane) tetraacrylate (DTPA) were obtained from Sigma Aldrich, St. Louis, MO, Trichloromethylsilane (TMCS) (GFS Organics, Columbus, OH), 150 kμS standard conductivity solution (Fisher Science, Hampton, NH). Poly lactic acid 1.75 mm diameter 3D printing filament was purchased from Hatchbox. Experiments involving tubing were carried out with 0.02 inch ID, 0.06 inch OD Tygon tubing (Cole-Parmer, Vernon Hills, IL), 22 gauge 90 °blunt needles (JG-22-0.5HPX-90,Santa Barbara, CA) and 25 x 75 mm float glass slides (VWR International, Radnor, PA).

PDMS Masking 3D printed models were created in Sketchup (Trimble) CAD software and printed at 0.1 mm layer resolution on a MakerBot Replicator 2 (Makerbot industries NY,NY) with 1.75 mm diameter PLA filament (Hatchbox). 30 g 10:1 (monomer: curing agent) Sylgard 184 PDMS mixed and degassed, poured onto a 100 mm diameter silicon wafer encased in aluminum foil, cured at 60 °C overnight, removed from wafer and cut to fit in clamps. Plasma oxidized PDMS enclosed in clamp at high power (18 w) 60 s (Harrick Plasma, Ithica, NY).

Microfluidic Master Wafer Fabrication Multi-layer microfluidic devices were created by standard processes[16]. The SU-8 masters for microfluidic device fabrication were created by designing masks in Adobe Illustrator (San Jose, CA), printing by Fineline Imaging (Colorado Springs, CO) at 50,800 DPI. A 100 mm diameter silicon wafer (Polishing Corporation of America, Santa Clare, CA) was cleaved by carbide tipped scribe and cleaned 30 min in 1 M H_2SO_4, rinsed 3X in DI-H_2O. For the control layer and fill layers SU-8 2050 was spin coated onto the surface at $\sim$40 μm thickness, soft baked at 65 °C - 1 min, 95 °C - 6 min and cooled to RT. Using an in-house built UV exposure system see chapter 5[17], the wafers were exposed 4 min for a total cumulative power of 370 mJ/cm^2 through the mask. The exposed wafers were post exposure baked at 65 °C – 1 min and 95 °C – 6 min then cooled to RT. Each wafer was developed separately 2.5 min in SU-8 developer, and 2.5 min in fresh developer (5 min total). Wafers were rinsed 10 s in IPA and dried under pressurized nitrogen.

Flow channels are created by reflowing AZ positive photoresist to form rounded channels as follows. New 100 mm diameter silicon wafers were cleaved by carbide tipped scribe and heated to 200 °C for >15 min in oven. HMDS was vapor deposited onto wafer halves in a hood by heating to 150 °C on hotplate for 10 min. Wafers cooled to RT and AZ photoresist spin coated to a thickness of 20 µm and soft baked 75 °C – 30 s, 95 °C – 2 min then ramped to 140 °C over 3.5 min. Wafers were exposed to UV through a mask at 2 min intervals of exposure and resting, total exposure time 4 min. Post exposure baked at 85 °C – 10 s ramped to 115 °C over 2 min, cooled to RT, developed in fresh AZ developer 1.5 min then transferred

to fresh developer 1.5 min. Wafer halves were placed on hotplate at 140 °C – 5.5 min and cooled to RT. Both SU-8 and AZ wafers were treated at RT to TMCS vapors for 30 min in a fume hood to aid in PDMS removal.

Multi-Layer PDMS Device Construction To create microfluidic devices 30 g PDMS was thoroughly mixed, degassed and transferred to upper layer wafer halve contained in aluminum foil boat. PDMS was spin coated onto the middle and lower layer wafer halves at 1700 rpm and 1000 rpm respectively for 60 s, creating PDMS layers 40 μm (middle) and 60 μm (lower) thick. All wafer halves were placed in PID controlled 60 °C oven overnight to cure.

Chip fabrication is performed in reverse, where the upper bulk PDMS layer is plasma bonded to the middle layer, upper/middle layer are plasma bonded to the lower layer and finally plasma bonded to a glass substrate. The bulk PDMS chips and middle layer are rinsed with MeOH dried by pressurized air, cleaned with Scotch Tape (3M, Maplewood, MN) and holes punched. The clean PDMS items were plasma oxidized at 10.2 W power (Harrick Plasma, Ithica, NY) 45 s, aligned carefully and united forming an irreversible bond, incubated at 60 °C for ∼5 min. Holes are punched, and vias drilled by CO_2 laser (Chapter 5) at 16% intensity, 4 ms duration in the now 2-layer device. The PDMS lower layer and two-layer device are cleaned as previous and are joined by plasma oxidization as previous. The 3-layer device has holes punched and is bonded to a glass slide as previous. 1.5 mm ID diameter holes punched for photopolymer (Miltex biopsy punch 33-31A, York, PA) and flow layer connections punched 0.75 mm ID (EMS-Core Sampling Tool 69039-07, Electron Microscopy Sciences, Hatfield, PA). A microfluidic chip from each batch was not bonded to glass instead, sliced to be imaged on Nikon Ti-E inverted microscope to verify channel/layer dimensions (Figure 6.3).

To reduce the adhesion between the flow layer and the deflecting membrane, 1% BSA in DDH_2O was flowed through chip. Photopolymer was weighed combined and mixed thoroughly, 0.9 g DTPA acrylate monomer to 0.1 g Esacure photo-initiator, stored in dark.

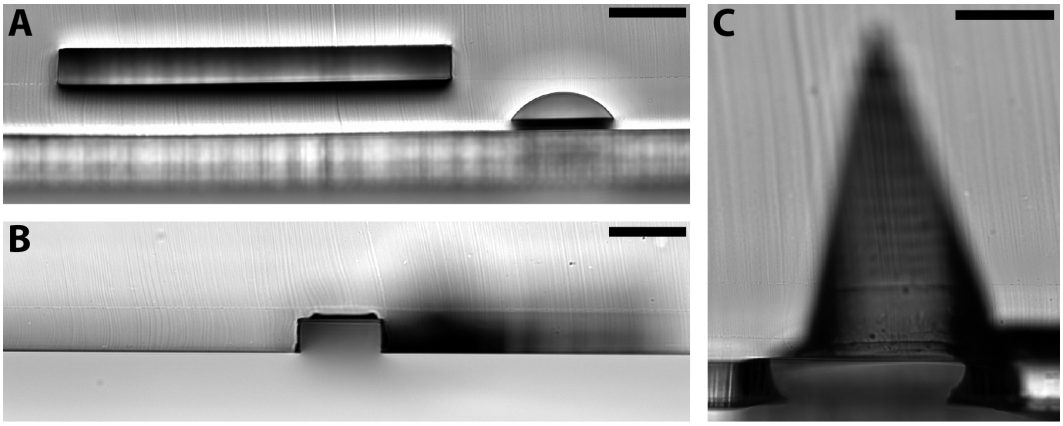

Figure 6.3: **PDMS channel cross sections.** (A)Fully assembled 3 layer device,depicted are upper layer chamber chamber, middle layer flow channel and lower layer fill line bisected. (B) Two layer device showing fill line channel cross section. (C) Laser drilled hole 16% intensity at 4 ms duration pulse. Scale bars all 100 μm.

Photopolymer was loaded into Tygon™tubing, connected to microfluidic chips fill line and pressurized by syringe pump (New Era Pump Systems, Farmingdale, NY) controlled by in-house built pressure meter (chapter 5). While still pressurized, chips were exposed to intense UV (365 nm) for 1 min, 12 cm under a single LED of the UV exposure system (chapter 5) (Figure 6.4). Remaining tubing on microfluidic chip was cut off, to verify UV curing was successful.

Diode Pressure Measurements Breakthrough pressure was measured by using the syringe pump configuration in Figure 6.4 where the pressure line filled partially with filtered food coloring or 100 nM fluorescein dye. The syringe pump was ramped continuously, while monitoring the diode structure for breakthrough and collecting Bluetooth transmitted serial data stream of pressure measurements. Optical measurements were collected on a 1X stereo microscope, fitted with 640 x 480 px CCD array (MD35) both from AmScope, Irvine, CA example breakthrough is shown in Figure 6.5. The CCD arrays USB output was collected as a movie file (AVI) in AmScopes software, pressure data collection began and ended when a fiducial marker was passed in front of the camera syncing pressure and time data. Data was processed by aligning optical data cues with pressure data, then averaging the 100 ms of pressure data at break through. Data also collected utilized same technique above, using

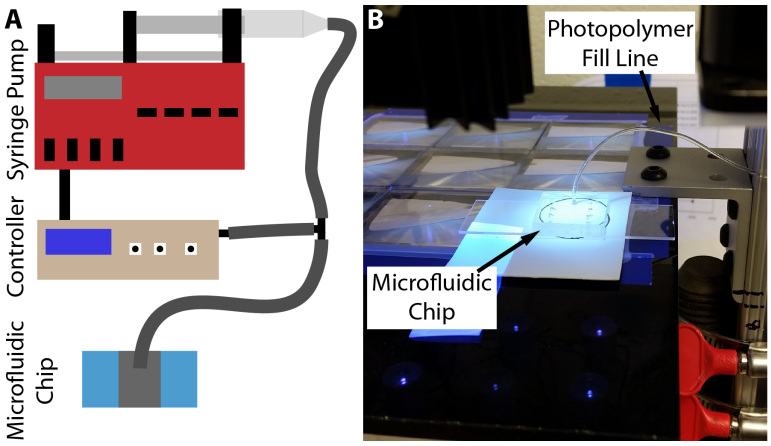

Figure 6.4: **Process to fill channel with photopolymer.** (A)Syringe pump controller connections. The pneumatic pressure line leads from the syringe to pressure meter to microfluidic chip. Syringe pump controlled by pressure meter feedback. (B) Total chip curing with UV LED (chapter 5).

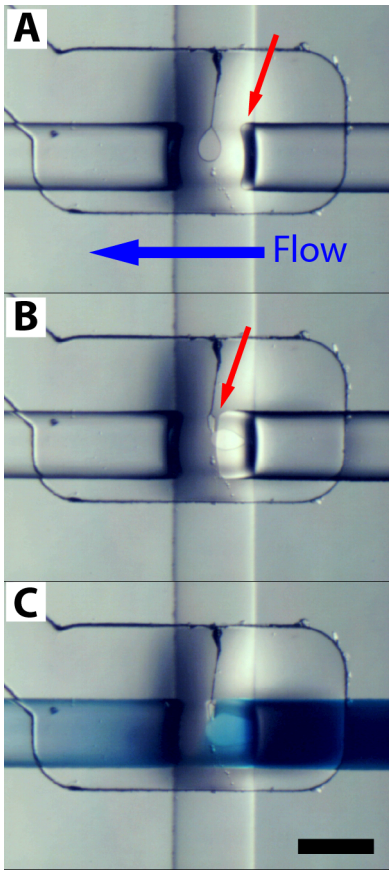

Figure 6.5: **Microfluidic diode breakthrough.** (A) Initially, low pressure on flow channel, red arrow indicates partial membrane deflection. (B) Pressure increasing, junction shows deflection at red arrow. (C) Breakthrough flowing blue dye. Scale bar 100 μm.

American Optical Fluorescence microscope (mercury vapor lamp), Filter cube AO 2073, 10x objective, Nikon J1 camera, in house-built LED illuminator (chapter 5) and 100 nM fluorescein dye. Flow rate measurements were performed by setting the pump at constant value and placing tubing at the output and waste ports, then measuring the meniscus travel distance over time, 10 min at 10 & 20 psi and 3 min at 30 psi.

Microfluidic Transistor Characterization Fabricated microfluidic transistors fill lines were pressurized as in previous section and UV cured at each junction location at 100 ms with focused 40 mW 405 nm laser (chapter 5). Manifold and control line pressures collected by triple pressure meter using LabVIEW (chapter 5). Video collected simultaneously as pressures, ROI 75 w X 840 h in imaging region on Nikon Ti-e inverted fluorescences microscope with FITC filter cube. Flow rate collected after each pressure cycle, by meniscus tracking as previous. See Appendix B for analysis of images and pressure data.

6.3 Results and Discussion

PDMS Masking Microfluidic diode structures have been demonstrated by others. Our efforts to simplify construction, will focus on combining works by Leslie, et al.[18] and Mosadegh et al. [14] The normally closed valve (NCV) structure functions by membrane deflection from a central post in Leslie et al. paper. The post if assembled by plasma oxidizing, requires masking, to prevent irreversible bonding at the NCV location and preventing membrane deflection. Mosadegh et al. show a method of creating PDMS templates by lithography to "stamp" the plasma oxidized surface, which transfers residual PDMS oligomers from the surface of the stamp, inactivating the surface of the plasma oxidized PDMS and preventing bonding at that point. The stamping process is very effective; however, it requires extra fabrication of the stamps before the device can be constructed. We applied 3D printing techniques to exclude plasma interaction at the PDMS surface, preventing bonding at the masked location.

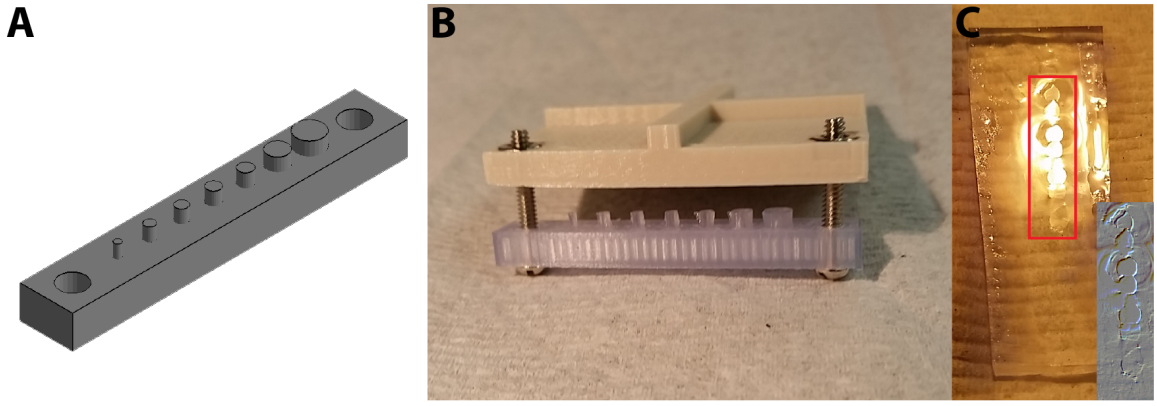

Figure 6.6: **Masking PDMS from plasma.** (A) Rendering of 3D printed masking mold, containing posts ranging between 1→4 mm in diameter. (B) 3D printed posts, and clamping jig assembled. (C) Bulk PDMS masked from plasma oxidizing and coated in MeOH to visualize hydrophobic pin locations, inset is pin region embossed to emphasize pin locations.

Our proof-of-concept model is shown in Figure 6.6, where a series of posts between 1 – 4 mm in diameter were 3D printed by FDM in PLA. A clamp assembly held the PDMS against the posts during plasma oxidation Figure 6.6B. Clamp was removed from PDMS, MeOH was applied to the surface after plasma treatment, causing masked inherently hydrophobic PDMS to repel MeOH verifying masking was successful (Figure 6.6C), embossed post location image inset to aid visualization. 3D printing yielded posts >1 mm diameter. To reduce structure size, a pyramid was printed rather than a post, however it did not yield reliable masking results. Unreliability maybe due to PLA/plasma interactions related to partial porosity of the PLA. Ultimately, this method was abandoned due to, unreliability and resolution limitations of the FDM printing process. With the advancement of SLA printing techniques this method is a good candidate for future exploration.

Fill Line Pressure Verification Tunable devices rely on a constant pressure at the NCV fill line and that pressure is set and held by the previously mentioned syringe pump/custom controller combination. To verify its functionality, data was collected over 100 s via Bluetooth connection at 30 ms intervals and the raw stream of data for 0 - 30 PSI in 5 PSI increments was plotted in Figure 6.7. The controller has a hysteresis set for 1 PSI, clearly seen in 30 PSI trace are steps corresponding to the controllers pump start/stop cycle after reaching 31

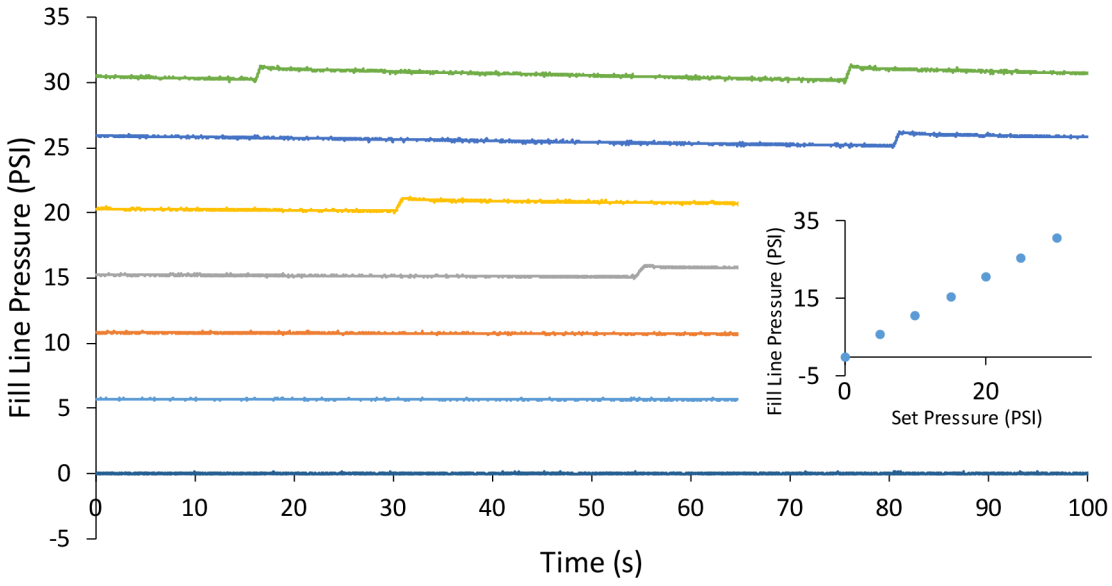

Figure 6.7: **Fill line pressure measurements.** Microfluidic chips fill lines were pressurized and cured between 0 and 30 PSI in 5 PSI increments. The collected serial data from each pressure point is overlaid above. The inset shows average data collected and plotted against the setpoint value.

PSI. The typical solidification time of the photopolymer is only seconds; however, the UV cure is extended to 1 min to avoid issues with curing and circumvent ruined microfluidic chips. The average measured pressure versus set point are plotted in Figure 6.7 inset, error bars are included, however the average standard deviation for the pump controller over the 30-psi range is ± 0.18 PSI.

Tunable Resistors A series two fluidic resistors were put in series at the center was a tap point. They were created to evaluate the possibility of tuning components after the device was fabricated, rather than during the mask/fabrication process which takes longer and limits the usability of the microfluidic structure. The microfluidic mask is shown in Figure 6.8 and the resulting microfluidic chip. Initial characterization was by flowing 150k μS/cm conductivity solution through R1 and varying the pressure applied to R1's fill line (red channel). The resulting voltage drop was applied to Godwin, et al. equation for calculating the fluidic resistance within a round channel geometry.[19] The plot shows a resistance versus applied pressure to the fill line relationship, in an exponential growth fitted curve. The

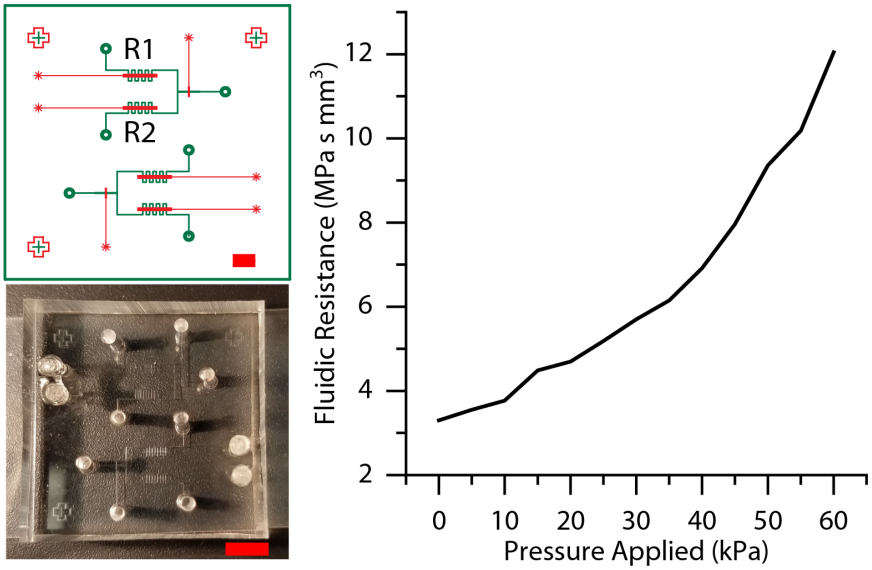

Figure 6.8: **Tunable microfluidic resistor chip.** The mask pattern for fluidic resistors consists of a series resistors tapped at the midpoint for output (scale bar 2 mm). The ratio of resistances will determine ratio of flows in output. The actual fluidic resistor chip is shown lower left (scale bar 5 mm). Fluidic resistance calculations by flowing conductive fluid and measuring voltage drop in channels and fitted curve.

clear demonstration of variable resistance components is valuable due to the fabrication complications within microfluidic channels to alter the fluidic resistance eg. longer or shorter channels, in the finite space of a monolithic device.

The previous experiment used a water filled photopolymer line, which may not be indicative of the actual cured photopolymer. The next experiment cures the photopolymer in R1 at 50 kPa, and R2 at 0 kPa, then flows red dye through 0 kPa (0kPa, stands for R1=R2= 0kpa fill line pressure), and green dye through 50 kPa (50kPa, R1=50kPa, R2=0 kPa fill line pressure). Data analysis, after extracting green channel, threshold correction and particle analysis were performed on the region of interest yielding areas, the ratio of those areas was compared, and the 50 kPa, had a 4.5X area increase over 0 kPa (Figure 6.9). In the earlier data collected varying the pressure in the fill line, we would expect 3x increase in the output. The results are similar, and will require further characterization to fully predict the fluidic resistance output from a specific applied and cured fill line pressure.

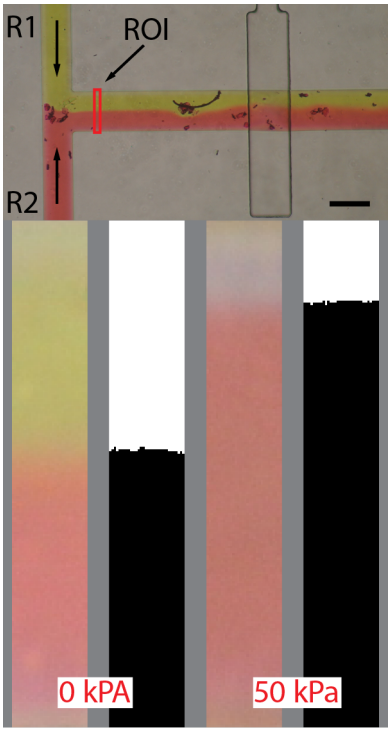

Figure 6.9: **Optical measurements of microfluidic resistors.** One microfluidic chips fill lines were cured both at 0 kPa, both open and flowing. The extracted data can be seen, where the ratio between green and red dyes is 50%. A second device was then filled and photopolymerized with one fill line at 0 kPa and the other at 50 kPa. It is clear from the second set of data, the 50 kPa is restricting flow. Scale bar 100 μm

Tunable Microfluidic Diodes A new diode function and architecture was investigated next. Devarju and Unger[9] introduced a new method which relies on a sacrificial fill line backfilled with photopolymer, pressurized and cured closing off the flow channel, creating a (NCV). They went on to use this in large scale fluidic logic circuits.

The response of the microfluidic diode is expected to follow an electrical diodes response, except the breakthrough pressure or forward voltage is tunable. Electrical diodes require a forward voltage 0.7 V, to start conducting current, red dashed line (Figure 6.10). The electrical diode when reverse biased, does not conduct current, until the diode breaks down at higher voltages, causing a large current to flow and destroying the diode. Similarly, the microfluidic diode when reverse pressure is applied, no flow is allowed past the normally closed valve, until the pressure is above the breakdown point, which causes damage to the

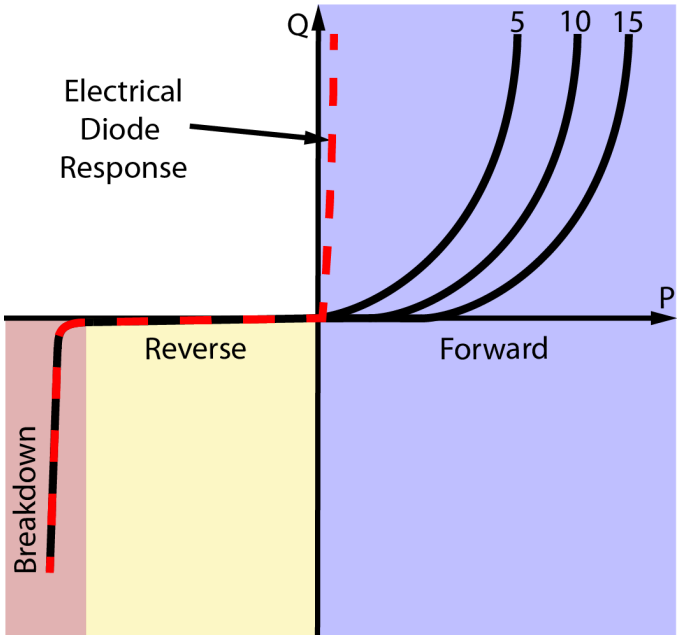

Figure 6.10: **Ideal microfluidic tunable diode P vs. Q response.** Stylized flow(Q) and pressure (P) responses of microfluidic diodes set at varying fill line pressures. In comparison to the electrical diode response overlayed (red dashed line) analogous to voltage, current response.

diode. In the forward direction the microfluidic diode has a much higher forward pressure required when compared to an electrical diode due to the NCV. To allow flow in the forward direction, a pressure must be applied above the NCV valve fill line pressure, shown in Figure 6.10 as 5-10-15 psi.

First Generation Diodes We applied photopolymer curing in the construction of microfluidic diodes by creating a separate chamber and connecting the chamber to the flow channel on one side of a push down NCV by a hole or via (Figure 6.11A). Microfluidic chips were then created from the mask shown in Figure 6.11A. If pressurized fluid is introduced to the flow channel in the forward direction above the NCV set pressure the membrane deflects into the chamber allowing forward flow (Figure 6.11B). When fluid is applied in the reverse direction, fluid pressure is transferred to a membrane under the NCV valve by a via. The membrane pressure is approximately equal to the input pressure plus the fill line pressure, causing the membrane to close further upon higher reverse pressures and stopping reverse flow (Figure 6.11C).

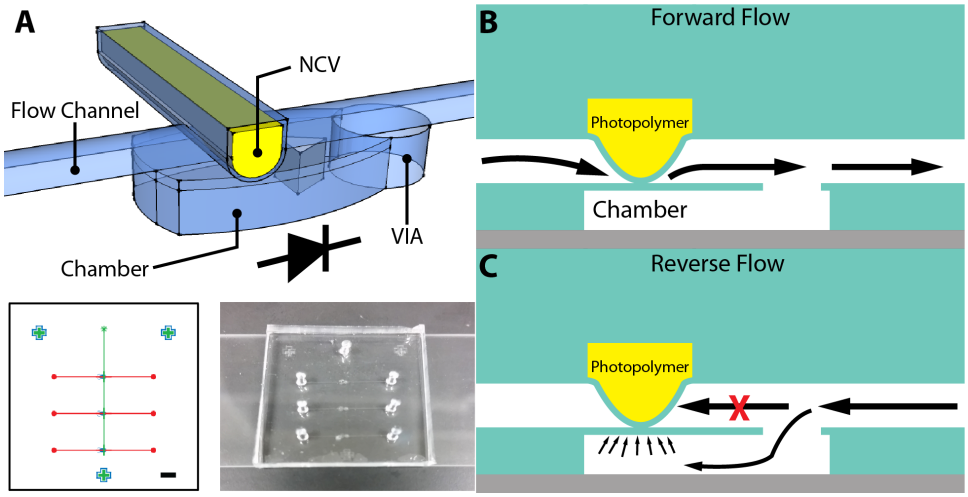

Figure 6.11: **First generation tunable microfluidic diodes.** (A)Generation 1 microfluidic diode rendering highlighting the structures and flow direction (left to right),mask and fabricated microfluidic chip. Scale bar 1 mm (B) Profile depiction of diode structure flowing in forward direction, under pressurized photopolymer line. (C) Reverse flow in microfluidic device, showing pressure closing off valve.

At lower NCV fill line pressures, the channel was not closed off, causing flow in both directions. The flow in both directions results from the pressure required to close the NCV but also the geometry of the device. Recall, that the flow channel is reflowed, to round over the channel creating an arch shape to seal the membrane. Arches are known for strength and stability, and on the microfluidic level this holds true. At moderate NCV fill line pressures, the arch is not fully compressed, creating voids at the edges of the channel allowing flow marked by arrows (Figure 6.12A). If a cross section of the channel is cut under the NCV, the shape is similar (Figure 6.12B). Although, it is possible to collapse the flow channel closing it off, the much higher NCV pressures require, higher forward pressure outside of the normal operating pressure (>40 psi) of standard microfluidic components, reducing the usefulness of the devices in common applications.

In following design, the arrangement of the layers in the microfluidic device were changed from a push-down architecture (Figure 6.12B) to a push-up type (Figure 6.12C). The closing force for each was discussed by Studer et al. requiring <1 psi to close a push-up type valve

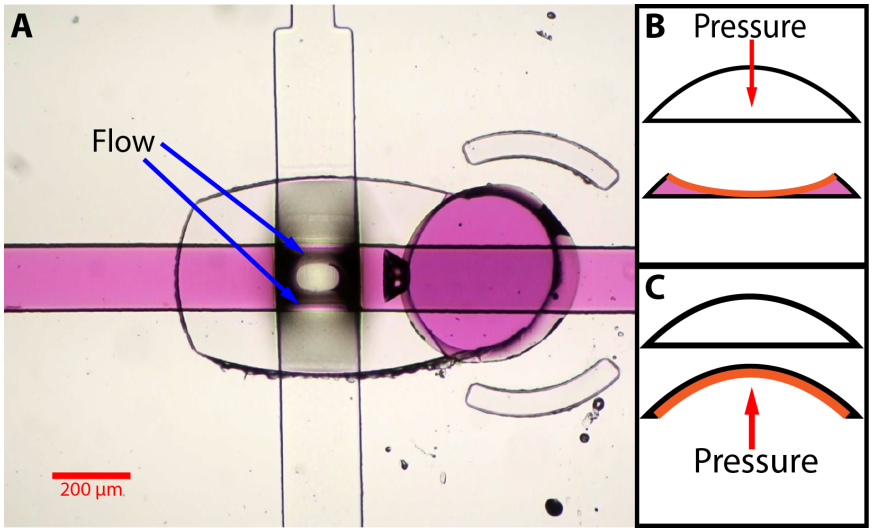

Figure 6.12: **Tunable diode architecture.** (A)Diode structure containing red dye, illustrating leak points under no forward pressure. (B) Push-down type valve, where a strong arch geometry requires greater force to close. (C) Push-up style valve, where a membrane is easily deflected to close the flow channel off.

over the almost 30 psi for a push down valve constructed with the same dimensions as the push-up[20].

We were also interested in the switching time of the diode, as large membranes can act as capacitors in this case causing hysteresis during pressurization, a higher resistance arm leading to the membrane may limit the capacitive effects. One way to test the opening/closing characteristics is to measure fluorescent intensity at a deflection point above the channel, as the fluorescent intensity increases greater deflection occurs. The arms higher resistance would potentially, slow the infusion of fluorescent dye being used to characterize the opening and closing into the chamber area which otherwise would ruin the measurement.

Second Generation Diode A second-generation diode containing an arm extending away from the chamber and active membrane was created (Figure 6.13A). The diode is assembled with the chamber in the upper layer, and fill line in lower layer to allow efficient pressure transfer closing the flow layer. The diode structure without photopolymer fill (Figure 6.13B) top, and pressurized fill line in (Figure 6.13B) bottom. The structure is shown where the filled photopolymer line obstructs the flow channel and requires approximately the fill line

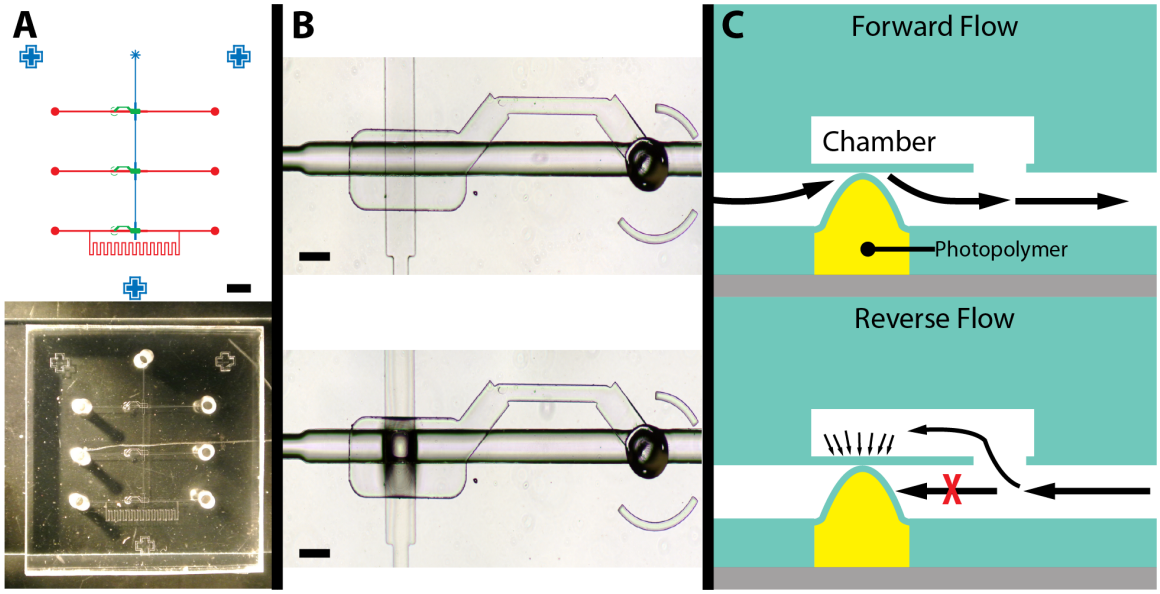

Figure 6.13: **Second generation tunable diode.** (A)Stacked diode masks and assembled PDMS molded microfluidic chip. 2 mm scale bar (B)Fluidic diode structure, unfilled photopolymer line (top), filled line (bottom) 200 μm scale bar (C) Forward flow versus reverse flow in the microfluidic device.

pressure to flow in the forward direction (Figure 6.13C) top. In the reverse direction like generation 1 diodes, the fluid flows into the structure, is forced into the chamber and the pressure acts on the NCV structure causing the device to close off by deflection of the membrane upper layer onto the NCV valve (Figure 6.13C) bottom.

To characterize generation 2 diodes, the breakthrough pressure (BTP) was measured. Breakthrough pressure is the pressure at which fluid starts to flow through the NCV valve. These measurements were made optically, while simultaneously collecting pressure data with time markers. Breakthrough pressure number 1 (BTP1) was plotted, it was the first time the valve was actuated and tended to be higher pressure and variability (Figure 6.14), going forward only BTP 2 and 3 will be plotted (Figure 6.14) due to the greater measurement stability. Ideally, BTP and NCV fill line pressure would be equal, however this is not the case. Devarju and Unger showed a similar plot which was linear between 5 – 25 PSI but shifted to the right eg. 5 PSI fill line pressure yielded 2 PSI BTP. In our case the curve shifts to the left, where a BTP is seen at zero fill line pressure. One possible explanation is

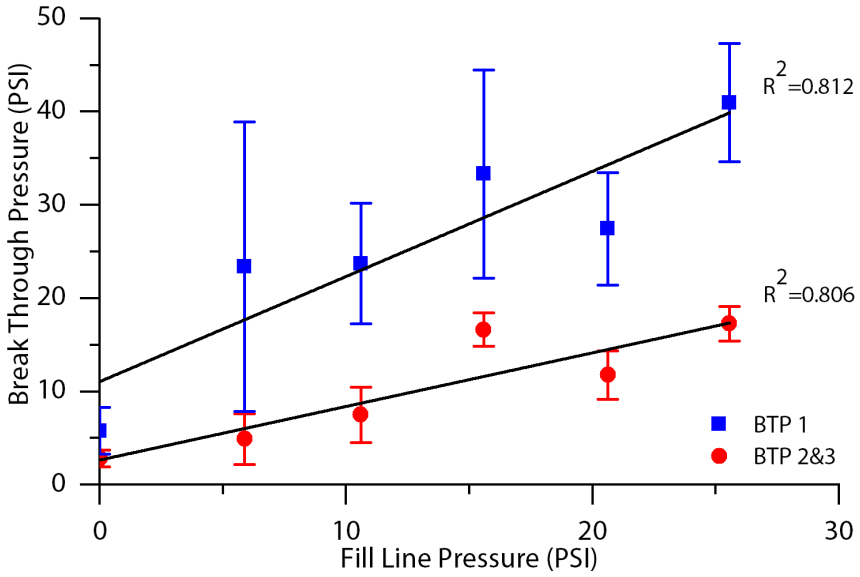

Figure 6.14: **Breakthrough pressure data.** Breakthrough pressure one (BTP1) is the initial data collected after a diode device was fabricated. Subsequent breakthrough pressures were collected two and three (BTP 2 & 3) showing a reduction in variability of BTP.

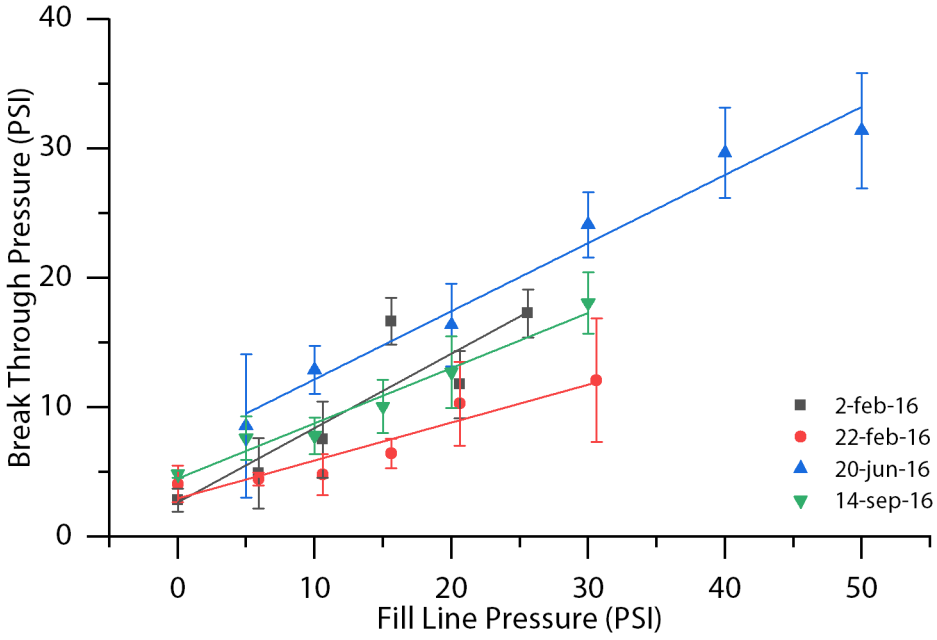

Figure 6.15: **Combined tunable diode breakthrough pressures.** Compiled breakthrough pressures of 56 chips, 148 measurements, over 7 months.

geometry of the device design, where the actuated membrane is 840 μm wide x 440 μm high x 60 μm deep and its large size can possibly sag or easily interact with the NCV valve causing a higher BTP. Our results do show a clear relationship between fill line pressure and BTP, showing we can program the diodes, allowing possible fluidic circuit designs.

Microfluidic devices are commonly fabricated in small batches demonstrating a new functionality, rather than device reproducibility over time. The next data set was then collected for diodes over the course of 7 months, and a total of 148 individual measurements and 56 chips then plotted in Figure 6.15. The diodes function similarly and cluster around a central point, however it varies from day to day/month to month. This can be attributed to variations in PDMS batches, small spin coating changes and other environmental factors.

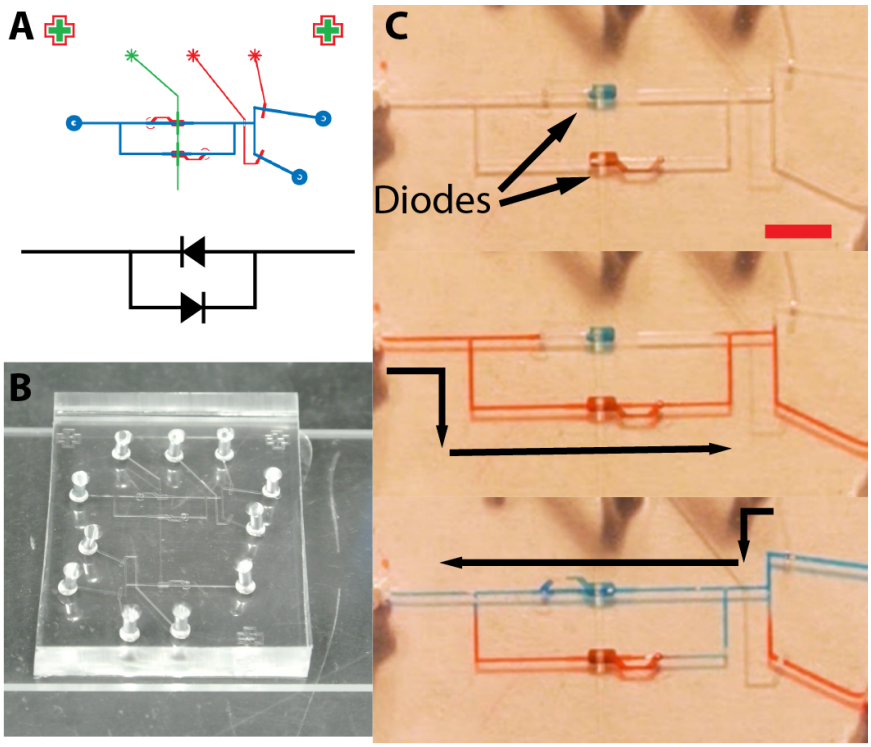

Figure 6.16: **Microfluidic tunable diode rectifier.** (A) Rectifier mask and diode directions overlayed. (B) Fabricated PDMS rectifier chip. (C) Function of diodes highlighted with red and blue dye. Red dye enters from left to right, follows lower diode path. Blue dye enters from right to left and follows upper diode path. Scale bar 2 mm

Microfluidic Diode Rectifier The microfluidic diodes function was next investigated by creating a rectifier circuit, where flow is directed through one path in one direction, and

another in the reverse direction. The mask and equivalent circuit is shown in Figure 6.16A. Flow is driven from left to right and out waste connection at lower right. The microfluidic chip constructed is shown in Figure 6.16B, where all connections are punched however the NCV fill valves are not filled but are later pressurized to 20 psi and cured via laser pulse 5 ms on each diode. The function of the diode is shown in Figure 6.16C moving from top to bottom. The circuit started unfilled where no flow is present, red dye is then injected from the left and flow proceeds through the lower channels being blocked from the upper channels flow by the diode. A reverse flow of blue dye is then introduced from the right, and the dye flows only in the upper diode structure. This example shows the possible leakage or dead space in the diode, when red dye is introduced to the system, it flows partially into the upper channel, closing off the second diode, but also requiring a volume of fluid to pressurize and deflect the membrane. This proof of concept device demonstrates the functionality of the microfluidic diodes.

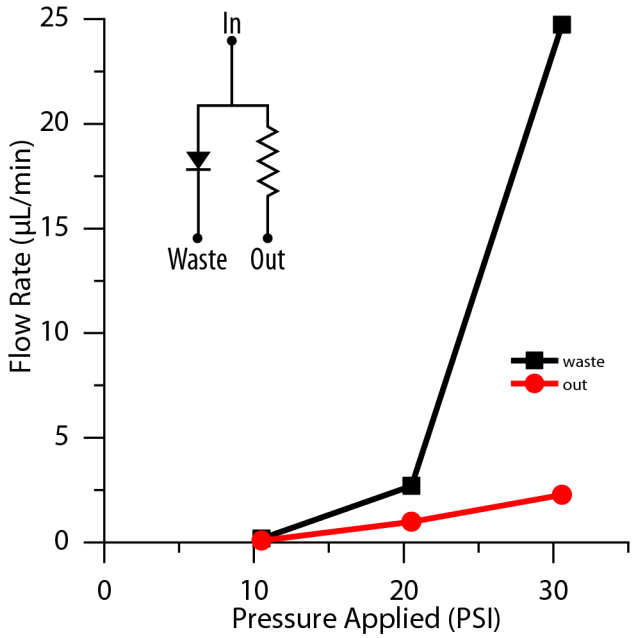

Figure 6.17: **Microfluidic tunable diode flow regulator.** A microfluidic chip containing a forward biased diode and parallel resistor was used to regulate flow in the device. The pressure increases and breaks through the diode causing a release in pressure and regulation of flow rate. Three set points were used in this device 10, 20, 30 PSI showing a correlation between flow rate and BTP.

Flow Regulator and Programmability The next application is a flow regulator, where the diodes fill line is pressurized at 10 PSI, the input is held at a fixed pressure (10,20,30 psi) and the flow rate is measured at the output. The regulator functions similarly to a Zener diode voltage regulator, where the Zener diode breaks down at specific voltage, allowing current to flow to ground, clamping the output voltage. The circuit inset in Figure 6.17, shows the diode needs to be forward biased, and allows flow only once the pressure is above the fill line pressure. At 10 PSI input pressure, little flow is allowed in the device, due to the fill line pressure at 10 PSI. Above the fill line pressure, flow begins where the waste flow rate is considerably higher, in comparison to the regulators output flow rate. This demonstrates the function of the regulator and future designs could test higher pressures and other fill line set points.

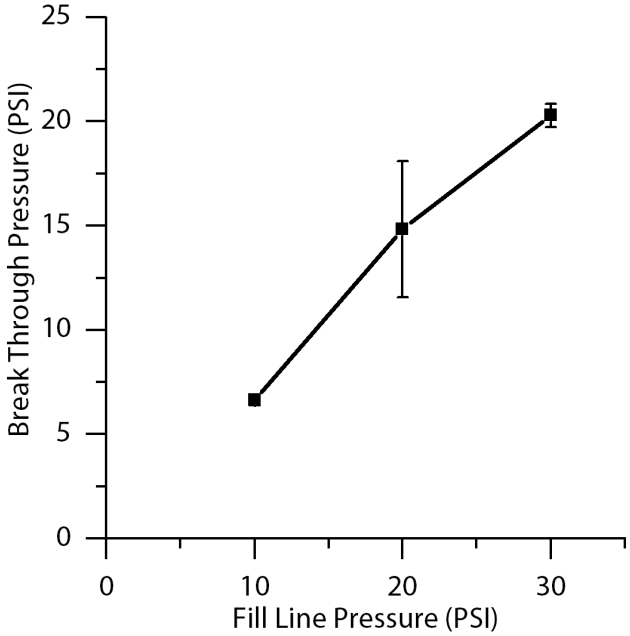

Figure 6.18: **Tunability of single microfluidic chip.** A single microfluidic device containing 3 diodes, each diode set at a different fill line pressure by UV laser curing. Fill line set pressures were 10,20,30 PSI in the same device.

Finally, a single chip containing 3 diodes, the first diode fill line was pressurized and cured by focused laser, the next diode was pressurized at a higher pressure and cured by laser diode, and the last diode was cured at yet another pressure. Average data was compiled for 4

chips and 3 individual pressures (10, 20, 30 PSI) and plotted (Figure 6.18). This experiment demonstrates the possible tuning which can be performed post fabrication of a microfluidic device. This can be applied to multiple components in a single chip and tailoring each devices function while maintaining a single set of wafer masters, or programming each chip to function differently.

Microfluidic Transistor Characterization The previous tunable microfluidic diode work was then applied to Devarju and Ungers original static gain valves or microfluidic transistors, adding the ability to tune them within a single microfluidic device[9]. Fluidic transistor layout is similar to the fluidic diodes in the previous section. The upper layer is the control chamber, middle layer is the flow channel and the lower layer is the NCV or fill layer (Figure 6.19A). At each junction point, the fill layer is pressurized and cured by focused UV laser at only that junction point closing off the flow channel. The remaining photopolymer is still liquid, allowing the pressure to be changed and another NCV structure cured (Figure 6.19B). The static gain valve in our case is modeled after a P-field effect transistor (FET) where the control channel is considered the gate "G", and flow proceeds from the source "S" to the drain "D" (Figure 6.19C).

An array of fluidic transistors was created to characterize the opening behavior of the valves after point curing NCVs. The fluidic mask design incorporates 5 p-FETs in parallel, with resistors and equivalent resistance for all lines leading from transistors to converge on the imaging region (Figure 6.20). This chip is designed as a baseline measurement device. At each NCV, a fill line interacts with a valve, rather than having a communal fill line channel serving all NCVs. A single control channel runs the length of the chip, able to actuate all valves simultaneous. The flow channel inputs have either fluorescence or buffer, creating a stack of laminar flowing bright and dark regions (Figure 6.20). The imaging region is fabricated in SU-8 photoresist and not reflowed, maintaining a uniform depth across its surface for fluorescents imaging. The interconnects between the channel and the imaging

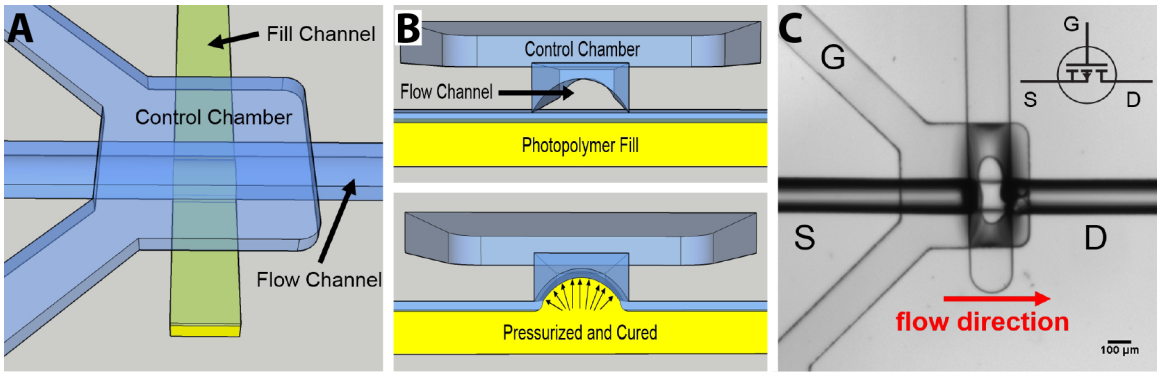

Figure 6.19: **Tunable microfluidic transistor structure.** (A) 3D rendering of the microfluidic transistor, where the upper layer is a control chamber, middle is flow channel and lower is photopolymer fill line. (B) Transistor structure, unfilled versus filled and cured. (C) PDMS device showing the flow channel and connections corresponding to a FET model, where "G" is the gate, "S" source, and "D" drain.

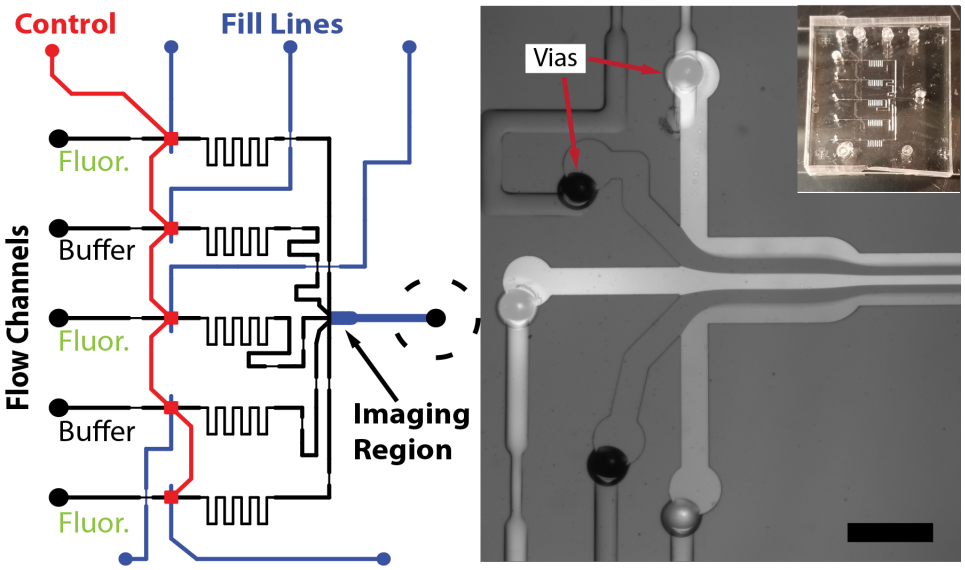

Figure 6.20: **Tunable fluidic transistor device.** The evaluation device consists of 5 separate transistors the control line varies the flow through the devices after the BTP is reached (red). Each transistors BTP can be set separately by individual fill lines (blue). To quantify opening pressures, flow channels are filled with alternating fluorescent dye and buffer, creating bands of laminar flowing fluid at the imaging region. Vias are punched to transition from rounded flow channels to square imaging channel to eliminate path length variability in optical measurements.The completed device is shown upper right. Scale bar 500 μm

region are all laser drilled vias, allowing the transition between round channels and square channels (Figure 6.20) and inset an image of the completed chip.

Characterization was carried out by pressurizing and filling each NCV fill line with between 0-143 kPa and UV curing at those pressures (Figure 6.21A). The flow channels either buffer or Fluorescein are pressurized and held constant at 100 kPa and the control line pressure is ramped from 0-110 kPa (Figure 6.21B). The raw output videos were analyzed to accentuate the laminar bands and images are shown in (Figure 6.21C). Initially, the control line is unpressurized, and all transistors are open and flowing yielding a stack of 5 bands, two dark (buffer) and three light (fluorescein). As the pressure is ramped up, each transistor turns off and in turn its fluidic contribution to the imaging region disappears, and bands are lost which can be seen from left to right in the 8 slices (Figure 6.21C). This data summarizes the basic function of the test chip.

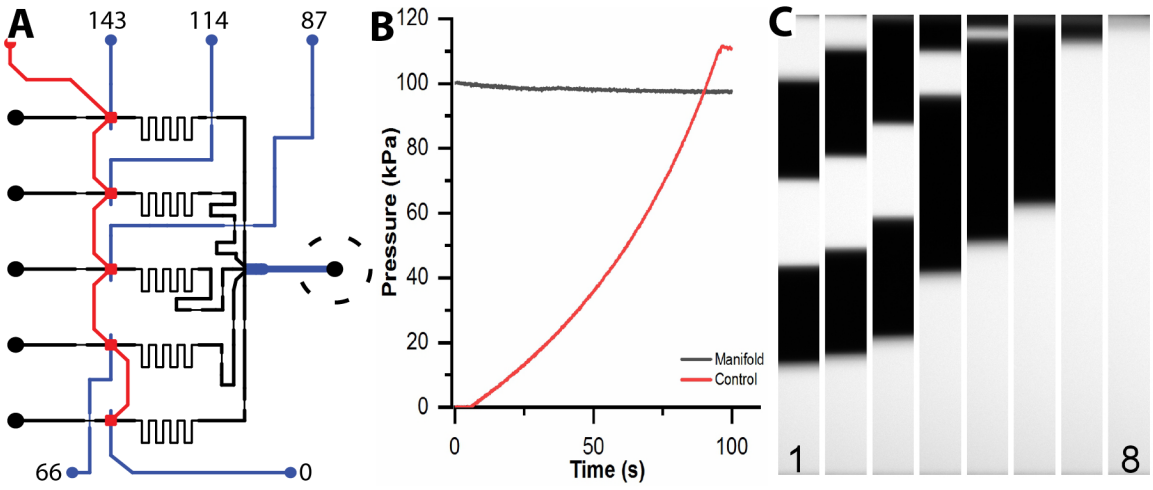

Figure 6.21: **Microfluidic transistor set point and data.** (A) The fluidic transistor fill lines were pressurized to 143, 114, 87, 66, 0 kPa and UV cured. (B) Experimental pressures, the manifold pressure (grey trace) was set to 100 kPa, and the control line was ramped by the syringe pump, while pressure and optical data was collected. (C) Raw optical output data advancing from 1-8 as the control pressure increased, closing off the valves from 143 kPa to 66 kPa.

The switching behavior of electronic devices is typically either digital or analog. Digital switching consists of discrete levels or either on or off states. A continuous signal is considered analog, where no discrete states are present[21]. When the microfluidic transistor

chips control line was scanned from low to high pressure, representing an analog sweep the fluorescence ratio output should follow similarly. A gradual reduction in output of each transistor should be reflected in the output. For the multi-fill line microfluidic chip used in Figure 6.22A, the switching behavior at each junction pressure varied. The high fill-line pressure junction (210 kPa) initially slowly closed off, then abruptly switched, exhibiting initially analog switching then a digital response. As fill-line pressure decreased, analog switching behavior became more pronounced (70 kPa). These behaviors could be useful in device design, potentially allowing data transmission via digital signal or an analog switching depending on how the specific junction is to be used keeping in mind that in an integrated microfluidic device, many junctions could be set individually. This functionality is like programmable logic arrays (field programmable arrays, programmable logic arrays etc.) in which a standard device can be programmed to function in many ways.

After proof-of-concept data showed the usefulness of single device tuning, four other devices were fabricated to further probe the characteristics of a microfluidic transistor (Figure 6.22B). Some device variability is expected in microfluidic fabrication, the multiple devices represented in (Figure 6.22B), demonstrates a much higher fluctuation of response than was expected. For 143 kPa fill line pressure, it is clear the left most trace (red) is not fully opening, in comparison to the 66 kPa trace at the far right (gray), where the valve is not completely closing. At the extreme fill line pressures, the valves do not perform reliably. The middle fill-line pressure curves (114 kPa and 87 kPa) cluster closely indicating high variability in multiple devices. The variation is likely caused by fabrication inconsistencies such as PDMS cure temperature, humidity etc. and further investigations are required to correct these issues.

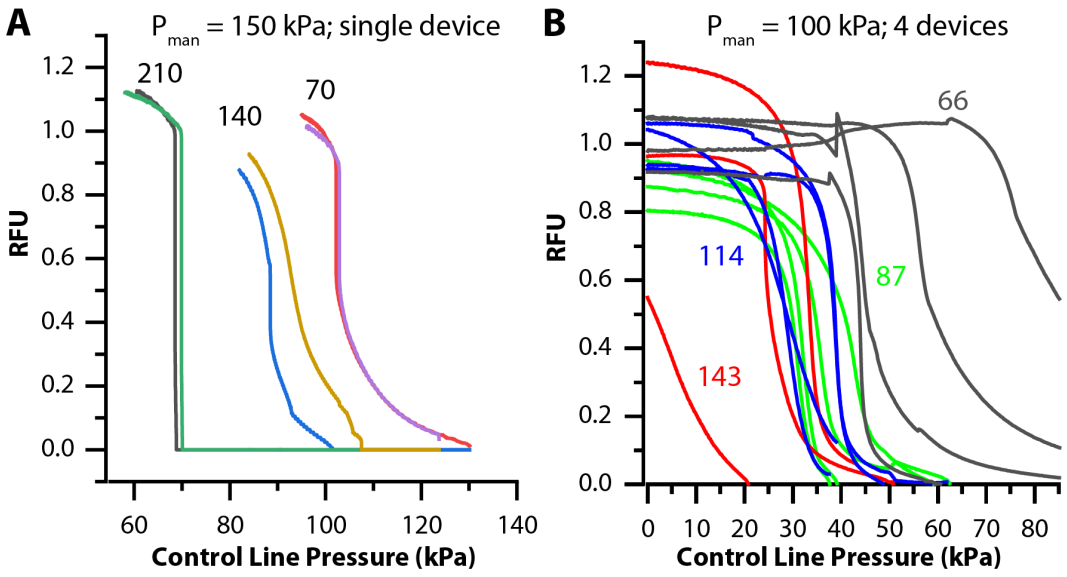

Figure 6.22: **Multiple device fluidic transistor comparison.** (A) Single device characterization, showed similar behavior at 3 control line pressures. (B) Multi-device characterization yielded significant variation from device to device when comparing closing pressure.

6.4 Conclusions

Microfluidic tunable devices which utilize pressurized and cured photopolymer were developed and characterized. Masking studies showed possibilities of incorporating 3D printed devices in fabrication of microfluidic valves, requiring unbonded structures. PDMS masking was abandoned due to low printer resolution and be investigated in the future with higher resolution 3D printing. Tunable microfluidic check valves or microfluidic diodes were created and evaluated using fluorescence microscopy with in-house developed pressure measurement systems. Microfluidic diodes were shown to function similarly as electrical diodes. The microfluidic diodes were applied to a rectifier and pressure regulator. The microfluidic diodes demonstrated single junction programming, where a pressurized NCV could be set at any desired breakthrough pressure, while others on the same device could be programmed separately. Finally, microfluidic transistor structures were created and individually programmed similarly to the microfluidic diodes. Tunable transistors were applied to a unique 5 transistor array proving functionality but requiring optimization in the future work.

References

[1] N. L. Jeon, S. K. Dertinger, D. T. Chiu, I. S. Choi, A. D. Stroock, G. M. Whitesides, *Langmuir* **2000**, *16*, 8311–8316.

[2] D. Kim, N. C. Chesler, D. J. Beebe, *Lab on a Chip* **2006**, *6*, 639–644.

[3] K. W. Oh, K. Lee, B. Ahn, E. P. Furlani, *Lab on a Chip* **2012**, *12*, 515–545.

[4] J. P. Urbanski, W. Thies, C. Rhodes, S. Amarasinghe, T. Thorsen, *Lab on a Chip* **2006**, *6*, 96–104.

[5] B. Mosadegh, T. Bersano-Begey, J. Y. Park, M. A. Burns, S. Takayama, *Lab on a Chip* **2011**, *11*, 2813–2818.

[6] P. N. Duncan, S. Ahrar, E. E. Hui, *Lab on a Chip* **2015**, *15*, 1360–1365.

[7] Q. Zhang, M. Zhang, L. Djeghlaf, J. Bataille, J. Gamby, A. M. Haghiri-Gosnet, A. Pallandre, *Electrophoresis* **2017**, 953–976.

[8] S. J. Kim, R. Yokokawa, S. Takayama, *Lab on a Chip* **2013**, *13*, 1644–1648.

[9] N. S. G. K. Devaraju, M. A. Unger, *Lab on a Chip* **2012**, *12*, 4809–4815.

[10] Q. Yu, J. M. Bauer, J. S. Moore, D. J. Beebe, *Applied Physics Letters* **2001**, *78*, 2589–2591.

[11] N. L. Jeon, D. T. Chiu, C. J. Wargo, H. Wu, I. S. Choi, J. R. Anderson, G. M. Whitesides, *Biomedical Microdevices* **2002**, *4*, 117–121.

[12] E. F. Hasselbrink, T. J. Shepodd, J. E. Rehm, *Analytical Chemistry* **2002**, *74*, 4913–4918.

[13] A. Groisman, S. R. Quake, *Physical Review Letters* **2004**, *92*, 1–4.

[14] B. Mosadegh, C. H. Kuo, Y. C. Tung, Y. S. Torisawa, T. Bersano-Begey, H. Tavana, S. Takayama, *Nature Physics* **2010**, *6*, 433–437.

[15] B. Mosadegh, H. Tavana, S. C. Lesher-Perez, S. Takayama, *Lab on a Chip* **2011**, *11*, 738–742.

[16] C. Duffy, David, J. C. McDonald, O. J. A. Schueller, G. M. Whitesides, *Analytical Chemistry* **1998**, *70*, 4974–4984.

[17] M. Erickstad, E. Gutierrez, A. Groisman, *Lab on a Chip* **2015**, *15*, 57–61.

[18] D. C. Leslie, C. J. Easley, E. Seker, J. M. Karlinsey, M. Utz, M. R. Begley, J. P. Landers, *Nature Physics* **2009**, *5*, 231–235.

[19] L. A. Godwin, A. Auburn, **2013**.

[20] V. Studer, G. Hang, A. Pandolfi, M. Ortiz, W. F. Anderson, S. R. Quake, *Journal of Applied Physics* **2004**, *95*, 393–398.

[21] P. Horowitz, W. Hill, *The Art of Electronics*, 2nd, Cambridge University Press, Cambridge, UK, **1990**, p. 1131.

Chapter 7

Conclusions

7.1 Summary

An electrode polishing robot was created to reduce the hand polishing time of electrodes in a research lab. The effectiveness of the EPBot was tested and the resulting electrode surfaces for either hand polishing or robot polishing were similar, supporting the usefulness of the EPBot. Analytical methods are influenced by temperature and require stabilization to remove temperature influence from these measurements. Peltier based temperature stabilizers were constructed and tested on both optical and electrochemical systems with thermal stability. Two architectures were used, both Arduino for portability and LabVIEW to interface with other programs used in instrumental measurements. The Arduino controller was extended to control a second Peltier element for use in development of gradients across the test surface, leading to faster measurements. The search for higher sensitivity in electrochemical systems drove the development of a differential potentiostat that was applied to nucleic acid systems and shown to increase the apparent sensitivity of the system by analog background correction before measurement. The device was shown to work on several different electrochemical experiments (CA, CV, SWV) and its potential application to other systems is promising.

To accomplish fabrication and characterization of microfluidic devices which are present in chapter 6 of this dissertation, support equipment was constructed. A laser drilling device was tested creating 120 μm diameter holes at varying depths. A UV LED exposure unit was assembled and modified for photolithography of microfluidic devices. Pressure sensors were created in both Arduino and LabVIEW programming environments to be either portable or interface with other systems. A fluorescence microscope was fitted with an

updated high-power LED. The LED provides increased efficiency and a higher brightness light source for imaging microfluidic devices. A PID driven controller was assembled to stabilize temperature within an oven for curing PDMS. Active microfluidic devices require air pressure driven control lines. To actuate these lines solenoid valves (LEE Inc. Valves) are used and require controllers to interface with digital logic devices such as LabVIEW. A controller based on transistor arrays was constructed and assembled for use in our lab's microfluidic device testing. When creating tunable microfluidic devices, a photopolymer is cured in a microfluidic channel. To spot cure photopolymer a UV laser was focused on a fluidic channel and pulsed to cure only that spot in the channel. A UV laser controller based on a microcontroller to allow accurately timed laser pulses. Finally, modern electronic printed circuit board fabrication requires surface mount components. To effectively solder these components to a printed circuit board a reflow soldering oven was assembled.

Microfluidic circuit analogies are convenient models for development of complex microfluidic devices, to perform multiple tasks with pre-programmed function. The function of microfluidic circuits is set by the master wafer fabrication process, requiring a redesign and further photolithographically to change a design. A solution to this tedious process is to create universal components that are tunable. Tunable components were shown in Chapter 6, where the devices were pressurized with a photopolymer and cured under pressure effectively programming the device. A second microfluidic chip from the same master molds could be programmed for different functionality, leading to faster fabrication times and more versatility in the design.

Resistors were initially investigated, showing the ability to set specific values at two different resistors and the flow characteristics varied in roughly the same proportion when measured. Diodes were then created where a breakthrough pressure was set to create diode logic or too modify the flow pressure within the device. Transistors were created previously by Devarjue and Unger[1] and although programmable, were not programmable at a single

junction. Programmability was demonstrated in Chapter 6, where device junctions were independently set and cured. The function of these devices was analyzed by a unique fluoresces detection method.

7.2 Future Work

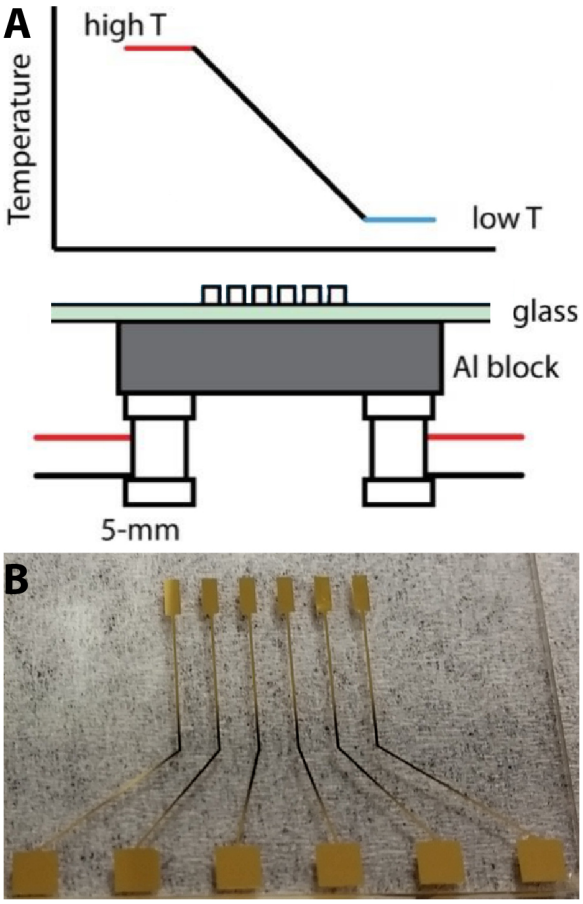

Figure 7.1: **Electrochemistry in thermal gradients.** (A)Electrodes contacting a thermal gradient formed by dual Peltiers. (B) Patterned gold on glass electrodes for thermal gradient experiments.

Impact of Temperature on Biosensors Temperature plays a significant role in detection methodology as was shown in Chapter 3. In that chapter all devices were presented in isothermal conditions, where a temperature was set, stabilized, and a measurement taken then stepped to the next temperature[2, 3]. These studies highlight the importance of temperature and demonstrate its utility in optical and electrochemical measurements. However,

they still require multiple measurements at multiple temperatures, rather than a single read event. One method to overcome this limitation is to generate a thermal gradient over the electrodes/optical surfaces detection area. A thermal gradient would be a continuum of temperatures and therefore contain a large amount of data. Thermal gradient generation is relatively straightforward with Peltier devices (Chapter 5), a depiction of the thermal gradient across a surface is presented in Figure 7.1A, where dual Peltiers are thermally coupled by a metal block, a thermal gradient develops over the surface. If electrodes are placed on that surface they will approximate the thermal gradients temperature, if each electrode is then measured thermally resolved electrochemical data could be captured almost instantly (Figure 7.1B). The challenges to using a thermal gradient in measurements is correlating a temperature with a specific measurement, say in a microfluidic channel. Physical measurements of gradients are possible, and thermally active optical probes are available to characterize a devices thermal response[4–6].

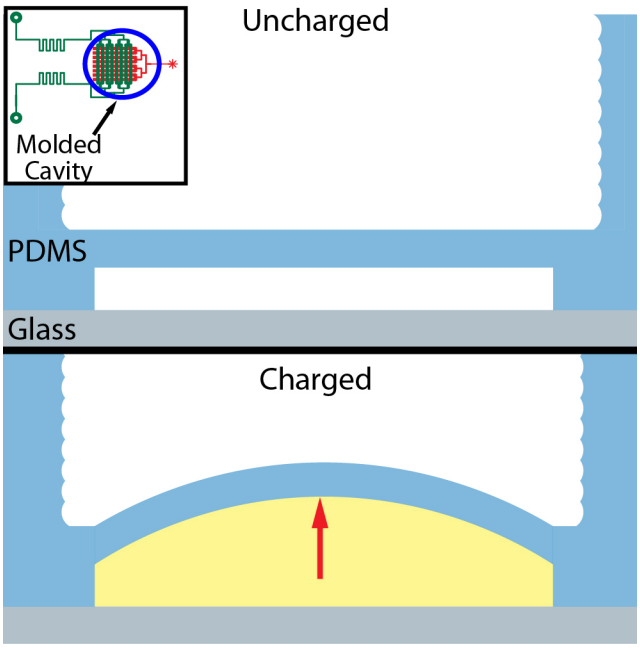

Figure 7.2: **Tunable microfluidic capacitor.** Microfluidic capacitor relies on membrane deflection, a 3D printed mold sets the thickness of membrane varying capacitance. Inset, capacitor chip molding region highlighted.

Microfluidic Circuit Analogy Components The microfluidic circuit analogy is a powerful technique for predicting the function of integrated microfluidic devices (IMD). In Chapter 6, tunable resistors, transistors and diodes were constructed and tested. Electronic components are categorized into either passive such as inductors, resistors or capacitors or active such as transistors, FETS, amplifiers, silicon-controlled rectifiers. A fluidic capacitor is an essential component to create more complex IMD's. Fluidic capacitors function by deflecting a membrane to store pressure in a cavity. To create these structures in microfluidics, 3D printed molds could be used to created cavities above microfluidic structures acting as capacitors. An example mask is shown in Figure 7.2, where a 3D printed mold is placed over the channels creating a molded cavity. The fluidic capacitor would function initially in an uncharged state upper illustration and the lower illustration demonstrates the charged state where the channels membrane is deflected into the molded cavity area above the channel (Figure 7.2). The device consists of two resistors on either side of the capacitors connection and when set, the devices characteristic charging/discharging time could be measured by fluorescence intensity at the channels and modulating the output connection.

Differential Potentiostat Gain Investigation The differential potentiostats function has been shown but it requires further optimization specifically in the gain stages. Recall, that the TIA gain is set 10X lower than the original Dstat values. The measured current which can be 10X larger than the final current range, is subtracted by the differential amplifier then amplified 10X to yield the final current range. The lower amplification at the current to voltage conversion, allows a higher baseline/background to be transmitted to the differential amplifier. The subtraction of the baseline/background current can bring signals into the current range before measurement.

The DiffStat has a total of 3 possible gain stages (Figure 7.3), which if optimized could enhance the selective amplification of the signal over its baseline. The current to voltage converter gain stage is the primary amplification point of the device, with a possible 1×10^8 gain factor in our devices case. The differential instrumentation amplifier can be sourced

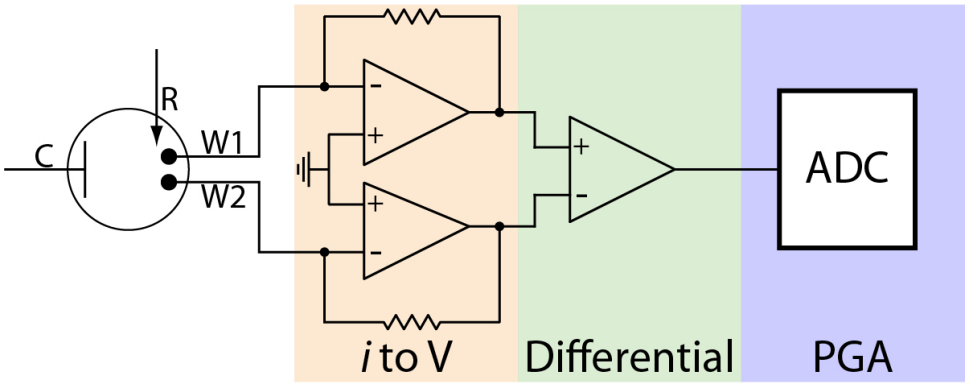

Figure 7.3: **DiffStat gain stages.** DiffStats gain stages are TIA, differential amplifier and ADC.

in gains between 10 and 1×10^4 gain factors, where some devices can switch between gain values. The third stage of amplification could be the analog to digital convert (ADC). Modern ADC's incorporate programmable gain stages, especially in higher resolution devices such as used in the DiffStat(24 bit), with up to 128x gain. Optimization between gain stages for a particular system would be worthy of investigation. Lower gain settings for the current to voltage stage, would provide a larger detection range while still maintaining a higher sensitivity in the final measurement. The gain of the instrumentation amplifier would then increase but the benefit of common mode noise reduction from the differential measurement would potentially reduce noise values when the signal arrives at the ADC. The potential issue with incorporating other gain stages is noise introduction from external components to set the gain at the instrumentation amplifier. A thorough noise budget analysis should be performed to predict if the overall device would benefit from gain stages other than the current to voltage converter. As an initial test the substitution of the AD8422 instrumentation amplifier in place of the MAX4462U, would allow gains between 1 and 1×10^3. This comes with a rewrite of the firmware and interface to produce properly scaled raw data output.

References

[1] N. S. G. K. Devaraju, M. A. Unger, *Lab on a Chip* **2012**, *12*, 4809–4815.

[2] S. Somasundaram, M. D. Holtan, C. J. Easley, *Analytical Chemistry* **2018**, *90*, 3584–3591.

[3] J. Hu, T. Wang, J. Kim, C. Shannon, C. J. Easley, *Journal of the American Chemical Society* **2012**, *134*, 7066–7072.

[4] X. Yang, J. Liu, Y. L. Xie, Y. Wang, H. Ying, Q. Wu, W. Huang, G. Jenkins, *Analyst* **2014**, *139*, 2683–2686.

[5] C. E. Wagner, L. J. Macedo, A. Opdahl, *Analytical Chemistry* **2015**, *87*, 7825–7832.

[6] H. Mao, T. Yang, P. S. Cremer, *Journal of American Chemical Soceity* **2002**, *124*, 4432–4435.

APPENDICES

Appendix A

Electronic Circuits and Associated Code

A.1 EPBot Arduino Code

```
1  //Electrode Polisher
2  //Mark Holtan Oct 2015
3  //based on Plotclock by Johannes Heberlein (www.
       thingiverse.com/thing:248009)
4
5  #include <elapsedMillis.h>
6  #include <Servo.h>
7
8  elapsedMillis timeElapsed; //global time
9
10 #define SERVOFAKTOR 695
11
12 // Zero-position of left and right servo
13 #define SERVOLEFTNULL 2250
14 #define SERVORIGHTNULL 984
15
16 #define SERVOPINLIFT 2
17 #define SERVOPINLEFT 3
18 #define SERVOPINRIGHT 4
19
20 // speed of liftimg arm, higher is slower
21 #define LIFTSPEED 1500
22
23 // length of arms
24 #define L1 35
25 #define L2 55.1
26 #define L3 13.2
27
28
29 // origin points of left and right servo
30 #define O1X 22
31 #define O1Y -25
32 #define O2X 47
33 #define O2Y -25
34
35 int servoLift = 800; //lower number is higher lift
36
37 Servo servo1; // define servos 1 2 3
38 Servo servo2;
39 Servo servo3;
40
41 volatile double lastX = 30;
42 volatile double lastY = 38;
43
44 int last_min = 0;
45 int buttonState1;
46 int buttonState2;
47 int buttonState3;
48 int buttonState4;
49 int buttonState;
50 int timer = 0; //timer function
51 int state3 = 0; //switch from lift height to cleaning
52 float currentTime = 0; //timer functions
53 float timeE = 0; //timer function
54 int led = 11; //pin 11 for led
55
56 void setup()
57 {
58         drawTo(30, 38); //initial starting position.
59
60         servo1.attach(SERVOPINLIFT); // lifting servo
61         servo2.attach(SERVOPINLEFT); // left servo
```

```
62          servo3.attach(SERVOPINRIGHT); // right servo
63          delay(10);
64          pinMode(buttonState1,INPUT); //initial lift servo up
65          pinMode(buttonState2,INPUT); //initial lift servo down
66          pinMode(buttonState3,INPUT); //start cleaning process
67          pinMode(buttonState4,INPUT); //stop cleaning after cycle finnishes
68          pinMode(led,OUTPUT); //led to show running
69
70
71  }
72
73  void loop() {
74          buttonState3 = analogRead(A3); //read start button value is 0 or 1024
75          state3 = buttonState3 + state3; //start button plus previous to keep loop cleaning if button has been pressed
76          if (state3 < 1000){ //if less than 1000 (no button press) then adjust lift otherwise keep cleaning
77                  servo1.attach(SERVOPINLIFT);
78                  servo1.writeMicroseconds(servoLift); // write to servo
79                  buttonState1 = digitalRead(A1); //lift up or down
80                  buttonState2 = digitalRead(A2);
81                  if (buttonState1 == HIGH){ //increase lift if button 1 is high.
82                          servoLift = servoLift + 20;
83                          delay(100);
84                  }
85
86                  if (buttonState2 == HIGH){ //decrease lift value if button2 is high
87                          servoLift = servoLift - 20;
88                          delay(100);
89                  }
90                  state3 = 0;//remain at lift change until button press.
91                  currentTime = timeElapsed; // start timing function over at zero when cleaning starts
92          }
93          //when timer is at 9 stop cleaning, reset variables to zero and sound a tone for 3 seconds.
94          else if (timer >= 10) {
95                  state3 = 0;
96                  timer = 0;
97                  timeElapsed = 0;
98                  tone(12,2500); //pin,frequency
99                  delay(2000);
100                 digitalWrite(led,LOW);
101                 noTone(12);
102                 servoLift = 800; //reset servo lift for new electrode
103                 servo1.attach(SERVOPINLIFT); // reactivate lifting servo, otherwise will not move when run is stopped
104                 servo1.writeMicroseconds(servoLift); // write to servo
105
106         }
107
108         else {
109
110                 timeE = timeElapsed; //timing function to use large numbers
111                 timer = (timeE-currentTime)/1000/60; //calculate time elapsed and generate minutes value.
112                 switch (timer) { //timing function
113                         case 0: digitalWrite(led,HIGH);
114                         case 9:
115                         break;
116                         break;
117                 }
```

```
118                 if (!servo1.attached()) servo1.attach(
                        SERVOPINLIFT);
119                 if (!servo2.attached()) servo2.attach(
                        SERVOPINLEFT);
120                 if (!servo3.attached()) servo3.attach(
                        SERVOPINRIGHT);
121
122                 servo1.writeMicroseconds(servoLift);
123
124                 number(30, 30, 8, 1);//30 = x,y, 8 is
                        number, 1 is squish of figure 8.
                        write figure 8 to the servos.
125
126                 delay(1); //stability
127                 servo1.detach();
128                 servo2.detach();
129                 servo3.detach();
130         }
131
132         buttonState4 = analogRead(A4); //check to see
                if stop button pressed to stop in middle of
                cleaning
133         if (buttonState4 > 1000){timer = 11;} //sets
                timer to greater than time period for
                cleaning, restarts system to initial
                conditions
134 }
135 //---------------
136 // Writing numeral with bx by being the bottom left
        originpoint. Scale 1 equals a 20 mm high font.
137 // The structure follows this principle: move to first
        startpoint ,draw numeral
138 void number(float bx, float by, int num, float scale) {
139
140         switch (num) {
141
142                 case 8:
143
144                 bogenUZS(bx + 5 * scale, by + 15 *
                        scale, 7.5 * scale, 4.7, -1.6, 1.5);
145                 bogenGZS(bx + 5 * scale, by + 5 *
                        scale, 7.5 * scale, -4.7, 2, 1.5);
146                 servoLift;
147                 break;
148
149         }
150 }
151
152 void bogenUZS(float bx, float by, float radius, int start,
        int ende, float sqee) {
153         float inkr = -0.05;
154         float count = 0;
155
156         do {
157                 drawTo(sqee * radius * cos(start +
                        count) + bx,
158                 radius * sin(start + count) + by);
159                 count += inkr;
160         }
161         while ((start + count) > ende);
162
163 }
164
165 void bogenGZS(float bx, float by, float radius, int start,
        int ende, float sqee) {
166         float inkr = 0.05;
167         float count = 0;
168
169         do {
170                 drawTo(sqee * radius * cos(start +
                        count) + bx,
171                 radius * sin(start + count) + by);
172                 count += inkr;
173         }
174         while ((start + count) <= ende);
175 }
176
177
178 void drawTo(double pX, double pY) {
179         double dx, dy, c;
180         int i;
```

```
181
182         // dx dy of new point
183         dx = pX - lastX;
184         dy = pY - lastY;
185         //path lenght in mm, times 4 equals 4 steps per
                mm
186         c = floor(4 * sqrt(dx * dx + dy * dy));
187
188         if (c < 1) c = 1;
189
190         for (i = 0; i <= c; i++) {
191             // draw line point by point
192             set_XY(lastX + (i * dx / c), lastY + (i
                    * dy / c));
193
194         }
195
196         lastX = pX;
197         lastY = pY;
198 }
199
200 double return_angle(double a, double b, double c) {
201         // cosine rule for angle between c and a
202         return acos((a * a + c * c - b * b) / (2 * a * c)
                );
203 }
204
205 void set_XY(double Tx, double Ty)
206 {
207         delay(1);
208         double dx, dy, c, a1, a2, Hx, Hy;
209
210         // calculate triangle between pen, servoLeft and
                arm joint
211         // cartesian dx/dy
212         dx = Tx - O1X;
213         dy = Ty - O1Y;
214
215         // polar lemgth (c) and angle (a1)
216         c = sqrt(dx * dx + dy * dy); //
217         a1 = atan2(dy, dx); //
218         a2 = return_angle(L1, L2, c);
219
220         servo2.writeMicroseconds(floor(((a2 + a1 -
                M_PI) * SERVOFAKTOR) +
                SERVOLEFTNULL));
221
222         // calculate joinr arm point for triangle of the
                right servo arm
223         a2 = return_angle(L2, L1, c);
224         Hx = Tx + L3 * cos((a1 - a2 + 0.621) + M_PI
                ); //36,5 degree
225         Hy = Ty + L3 * sin((a1 - a2 + 0.621) + M_PI)
                ;
226
227         // calculate triangle between pen joint,
                servoRight and arm joint
228         dx = Hx - O2X;
229         dy = Hy - O2Y;
230
231         c = sqrt(dx * dx + dy * dy);
232         a1 = atan2(dy, dx);
233         a2 = return_angle(L1, (L2 - L3), c);
234
235         servo3.writeMicroseconds(floor(((a1 - a2) *
                SERVOFAKTOR) + SERVORIGHTNULL
                ));
236
237 }
```

A.2 Peltier Controller Program

LabVIEW Controller

Arduino Dual Peltier Controller

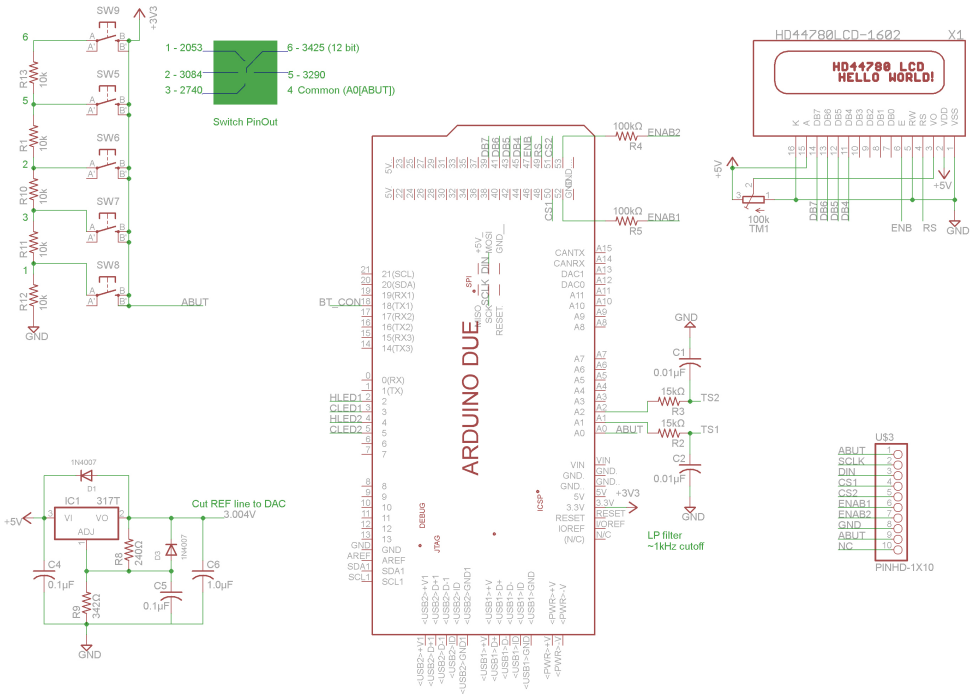

Figure A.1: **Dual Peltier schematic.**

Dual Peltier Controller Arduino Code.

```
1  /*
2  PID Loop for Dual Peltier Temperature Controller
3  Mark D. Holtan
4  18May2017
5  Arduino DUE
6  Changed MAX5144 (14bit DAC) reference to 3.004V,
       connect output to CTLI (direct driver control)
7  DAC output between 0V(Full cooling) to 3V(full heating
       ).
8  Thermistors read by Arduino analog pins 12bit (4096)
9
10 LCD:
11 RS pin to D49 Arduino
12 Enable pin D47 Arduino
13 DB4 pin to D45 Arduino
14 DB5 pin to D43 Arduino
15 DB6 pin to D41 Arduino
16 DB7 pin to D39 Arduino
17 R/W pin to ground
18 V0 pin contrast - center of potentiometer
19 A (backlight) - 5V
20 K (backlight) - GND
21
22 SPI:
```

```
23  DUE SPI Pin on
24  Connector Pins Eval board
25  MOSI - 4 DIN
26  MISO - NA
27  SCK - 3 SCLK
28  SS1 (slave) -D50 CS1
29  SS2 (slave) -D51 CS2
30
31  Bluetooth Serial Connection
32  Serial1 on due
33  TX - D18
34  RX - D19 (not used)
35
36  Buttons:
37  Button - A0
38
39  LEDs:
40  HLED1 - D2
41  CLED1 - D3
42  HLED2 - D4
43  CLED2 - D5
44
45  Thermistor Pins
46  TS1 - A1
47  TS2 - A2
48
49  Enable MAX1978 Pins:
50  D52
51  D53
52
53  Current Pins
54  Cur1 - A3
55  Cur2 - A4
56  */
57
58  #include <LiquidCrystal.h>
59  #include <PID_v1.h>
60  #include <math.h>
61  #include <SPI.h> //SPI for control of the DAC
62
63
64  //DAC constants
65  int DACValue1 = 8190; //center of DAC value for start
66  int DACValue2 = 8190;
67  const int ssPin1 = 50; //Slave Select pin for SPI
        communication
68  const int ssPin2 = 51;
69  const int enableA = 52; //pin to shutdown/enable board
        A
70  const int enableB = 53;
71
72  //ADC read & Smoothing variables
73  const int TS1 = A1; //assign A2 thermistor pins
74  const int TS2 = A2; //assign A1
75
76  //PID Variables
77  double Setpoint1,Input1,Output1; //Define Variables we
        'll be connecting to
78  double Setpoint2,Input2,Output2;
79  //Define the aggressive and conservative Tuning
        Parameters
80  double aggKp=2000, aggKi=1000, aggKd=10;
81  double consKp=500, consKi=50, consKd=100;
82  int tDiff=5; //number of degrees away from setpoint to
        switch tuning parameters.
83
84  //Specify the links and initial tuning parameters
85  PID myPID1(&Input1, &Output1, &Setpoint1, consKp,
        consKi, consKd, DIRECT);
86  PID myPID2(&Input2, &Output2, &Setpoint2, consKp,
        consKi, consKd, DIRECT);
87
88  //Heat/Cool LEDs
89  const int HLED1 = 2; //Red LED
90  const int CLED1 = 3; //Blue LED
91  const int HLED2 = 4;
92  const int CLED2 = 5;
93
94  //Button Pin
95  const int Bpin = A0;
96
97  //Peltiers Max Temperature
```

```
98  float pMax = 85; //Marlow peltiers
99
100 //LCD setup and degree symbol
101 LiquidCrystal lcd(49, 47, 45, 43, 41, 39);
102 byte degree[8] = {B00011, B00011, B00000, B00000,
        B00000, B00000, B00000,}; //degree symbol for
        LCD
103
104 //Current Variables
105 int Iin1 = A3; //Current measurement pins
106 int Iin2 = A4;
107
108 float Cur1;//after calculating current, store in this
        variable
109 float Cur2;
110
111 //------------------------
112 void setup() {
113
114 //Initialize DAC I/O - Must be 1st to set MAX1978
        boards in standby (Enable-Low)
115 pinMode(enableA, OUTPUT); //set enable A&B pin
        output
116 pinMode(enableB, OUTPUT);
117 digitalWrite(enableA, LOW);//set enable pins low
        before ANYTHING else
118 digitalWrite(enableB, LOW);
119 SPI.begin();
120 SPI.setBitOrder(MSBFIRST); //Most Significant Bit
        first for SPI
121 pinMode(ssPin1, OUTPUT); //set slave select pin as
        output only
122 pinMode(ssPin2, OUTPUT);
123 digitalWrite(ssPin1, HIGH); //set SS pin high to
        prevent data
124 digitalWrite(ssPin2, HIGH);
125
126
127 //LCD Start
128 lcd.begin(16, 2); //set LCD to 16X2
129 lcd.clear();
130 lcd.home();
131 lcd.print(" PID Temp Boss");
132 lcd.setCursor(0, 1);
133 lcd.print(" Version 1.0 ");
134 delay(2500);
135 lcd.clear();
136 lcd.createChar(1, degree);
137 lcd.home();
138
139 //Initialize ADC for thermistors
140 pinMode(TS1, INPUT); //initialize thermistor pins as
        analog inputs
141 pinMode(TS2, INPUT);
142
143 //Configure button pin
144 pinMode(Bpin, INPUT); //button pin
145
146 //Current Intputs
147 pinMode(Iin1,INPUT);
148 pinMode(Iin2,INPUT);
149
150 //Initialize Serial Com
151 Serial.begin(9600);
152 Serial1.begin(9600); //start BT serial connection leaving
        standard serial available for troubleshooting
153
154 //Initialize PID loops (set to run)
155 myPID1.SetMode(MANUAL);
156 Setpoint1 = 8192; //Initial starting point
157 Input1 = 8192;
158 Output1 = 8192;
159
160 myPID2.SetMode(MANUAL);
161 Setpoint2 = 8192;
162 Input2 = 8192;
163 Output2 = 8192;
164
165 myPID1.SetOutputLimits(0,16383);
166 myPID2.SetOutputLimits(0,16383);
167
```

```
168  pinMode(HLED1, OUTPUT);//PID output LED
         indicators (Heating/Cooling)
169  pinMode(CLED1, OUTPUT);
170  pinMode(HLED2, OUTPUT);
171  pinMode(CLED2, OUTPUT);
172
173  SYSready();//shut system down until button press to
         activate
174
175  }
176  //--------------------------
177  void loop() {
178  button(); //check for user input
179
180  Input1 = tVal1(); //pass acutal value to calc
         temperature,return temps to PID program
181  Input2 = tVal2();
182
183  highTemp(Input1,Input2); //if temp is above Peltiers
         max temp shutsystem down
184
185  //run pid loop programs, difference from setpoint,
         output value, map to 16bit
186  double gap1 = abs(Setpoint1-Input1); //distance
         setpoint is from acutal value
187  if(gap1<tDiff){myPID1.SetTunings(consKp,consKi,
         consKd);} //if temp diff is less than 5, set
         conservative tunings, otherwise agressive tunings.
188  else {myPID1.SetTunings(aggKp,aggKi,aggKd);}
189
190  double gap2 = abs(Setpoint2-Input2);
191  if(gap2<tDiff){myPID2.SetTunings(consKp,consKi,
         consKd);}
192  else {myPID2.SetTunings(aggKp,aggKi,aggKd);}
193
194  myPID1.Compute(); //calculate PID values
195  delay(1); //stability delays
196  myPID2.Compute(); //calculate PID values
197  delay(1);
198
199  DACValue1 = Output1; //pass PID outputs (64bit - 8
         byte - precision) to DAC - 14bit integer
200  DACValue2 = Output2;
201
202  digitalDACWrite1(DACValue1); //value to write to
         DAC 14 bit out of 16384 (8192) | sets DAC
         between 0-3V where 1.5V is zero input(0V full
         cooling,3V full heating)
203  digitalDACWrite2(DACValue2);
204
205  pidLED1(DACValue1);//send dac value to heat/cool
         LEDs
206  pidLED2(DACValue2);
207
208  Cur1 = iTEC1();//measure current in peltiers
209  Cur2 = iTEC2();
210
211  //Write updated data to LCD screen
212  lcd.setCursor(13, 0);
213  lcd.print(" ");//clear the last 3 characters, as the
         negative sign pushes the characters out
214  lcd.home();
215  lcd.print("#1 S"); //#1 S20.1 A20.1
216  lcd.print(Setpoint1,1);
217  lcd.print(" ");
218  lcd.print("A");
219  lcd.print(Input1,1);
220  //print second line
221  lcd.setCursor(13, 1);
222  lcd.print(" ");//clear the line
223  lcd.setCursor(0, 1);
224  lcd.print("#2 S");
225  lcd.print(Setpoint2,1);
226  lcd.print(" ");
227  lcd.print("A");
228  lcd.print(Input2,1);
229
230
231  //Bluetooth Transmit
232  Serial1.print(Cur1);
233  Serial1.print(",");
```

```
234  Serial1.print(Cur2);
235  Serial1.print(",");
236  Serial1.print(DACValue1);//send data to BT
237  Serial1.print(",");
238  Serial1.print(DACValue2);
239  Serial1.print(",");
240  Serial1.print(Setpoint1);
241  Serial1.print(",");
242  Serial1.print(Input1);
243  Serial1.print(",");
244  Serial1.print(Setpoint2);
245  Serial1.print(",");
246  Serial1.println(Input2);
247  delay(1);
248
249  //PID serial print
250  Serial.print(Input1);
251  Serial.print(",");
252  Serial.print(Output1);
253  Serial.print(",");
254  Serial.print(Input2);
255  Serial.print(",");
256  Serial.println(Output2);
257
258  }
259  //------------------------
260
261  //Write data to DAC(MAX5144) to set temperature
262
263  void digitalDACWrite1(int value) {
264
265  digitalWrite(ssPin1, LOW); //select slave
266  byte byte1 = (value >> 6); //shift right 6 in binary
267  byte byte0 = (value & 0xFC); //0xFC = B11111100 |
         And function to write zeros to the other 6 bits
268  SPI.transfer(byte1); //send first 8 bits MSB first
269  SPI.transfer(byte0); //send 2nd 8 bits, LSB bits are
         dropped to zero
270  digitalWrite(ssPin1, HIGH); //de-select slave
271  }
272
273  void digitalDACWrite2(int value) {
274
275  digitalWrite(ssPin2, LOW); //select slave
276  byte byte1 = (value >> 6); //shift right 6 in binary
277  byte byte0 = (value & 0xFC); //0xFC = B11111100 |
         And function to write zeros to the other 6 bits
278  SPI.transfer(byte1); //send first 8 bits MSB first
279  SPI.transfer(byte0); //send 2nd 8 bits, LSB bits are
         dropped to zero
280  digitalWrite(ssPin2, HIGH); //de-select slave
281  }
282
283  //------------------------
284  float tVal1() {
285  analogReadResolution(12);
286  int result1 = analogRead(TS1); //read thermistor value
287  delay(1);
288  //Temp Calc
289  float volt1 = result1 * (3.3/4095); //convert 12 bit data
         from ADC to voltage with respect to 3.3V/4095
         reference
290  float resist1 = 10000 / ((1.499 / volt1) - 1); //calculate
          thermistor resistance from voltage
291  float lnres1 = log(resist1); //perform natural log on
         resistance instead of doing it twice
292  float tempK1 = 0.001126965682122 +
         (0.000234474477172 * lnres1) +
         (0.000000086313768 * pow(lnres1, 3)) +
         (0.000000000117512193579615 * pow(lnres1, 5));
         //Steinhart-Hart temperature calc for micro
         thermistor
293  float tempC1 = (1 / tempK1) - 273.15; //convert from
         Kelvin to Celcius
294  return tempC1;//pass actual temperature back to void
         loop
295  }
296
297  float tVal2() {
298  analogReadResolution(12);
299  int result2 = analogRead(TS2); //read thermistor value
300  delay(1);
```

```
301  //Temp Calc
302  float volt2 = result2 * (3.3/4095);
303  float resist2 = 10000 / ((1.499 / volt2) - 1);
304  float lnres2 = log(resist2);
305  float tempK2 = 0.001126965682122 +
         (0.000234474477172 * lnres2) +
         (0.000000086313768 * pow(lnres2, 3)) +
         (0.000000000117512193579615 * pow(lnres2, 5));
306  float tempC2 = (1 / tempK2) - 273.15;
307  return tempC2;//pass actual temperature back to void
         loop
308  }
309
310  //-----------------------
311  void SYSready() {
312  digitalWrite(enableA, LOW); //Enable MAX1978
         boards
313  digitalWrite(enableB, LOW);
314  int SYSpin=5000;
315  analogWriteResolution(12);//12bit analog write
316  analogWrite(HLED1, 4095);
317  analogWrite(CLED1, 4095);
318  analogWrite(HLED2, 4095);
319  analogWrite(CLED2, 4095);
320  lcd.clear();
321  lcd.home();
322  lcd.print(" System Ready? ");
323  lcd.setCursor(0, 1);
324  lcd.print(" Push Any Key ");
325  analogReadResolution(12);
326  while(SYSpin>4000) {SYSpin = analogRead(Bpin);
         delay(10);} //waiting for input to move forward
327  initPID(); //call system to initialize the PID loops to
         8192
328  Setpoint1=23; //initial setpoints
329  Setpoint2=23;
330  Input1=23;
331  Input2=23;
332  digitalWrite(enableA, LOW); //Enable MAX1978
         boards
333  digitalWrite(enableB, LOW);
334  analogWrite(HLED1, 0); //LEDs off
335  analogWrite(CLED1, 0);
336  analogWrite(HLED2, 0);
337  analogWrite(CLED2, 0);
338  lcd.clear();
339  delay(1); //stability
340  }
341
342  void shutDN () { //if button is pushed, the system shuts
         down, puts MAX1978 into shutdown mode
343  int SDpin = 5000;
344  digitalWrite(enableA, LOW);//set enable pins low at
         startup
345  digitalWrite(enableB, LOW);
346  lcd.clear();
347  lcd.home();
348  lcd.print("System Shutdown");
349  lcd.setCursor(0, 1);
350  lcd.print("This is NOT Good");
351  analogWriteResolution(12);
352  analogWrite(HLED1,4095);
353  analogWrite(CLED1,4095);
354  analogWrite(HLED2,4095);
355  analogWrite(CLED2,4095);
356  delay(5000);
357  lcd.clear();
358  lcd.home();
359  lcd.print("Over Temp?");
360  lcd.setCursor(0, 1);
361  lcd.print("Button Pressed?");
362  analogWriteResolution(12);
363  analogWrite(HLED1,0);
364  analogWrite(CLED1,0);
365  analogWrite(HLED2,0);
366  analogWrite(CLED2,0);
367  delay(5000);
368  lcd.clear();
369  lcd.home();
370  lcd.print("Press Any Button");
371  lcd.setCursor(0, 1);
372  lcd.print(" To Resume ");
```

```
analogReadResolution(12);
while(SDpin > 4000) {SDpin = analogRead(Bpin);delay(10);} //waiting for input to move forward, typical value no inputs is ~1000
delay(500);
//Write default setpoints to all devices
Setpoint1 = 23; //Initial starting point
Input1 = 23;
DACValue1 = 8192; //Set back to 25 deg C to
Setpoint2 = 23; //Initial starting point
Input2 = 23;
DACValue2 = 8192; //Set back to 25 deg C to
digitalDACWrite1(DACValue1);//write default values to dac before restarting loop
digitalDACWrite2(DACValue2);
digitalWrite(enableA, HIGH); //Turn on system again
digitalWrite(enableB, HIGH);
lcd.clear();
delay(10);
}

//----------------------

void button() {
analogReadResolution(12);
int pin = analogRead(Bpin);
delay(1);//delay for Aread stability

if (pin > 4000) {}
else
if (pin >2030 && pin < 2070){ //up button incraese
double dUP1 = Setpoint1 + 0.1;
Setpoint1 = dUP1;
}
else
if (pin >2700 && pin < 2850){ //down button decrease
double dDN1 = Setpoint1 - 0.1;
Setpoint1 = dDN1;
}
else
if (pin >3070 && pin < 3100){ //left button increase
double dUP2 = Setpoint2 + 0.1;
Setpoint2 = dUP2;
}
else
if (pin >3270 && pin < 3300){ //right button decrease
double dDN2 = Setpoint2 - 0.1;
Setpoint2 = dDN2;
}
else
if (pin >3400 && pin < 3500){ //Shutdown System
shutDN();
}
}

//----------------------

void pidLED1(int dacNum1){//Red and Blue LED's inputs remapped from 16bit to 12bit PWM output
if(dacNum1 > 8192){ //Blue LED off, red on mapped to full range
int EITBit1 = map(dacNum1,8191,16383,0,4095);
analogWriteResolution(12);
analogWrite(CLED1,0);
analogWrite(HLED1,EITBit1);}
else{
if(dacNum1 < 8192){ //Red LED off, blue mapped to full range
int EITBit1 = map(dacNum1,8192,0,0,4095);
analogWriteResolution(12);
analogWrite(HLED1,0);
analogWrite(CLED1,EITBit1);}
}
}

void pidLED2(int dacNum2){
if(dacNum2 > 8192){
int EITBit2 = map(dacNum2,8191,16383,0,4095);
analogWriteResolution(12);
analogWrite(CLED2,0);
analogWrite(HLED2,EITBit2);}
else{
```

```
449 if(dacNum2 < 8192){
450 int EITBit2 = map(dacNum2,8192,0,0,4095);
451 analogWriteResolution(12);
452 analogWrite(HLED2,0);
453 analogWrite(CLED2,EITBit2);}
454 }
455 }
456
457 void highTemp(float T1,float T2){
458
459 if(T1 > pMax){shutDN();}
460 if(T2 > pMax){shutDN();}
461 }
462
463 //----------------------
464
465
466 float iTEC1 () {
467 analogReadResolution(12);
468 int Vcur1 = analogRead(Iin1);
469 delay(10);
470 float VC1 = Vcur1 * (3.3 / 4095.0); //scale voltage from
      circuit
471 float Vitec1 = (VC1 - 1.499) / (8 * 0.068); //current
      calculation formula from datasheet. 1.499=
      reference voltage, 0.068 ohms = current resistor in
      circuit voltage swings positive/negative
472 return Vitec1;//send value back to loop
473 }
474
475 float iTEC2 () {
476 analogReadResolution(12);
477 int Vcur2 = analogRead(Iin2);
478 delay(10);
479 float VC2 = Vcur2 * (3.3 / 4095.0); //scale voltage from
      circuit
480 float Vitec2 = (VC2 - 1.499) / (8 * 0.068); //current
      calculation formula from datasheet. 1.499=
      reference voltage, 0.068 ohms = current resistor in
      circuit voltage swings positive/negative
481 return Vitec2;
482 }
483
484 //---------------
485 float initPID(){ //Idea is to run the PID loop until it
      shows an output close too the original setpoint
      without sending data to the peltiers.
486 myPID1.SetMode(MANUAL);
487 myPID2.SetMode(MANUAL);
488 Setpoint1=8190;
489 Setpoint2=8190;
490 Input1=8190;
491 Input2=8190;
492 Output1=8190;
493 Output2=8190;
494 myPID1.SetMode(AUTOMATIC);
495 myPID2.SetMode(AUTOMATIC);
496 }
497
498
499
500
501 [/code]
```

A.3 DiffStat Schematic

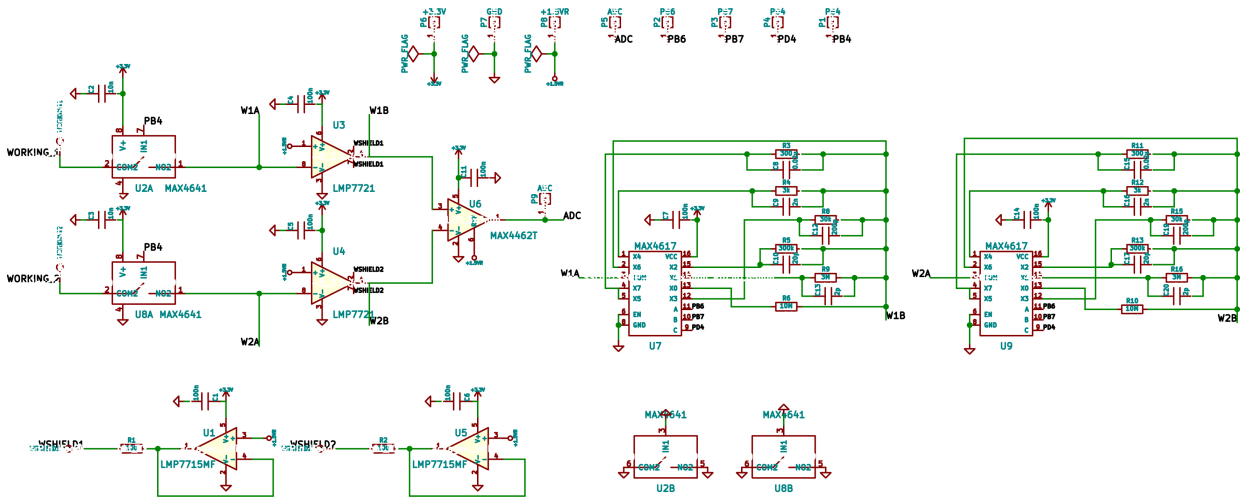

Figure A.2: **Differential potentiostat schematic.**

A.4 CO_2 Laser Electronics

CO_2 laser controller Arduino code.

```
/*
CO2 Laser Control
Mark Holtan
Added 1−50 ms in 1 ms increments

TH − TTL High = +5 volts will turn psu on , 0v = Off
TL − TTL Low = Connecting this to ground will turn
    the laser on ,
G − Ground
IN − Signal In − Analog 0−5 volts − 20kHz PWM
    minimum
5V − 5 volts DC

Pin assignments:
LCD:
RS pin to D9 Arduino
Enable pin D8 Arduino
D4 pin to D4 Arduino
D5 pin to D3 Arduino
D6 pin to D2 Arduino
D7 pin to D1 Arduino
R/W pin to ground
V0 pin contrast − center of potentiometer
A (backlight) − 5V
K (backlight) − GND

Indicator:
Laser On − A3

Buttons:
Buttons − A5
Fire − D11

PWM Pin − D10
FireEnable − D5 Writes to the TTL− line to deactivate
    /inactivate the system
Door interlock − D6 − with 10k pull down resistor
Air Solenoid − D12 − sends data to 1K resistor,too
    IRF520 Nchannel mosfet, to control ˜600mA
    solenoid at 12 volts.
```

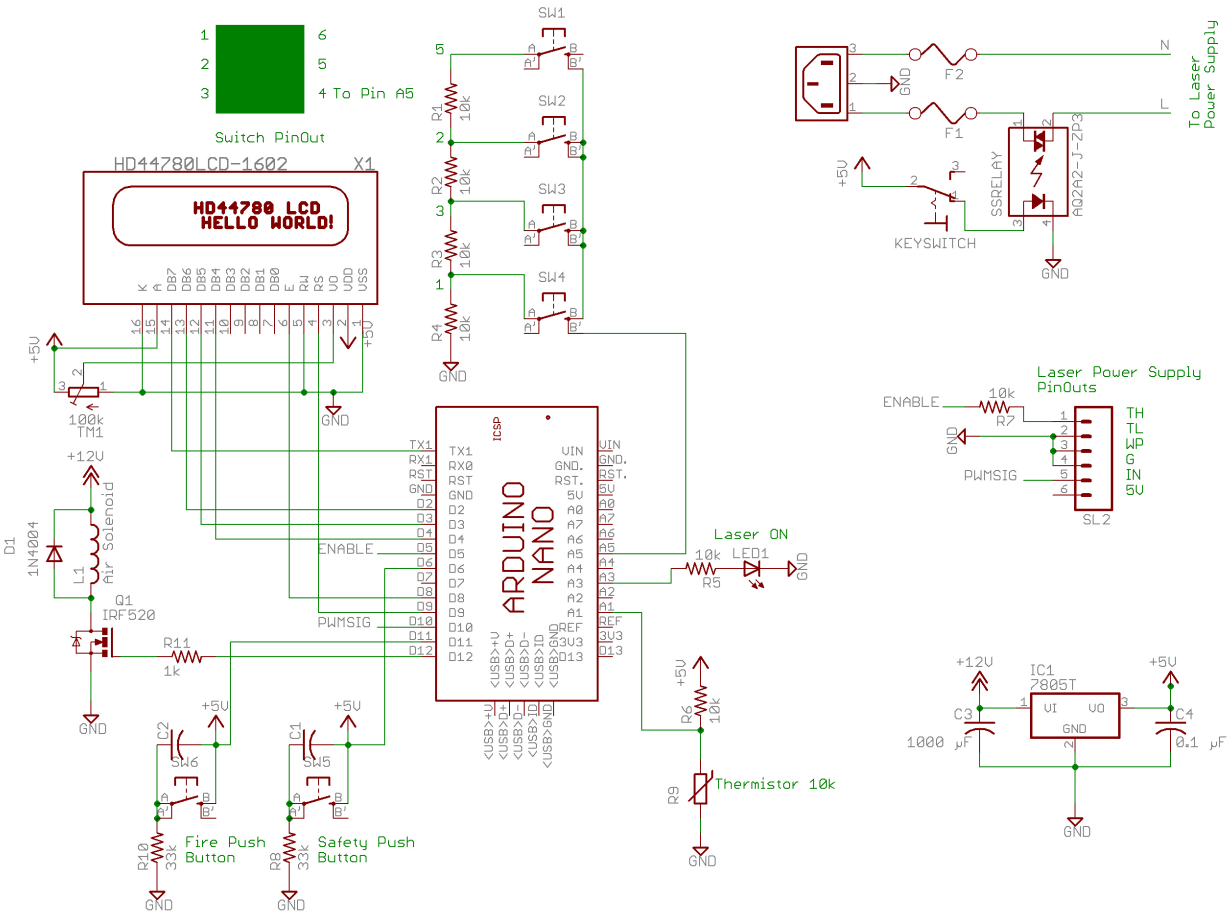

Figure A.3: **CO_2 Laser Schematic.**

```
36
37  Sensors:
38  A1 - Thermistor1
39  D7 - Flow sensor - produces square wave signal ~2volts
        (at 12 volt input) based on flow speed - pump
        produced ~14Hz signal on bench (71428 us length)
40  removed from sketch due to interupt timing issues.
        Consider replacing with frequency to voltage
        converter KA331 or LM2907
41  */
42
43  #include <math.h>
44  #include <LiquidCrystal.h>
45  #include <Wire.h>
46  #include <PWM.h>
47
48
49  LiquidCrystal lcd(9, 8, 4, 3, 2, 1, true, POSITIVE);//
        setup pins for LCD.
50  byte degree[8] = {B00011, B00011, B00000, B00000,
        B00000, B00000, B00000,}; //degree symbol for
        LCD
51
52  int pulseWM = 10; //duty cycle pin, pwm
53  int32_t frequency = 20000; //pwm frequency (Hz)
54
55  int eSTOP; //emergency stop
56  int dintlock = 6; //interlock status
57
58  int dutycycle = 36; //duty cycle set to 10% (0-255
        values)
59  int duration = 10; //set duration to 0.1 second intially
```

```
60
61  int firePin = 11; //fire pin
62  int fireLED = A3;//fire led pin
63  float dcPer; //duty cycle percentage
64  int FP = LOW; //firepin initially set to zero
65  int fenablePin = 5; //fire enable pin
66
67  const int numReadingsT = 20; //set to 20 due to noise?
        in therm data.
68  int readingsT[numReadingsT];// the readings from the
        analog input
69  int readIndexT = 0; // the index of the current reading
70  int totalT = 0; // the running total
71  int averageT = 0; // the average
72
73
74  //int flowPin = 7; //flow sensor data on digital Pin7-
        removed
75
76  int SoleNd = 12; //digital pin 12 for solenoid
77
78
79  void setup() {
80
81  InitTimersSafe(); //initialize all timers except for 0, to
        save time keeping functions (PWM function)
82  bool success = SetPinFrequencySafe(pulseWM,frequency
        ); //set frequency for pwm pin, then test to see if
        pin responds
83  //with frequency by setting LED on board high
84  if(success) {
85  pinMode(13, OUTPUT);
86  digitalWrite(13,HIGH);
87  delay(1000);
88  digitalWrite(13,LOW);
89  }
90
91  /* Set I/O pins */
92  //pinMode(eSTOP, INPUT); //emergency stop pin
93  pinMode(A5, INPUT_PULLUP); //button pin set with
        pullup resistor
94  pinMode(firePin, INPUT); //firepin setup
95  pinMode(fireLED, OUTPUT);
96  pinMode(fenablePin,OUTPUT);
97  pinMode(dintlock,INPUT);
98  pinMode(SoleNd,OUTPUT);
99
100 /*Temperature Probe Smoothing due to noise*/
101 for (int thisReading = 0; thisReading < numReadingsT;
        thisReading++)
102 readingsT[thisReading] = 0;
103
104 /*Solenoid Set Low*/
105 digitalWrite(SoleNd,LOW);
106
107 /* PWM setup */
108 digitalWrite(fenablePin,HIGH); //set pin high, enabled
        when low
109 pwmWrite(pulseWM,0);//turn off the system //set pwm
        at zero otherwise laser powers up and burns things
110 delay(50);
111
112 /* LCD start */
113
114 lcd.begin(20, 4); //set LCD to 20X4
115 lcd.createChar(1, degree);
116 lcd.clear();
117 lcd.print("CO2 Laser Controller");
118 lcd.setCursor(0,1);
119 lcd.print(" Version 2.5 ");
120 delay(2000);
121 lcd.clear();
122 delay(10);
123
124 /*Airflow Check*/
125 lcd.print(" Shield Gas Check ");
126 delay(500);
127 digitalWrite(SoleNd,HIGH);
128 delay(750);
129 digitalWrite(SoleNd,LOW);
130 delay(250);
131 lcd.clear();
```

```
132  lcd.print("Shield Gas Present? ");
133  lcd.setCursor(0,1);
134  lcd.print(" Press Fire Button ");
135  lcd.setCursor(0,2);
136  lcd.print(" To Continue ");
137  while(digitalRead(firePin) == LOW){delay(10);}
138  lcd.clear();
139  digitalWrite(SoleNd,LOW);//ensure air is off
140  delay(250);//delayed to remove error from switch still in
         on state
141
142  }
143  void loop() {
144
145
146  // Button Read
147  int pin = analogRead(A5);
148  if (pin > 1000) {}
149  else
150  if (pin >200 && pin < 250){ //up button increase
151  int dcUP = dutycycle + 5;//move up or down by 5/255
         = 2%
152  if (dcUP >= 255) {dcUP = 255;} //nothing above 100%
         duty cycle
153  dutycycle = dcUP;
154  delay(50);
155  }
156  else
157  if (pin >350 && pin < 400){ //down button decrease
158  int dcDN = dutycycle - 5;//move up or down by 5/255
         = 2%
159  if (dcDN <= 25 ) {dcDN = 25;} //nothing lower than
         10% duty cycle, damage to the laser may occur at
         this setting also
160  dutycycle = dcDN;
161  delay(50);
162  }
163  else
164  if (pin >440 && pin < 480){ //left button increase
165  int durUP = duration;
166  if (durUP < 50) {durUP = duration + 1;} else durUP =
         duration + 10; //when less than 10 ms, decrease
         by 1 ms
167  duration = durUP;
168  delay(50);
169  }
170  else
171  if (pin >510 && pin < 550){ //right button decrease
172  int durDN = duration;
173  if (durDN <= 50) {durDN = duration - 1;} else durDN
         = duration - 10; //decrease increment by 1ms
         instead of 10ms.
174  if (durDN <= 1) {durDN = 1;} //We can't go BACK
         TO THE FUTURE!
175  duration = durDN;
176  delay(50);
177  }
178  FP = digitalRead(firePin);
179  if (FP == HIGH) {fire(dutycycle,duration);} //check to
         see if fire button pushed, fire)
180
181  // Thermistor Program
182  int thermVal1 = analogRead(A1);//read voltage of
         THERM connection
183  float volt1 = thermVal1 * (5.0 / 1023.0); //convert 10
         bit data from ADC to voltage with respect to 1.499
          v reference
184  float resist21 = 10000 / ((5.0 / volt1) - 1); //calculate
         thermistor resistance from voltage
185  float lnres21 = log(resist21); //perform natural log on
         resistance instead of doing it twice
186  float tempK1 = 0.001126965682122 +
         (0.000234474477172 * lnres21) +
         (0.000000086313768 * pow(lnres21, 3)) +
         (0.000000000117512193579615 * pow(lnres21, 5));
         //Steinhart-Hart temperature calc for thermistor
         USP12837
187  float tempC1 = (1 / tempK1) - 273.15;
188  if (tempC1 > 60) {emSTOP(1020);} //if temperature is
         above 60 C, then shut system down
189
```

```
/*Temp smoothing*/
totalT = totalT - readingsT[readIndexT];
readingsT[readIndexT] = tempC1;// read data to add
totalT = totalT + readingsT[readIndexT];// add the reading to the total
readIndexT = readIndexT + 1;// advance to the next position in the array
if (readIndexT >= numReadingsT)// if we're at the end of the array...
readIndexT = 0;// ...wrap around to the beginning
averageT = totalT / numReadingsT;// calculate the average


float cycle = dutycycle; //converts integer to decimal to display on LCD
dcPer = (cycle/255)*100; //calc duty cycle percentage
float rndcyc = double round(dcPer); //rounds decimal calculation to nearest integer


lcd.home();
lcd.print("Intensity: ");
lcd.print(rndcyc);
lcd.print("%");
lcd.setCursor(0, 1);
lcd.print("Pulse Time: ");
lcd.print(duration);
lcd.print(" ms");
lcd.setCursor(0, 2);
lcd.print("Mirror Temp: ");
lcd.print(averageT);
lcd.write(byte(1));
lcd.print("C");
delay(100);
lcd.home();
lcd.setCursor(12,0);
lcd.print(" ");//clears extra decimal places from display
lcd.setCursor(12,1);
lcd.print(" ");//clears extra decimal places from display

}

//-----------------------

void fire(int dutycycle,int duration) {
if (digitalRead(dintlock) == LOW ) {emSTOP(500); return;} //if interlock is open go to emergency stop ,
digitalWrite(SoleNd,HIGH);//turn air on
delay(100);
for(int x = 3; x > 0; x--){ //count down before firing)
lcd.clear();
lcd.setCursor(10,1);
lcd.print(x);
delay(500);
}
if (digitalRead(dintlock) == LOW ) {emSTOP(500); return;} //Check door interlock again
digitalWrite(fenablePin,LOW);//enable fire
lcd.clear();
lcd.home();
lcd.print("******************");
lcd.setCursor(0,1);
lcd.print("!!!!!!LASER ON!!!!!!");
lcd.setCursor(0,2);
lcd.print("******************");
analogWrite(fireLED,1000);//turn on fireLED
pwmWrite(pulseWM,dutycycle); //set pin at dutycycle value.
delay(duration); //run for specific amount of time.
pwmWrite(pulseWM,0);//set PWM to zero value
analogWrite(fireLED,0);//turn off fireLED
digitalWrite(fenablePin,HIGH); //disable fire system
digitalWrite(SoleNd,LOW);
delay(100);
lcd.clear();
lcd.begin(20, 4); //LCD locks up after certain number of pulses, reinitializeing LCD after firing.
lcd.clear();
}
```

```
261
262 //----------------------
263
264 void emSTOP (int eSTOP) {
265 digitalWrite(SoleNd,LOW);//turn off air
266 delay(100);
267 if (eSTOP > 1000) {//laser is over 60 deg C should be
        cooled before moving forward
268 lcd.clear();
269 lcd.print("XXXXXXXXXXXXXXXXXXXX");
270 lcd.setCursor(0, 1);
271 lcd.print("--System Suspended--");
272 lcd.setCursor(0, 2);
273 lcd.print("XXXXXXXXXXXXXXXXXXXX");
274 lcd.setCursor(0, 3);
275 lcd.print("XXXXXXXXXXXXXXXXXXXX");
276 delay(5000);
277 lcd.clear();
278 lcd.setCursor(0,1);
279 lcd.print("Laser Tube Temp");
280 lcd.setCursor(0, 2);
281 lcd.print(" Above 60 Deg C ");
282 lcd.setCursor(0, 3);
283 lcd.print(" Check Water Flow ");
284 delay(10000);
285 lcd.clear();
286 }
287 else // door interlock open
288 lcd.clear();
289 lcd.home();
290 lcd.print(" Check Keyswitch ");
291 lcd.setCursor(0,1);
292 lcd.print(" or ");
293 lcd.setCursor(0,2);
294 lcd.print(" Hold PushButton ");
295 delay(3000);
296 lcd.clear();
297
298 }
299 [/code]
```

A.5 UV LED system circuit and code

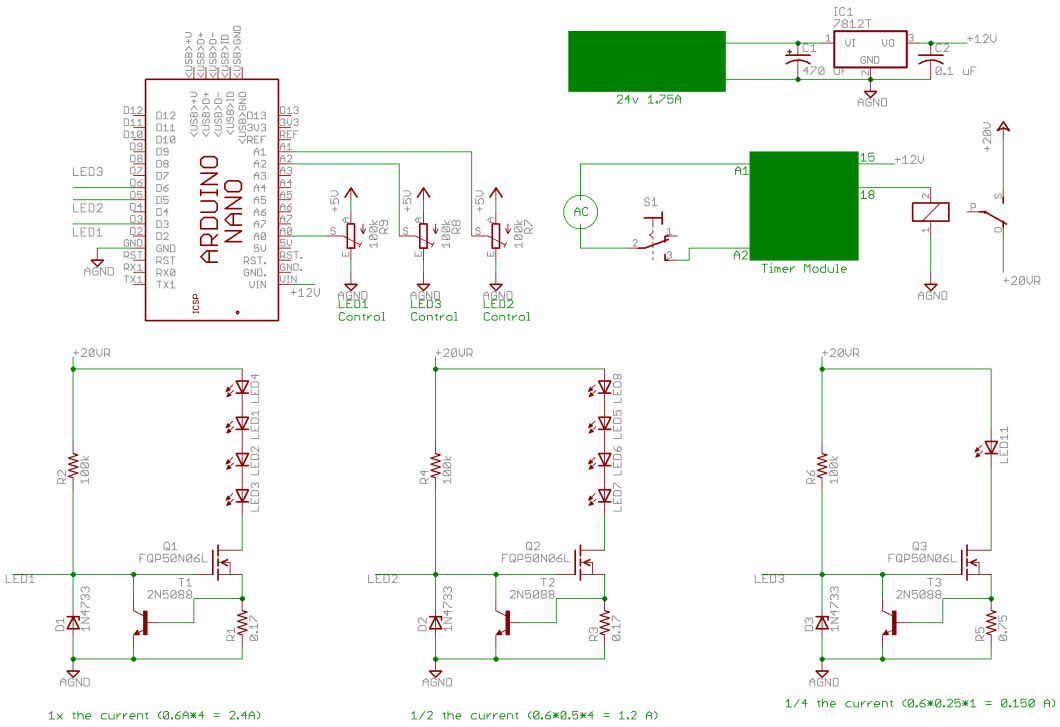

Figure A.4: UV LED array schematic

```
[code]

//dimmingcircuitV1

int inputPin1 = A0; // set input pin for the
    potentiometer
int inputValue1 = 0; // potentiometer input variable
int ledPin1 = 3;
int inputPin2 = A1;
int inputValue2 = 0;
int ledPin2 = 5;
int inputPin3 = A2;
int inputValue3 = 0;
int ledPin3 = 6;

void setup() {
// declare the ledPins as OUTPUTs:
pinMode(ledPin1, OUTPUT);
pinMode(ledPin2, OUTPUT);
pinMode(ledPin3, OUTPUT);
}

void loop() {
// read the value from the potentiometers:
inputValue1 = analogRead(inputPin1);
inputValue2 = analogRead(inputPin2);
inputValue3 = analogRead(inputPin3);

// send the square wave signal to the LEDs:
analogWrite(ledPin1, inputValue1/4);
analogWrite(ledPin2, inputValue2/4);
analogWrite(ledPin3, inputValue3/4);
}
[/code]
```

A.6 Laser Diode Controller Circuit

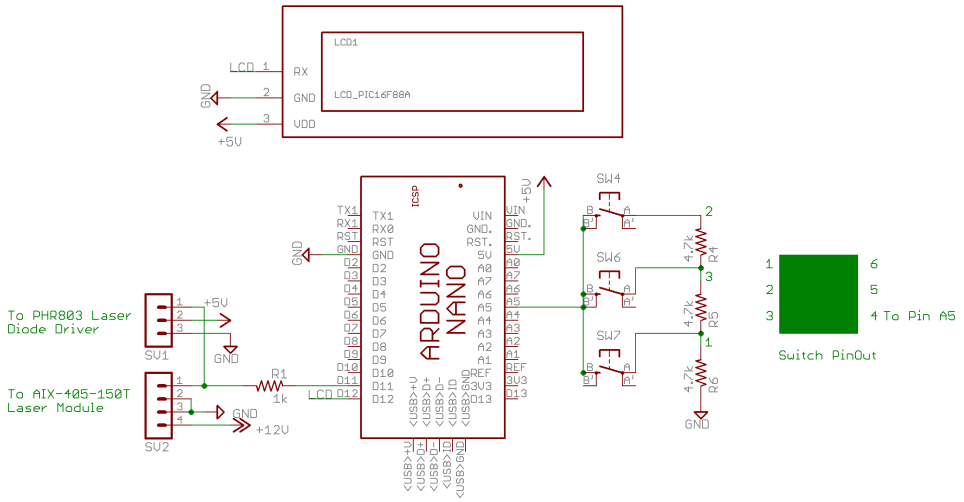

Figure A.5: Laser diode controller circuit.

```
1  [code]
2  /*
3
4  405nm Laser Controller
5  Mark Holtan
6  16mar16
7  Serial Connection - D12
8  TTL Output - D11
9  */
10
11 #include <serLCD.h>
12 #include <SoftwareSerial.h>
13
14 serLCD lcd(12); //LCD digital data pin
15
16 int duration = 10; //set duration to 0.1 second intially
17
18 int firePin = 11; //fire pin
19
20
21 const int numReadings = 20; //set to 20 due to noise?
       in therm data.
22 int readings[numReadings]; // the readings from the
       analog input
23 int readIndex = 0; // the index of the current reading
24 int total = 0; // the running total
25 int average = 0; // the average
26
27 void setup() {
28
29 /* Set I/O pins */
30 pinMode(A5, INPUT_PULLUP); //button pin set with
       pullup resistor
31 pinMode(firePin, OUTPUT); //firepin setup
32 digitalWrite(firePin,LOW);//set firepin off
33
34 /* LCD start */
35 lcd.setType(3);//set to 16X2
36 lcd.clear();
37 lcd.print("405nm Laser V1.0");
38 delay(3000);
39 lcd.clear();
40 }
41
42 void loop() {
43
44
45 // Button Read
```

```
46  int pin = analogRead(A5);
47  if (pin > 1000) {}
48  else
49  if (pin >200 && pin < 273){ //up button incraese
50  int dUP = duration;
51  if (dUP <10) {dUP = duration + 1;}else dUP =
        duration + 10;
52  duration = dUP;
53  delay(50);
54  }
55  else
56  if (pin >100 && pin < 150){ //down button decrease
57  int dDN = duration;
58  if(dDN <= 10) {dDN = duration - 1;} else dDN =
        duration - 10;
59  if (dDN <= 1 ) {dDN = 1;} //nothing lower than 1ms
60  duration = dDN;
61  delay(50);
62  }
63  else
64  if (pin >280 && pin < 290 ){ //Press button to fire
65  fire(duration);
66  delay(50);
67  }
68
69  lcd.clear();
70  lcd.print("Pulse Time: ");
71  lcd.setCursor(1,0);
72  lcd.print(duration);
73  delay(100);
74
75
76  }
77
78  //------------------------
79
80  void fire(int duration) {
81  for(int x = 3; x > 0; x--){ //count down before firing)
82  lcd.clear();
83  lcd.print(" ");
84  lcd.print(x);
85  delay(1000);
86  }
87  if (analogRead(A5) >200 && analogRead(A5) < 275 ){
        return;}//fire button pressed, aborts fire.
88  digitalWrite(firePin,HIGH);//laser on
89  lcd.clear();
90  lcd.home();
91  lcd.print("******************");
92  lcd.setCursor(0,1);
93  lcd.print(" Fire ");
94  delay(duration); //run for specific amount of time.
95  digitalWrite(firePin,LOW); //laser off
96  lcd.clear();
97  }
98
99  //--------------------
100
101 [/code]
```

A.7 Fluidic Valve Controller Circuit

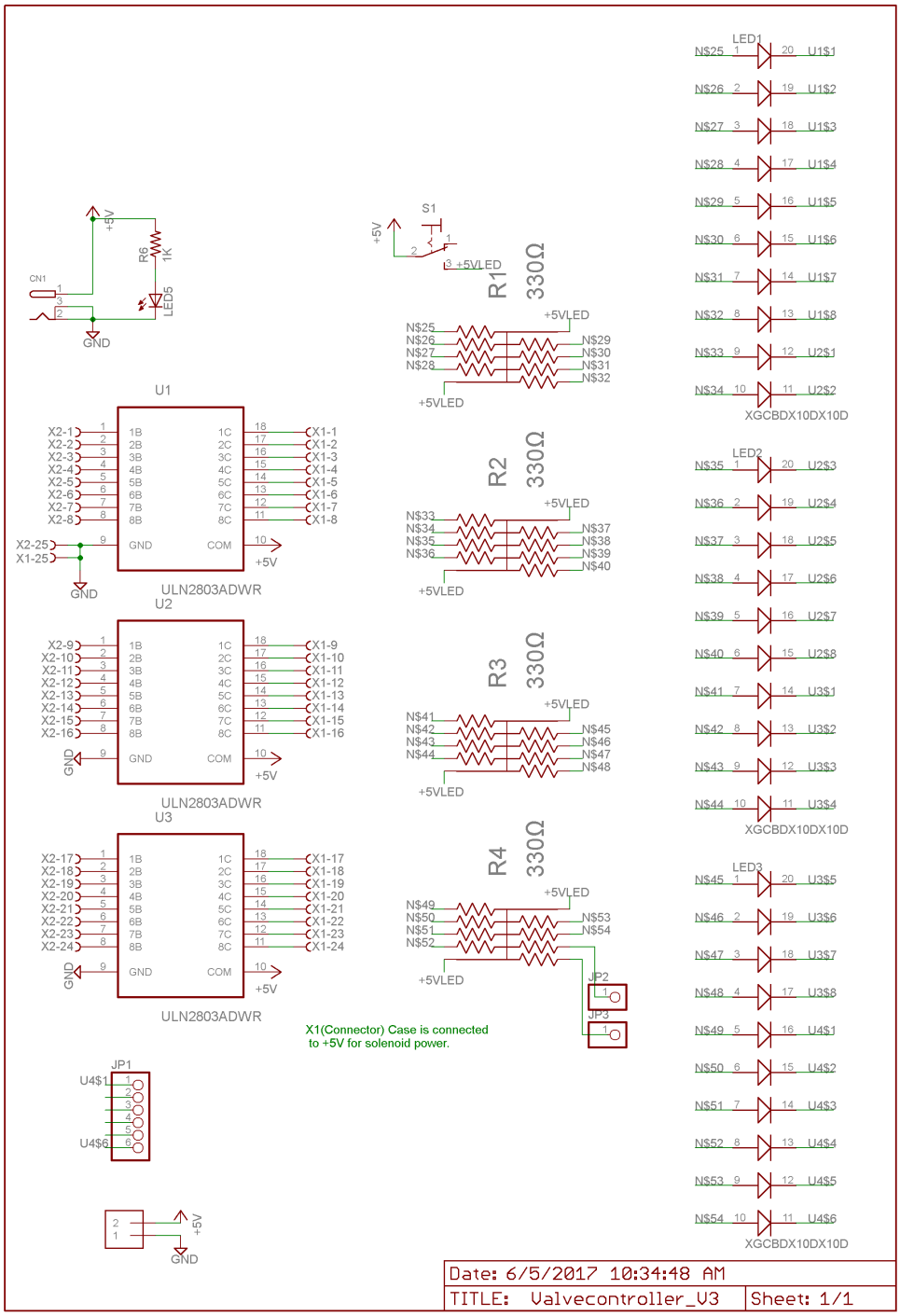

Figure A.6: Valve controller schematic

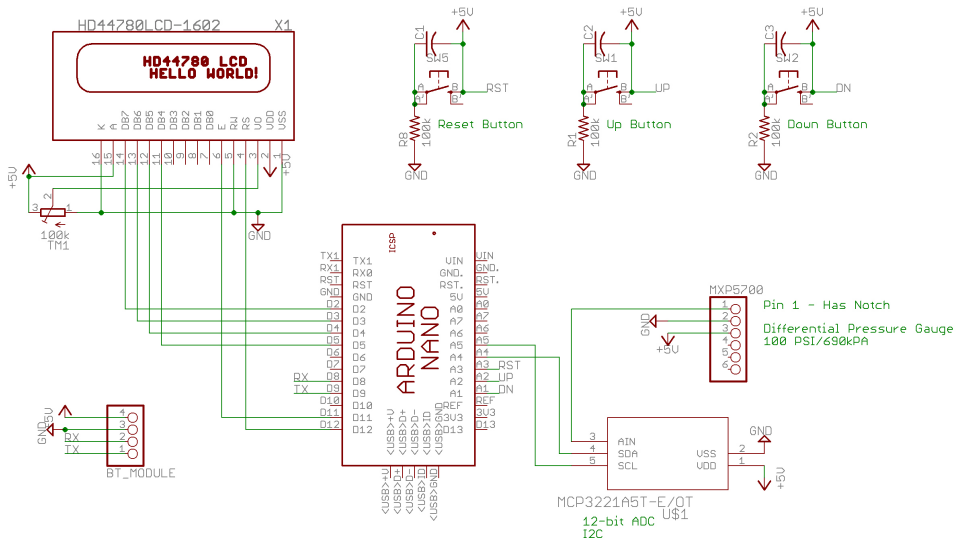

Figure A.7: Arduino pressure meter schematic

A.8 Pressure Meter Circuits

A.8.1 Arduino Pressure Meter

Arduino Pressure Meter Code

```
[code]
//Version 2.5
//This sets up the Arduino to measure pressure as determined by a Motorola MPX5700DP sensor
//Includes function for syringe pump
//Buttons to adjust pressure added
//Added clear function to LCD
//includes choice of PSI or kPa
//slowed LCD refresh for easy reading

/*LCD Parameters 16X2 display
* LCD RS pin to digital pin 12
* LCD Enable pin to digital pin 11
* LCD D4 pin to digital pin 5
* LCD D5 pin to digital pin 4
* LCD D6 pin to digital pin 3
* LCD D7 pin to digital pin 2
* LCD R/W pin to ground
* LCD VSS pin to ground
* LCD VCC pin to 5V
*/

//include ADC library
#include <MCP3221.h>
byte i2cAddress = 0x4D; //others available
const int I2CadcVRef = 4948; //measured reference voltage in millivolts
MCP3221 i2cADC(i2cAddress, I2CadcVRef);
//A4 = SDA A5=SCL

//include software serial for bluetooth logging
#include <SoftwareSerial.h>
SoftwareSerial btSerial(8,9); //RX,TX

//include time element for data logging purposes
#include <elapsedMillis.h>

elapsedMillis timeElapsed; //global time elapsed value

//LCD Parameters
#include <LiquidCrystal.h>
#include <Wire.h>
```

```
41  LiquidCrystal lcd(12, 11, 5, 4, 3, 2);
42
43  //INPUTS
44  int button1=A3;
45  int button2=A2;
46  int button3=A1;
47
48  //OUTPUTS
49  const int PUMP = 6; //sets pump to digital 6
50
51  //variables
52  int collectBaseLine = 80; //Collect half a second of
        baseline values to average together
53  float baseline = 0;
54  float minSensorVoltage=0.2; //The minimum voltage
        from the sensor according to the manufcacturer
55  float maxSensorVoltage=4.7; //The maximum voltage
        from the sensor
56  float maxPinVoltage = 5; //This is the maximum
        voltage an Analog input can read on an Arduino
57  float maxInputValue=4095; //The MCP3221 is a 12-bit
        ADC and reports integers ranging therefore from 0
        to 2^12 - 1 which is 4095
58  float minPressure=0;
59  float maxPressure=700; //The maximum pressure
        capable of detection given in kPa according to the
        manufacturer
60  float PSI=0; //set psi conversion to 0
61  float kPa=0; //set kPa conversion to 0
62  float PressOut; //after conversion to either unit pressure
        is saved in this unit
63  float unitOut; //sets the unit to display
64  float maxRead=0; //maxium reading printout
65  float SetPoint=10; //setpoint for pump to maintain
66  float UPSP=0; //upper limit of system
67  int buttonState1=0; //button state
68  int buttonState2=0; //up button
69  int buttonState3=0; //down button
70  int SP1=10; //variable for setpoint adjust
71
72  int adcRaw = 0; //ADC value
73  int conduct = 0; //set initial conductance value at 0
74
75  //conversion factor assuming a linear relationship (y =
        m*input + b)
76  float maxPinInput = maxInputValue*maxSensorVoltage
        /maxPinVoltage; //this converts the expected
        maximum voltage from the sensor into the
        expected maximum integer value on our input pin
77  float minPinInput = maxInputValue*minSensorVoltage/
        maxPinVoltage; //converts the minimum Voltage
        from the sensor to the relevant number
78  float m = (maxPressure - minPressure)/(maxPinInput
        - minPinInput); //classic slope of line (rise/run)
79  float b = -m*minPinInput + minPressure; //the y-
        intercept
80  float y = 0;
81  int x = 0;
82
83  //running average variables
84  const int numReadings = 10;
85  float readings[numReadings];
86  int readIndex = 0;
87  float total = 0;
88  float average = 0;
89
90  #define kPa //uncomment if PSI unit required
91
92  //the setup routine only runs once when you press reset
93  void setup() {
94  lcd.begin(16,2);
95  lcd.clear();
96  lcd.home();
97  lcd.print(" Pressure Meter");
98  lcd.setCursor(0,1);
99  lcd.print(" Version 2.5");
100 delay(2000);
101
102 Wire.begin(); //intialize I2C communication
103 adcRaw = i2cADC.readI2CADC(); //reads value from
        ADC and stores to adcRaw
104 pinMode(button1, INPUT);
```

```
105  lcd.clear();
106  lcd.home();
107  lcd.print("Calibration");
108  lcd.setCursor(0,1);
109  lcd.print(" Start");
110  delay(2000);
111  int addPressure = 0;
112  int i = 0;
113  for(i = 0; i<collectBaseLine; i++){
114  addPressure = addPressure + i2cADC.readI2CADC();
115  }
116  baseline = addPressure/i;
117  delay(2000);
118  lcd.clear();
119  lcd.print("Measured ");lcd.print(baseline);
120  lcd.setCursor(0,1);
121  lcd.print("Manufact ");lcd.print(minPinInput);
122  delay(3000);
123  lcd.clear();
124  //readjust calibrations
125  minPinInput = baseline;
126  m = (maxPressure - minPressure)/(maxPinInput -
         minPinInput); //classic slope of line (rise/run)
127  b = -m*minPinInput + minPressure; //the y-intercept
128
129  btSerial.begin(9600); //start the bluetooth serial
         connection
130
131  while(buttonState1 < 8){
132  buttonState1 = analogRead(button1); //to escape while
         loop
133  if(buttonState2 = analogRead(button2) > 500) {(SP1 =
         SetPoint + 1);} //increase setpoint by 1 kpa
134  if(buttonState3 = analogRead(button3) > 500) {(SP1 =
         SetPoint - 1);} //decrease setpoint by 1 kpa
135  SetPoint = SP1;
136  lcd.print("Setpoint= ");lcd.print(SetPoint);
137  delay(100);
138  lcd.clear();
139  }
140
141  pinMode(PUMP, OUTPUT); //set pin 6 to output
142  digitalWrite(PUMP,LOW); //set pump pin 6 to low
         initially (not running)
143  UPSP = SetPoint + 1; //set upper limit to 1+ setpoint.
144  lcd.print("Setpoint= ");lcd.print(SetPoint); //print
         current setpoint for user
145  lcd.setCursor(0,1);
146  lcd.print("UpperLimit= ");lcd.print(UPSP);
147  delay(3000);
148
149
150  for (int thisReading = 0; thisReading < numReadings;
         thisReading++)
151  readings[thisReading] = 0;
152
153  } //end of void setup
154
155  void loop() {
156  x = i2cADC.readI2CADC();
157  y = m*x+b; //convert the value read in into kPa
158  if(y > 699){shutdown();} //over pressure loop to alter
         user potential damage to device
159
160  #ifdef kPa
161  PressOut = y;
162  #else
163  PressOut = y*0.145037738; //convert to PSI
164  #endif
165
166  aVe(y);
167
168  if(PressOut > maxRead) { maxRead = PressOut;} //
         read pressure and write maxium pressure
169
170  buttonState1 = analogRead(button1);
171  if(buttonState1 > 500) { maxRead = 0;} //clear max
         value when button pressed
172
173  if(PressOut < SetPoint) {digitalWrite(PUMP,HIGH);}
         //turn syringe pump on at lower limit
```

```
174 if(PressOut >= UPSP) { digitalWrite(PUMP,LOW);}
        //turn syringe pump off at upper limit
175
176 buttonState2 = analogRead(button2);
177 if(buttonState2 > 500) {LCDclear();};
178
179 lcd.clear();
180 lcd.home();
181 //lcd.print("Pressure ");
182 lcd.print(PressOut);
183 btSerial.print(timeElapsed);
184 btSerial.print(" ");//tab delimited
185 btSerial.println(PressOut);
186 /*#ifdef kPa //unit switch between kPa and PSI
187 lcd.print(" kPa");
188 lcd.setCursor(0,1);
189 lcd.print("Max ");
190 lcd.print(maxRead);
191 lcd.print(" kPa");
192 delay(250);
193 #else
194 lcd.print(" PSI");
195 lcd.setCursor(0,1);
196 lcd.print("Max ");
197 lcd.print(maxRead);
198 lcd.print(" PSI");
199 #endif
200 */
201 delay(10); //decreased delay to increase number of
        readings
202 }
203
204 void LCDclear(){ //resets display
205 lcd.begin(16,2);
206 lcd.clear();
207 lcd.home();
208 delay(50);
209 }
210
211 void aVe(float y){
212 total = total-readings[readIndex];
213 readings[readIndex]=y;
214 total = total + readings[readIndex];
215 readIndex = readIndex + 1;
216 if (readIndex >= numReadings)
217 readIndex = 0;
218 average = total / numReadings;
219 lcd.print(" kPa")
220 lcd.setCursor(0,1);
221 lcd.print("Ave ");
222 lcd.print(average);
223 lcd.print(" kPa");
224 delay(150);
225
226 }
227
228 void shutdown(){ //display message that system has
        exceeded max pressure.
229 lcd.clear();
230 lcd.print("**OVERPRESSURE**");
231 btSerial.println("OVERPRESSURE");
232 lcd.setCursor(0,1);
233 lcd.print("****************");
234 delay(10000);
235 }
236
237 [/code]
```

A.8.2 LabVIEW Pressure Meter

LabVIEW Pressure meter VIs

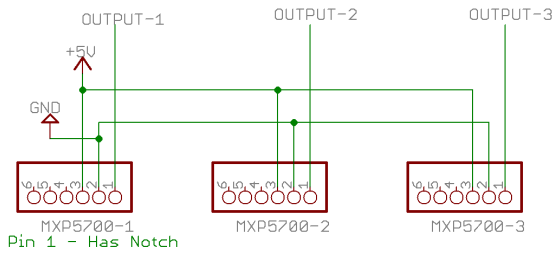

Figure A.8: LabVIEW pressure meter schematic

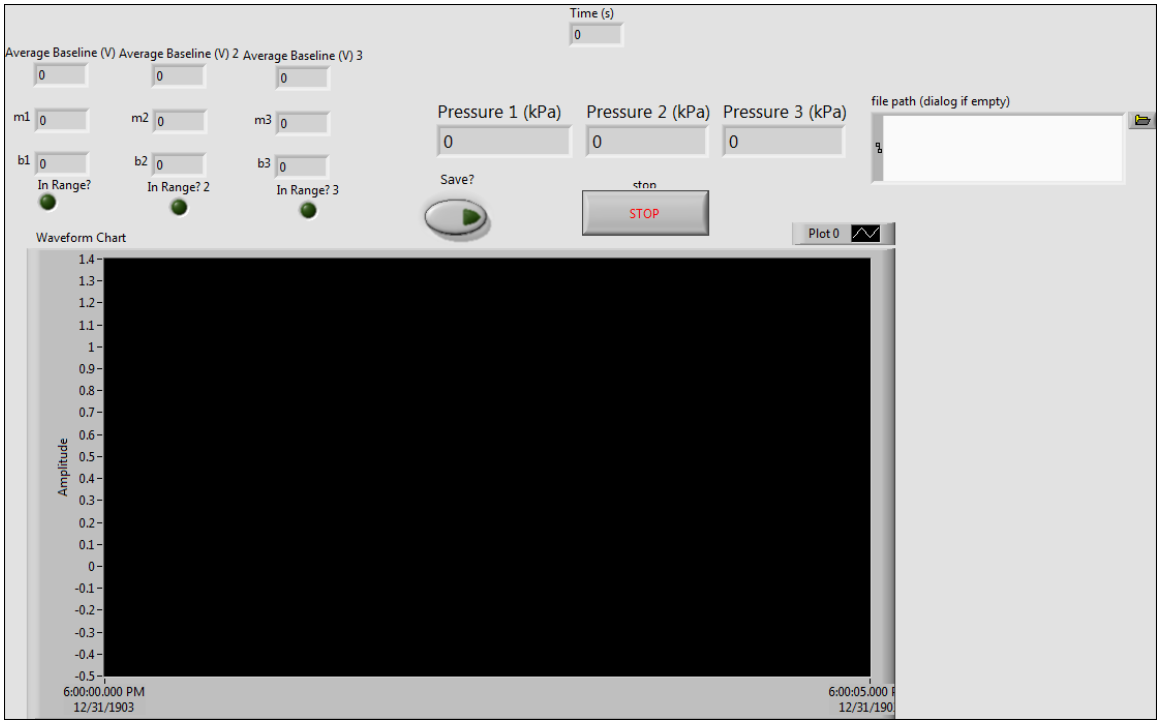

Figure A.9: LabVIEW Pressure Meter, Front Panel.

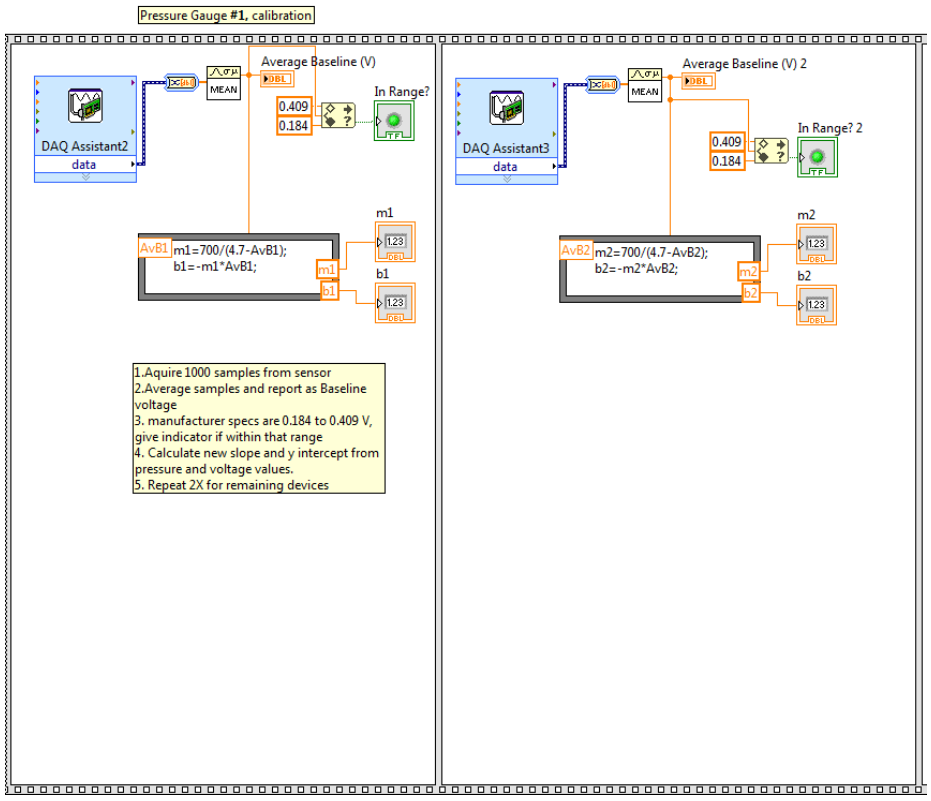

Figure A.10: LabVIEW Pressure Meter,Calibration Frames.

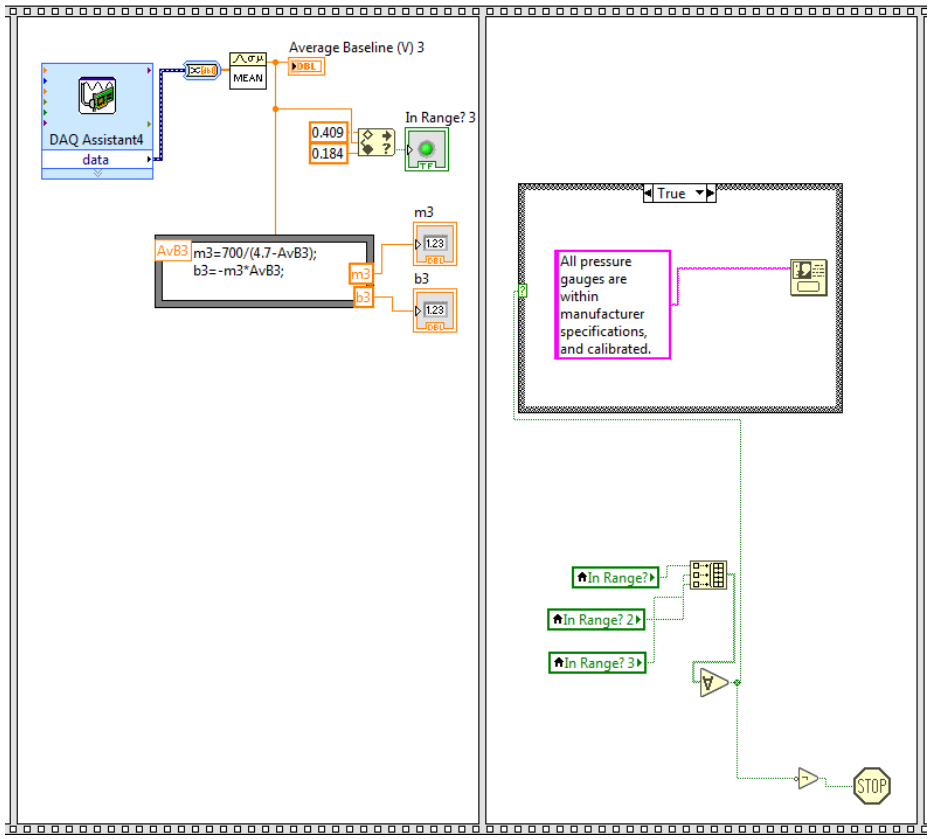

Figure A.11: LabVIEW Pressure Meter, Calibration Frames.

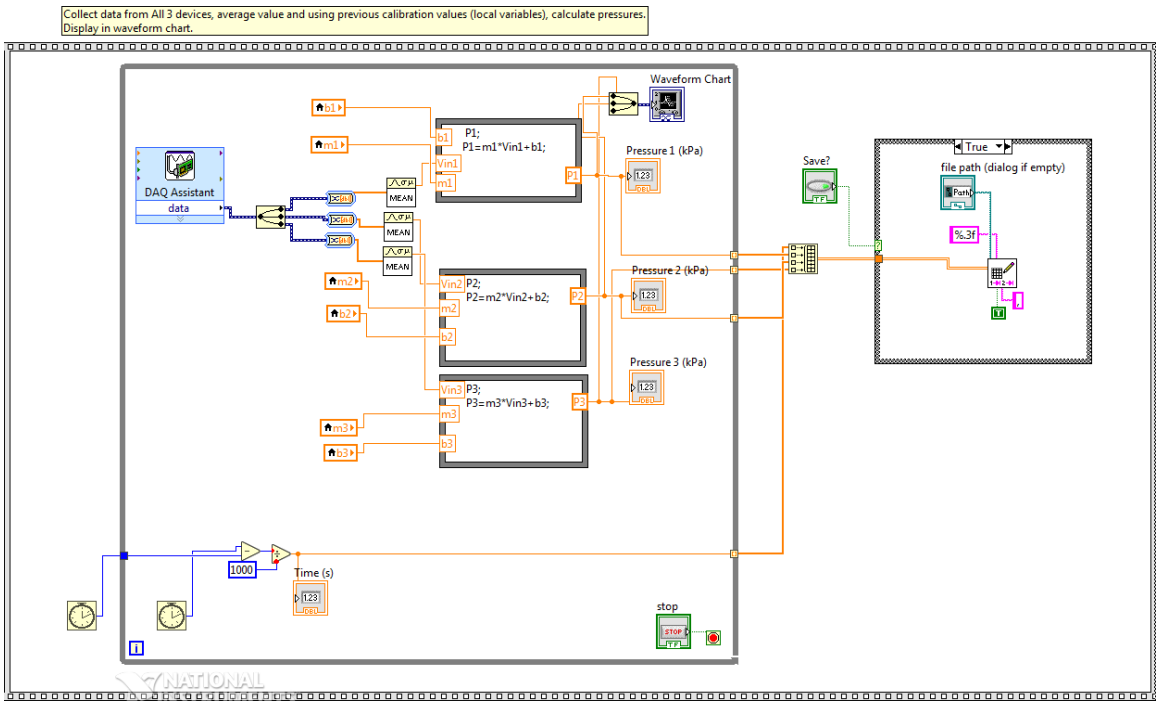

Figure A.12: LabVIEW Pressure Meter, Sensor Read Frame.

Appendix B

Calculations and Data Analysis

B.1 Steinhart-Hart temperature calculations

USP12837 10k resistor Steinhart-Hart equation constants, acquired from directly from USP company. Where R_{in} is the calculated resistance of the thermistor. Temperature output is T in Kelvin and constants are A=0.001126965682122 , B=0.000234474477172 , C=0.000000086313768

$$T_{\text{out}} = \frac{1}{A + B \cdot \ln(R_{\text{in}}) + C \cdot (\ln(R_{\text{in}}))^3} \tag{B.1}$$

B.2 Microfluidic optical measurement processing

Commands for ImageJ. Extracted data from Nikon native format (.nd2) format using NIS-Elements viewer, by File→Export ND→Multi-page TIFF (creates stack of TIFF files). Cropped data region as follows, to maintain same overall area but shifted y axis. Cropped using Edit→Selection→Specify command as follows: X=0, Y=149, W=72 px(full width of image collected), H=788 px, then images cropped in stack. Background contrast corrected (maintain "white" on upper edge channel) as follows Min slider=3100, Max slider=9877 then threshold corrected/converted to 8bit image. Analyze particles (10 pixel →infinity particle size), only bright regions are extracted, then invert image to extract dark regions.

Excel data analysis. Data was exported for each tiff file for all analyzed regions creating csv files, containing all areas for tiff. The first tiff has two ROI's (fluorescence bands), 2 data points were generated with the same time corresponding to the areas of the bands. An excel offset function was used to separate channel information from analyze particles command: OFFSET(reference,rows,columns,height,width). Usage follows: (=OFFSET(AD2,

(ROW(AD2)*3)-5,0) where: AD2 is the data column, and the "starting" point which it references ROW(AD2) either *2 or *3 to extract every 2nd data point or every 3rd data point. "0" is column advance, leave at zero. Create relative data by background correction with 0 kPa lines output. Pressure data is analyzed in full set of data NOT parts, data is imported from pressure sensor, timing between samples is determined, then used to calculate the approximate time. Data is graphed, then fit to a 3-5 order polynomial to then correlate the higher frame rate image data with the pressure sensor data.

Appendix C

Microfluidic Supplemental

C.1 CO_2 Laser Alignment

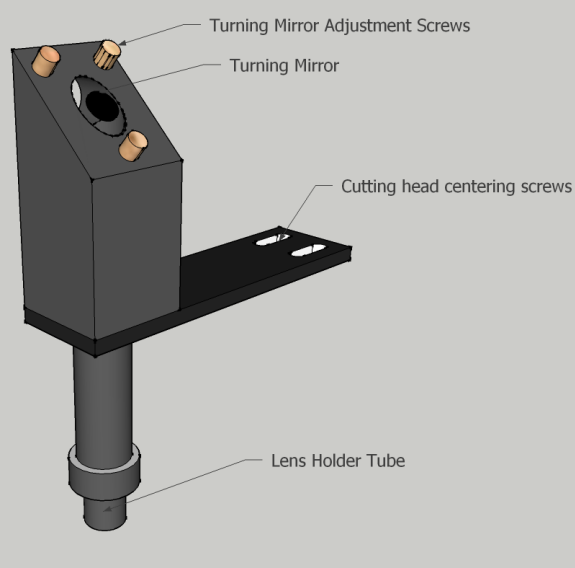

Figure C.1: **CO_2 laser optical module** Optical module contains, a Si turning mirror and a ZnSe 38 mm FL focusing lens

Safety

1. Place the "Alignment" sign on the door and make certain it is closed
2. Wear proper CO_2 laser safety glasses (Block 10.6 μm wavelength)
3. When handling optics wear gloves (preferably lint free cotton), and properly dispose of ZnSe optics.

Alignment Procedure

1. Power on the system including computer/camera

2. Remove the lens holder tube from the end of the cutting head, inspect the lens for damage. Clean if needed, by proper techniques[1].

3. Remove the 45° turning mirror from its mount by using a flat blade screw driver to remove the cap, and gently remove the optic by hand. Inspect for debris and clean as needed. Set the mirror in a dust free location and place a suitable beam visualizing material over the hole.

4. Set the laser system to 100 mS and 15 % power

5. Pulse the laser to identify where the beam is hitting at the turning mirror, if required loosen the cutting head screws and reposition the cutting head.

6. Replace the turning mirror by gently placing it in the mount with the gold side facing the laser head. Gently tighten the screw until resistance is just barely felt, no need to tighten. (the silicon mirror may shatter if compressed)

7. At the open end of the lens holder tube (no focusing lens in place), place a suitable beam visualizing material and pulse the laser again. Using the three screws on the mirror mount (freeing the locking nuts first), adjust the beam until it is in the center of the tube. Re-engage the locking nuts.

8. Replace the lens, flat side facing stage in tube assembly and adjust the working distance from the lens (inside of the tube) to the substrate to 38 mm's.

C.2 PDMS Spin Coating Data

3-year (560 measurements) aggregation of spin speed versus resulting PDMS thickness. All measurements created by slicing PDMS devices, and measuring on Nikon-Ti microscope. Average values for each speed were calculated from the data and plotted in Figure C.2.

[1] II-VIafterCat2012-01.pdf

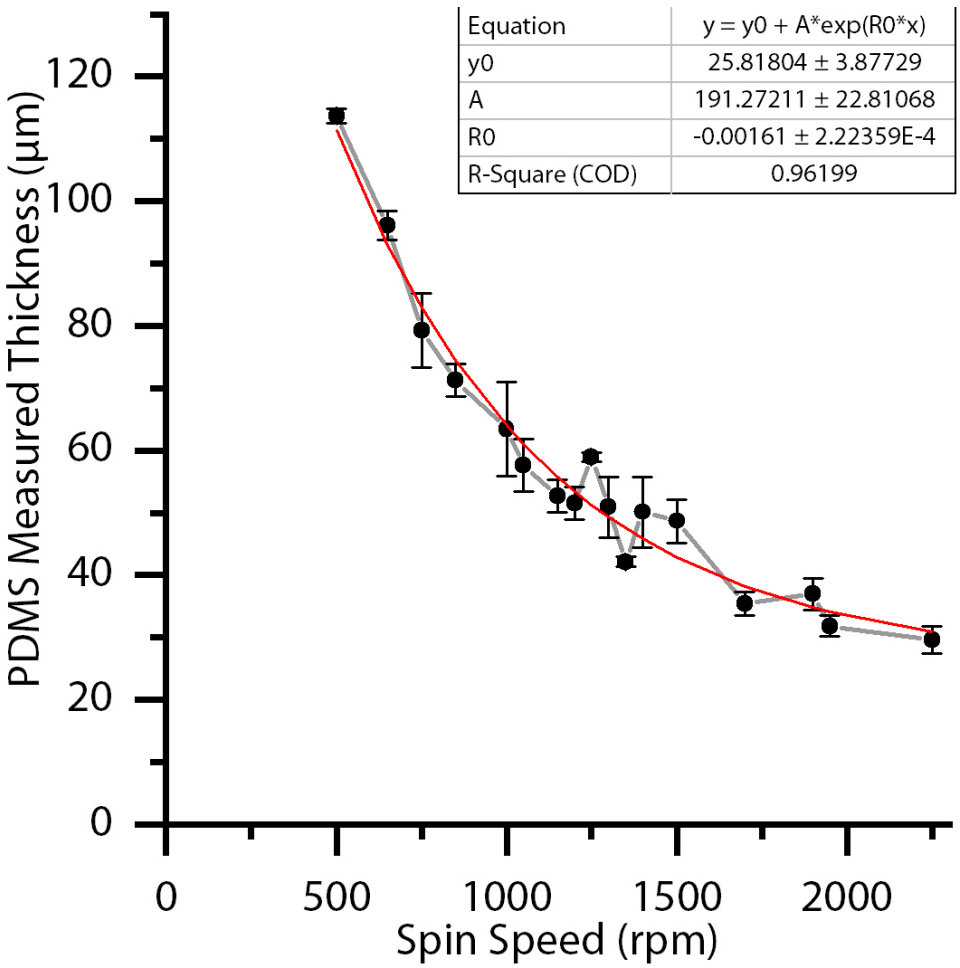

Figure C.2: Spin coating speed vs. measured PDMS thickness.

Appendix D

Copyright Permissions

Copyright Clearance Center

Note: Copyright.com supplies permissions but not the copyrighted content itself.

1 PAYMENT 2 REVIEW 3 CONFIRMATION

Step 3: Order Confirmation

Thank you for your order! A confirmation for your order will be sent to your account email address. If you have questions about your order, you can call us 24 hrs/day, M-F at +1.855.239.3415 Toll Free, or write to us at info@copyright.com. This is not an invoice.

Confirmation Number: 11755921
Order Date: 10/12/2018

If you paid by credit card, your order will be finalized and your card will be charged within 24 hours. If you choose to be invoiced, you can change or cancel your order until the invoice is generated.

Payment Information

Mark Holtan
Auburn University
mdh0035@auburn.edu
+1 (334) 844-6965
Payment Method: n/a

Order Details

Journal of micromechanics and microengineering : structures, devices, and systems

Order detail ID:	71601332
Order License Id:	4446630503603
ISSN:	0960-1317
Publication Type:	Journal
Volume:	
Issue:	
Start page:	
Publisher:	INSTITUTE OF PHYSICS PUBLISHING
Author/Editor:	Institute of Physics (Great Britain) ; American Institute of Physics

Permission Status: Granted
Permission type: Republish or display content
Type of use: Thesis/Dissertation

Requestor type	Academic institution
Format	Print, Electronic
Portion	image/photo
Number of images/photos requested	1
The requesting person/organization	Mark Holtan
Title or numeric reference of the portion(s)	Figure 1
Title of the article or chapter the portion is from	Polydimethylsiloxane based microfluidic diode

Figure D.1

Editor of portion(s)	n/a
Author of portion(s)	MLAdams1, M L Johnston2, A Scherer2 and S R Quake3 1
Volume of serial or monograph	n/a
Issue, if republishing an article from a serial	15
Page range of portion	1517
Publication date of portion	14 June 2005
Rights for	Main product
Duration of use	Life of current edition
Creation of copies for the disabled	no
With minor editing privileges	yes
For distribution to	Worldwide
In the following language(s)	Original language of publication
With incidental promotional use	no
Lifetime unit quantity of new product	Up to 499
Title	Customized instrumentation for small-volume electrochemistry and microfluidics used in bioanalytical applications
Instructor name	n/a
Institution name	n/a
Expected presentation date	Jan 2019

Note: This item will be invoiced or charged separately through CCC's **RightsLink** service. More info **$ 0.00**

Figure D.2

Copyright Clearance Center

Note: Copyright.com supplies permissions but not the copyrighted content itself.

1 PAYMENT 2 REVIEW 3 CONFIRMATION

Step 3: Order Confirmation

Thank you for your order! A confirmation for your order will be sent to your account email address. If you have questions about your order, you can call us 24 hrs/day, M-F at +1.855.239.3415 Toll Free, or write to us at info@copyright.com. This is not an invoice.

Confirmation Number: 11755926
Order Date: 10/12/2018

If you paid by credit card, your order will be finalized and your card will be charged within 24 hours. If you choose to be invoiced, you can change or cancel your order until the invoice is generated.

Payment Information

Mark Holtan
Auburn University
mdh0035@auburn.edu
+1 (334) 844-6965
Payment Method: n/a

Order Details

Chemical Society reviews

Order detail ID:	71601338
Order License Id:	4446631022577
ISSN:	1460-4744
Publication Type:	e-Journal
Volume:	
Issue:	
Start page:	
Publisher:	ROYAL SOCIETY OF CHEMISTRY
Author/Editor:	Royal Society of Chemistry (Great Britain)

Permission Status: Granted
Permission type: Republish or display content
Type of use: Thesis/Dissertation

Requestor type	Academic institution
Format	Print, Electronic
Portion	image/photo
Number of images/photos requested	3
The requesting person/organization	Mark Holtan
Title or numeric reference of the portion(s)	Figures, 3, 4, 5
Title of the article or chapter the portion is from	3D-printing technologies for electrochemical applications

Figure D.3

Editor of portion(s)	n/a
Author of portion(s)	Adriano Ambrosi* and Martin Pumera
Volume of serial or monograph	n/a
Issue, if republishing an article from a serial	45
Page range of portion	2743-2744
Publication date of portion	3rd November 2015
Rights for	Main product
Duration of use	Life of current edition
Creation of copies for the disabled	no
With minor editing privileges	yes
For distribution to	Worldwide
In the following language(s)	Original language of publication
With incidental promotional use	no
Lifetime unit quantity of new product	Up to 499
Title	Customized instrumentation for small-volume electrochemistry and microfluidics used in bioanalytical applications
Instructor name	n/a
Institution name	n/a
Expected presentation date	Jan 2019

Note: This item will be invoiced or charged separately through CCC's **RightsLink** service. More info **$ 0.00**

Figure D.4

JOHN WILEY AND SONS LICENSE TERMS AND CONDITIONS

Oct 10, 2018

This Agreement between Auburn University -- Mark Holtan ("You") and John Wiley and Sons ("John Wiley and Sons") consists of your license details and the terms and conditions provided by John Wiley and Sons and Copyright Clearance Center.

License Number	4445431433100
License date	Oct 10, 2018
Licensed Content Publisher	John Wiley and Sons
Licensed Content Publication	Wiley Books
Licensed Content Title	Electrochemical Methods: Fundamentals and Applications, 2nd Edition
Licensed Content Author	Allen J. Bard Larry R. Faulkner
Licensed Content Date	Dec 1, 2001
Licensed Content Pages	1
Type of use	Dissertation/Thesis
Requestor type	University/Academic
Format	Print and electronic
Portion	Figure/table
Number of figures/tables	1
Original Wiley figure/table number(s)	15.4.5
Will you be translating?	No
Title of your thesis / dissertation	Customized instrumentation for small-volume electrochemistry and microfluidics used in bioanalytical applications
Expected completion date	Jan 2019
Expected size (number of pages)	150
Requestor Location	Auburn University 179 Chemistry Building AUBURN UNIVERSITY, AL 36849 United States Attn: Mark Holtan
Publisher Tax ID	EU826007151
Total	0.00 USD
Terms and Conditions	

TERMS AND CONDITIONS

This copyrighted material is owned by or exclusively licensed to John Wiley & Sons, Inc. or one of its group companies (each a"Wiley Company") or handled on behalf of a society with which a Wiley Company has exclusive publishing rights in relation to a particular work (collectively "WILEY"). By clicking "accept" in connection with completing this licensing transaction, you agree that the following terms and conditions apply to this transaction

Figure D.5

Copyright Clearance Center

Note: Copyright.com supplies permissions but not the copyrighted content itself.

1 PAYMENT 2 REVIEW 3 CONFIRMATION

Step 3: Order Confirmation

Thank you for your order! A confirmation for your order will be sent to your account email address. If you have questions about your order, you can call us 24 hrs/day, M-F at +1.855.239.3415 Toll Free, or write to us at info@copyright.com. This is not an invoice.

Confirmation Number: 11758441
Order Date: 10/21/2018

If you paid by credit card, your order will be finalized and your card will be charged within 24 hours. If you choose to be invoiced, you can change or cancel your order until the invoice is generated.

Payment Information

Mark Holtan
Auburn University
mdh0035@auburn.edu
+1 (334) 844-6965
Payment Method: n/a

Order Details

Lab on a chip

Order detail ID:	71621428
Order License Id:	4453980292311
ISSN:	1473-0189
Publication Type:	e-Journal
Volume:	
Issue:	
Start page:	
Publisher:	ROYAL SOCIETY OF CHEMISTRY
Author/Editor:	Royal Society of Chemistry (Great Britain)

Permission Status: Granted
Permission type: Republish or display content
Type of use: Thesis/Dissertation

Requestor type	Academic institution
Format	Print, Electronic
Portion	image/photo
Number of images/photos requested	1
The requesting person/organization	Mark Holtan
Title or numeric reference of the portion(s)	Figure 2.
Title of the article or chapter the portion is from	Pressure driven digital logic in PDMS based microfluidic devices fabricated by multilayer soft lithography

Figure D.6

Editor of portion(s)	N/A
Author of portion(s)	Naga Sai Gopi K. Devaraju * and Marc A. Unger
Volume of serial or monograph	n/a
Issue, if republishing an article from a serial	n/a
Page range of portion	4811
Publication date of portion	31st August 2012
Rights for	Main product
Duration of use	Life of current edition
Creation of copies for the disabled	no
With minor editing privileges	yes
For distribution to	Worldwide
In the following language(s)	Original language of publication
With incidental promotional use	no
Lifetime unit quantity of new product	Up to 499
Title	Customized instrumentation for small-volume electrochemistry and microfluidics used in bioanalytical applications
Institution name	n/a
Expected presentation date	Jan 2019

Note: This item will be invoiced or charged separately through CCC's **RightsLink** service. More info **$ 0.00**

This is not an invoice.

Total order items: 1 **Order Total: 0.00 USD**

Figure D.7

Copyright Clearance Center

Note: Copyright.com supplies permissions but not the copyrighted content itself.

1 PAYMENT 2 REVIEW 3 CONFIRMATION

Step 3: Order Confirmation

Thank you for your order! A confirmation for your order will be sent to your account email address. If you have questions about your order, you can call us 24 hrs/day, M-F at +1.855.239.3415 Toll Free, or write to us at info@copyright.com. This is not an invoice.

Confirmation Number: 11755904
Order Date: 10/12/2018

If you paid by credit card, your order will be finalized and your card will be charged within 24 hours. If you choose to be invoiced, you can change or cancel your order until the invoice is generated.

Payment Information

Mark Holtan
Auburn University
mdh0035@auburn.edu
+1 (334) 844-6965
Payment Method: n/a

Order Details

Lab on a chip

Order detail ID:	71601260
Order License Id:	4446591328589
ISSN:	1473-0189
Publication Type:	e-Journal
Volume:	
Issue:	
Start page:	
Publisher:	ROYAL SOCIETY OF CHEMISTRY
Author/Editor:	Royal Society of Chemistry (Great Britain)

Permission Status: Granted
Permission type: Republish or display content
Type of use: Thesis/Dissertation

Requestor type	Academic institution
Format	Print, Electronic
Portion	image/photo
Number of images/photos requested	1
The requesting person/organization	Mark Holtan
Title or numeric reference of the portion(s)	Figure 6
Title of the article or chapter the portion is from	Pressure driven digital logic in PDMS based microfluidic devices fabricated by multilayer soft lithography

Figure D.8

Editor of portion(s)	n/a
Author of portion(s)	Naga Sai Gopi K. Devaraju * and Marc A. Unger
Volume of serial or monograph	n/a
Issue, if republishing an article from a serial	12
Page range of portion	4114
Publication date of portion	29th August 2012
Rights for	Main product
Duration of use	Life of current edition
Creation of copies for the disabled	no
With minor editing privileges	yes
For distribution to	Worldwide
In the following language(s)	Original language of publication
With incidental promotional use	no
Lifetime unit quantity of new product	Up to 499
Title	Customized instrumentation for small-volume electrochemistry and microfluidics used in bioanalytical applications
Instructor name	n/a
Institution name	n/a
Expected presentation date	Jan 2019

Note: This item will be invoiced or charged separately through CCC's **RightsLink** service. More info **$ 0.00**

Lab on a chip

Figure D.9

Order detail ID:	71601261
Order License Id:	4446591330038
ISSN:	1473-0189
Publication Type:	e-Journal
Volume:	
Issue:	
Start page:	
Publisher:	ROYAL SOCIETY OF CHEMISTRY
Author/Editor:	Royal Society of Chemistry (Great Britain)

Permission Status: Granted

Permission type: Republish or display content
Type of use: Thesis/Dissertation

Requestor type	Academic institution
Format	Print, Electronic
Portion	image/photo
Number of images/photos requested	1
The requesting person/organization	Mark Holtan
Title or numeric reference of the portion(s)	figure 1
Title of the article or chapter the portion is from	Microfluidic bead-based diodes with targeted circular microchannels for low Reynolds number applications
Editor of portion(s)	n/a
Author of portion(s)	Ryan D. Sochol,*a Albert Lu,b Jonathan Lei,a Kosuke Iwai,a Luke P. Leeb and Liwei Lin
Volume of serial or monograph	n/a
Issue, if republishing an article from a serial	14
Page range of portion	1586
Publication date of portion	28th February 2014
Rights for	Main product
Duration of use	Life of current edition
Creation of copies for the disabled	no
With minor editing privileges	yes
For distribution to	Worldwide

Figure D.10

In the following language(s)	Original language of publication
With incidental promotional use	no
Lifetime unit quantity of new product	Up to 499
Title	Customized instrumentation for small-volume electrochemistry and microfluidics used in bioanalytical applications
Instructor name	n/a
Institution name	n/a
Expected presentation date	Jan 2019

Note: This item will be invoiced or charged separately through CCC's **RightsLink** service. More info **$ 0.00**

This is not an invoice.

Total order items: 2 **Order Total: 0.00 USD**

Figure D.11

Copyright Clearance Center

Note: Copyright.com supplies permissions but not the copyrighted content itself.

1 PAYMENT 2 REVIEW 3 CONFIRMATION

Step 3: Order Confirmation

Thank you for your order! A confirmation for your order will be sent to your account email address. If you have questions about your order, you can call us 24 hrs/day, M-F at +1.855.239.3415 Toll Free, or write to us at info@copyright.com. This is not an invoice.

Confirmation Number: 11755933
Order Date: 10/12/2018

If you paid by credit card, your order will be finalized and your card will be charged within 24 hours. If you choose to be invoiced, you can change or cancel your order until the invoice is generated.

Payment Information

Mark Holtan
Auburn University
mdh0035@auburn.edu
+1 (334) 844-6965
Payment Method: n/a

Order Details

Lab on a chip

Order detail ID:	71601357
Order License Id:	4446640472152
ISSN:	1473-0189
Publication Type:	e-Journal
Volume:	
Issue:	
Start page:	
Publisher:	ROYAL SOCIETY OF CHEMISTRY
Author/Editor:	Royal Society of Chemistry (Great Britain)

Permission Status: Granted
Permission type: Republish or display content
Type of use: Thesis/Dissertation

Requestor type	Academic institution
Format	Print, Electronic
Portion	image/photo
Number of images/photos requested	1
The requesting person/organization	Mark Holtan
Title or numeric reference of the portion(s)	Figure 8
Title of the article or chapter the portion is from	3D printed high density, reversible, chip-to-chip microfluidic interconnects

Figure D.12

Editor of portion(s)	n/a
Author of portion(s)	Hua Gong,a Adam T. Woolley b and Gregory P. Nordin *a
Volume of serial or monograph	n/a
Issue, if republishing an article from a serial	18
Page range of portion	646
Publication date of portion	11th January 2018
Rights for	Main product
Duration of use	Life of current edition
Creation of copies for the disabled	no
With minor editing privileges	yes
For distribution to	Worldwide
In the following language(s)	Original language of publication
With incidental promotional use	no
Lifetime unit quantity of new product	Up to 499
Title	Customized instrumentation for small-volume electrochemistry and microfluidics used in bioanalytical applications
Instructor name	n/a
Institution name	n/a
Expected presentation date	Jan 2019

Note: This item will be invoiced or charged separately through CCC's **RightsLink** service. More info **$ 0.00**

Figure D.13

JOHN WILEY AND SONS LICENSE TERMS AND CONDITIONS

Nov 15, 2018

This Agreement between Auburn University -- Mark Holtan ("You") and John Wiley and Sons ("John Wiley and Sons") consists of your license details and the terms and conditions provided by John Wiley and Sons and Copyright Clearance Center.

License Number	4445630964102
License date	Oct 10, 2018
Licensed Content Publisher	John Wiley and Sons
Licensed Content Publication	Electroanalysis
Licensed Content Title	Square-Wave Voltammetry: A Review on the Recent Progress
Licensed Content Author	Markus Hoth, Reinhard Kappl, Ivan Bogeski, et al
Licensed Content Date	Oct 31, 2013
Licensed Content Volume	25
Licensed Content Issue	11
Licensed Content Pages	12
Type of use	Dissertation/Thesis
Requestor type	University/Academic
Format	Print and electronic
Portion	Figure/table
Number of figures/tables	1
Original Wiley figure/table number(s)	Figure 1
Will you be translating?	No
Title of your thesis / dissertation	Customized instrumentation for small-volume electrochemistry and microfluidics used in bioanalytical applications
Expected completion date	Jan 2019
Expected size (number of pages)	150
Requestor Location	Auburn University 179 Chemistry Building AUBURN UNIVERSITY, AL 36849 United States Attn: Mark Holtan
Publisher Tax ID	EU826007151
Total	0.00 USD
Terms and Conditions	

TERMS AND CONDITIONS

This copyrighted material is owned by or exclusively licensed to John Wiley & Sons, Inc. or one of its group companies (each a"Wiley Company") or handled on behalf of a society with which a Wiley Company has exclusive publishing rights in relation to a particular work

Figure D.14

SPRINGER NATURE

Title: Microfluidics Section: Design and Fabrication of Integrated Passive Valves and Pumps for Flexible Polymer 3-Dimensional Microfluidic Systems

Author: Noo Li Jeon, Daniel T. Chiu, Christopher J. Wargo et al

Publication: Biomedical Microdevices

Publisher: Springer Nature

Date: Jan 1, 2002

Logged in as:
Mark Holtan
Auburn University
Account #:
3001348422

LOGOUT

Order Completed

Thank you for your order.

This Agreement between Auburn University -- Mark Holtan ("You") and Springer Nature ("Springer Nature") consists of your license details and the terms and conditions provided by Springer Nature and Copyright Clearance Center.

Your confirmation email will contain your order number for future reference.

printable details

License Number	4446601022256
License date	Oct 12, 2018
Licensed Content Publisher	Springer Nature
Licensed Content Publication	Biomedical Microdevices
Licensed Content Title	Microfluidics Section: Design and Fabrication of Integrated Passive Valves and Pumps for Flexible Polymer 3-Dimensional Microfluidic Systems
Licensed Content Author	Noo Li Jeon, Daniel T. Chiu, Christopher J. Wargo et al
Licensed Content Date	Jan 1, 2002
Licensed Content Volume	4
Licensed Content Issue	2
Type of Use	Thesis/Dissertation
Requestor type	academic/university or research institute
Format	print and electronic
Portion	figures/tables/illustrations
Number of figures/tables/illustrations	1
Will you be translating?	no
Circulation/distribution	<501
Author of this Springer Nature content	no
Title	Customized instrumentation for small-volume electrochemistry and microfluidics used in bioanalytical applications
Instructor name	n/a
Institution name	n/a
Expected presentation date	Jan 2019
Portions	Figure 1
Requestor Location	Auburn University

Figure D.15

	179 Chemistry Building AUBURN UNIVERSITY, AL 36849 United States Attn: Mark Holtan
Billing Type	Invoice
Billing address	Auburn University 179 Chemistry Building AUBURN UNIVERSITY, AL 36849 United States Attn: Mark Holtan
Total	0.00 USD

ORDER MORE CLOSE WINDOW

Figure D.16

Title: Protein Quantification Using Controlled DNA Melting Transitions in Bivalent Probe Assemblies

Author: Joonyul Kim, Juan Hu, Andresa B. Bezerra, et al

Publication: Analytical Chemistry

Publisher: American Chemical Society

Date: Oct 1, 2015

PERMISSION/LICENSE IS GRANTED FOR YOUR ORDER AT NO CHARGE

This type of permission/license, instead of the standard Terms & Conditions, is sent to you because no fee is being charged for your order. Please note the following:

- Permission is granted for your request in both print and electronic formats, and translations.
- If figures and/or tables were requested, they may be adapted or used in part.
- Please print this page for your records and send a copy of it to your publisher/graduate school.
- Appropriate credit for the requested material should be given as follows: "Reprinted (adapted) with permission from (COMPLETE REFERENCE CITATION). Copyright (YEAR) American Chemical Society." Insert appropriate information in place of the capitalized words.
- One-time permission is granted only for the use specified in your request. No additional uses are granted (such as derivative works or other editions). For any other uses, please submit a new request.

If credit is given to another source for the material you requested, permission must be obtained from that source.

Figure D.17

Copyright Clearance Center

Note: Copyright.com supplies permissions but not the copyrighted content itself.

1 PAYMENT 2 REVIEW 3 CONFIRMATION

Step 3: Order Confirmation

Thank you for your order! A confirmation for your order will be sent to your account email address. If you have questions about your order, you can call us 24 hrs/day, M-F at +1.855.239.3415 Toll Free, or write to us at info@copyright.com. This is not an invoice.

Confirmation Number: 11755902
Order Date: 10/12/2018

If you paid by credit card, your order will be finalized and your card will be charged within 24 hours. If you choose to be invoiced, you can change or cancel your order until the invoice is generated.

Payment Information

Mark Holtan
Auburn University
mdh0035@auburn.edu
+1 (334) 844-6965
Payment Method: n/a

Order Details

Lab on a chip

Order detail ID:	71601254
Order License Id:	4446590597806
ISSN:	1473-0189
Publication Type:	e-Journal
Volume:	
Issue:	
Start page:	
Publisher:	ROYAL SOCIETY OF CHEMISTRY
Author/Editor:	Royal Society of Chemistry (Great Britain)

Permission Status: Granted
Permission type: Republish or display content
Type of use: Thesis/Dissertation

Requestor type	Academic institution
Format	Print, Electronic
Portion	image/photo
Number of images/photos requested	1
The requesting person/organization	Mark Holtan
Title or numeric reference of the portion(s)	Figure 1
Title of the article or chapter the portion is from	Design of pressure-driven microfluidic networks using electric circuit analogy

Figure D.18

Editor of portion(s)	n/a
Author of portion(s)	Kwang W. Oh, Kangsun Lee, Byungwook Ahn and Edward P. Furlani
Volume of serial or monograph	n/a
Issue, if republishing an article from a serial	12
Page range of portion	515
Publication date of portion	22nd November 2011
Rights for	Main product
Duration of use	Life of current edition
Creation of copies for the disabled	no
With minor editing privileges	yes
For distribution to	Worldwide
In the following language(s)	Original language of publication
With incidental promotional use	no
Lifetime unit quantity of new product	Up to 499
Title	Customized instrumentation for small-volume electrochemistry and microfluidics used in bioanalytical applications
Instructor name	n/a
Institution name	n/a
Expected presentation date	Jan 2019

Note: This item will be invoiced or charged separately through CCC's **RightsLink** service. More info **$ 0.00**

Figure D.19

Title: Using Printing Orientation for Tuning Fluidic Behavior in Microfluidic Chips Made by Fused Deposition Modeling 3D Printing

Author: Feng Li, Niall P. Macdonald, Rosanne M. Guijt, et al

Publication: Analytical Chemistry

Publisher: American Chemical Society

Date: Dec 1, 2017

Logged in as:
Mark Holtan
Auburn University
Account #:
3001348422

LOGOUT

PERMISSION/LICENSE IS GRANTED FOR YOUR ORDER AT NO CHARGE

This type of permission/license, instead of the standard Terms & Conditions, is sent to you because no fee is being charged for your order. Please note the following:

- Permission is granted for your request in both print and electronic formats, and translations.
- If figures and/or tables were requested, they may be adapted or used in part.
- Please print this page for your records and send a copy of it to your publisher/graduate school.
- Appropriate credit for the requested material should be given as follows: "Reprinted (adapted) with permission from (COMPLETE REFERENCE CITATION). Copyright (YEAR) American Chemical Society." Insert appropriate information in place of the capitalized words.
- One-time permission is granted only for the use specified in your request. No additional uses are granted (such as derivative works or other editions). For any other uses, please submit a new request.

If credit is given to another source for the material you requested, permission must be obtained from that source.

BACK CLOSE WINDOW

Figure D.20

Title: Replication and Compression of Surface Structures with Polydimethylsiloxane Elastomer

Author: George C. Lisensky, Dean J. Campbell, Katie J. Beckman, et al

Publication: Journal of Chemical Education

Publisher: American Chemical Society

Date: Apr 1, 1999

Logged in as:
Mark Holtan
Auburn University
Account #:
3001348422

LOGOUT

PERMISSION/LICENSE IS GRANTED FOR YOUR ORDER AT NO CHARGE

This type of permission/license, instead of the standard Terms & Conditions, is sent to you because no fee is being charged for your order. Please note the following:

- Permission is granted for your request in both print and electronic formats, and translations.
- If figures and/or tables were requested, they may be adapted or used in part.
- Please print this page for your records and send a copy of it to your publisher/graduate school.
- Appropriate credit for the requested material should be given as follows: "Reprinted (adapted) with permission from (COMPLETE REFERENCE CITATION). Copyright (YEAR) American Chemical Society." Insert appropriate information in place of the capitalized words.
- One-time permission is granted only for the use specified in your request. No additional uses are granted (such as derivative works or other editions). For any other uses, please submit a new request.

If credit is given to another source for the material you requested, permission must be obtained from that source.

BACK CLOSE WINDOW

Figure D.21

Title: Understanding Signal and Background in a Thermally Resolved, Single-Branched DNA Assay Using Square Wave Voltammetry

Author: Subramaniam Somasundaram, Mark D. Holtan, Christopher J. Easley

Publication: Analytical Chemistry

Publisher: American Chemical Society

Date: Mar 1, 2018

PERMISSION/LICENSE IS GRANTED FOR YOUR ORDER AT NO CHARGE

This type of permission/license, instead of the standard Terms & Conditions, is sent to you because no fee is being charged for your order. Please note the following:

- Permission is granted for your request in both print and electronic formats, and translations.
- If figures and/or tables were requested, they may be adapted or used in part.
- Please print this page for your records and send a copy of it to your publisher/graduate school.
- Appropriate credit for the requested material should be given as follows: "Reprinted (adapted) with permission from (COMPLETE REFERENCE CITATION). Copyright (YEAR) American Chemical Society." Insert appropriate information in place of the capitalized words.
- One-time permission is granted only for the use specified in your request. No additional uses are granted (such as derivative works or other editions). For any other uses, please submit a new request.

If credit is given to another source for the material you requested, permission must be obtained from that source.

BACK CLOSE WINDOW

Figure D.22

Title: Poly(dimethylsiloxane) as a Material for Fabricating Microfluidic Devices

Author: J. Cooper McDonald, George M. Whitesides

Publication: Accounts of Chemical Research

Publisher: American Chemical Society

Date: Jul 1, 2002

Logged in as:
Mark Holtan
Auburn University
Account #:
3001348422

LOGOUT

PERMISSION/LICENSE IS GRANTED FOR YOUR ORDER AT NO CHARGE

This type of permission/license, instead of the standard Terms & Conditions, is sent to you because no fee is being charged for your order. Please note the following:

- Permission is granted for your request in both print and electronic formats, and translations.
- If figures and/or tables were requested, they may be adapted or used in part.
- Please print this page for your records and send a copy of it to your publisher/graduate school.
- Appropriate credit for the requested material should be given as follows: "Reprinted (adapted) with permission from (COMPLETE REFERENCE CITATION). Copyright (YEAR) American Chemical Society." Insert appropriate information in place of the capitalized words.
- One-time permission is granted only for the use specified in your request. No additional uses are granted (such as derivative works or other editions). For any other uses, please submit a new request.

If credit is given to another source for the material you requested, permission must be obtained from that source.

BACK CLOSE WINDOW

Figure D.23

SPRINGER NATURE

Title: Integrated elastomeric components for autonomous regulation of sequential and oscillatory flow switching in microfluidic devices

Author: Bobak Mosadegh, Chuan-Hsien Kuo, Yi-Chung Tung, Yu-suke Torisawa, Tommaso Bersano-Begey et al.

Publication: Nature Physics

Publisher: Springer Nature

Date: Apr 18, 2010

Logged in as:
Mark Holtan
Auburn University
Account #:
3001348422

LOGOUT

Order Completed

Thank you for your order.

This Agreement between Auburn University -- Mark Holtan ("You") and Springer Nature ("Springer Nature") consists of your license details and the terms and conditions provided by Springer Nature and Copyright Clearance Center.

Your confirmation email will contain your order number for future reference.

printable details

License Number	4446600104265
License date	Oct 12, 2018
Licensed Content Publisher	Springer Nature
Licensed Content Publication	Nature Physics
Licensed Content Title	Integrated elastomeric components for autonomous regulation of sequential and oscillatory flow switching in microfluidic devices
Licensed Content Author	Bobak Mosadegh, Chuan-Hsien Kuo, Yi-Chung Tung, Yu-suke Torisawa, Tommaso Bersano-Begey et al.
Licensed Content Date	Apr 18, 2010
Licensed Content Volume	6
Licensed Content Issue	6
Type of Use	Thesis/Dissertation
Requestor type	academic/university or research institute
Format	print and electronic
Portion	figures/tables/illustrations
Number of figures/tables/illustrations	1
High-res required	no
Will you be translating?	no
Circulation/distribution	<501
Author of this Springer Nature content	no
Title	Customized instrumentation for small-volume electrochemistry and microfluidics used in bioanalytical applications
Instructor name	n/a
Institution name	n/a

Figure D.24

Expected presentation date	Jan 2019
Portions	Figure 1
Requestor Location	Auburn University 179 Chemistry Building AUBURN UNIVERSITY, AL 36849 United States Attn: Mark Holtan
Billing Type	Invoice
Billing address	Auburn University 179 Chemistry Building AUBURN UNIVERSITY, AL 36849 United States Attn: Mark Holtan
Total	0.00 USD

ORDER MORE CLOSE WINDOW

Figure D.25

Title: Theory of square wave voltammetry
Author: Louis. Ramaley, Matthew S. Krause
Publication: Analytical Chemistry
Publisher: American Chemical Society
Date: Sep 1, 1969

PERMISSION/LICENSE IS GRANTED FOR YOUR ORDER AT NO CHARGE

This type of permission/license, instead of the standard Terms & Conditions, is sent to you because no fee is being charged for your order. Please note the following:

- Permission is granted for your request in both print and electronic formats, and translations.
- If figures and/or tables were requested, they may be adapted or used in part.
- Please print this page for your records and send a copy of it to your publisher/graduate school.
- Appropriate credit for the requested material should be given as follows: "Reprinted (adapted) with permission from (COMPLETE REFERENCE CITATION). Copyright (YEAR) American Chemical Society." Insert appropriate information in place of the capitalized words.
- One-time permission is granted only for the use specified in your request. No additional uses are granted (such as derivative works or other editions). For any other uses, please submit a new request.

If credit is given to another source for the material you requested, permission must be obtained from that source.

BACK CLOSE WINDOW

Figure D.26

Copyright Clearance Center

Note: Copyright.com supplies permissions but not the copyrighted content itself.

1 PAYMENT 2 REVIEW 3 CONFIRMATION

Step 3: Order Confirmation

Thank you for your order! A confirmation for your order will be sent to your account email address. If you have questions about your order, you can call us 24 hrs/day, M-F at +1.855.239.3415 Toll Free, or write to us at info@copyright.com. This is not an invoice.

Confirmation Number: 11755403
Order Date: 10/11/2018

If you paid by credit card, your order will be finalized and your card will be charged within 24 hours. If you choose to be invoiced, you can change or cancel your order until the invoice is generated.

Payment Information

Mark Holtan
Auburn University
mdh0035@auburn.edu
+1 (334) 844-6965
Payment Method: n/a

Order Details

Chemical Society reviews

Order detail ID:	71599981
Order License Id:	4445740430015
ISSN:	1460-4744
Publication Type:	e-Journal
Volume:	
Issue:	
Start page:	
Publisher:	ROYAL SOCIETY OF CHEMISTRY
Author/Editor:	Royal Society of Chemistry (Great Britain)

Permission Status: Granted
Permission type: Republish or display content
Type of use: Thesis/Dissertation

Requestor type	Academic institution
Format	Print, Electronic
Portion	image/photo
Number of images/photos requested	2
The requesting person/organization	Mark Holtan/Auburn University
Title or numeric reference of the portion(s)	Figure 1, and Figure 5
Title of the article or chapter the portion is from	Electrochemical biosensors

Figure D.27

Editor of portion(s)	N/A
Author of portion(s)	Niina J. Ronkainen *a, H. Brian Halsall b and William R. Heineman
Volume of serial or monograph	N/A
Issue, if republishing an article from a serial	39
Page range of portion	1747,1752
Publication date of portion	1st February 2010
Rights for	Main product
Duration of use	Life of current edition
Creation of copies for the disabled	no
With minor editing privileges	no
For distribution to	Worldwide
In the following language(s)	Original language of publication
With incidental promotional use	no
Lifetime unit quantity of new product	Up to 499
Title	Customized instrumentation for small-volume electrochemistry and microfluidics used in bioanalytical applications
Instructor name	n/a
Institution name	n/a
Expected presentation date	Jan 2019

Note: This item will be invoiced or charged separately through CCC's **RightsLink** service. More info **$ 0.00**

Figure D.28